LAWRENCE TECHNOLOGICAL UNIVERSITY

EVALUATION AND ANALYSIS OF DECKED BULB T BEAM BRIDGES

Submitted to

MICHIGAN DEPARTMENT OF TRANSPORTATION
IOWA DEPARTMENT OF TRANSPORTATION
MINNESOTA DEPARTMENT OF TRANSPORTATION
WISCONSON DEPARTMENT OF TRANSPORTATION
OREGON DEPARTMENT OF TRANSPORTATION

Research Administration
Bureau of Field Services
Transportation Pooled Fund Program, Federal Project Number: TPF-5(254)

By

Nabil F. Grace, PhD, P.E., Project Investigator
Mena Bebawy, PhD, Co-Project Investigator

Department of Civil Engineering
Lawrence Technological University
Southfield, MI 48075-1058, U.S.A.

March 2015

TECHNICAL REPORT DOCUMENTATION PAGE

1. Report No. RC-1620	2. Government Accession No.	3. MDOT Project Manager David Juntunen
4. Title and Subtitle Evaluation and Analysis of Decked Bulb T Beam Bridge		5. Report Date March 2015
7. Author(s) Dr. Nabil Grace, Dr. Mena Bebawy, and Marc Kasabasic		6. Performing Organization Code
9. Performing Organization Name and Address Center for Innovative Material Research (CIMR), Dept. of Civil Engineering, Lawrence Technological University, 21,000 West Ten Mile Road, Southfield, MI-48075		8. Performing Org. Report No.
12. Sponsoring Agency Name and Address Michigan Department of Transportation (MDOT) Construction and Technology Division P.O. Box 30049 Lansing, MI-48909		10. Work Unit No. 11. Contract Number: 2010-0293 11(a). Authorization Number:
15. Supplementary Notes		13. Type of Report & Period Covered Final Report, Oct., 2011-Mar. 2015 14. Sponsoring Agency Code

16. Abstract

A new corrosion-free decked bulb T beam bridge system has been developed to overcome some of the problems associated with the construction of side-by-side box beam bridges such as the lack of inspection space between beams and the longitudinal deck cracking. The new bridge system is reinforced and prestressed with carbon fiber reinforced polymer (CFRP) materials instead of the conventional steel reinforcement. In addition, the longitudinal keyways between the top flanges of the beams are grouted using ultra-high performance concrete (UHPC) instead of conventional non-shrink grout. The top flange of the beams with the UHPC shear key joints substitutes the need for a cast-in-place deck slab, a technique that saves time and labor at construction site and ensure the quality control of the product. Through this research project, an experimental investigation and a numerical analysis were conducted to confirm the superiority of the new system. The experimental investigation included the flexural and shear testing of five control beams and a complete bridge model as well, while the numerical analysis was developed, after verification, to evaluate the need for transverse post-tensioning in the system. Results from the experimental investigation and the numerical study indicated that the flexural and shear performance of the new bridge system conforms to the theoretical prediction and the UHPC shear key joints are sufficient to laterally distribute the loads across the bridge width. No signs of longitudinal cracks were observed over the shear key joints of the bridge model even when loading an exterior beam to twice its load carrying capacity. In addition, the CFRP reinforcement was proven to be a proper alternative to steel reinforcement in decked bulb T beams. No premature failure or un-predicable behavior was experienced. The study also showed that a transverse post-tensioning may not be necessary for the system provided that the shear key joints are properly constructed using UHPC. Overall, it can be concluded that decked bulb T beam bridge system with CFRP reinforcement and UHPC shear key joints is an excellent alternative for side-by-side box beam bridge system that promotes expedited construction, access to inspection, reduced maintenance work, and an effective approach to eliminate the longitudinal deck cracking problem.

17. Key Words Decked bulb T beam, bridges, transverse post-tensioning, longitudinal cracks, transverse diaphragms, ultra high performance concrete. CFRP prestressing strands, Un-bonded strands	18. Distribution Statement No Restrictions. This document is available to the public through the Michigan Department of Transportation (MDOT).		
19. Security Classification (Report) Unclassified	20. Security Classification (Page) Unclassified	21. No. of Pages	19. Price

EXECUTIVE SUMMARY

The side-by-side box beam bridge system has been used extensively since 1950s as one of the preferred precast prestressed bridge systems. This is because of its shallow depth, aesthetic appearance, fast and easy construction, needless deck formwork on site, and significant torsional capacity. However, in the last few decades, problems started to emerge with the use of this bridge system, most notably the development of longitudinal deck cracks between the box beams. These cracks often lead to accelerated deterioration of the superstructure as water and deicing chemicals seeps through them into the sides of the beams. With the lack of space between box beams hindering the full inspection and maintenance, early treatment of the deterioration becomes unfeasible. Subsequently, the structural integrity of the bridge becomes comprised over time.

While, extensive effort has been deployed to mitigate the longitudinal deck cracking problem in side-by-side box beam bridges by providing adequate transverse post-tensioning system, the lack of space for inspection and maintenance between beams remains unaddressed. Therefore, this research investigation aims at addressing this problem by offering an alternative to the side-by-side box beam bridge system. The proposed system consists of precast prestressed decked bulb T beams reinforced and prestressed with carbon fiber reinforced polymer (CFRP) materials instead of the conventional steel reinforcement. The new system does not have a separate deck slab. Instead, the flanges of the bulb T beams are connected together to form a smooth riding surface. To ensure a proper lateral load distribution between the beams and to minimize the potential of longitudinal deck cracking, the connection between the beams is cast using ultra-high performance concrete (UHPC) instead of the conventional non-shrink grout that is typically used for cold connections. In addition, the beams are also connected together using transverse diaphragms. Part of the diaphragm may be pre-cast as an integral body of the beam and then the diaphragms are connected together using UHPC. Furthermore, the diaphragms are provided with conduits for possible un-bonded transverse post-tensioning if deemed necessary by the designer, or for future needs.

To verify the concept of the new bridge system, an experimental investigation accompanied by a numerical study was conducted. The experimental investigation included the construction and testing of five control decked bulb T beams and a complete bridge model composed of five beams connected together as mentioned earlier. Several loading scenarios were performed on the control

beams and the bridge model. Four control beams were tested to failure under flexural loading setup. One beam was reinforced and prestressed with conventional steel reinforcement while the other three beams were reinforced with carbon fiber composite cable (CFCC) strands with different reinforcement ratios (under-reinforced, balanced, and over reinforced). The four flexurally tested beams were provided with steel stirrups. On the other hand, the fifth beam was provided with CFCC stirrups and tested under shear loading setup to failure. The bridge model was loaded through three states: service, post-cracking, and strength limit states. The loading was performed with and without transverse post-tensioning system. The strength limit state loading of the bridge model was executed by loading the intermediate beam of the bridge model under four-point loading to failure. The loading was performed without transverse post-tensioning leaving only the UHPC shear keys to distribute the loads to the adjacent beams.

The numerical investigation included two stages of analysis: verification and parametric study. Through the verification stage, the results from the experimental investigation were used to verify the accuracy of the analysis and to adjust different input parameters of the developed numerical model. After adequate confidence was established in the analysis, the second stage was initiated and included modeling prototype decked bulb T beam bridges with widths ranging from 24 ft to 78 ft and spans ranging from 50 ft to 100 ft. The main target of the study was to establish the proper number of transverse diaphragms and to establish the level of transverse post-tensioning force to ensure the integrity of the superstructure and the mitigation of the longitudinal deck cracking. In addition, bridge models with skew angle were also generated to evaluate the relationship between the skew angle and the transverse post-tensioning system.

The experimental investigation and the numerical analysis revealed that decked bulb T beam bridge system is an excellent alternative to side-by-side box beams. It offers the necessary inspection space between beams and maintains its structural integrity to failure. The study also revealed that transverse post-tensioning may not be necessary if the bridge system is provided with adequate number of diaphragms and the connection between the beams are properly constructed using UHPC. Finally, CFCC materials demonstrated its potential as a replacement of steel strands, where corrosion of reinforcement is an issue. The failure loads in all test beams and bridge model surpassed those anticipated by calculations and no premature failure or any unpredictable behavior was experienced.

TABLE OF CONTENT

LIST OF FIGURES

LIST OF TABLES

CHAPTER 1: LITERATURE REVIEW

1.1 Overview

According to Bhide (2008), there are more than 150,000 bridges in United States that are structurally deficient or obsolete and more than 3000 new bridges are added each year. Therefore, there is always a call to build better bridges, reduce travel times, and improve rehabilitation techniques. In addition, the bridge rehabilitation process is often faced with strict and tight schedule to avoid possible traffic interruption.

Accelerated bridge construction (ABC) is gaining popularity daily because of its exceptional benefits such as: reducing onsite construction time, minimizing traffic disruption, reducing environmental impact, improving worker and motorist safety, improving constructability, and increasing the quality of the final product. The increased quality of the final product comes as a result of the increased quality control, adequate cure time, ease of access, and controlled environment. Some projects have been executed in different states using some of the ABC techniques. For instance, for the George Washington Memorial Parkway Bridge, in Virginia, the deck was replaced using precast panels in 2002 while the bridge was open for traffic on weekdays. For the Live Oak Creek Bridge, in Texas, 86 full-depth and full-width precast deck panels were erected over the beams using shear studs to form the deck for a 700-ft long, 32-ft wide bridge with a total surface area of around 22,400 ft^2. Fiber reinforced polymer (FRP) deck replacement was employed in the rehabilitation of the Rt. 24 Bridge over Deer Creek, MD in 2001.

Side-by-side precast prestressed box beam bridges are considered one of the most common ABC techniques. They are commonly used in the construction of short and medium-span highway bridges in the United States. The superstructure of a side-by-side box beam bridge can be assembled in a few days and does not require formwork to support the deck slab. However, longitudinal deck cracking between adjacent box beams has been reported frequently in this type of bridge superstructure. For instance, out of 219 adjacent box beam bridges constructed in the state of New York (NYSDOT 1992) between 1985 and 1990, 101 bridges exhibited longitudinal deck cracking that extended as far as from support to support. Deck cracking was identified as one of the major causes for deck deterioration in some nation-wide surveys (Grace et al. 2007 and Koch et al. 2001). When deck cracking occurs, water and deicing agents penetrate into the sides

of the box beams and cause spalling of concrete and corrosion of steel reinforcement. Meanwhile, the lack of space between the adjacent beams hinders the regular inspection and maintenance. Consequently, with such accelerated deterioration and absence of preventive maintenance, the bridge engineer is compelled to replace the bridge superstructure after a shorter lifespan.

An appropriate solution for the problem of deck cracking and deterioration in side-by-side box beam bridges can be executed on three different levels: (1) modifying the cross section of the bridge superstructure to allow enough space between the beams for inspection and maintenance, (2) modifying the connection between adjacent beams to ensure the integrity of the superstructure and eliminate the development of longitudinal deck cracking, and (3) replacing the steel reinforcement of the beams with corrosion-free reinforcement such as CFRP reinforcement to extend the service lifespan of the bridge superstructure.

By addressing all three levels of the solution, the current investigation provides the bridge construction community with an innovative corrosion-free ABC system. The outlines for the investigation were established by conducting a detailed literature review presented through the following subsections. The detailed literature review highlights the current challenges associated with the use of side-by-side box beam bridges along with the possible solutions.

1.2 Side-by-side box beam bridges

Precast prestressed concrete side-by-side box beams are widely used in short and medium-span highway bridges because of their simple design, low life cycle costs, quick and easy construction, and low depth-to-span ratio. Side-by-side box beam bridges are strong, tough, durable, and attractive in appearance. Different techniques can be used in side-by-side beam bridge construction. For instance, in Michigan, the superstructure (Figure 1.2-1) is constructed by: (1) placing precast, prestressed concrete box beams adjacent to each other with gaps of a width ranging from 1.5 in. to 3.0 in. (38 mm to 76 mm), (2) filling the gaps between the box beams with a non-shrink grout to form interlocking full-depth shear keys, (3) applying transverse post-tensioning (TPT) through transverse diaphragms, and (4) casting a 3 to 6-in.-thick reinforced concrete deck slab. Successful integration of the box beams, shear keys, transverse post-tensioning, and the deck slab enables the bridge to behave monolithically.

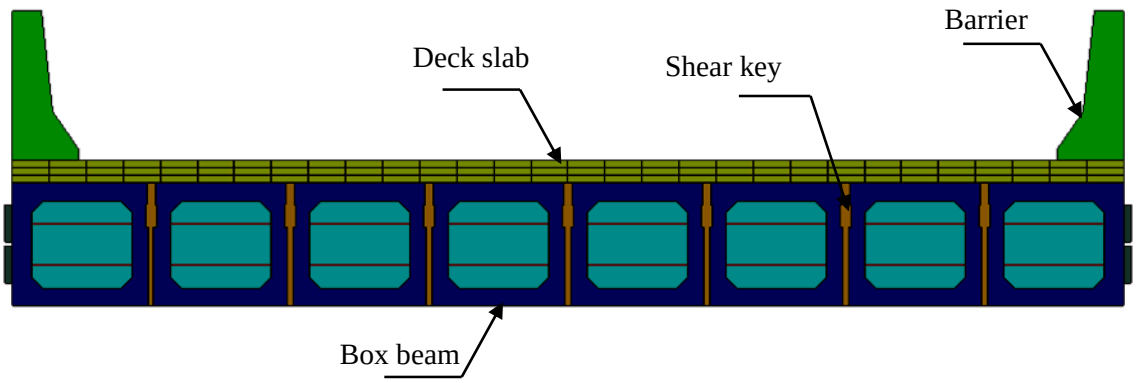

Figure 1.2-1 Typical cross section of side-by-side box beam bridges

The development of longitudinal cracks in the deck slab between the box beams is a major concern (Figure 1.2-2 and Figure 1.2-3) and is frequently reported by inspectors (MDOT 2005 and Lall et al. 1998). For instance, in 1990, an investigator from New York State Department of Transportation reported longitudinal cracks over the concrete overlay shortly after construction. A survey was conducted immediately after the report and included 219 bridges constructed between the years 1985 and 1990 in the state of New York. The results from the survey indicated that 54 % of the bridges built within the given period experienced longitudinal cracking as shown in Table 1.2-1 (Lall et al. 1998). The survey also indicated that longitudinal cracks extended from support to support in many bridges with a crack width in a range of 1/32 to 1/16 in.

Figure 1.2-2 Crack development along the joints in side-by-side box beam bridges

Table 1.2-1 NYSDOT survey for box-beam bridges in 1990 (Lall et al. 1998)

Year built	No. of bridges inspected	No. of bridges with longitudinal cracks	Percent Cracking
1985	36	22	61
1986	34	18	53
1987	36	21	58
1988	33	15	45
1989	34	19	56
1990	14	6	43
Total	187	101	54

Figure 1.2-3 Deterioration of box beams at the shear key joints

Based on the above survey and investigation, NYSDOT concluded that the longitudinal cracks developed due to differential rotation of the beams and the shear key joints were incapable of restraining the differential rotation. In addition, it was concluded that the location of transverse post-tensioning tendons and the number of tendons were also important factors to avoid longitudinal cracking. Furthermore, the research report by NYSDOT suggested that improper location of post-tensioning tendons may lead to the application of eccentric forces on box-beams, which causes differential rotation of the bridge model and results in longitudinal cracking.

Gilbertson et al. (2006) attributed the development of longitudinal cracks to the improper and irregular maintenance along with improper construction techniques. On the other hand, Martin and Osborn (1983) attributed the development of cracks to the poor design of the joints, which degrades their ability to transfer both bending and shear and avoid differential rotation between the bridge components. This was restated by Lall et al. (1998), who assumed that the inability of the longitudinal joints to transfer moments in transverse direction led them to behave as elastic hinges.

Hlavacs et al. (1996) conducted non-destructive tests on shear keys by exposing them to environmental and structural cyclic loading and concluded that longitudinal cracks might initiate as early as immediately after casting the shear keys due to thermal strains. These cracks may propagate partially or fully through the shear key joints. In addition, it was seen that the cracks initiated by thermal strain propagated in the longitudinal direction and through the shear key depth after repeated cyclic loading.

Cracking and failure of the shear key joints leads to the failure of the bridge waterproofing system, which in turn allows water and deicing chemicals to penetrate into the sides of the box beams and cause corrosion of the steel reinforcement with associated concrete spalling. Over time, this deterioration requires costly repairs ranging from concrete patching to deck or beam replacement, or in some severe cases to superstructure replacement.

To mitigate longitudinal deck cracking, different methods have been developed to analyze and design the connection between the box beams. For example, Bakht et al. (1983) assumed that the load is transferred from one beam to another primarily through transverse shear, while transverse flexural rigidity may be neglected. El-Remaily et al. (1996) determined the required transverse post-tensioning force based on flexural rigidity and the lateral moment due to moving traffic. The methods used for analyzing the shear key joint assume that traffic loads are responsible for the

initiation and propagation of longitudinal cracks in side-by-side box beam bridges. However, some experimental investigations indicated that stresses associated with thermal gradients were the main cause of crack initiation, while crack propagation was controlled by traffic loads (Miller et al. 1999). A recent experimental/numerical study (Grace et al. 2008) confirmed that temperature gradients initiate the longitudinal shear key cracks, which propagate with applying traffic loads. Grace et al. (2008) recommended adjusting the transverse post-tensioning system based on the bridge geometry in order to mitigate the longitudinal deck cracking between the box beams.

In summary, side-by-side box beam bridges, though very popular and efficient, come along with several durability issues primarily due to the improper design of the connections between the beams and the lack of adequate space between them. This lack of space impedes the procedure of regular inspection and maintenance. In addition, using non-shrink grout for filling the shear keys was proven inadequate through several research and field investigations. Furthermore, in case of beam replacement, the grouted transverse post-tensioning strands are often abandoned. Therefore, even partial maintenance or replacement of side-by-side box beam bridges can be a complex procedure and may jeopardize the structural integrity of the entire superstructure.

1.3 Decked bulb T beam bridges

A bulb T beam bridge superstructure may be regarded as a potential alternative to a box beam bridge superstructure. This type of superstructure has emerged rapidly in bridge design and construction during the last few decades. Several design agencies have implemented bulb T beams in their design guidelines with some differences in dimensions and construction techniques. For example, Utah Department of Transportation (UDOT) uses three classes to categorize bulb T beam bridges according to construction technique. These classes are: (1) Bulb T beams with concrete deck, (2) decked bulb T beams without concrete deck, and (3) post-tensioned bulb T beams with concrete deck and post-tensioning strands. Likewise, Washington State Department of Transportation (WSDOT) provides details for both bulb T beams with deck and decked bulb T beams without decks (WSDOT 2008).

Examples for the construction of decked bulb T beams can be traced back to 1986 with the construction of a six-span prestressed concrete decked bulb T beam bridge in Minnesota (Hill et al. 1988). Each span was assembled with five adjacent decked bulb T beams that had a depth of 40 in. and top flange width of 6 ft. The end spans had a length of 70 ft, while the interior spans had

a length of 85 ft. Steel bars with a diameter of 1.0 in. were used to transversely post-tension the top flange.

In 1987, a 142-ft long three-span continuous decked bulb T beam bridge was built in the Southeast of Forks, Washington over South Fork Hoh River (Owen 1987). The bridge replaced a 22-year old deteriorated wooden bridge. The new bridge deck was composed of three decked bulb T beams with a depth of 42.5 in. (Figure 1.3-1). The beams were designed as simply supported for dead loads and continuous for live loads. The continuity of the spans was achieved by applying post-tensioning force of 300 kips through draped post-tensioned strands (Figure 1.3-2). An intermediate diaphragm made of galvanized steel pipes was placed at the location of the maximum bending moment in each span. In addition, no end blocks were provided at the location of the interior supports.

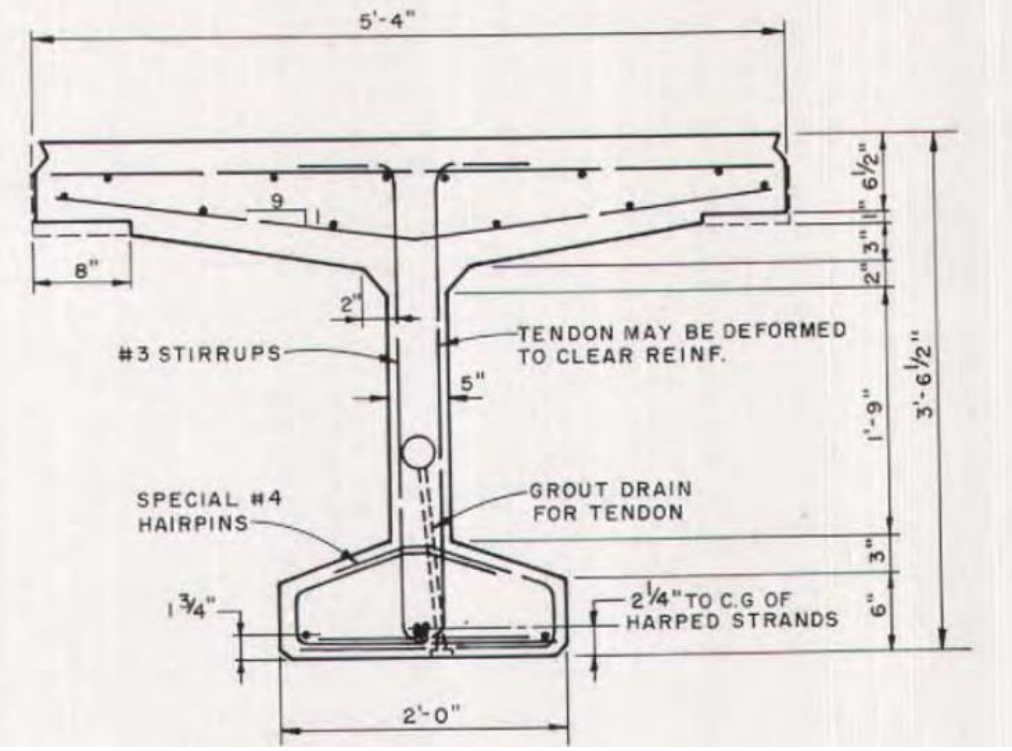

Figure 1.3-1 Cross section of decked bulb T beam used for bridge construction (Owen 1987)

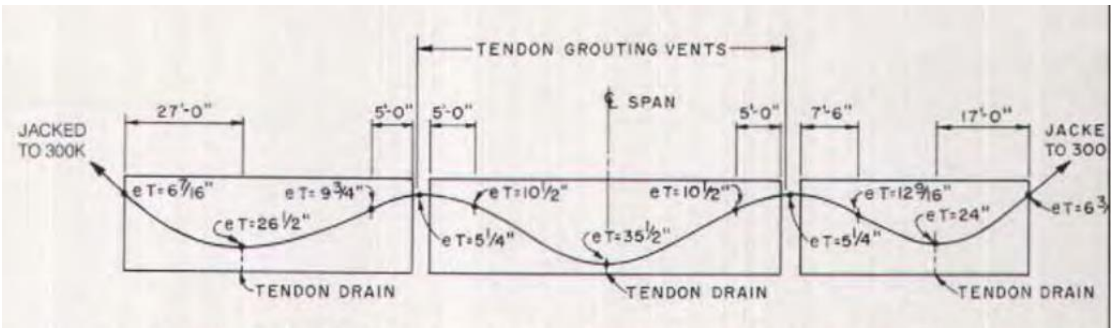

Figure 1.3-2 Layout of postensioning strands in the bridge deck (Owen 1987)

In 2009, a decked bulb T beam bridge was constructed in Kittitas County, WA to replace a deteriorated bridge. The beams were interconnected using welded steel joints. In addition, to overcome longitudinal joint leakage, the new bridge was provided with a waterproof membrane in addition to an asphalt emulsion used to hold the membrane in place.

In spite of their benefits, the use of decked precast, prestressed concrete girders has been limited because of concerns regarding certain design and construction issues that may affect the structural integrity of the bridge system. These concerns include the connections between adjacent units, longitudinal joints, longitudinal camber, cross slope, live load distribution, live load continuity, lateral load resistance, skew effects, maintenance, replaceability and other factors that influence constructability and performance (Oesterle et al. 2009). Therefore, some states (e.g. Washington) impose restrictions on the use of this system for roads with high average daily traffic (ADT) and for continuous bridges.

A recent research project was conducted jointly between the University of Minnesota–Twin Cities and the University of Tennessee–Knoxville. This research project was used to evaluate the performance of cast-in-place connections between decked bulb T beams. The research project investigated different reinforcement details for the connection and different grout materials (French et al. 2011). An experimental phase was executed to test connection specimens under static and cyclic loading. Based on the results of the research project, the research team recommended specific reinforcement configurations and grout materials. However, the realistic performance of the shear key connection was not evaluated. It should be noted that the experimental investigation showed the development of undesirable wide cracks under service loads when high grade steel

reinforcement was used for the connections because a less amount of reinforcement crossed the interface.

Oesterle and Elremaily (2009) focused on the development of design guidelines for precast prestressed decked girder bridges. The guidelines included the design of the longitudinal joints between the flanges of adjacent girders. This was defined as a major issue inhibiting the general use of decked girders. From that research project, an improved joint was proposed. The improved joint included headed reinforcing bars lap spliced to develop moment and shear continuity in narrow grouted joints. The findings of the study indicated that the improved joint detail was viable in transferring the force between adjacent decked bulb T girders.

Through a finite element analysis, Li et al. (2010) studied the effects of adding intermediate diaphragms to the decked bulb T beam bridge system. The research project addressed aspects such as deflections and flexural strains in the beams at the mid-span. Steel and concrete diaphragms were considered. The study showed that at least one intermediate diaphragm should be provided at the mid-span regardless of the diaphragm details, which did not seem to influence the deflection of the girders or the strain level. On the other hand, the influence of having intermediate diaphragms on the deflection of the beams was more prominent in short-span bridge models than in long-span bridge models.

In summary, decked bulb T beam bridges can be a promising technique for ABC if the issues regarding the connection between the beams are fully investigated and resolved. Therefore, special attention is given in the current investigation to the connection design. An in-depth literature review and analysis was performed to evaluate the performance of shear key connections between adjacent decked bulb T beams.

1.4 Shear key joints in decked bulb T beam bridges

The current practice for constructing the shear key joints is to fill the gaps between adjacent precast concrete elements with a no-shrink grout. However, the adequacy of this practice has been critically questioned with the development of longitudinal shear key cracks under high traffic volumes or under harsh environmental conditions (Miller et al. 1999). Some jurisdictions and districts recommend extending the reinforcement from the precast units to form the reinforcement of the shear key connections. However, there was always a concern regarding the development

length of the extended reinforcement because the shear key connection is usually narrow, within the range from 3 to 6 in. wide. Therefore, the extended reinforcement may need to have different configurations to ensure an adequate development length over a relatively narrow connection (Figure 1.4-1 and Figure 1.4-2). Other districts recommend providing welded steel joints at intervals along the span of the bridge (Figure 1.4-3). This practice has often been criticized due to problems associated with the crack development over the distances between the welded steel plates (French et al. 2011).

Figure 1.4-1 Reinforcement configuration for shear key connections (French et al. 2011)

Figure 1.4-2 Headed reinforcement for shear key connections (Oesterle and Elremaily 2009)

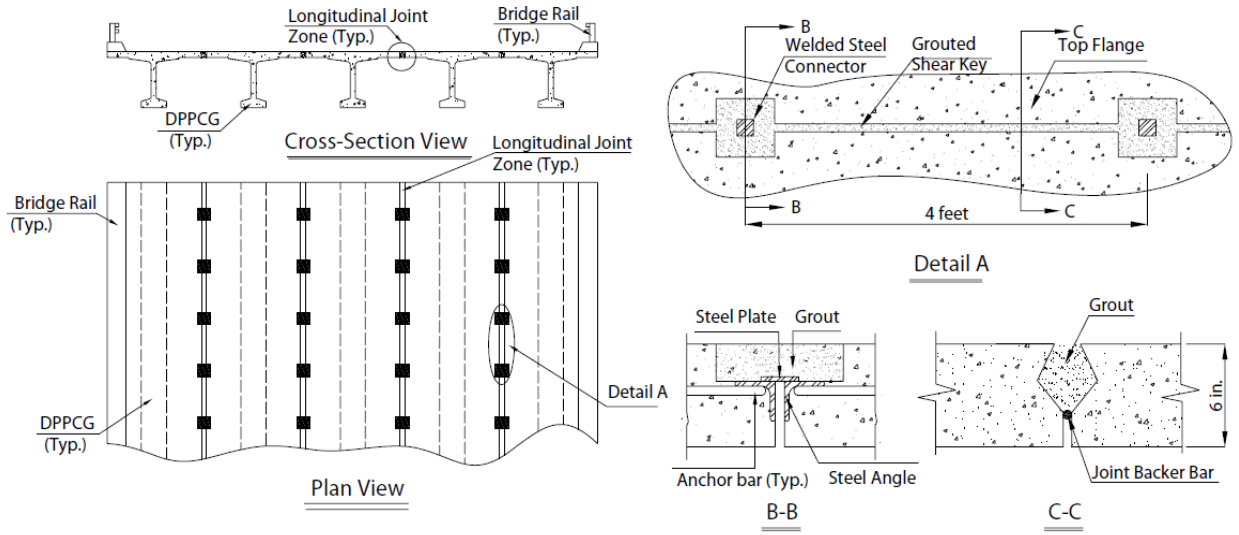

Figure 1.4-3 Former techniques in constructing the connection between decked bulb T beams using welded steel connectors (French et al. 2011)

With the development of advanced engineering materials, alternatives to the non-shrink grout have emerged. A plausible alternative to the non-shrink grout is the ultra-high performance concrete (UHPC). The innovation of UHPC can be traced back to Bache (1981), who developed the approach of manufacturing a tightly packed dense concrete matrix to increase both tensile and compressive strength. Steel fibers are added to overcome the brittleness of the material that arises due to the dense matrix. The dense matrix ensures strong bond to the fibers that increases the post cracking strength as long as high strength fibers are used. UHPC is designed for use in the elastic stage so the fibers action becomes effective only when the ultimate limit state is approached. UHPC is slightly heavier than normal weight concrete with an average unit weight of 156 lb/ft^3.

The uniaxial stress-strain behavior of UHPC differs from conventional concrete in several ways. Most notably, the UHPC can achieve a compressive strength of 26 ksi (Figure 1.4-4) and direct tensile strength in excess of 1.5 ksi. UHPC exhibits tensile capacity exceeding the initial tensile cracking and maintains this tensile capacity until pullout of the fiber reinforcement. At fiber pull out, the average tensile strain of the UHPC is 0.007 (Graybeal 2006). In addition, when subjected to compression, UHPC exhibits a significantly more linear stress-strain response than that observed in normal weight concrete.

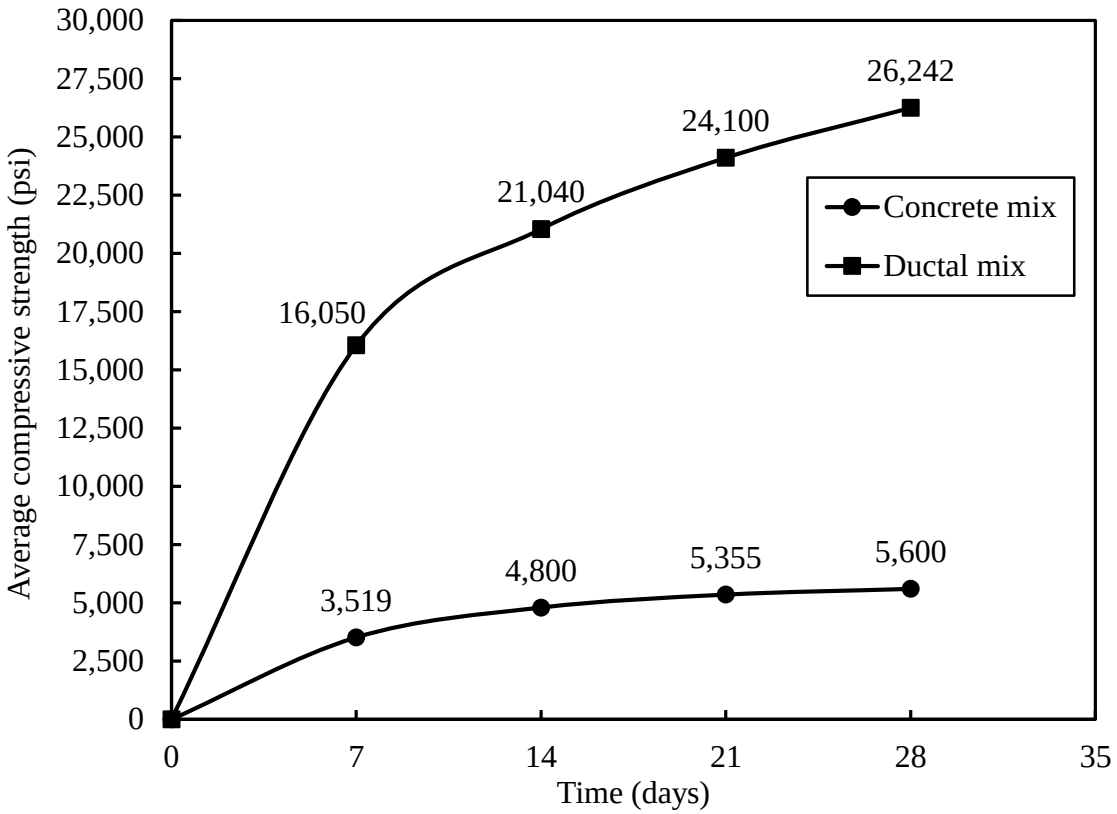

Figure 1.4-4 Compressive strength of UHPC vs. compressive strength of regular-mix concrete

A typical composition of UHPC is shown in Figure 1.4-5. This innovative material can be classified as a reactive powder concrete. It is a special type of ultra-high-strength superplasticized fiber-reinforced silica fume concrete, with improved homogeneity. Traditional coarse and fine aggregate are replaced by fine sand with particle sizes in the range of 4-16 thousands of an inch (Shaheen et. al., 2007). A commercially available UHPC is manufactured by Lafarge under a commercial name Ductal®. The components of Ductal® are micro silica, silica fumes, cement, quartz sand, superplasticizer, and short fibers. Steel or polyvinyl alcohol (PVA) fibers have been used successfully with the dense concrete mix. However, durability issues related to the corrosion of steel fibers remain a concern.

Through various experimental investigations, Ductal® has shown exceptional high strength and durability (Perry and Zakariasen 2004). For instance, Ductal® can achieve a compressive strength ranging from 22 to 28 ksi, a flexural strength ranging from 2.2 to 3.6 ksi, and a modulus of elasticity ranging from 6,500 to 7,300 ksi. Ductal® has a relative dynamic modulus (RDM) of 112 % under

freeze/thaw cycles (ASTM C666). It also has abrasion loss of less than 0.026 oz (ASTM C944) and chloride ion (CL^-) permeability less than 0.10 lb/yd^3 (AASHTO T259).

Small brass-coated steel fibers with a diameter of 0.008 in and a length of 0.5 in. are commonly used as fiber reinforcement in Ductal®. Synthetic fibers such as poly-vinyl alcohol have also been used (Parsekian et al. 2008). Besides their structural performance, the added fibers enhance the overall durability of the mix by changing the cracking pattern from a few large cracks to many small cracks. Wide cracks allow for intrusion of aggressive solutions. However, small and tight cracks prevent water and solutions from seeping into the concrete and thereby reduce the permeability of the element. The low permeability of Ductal® enhances various durability aspects such as the resistance to freeze and thaw cycles, which in turn leads to an extended service life and reduced maintenance costs.

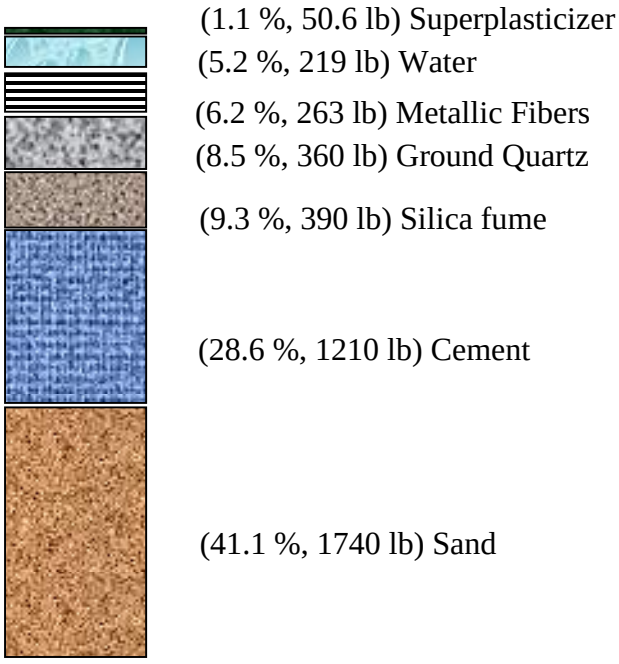

Figure 1.4-5 Components of UHPC Ductal® by weight for one cubic yard

UHPC was first used in the bridge industry in the construction of a pedestrian bridge in Quebec, Canada in 1997. Another pedestrian bridge in South Korea and a highway bridge in France were also constructed using UHPC in 2002. In 2006, the Iowa DOT worked cooperatively with Wapello County and Bridge Engineering Center (BEC) at Iowa State University (ISU) to design, construct, and evaluate the first UHPC bridge built in the United States. The simply supported bridge had a span of 110 ft and a deck width of 27 ft. The bridge was constructed using three UHPC modified I-shaped girders (Figure 1.4-6 and Figure 1.4-7). Other components of the bridge, including the deck slab and diaphragms, were constructed using a conventional concrete mix. The second use of UHPC beams in the U.S.A. was for the Jakway Park Bridge in Buchanan County, Iowa. Three UHPC Π-shaped beams with a length of 51ft were used to construct the center span of this three-span bridge. The bridge was opened for traffic in 2008.

Figure 1.4-6 Iowa UHPC Mars Hill Bridge, Ottumwa, Iowa (Iowa DOT 2011)

Figure 1.4-7 Flexural/shear load testing of a full-scale I girder beam (Iowa DOT 2011)

The use of UHPC in field-cast deck connections has drawn the attention of many research groups. The concept of using UHPC in shear key connections takes advantage of the high strength material in reducing the development length of the reinforcement and thereby, reducing the overall width of the connection. In addition, cracks are significantly controlled and mitigated due to the high strength of the material. Unlike non-shrink grout materials, UHPC can achieve excellent bond strength with the adjacent precast element. Therefore, the development of interface cracking becomes less likely. Besides, because of the low permeability of UHPC, shear key connections made from UHPC are expected to last longer than grouted shear keys.

UHPC was used to form deck connections between precast deck panels such as those in Rainy Lake Bridge (2006) and Chukuni River Bridge (2010) or to form shear key connections between adjacent box beams such as those in Sunshine Greek Bridge (2007), Hawk Lake Bridge (2008), Buller Greek Bridge (2009), Log River Bridge (2009), Eagle River Bridge (2009), and Wabigoon River Bridge (2010). The Ministry of Transportation of Ontario (MTO) is the leader in the deployment of field-cast UHPC connection technology. By the end of 2011, the MTO completed the construction of sixteen bridges with UHPC used in the connections between precast concrete elements.

The Rainy Lake Bridge is a highway bridge over the Canadian National Railway (CNR) at Rainy Lake, near Fort Frances, Ontario. This skewed simply supported bridge was originally built in 1963 with a span of 80 ft and a deck width of 36 ft. The superstructure of the bridge was composed of five steel plate girders supporting a 7 in. thick cast-in-place deck slab. In 2006, a project was conducted to replace the deteriorated cast-in-place bridge deck with new precast deck units. No transverse post-tensioning was allowed due to technical and economic factors. In addition, it was mandatory to keep the bridge open to traffic during the retrofit. The new deck replacement was formed of precast rectangular deck panels with dimensions of 19 ft × 12 ft × 9 in. The panels were reinforced with Glass Fiber Reinforced Polymer (GFRP) bars as top mat reinforcement and conventional steel bars as bottom mat reinforcement. The new deck system was designed to be fully composite with the existing steel girders. This was accomplished using standard Nelson shear studs welded to the top flanges of the girders at the precast panel pockets. The shear studs were fixed to the panels using UHPC. In addition, precast continuity was provided

by the field-cast UHPC construction joints as shown in Figure 1.4-8 and Figure 1.4-9 (Perry et al. 2009).

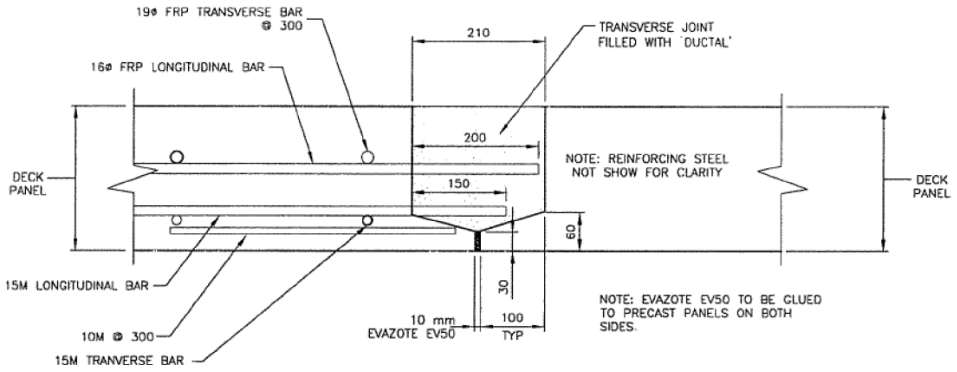

Figure 1.4-8 Details of transverse joints between precast deck panels in Rainy Lake Bridge, ON, Canada (Perry et al. 2009)

Figure 1.4-9 Joints ready for casting (left) and filling the joints with UHPC (right) in Rainy Lake Bridge, ON, Canada (Perry et al. 2009)

The Hawk Lake Bridge (Figure 1.4-10) carries Trans-Canada Highway 17 traffic over the Canadian Pacific Railway. It is a single-span bridge with a span length of 89.3 ft and a deck width of 45.3 ft. The bridge superstructure was composed of 12 adjacent precast box girders connected

together using shear key joints made of Ductal®. Due to the remote location of the bridge, the UHPC Ductal® was mixed on site and thermal blankets and heated water coils were used to ensure proper curing at night-time temperatures (32° to 59° F). The average 28-day concrete compressive strength of the field-cured UHPC joints was 21.0 ksi.

Figure 1.4-10 Hawk Lake Bridge, ON, Canada

The Eagle River Bridge (Figure 1.4-11) carries Highway 17 over Eagle River in Ontario, Canada. The superstructure of this bridge consists of three spans with each span constructed with 12 side-by-side precast prestressed box beams. The box beams were reinforced with V-ROD® #5 and #8 bar and carbon bar for pre-stressing. Also, #6 bars were used in the approach slabs. The continuity for live loads between the three spans was achieved by grouting the joints between the spans using UHPC in addition to grouting the longitudinal joints between the box beams.

Figure 1.4-11 Construction of Eagle River Bridge, Ontario Canada

New York State Department of Transportation (NYSDOT) employed UHPC in two projects. The first project was the Route 31 Bridge in Lyons, New York (Figure 1.4-12 and Figure 1.4-13). In this project, a deteriorated superstructure was replaced with a new superstructure composed of eight 41-in. deep decked bulb T beams. The new superstructure was simply supported over a span of 87.4 ft with a total deck width of 42.8 ft. The beams were interconnected at their top flanges using longitudinal UHPC shear key connections with a width of 6 in. and a depth of 6 in. To provide reinforcement through the connections, straight epoxy-coated reinforcing bars were projected from precast beams into the connection. After adjusting the cambers in the beams and forming the connections, the UHPC was mixed and cast. After casting, the exposed surfaces were covered to prevent dehydration and the UHPC was then allowed to cure under ambient environmental conditions. After curing, the bridge deck surface was ground. Finally, a waterproof membrane and asphalt overlay were installed.

Figure 1.4-12 Longitudinal connections in Route 31 Bridge in Lyons, New York (Graybeal 2010)

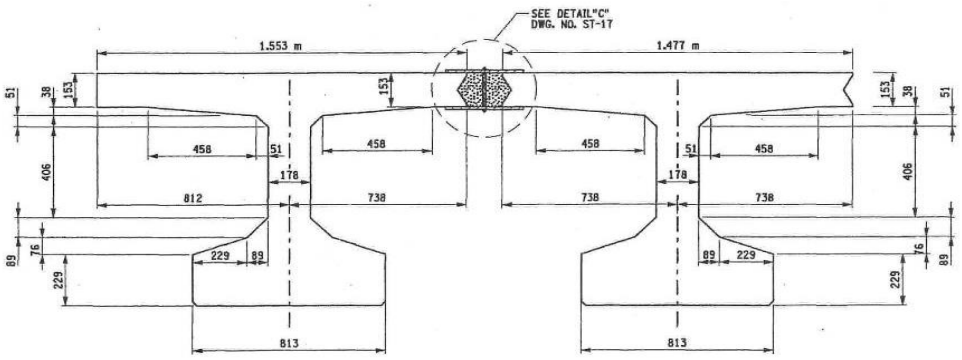

Figure 1.4-13 Dimensions and shear key connection in NYS DOT bridge replacement for Route 31 over Canandaigua outlet (Graybeal 2006, dimensions are in mm)

The second project was the replacement of the Route 23 Bridge over the Otego Creek in Oneonta, New York. The bridge deck construction included the use of precast deck panels and field-cast UHPC connections. After setting the precast panels on the steel girders and forming the connections, the UHPC was mixed, cast and allowed to cure at the ambient environmental conditions (Figure 1.4-14). After curing, a 1.6 in. minimum thickness concrete overlay was provided for a smooth riding surface.

Figure 1.4-14 Field-casting of UHPC, Route 23 Bridge in Oneonta, New York (Graybeal 2010)

The Virginia Department of Transportation (VDOT) has used UHPC with steel fibers in the construction of five beams located in one of ten spans of the bridge on Route 624 over Cat Point Creek. Each span of the bridge had a length of 81.5 ft and was composed of five 45-in. bulb T beams. A test beam with a span of 20 ft was also fabricated and tested to failure (Figure 1.4-15). The beams had longitudinal strands but no shear reinforcement was provided. Test beam results indicated satisfactory load-carrying capacity. Preparation of the beams involved a longer mixing time and a two-stage steam curing to ensure optimum concrete properties. Testing of specimens at the hardened state showed that UHPC has high strength and high durability attributed to a very low water–cementitious materials ratio, low permeability, high resistance to cycles of freezing and thawing, and tight cracks (Ozyildirim 2011).

Figure 1.4-15 Building and testing UHPC bulb T beam (Ozyildirim 2011)

An experimental study was performed at Michigan Technological University (MTU) to evaluate the bond strength between an UHPC overlay and normal concrete substrate with different types of surface textures including smooth, low roughness, and high roughness texture. Slant shear (ASTM C 882-05) and splitting prism (modified ASTM C 496) tests were performed to quantify the bond strength under combined compression/shear and indirect tension. Test results demonstrated that under compressive loading (slant shear test), the bond strength is greater than the strength of the substrate, provided that a surface texture greater than the standard smooth finished mortar surface is used. Splitting prism test results were not highly sensitive to the surface roughness. In both cases, the measured bond strengths fell within the ranges specified in the ACI design guidelines for the Selection of Materials for the Repair of Concrete. The study concluded that UHPC provides adequate bond performance for a variety of substrate surface conditions.

Graybeal (2010) performed a study to evaluate the performance of UHPC deck connections under cyclic and static loading. Four 7.8-in. thick specimens were constructed to simulate transverse deck connections with different reinforcement layouts. Two 6-in. thick specimens were constructed to simulate longitudinal deck connections. The specimens had a rectangular shape with dimensions of 94.5 in. × 84.7 in. The UHPC connection was placed at the mid-span of each specimen with a width of 6 in. All the specimens were loaded at their mid-spans with a point load near the connection (Figure 1.4-16). The cyclic loading test included applying a minimum of two million cycles of loading/unloading at a load level just below the cracking strength of the specimen and a minimum of five million cycles of loading/unloading at a load level above the cracking

strength of the specimens. After completion of the load cycles, the specimens were loaded with a static load to failure. Overall, it was determined that the performance of UHPC field-cast connections in this experimental investigation surpassed that anticipated in monolithic decks with no connection debonding. However, it was noted that the connection was neither susceptible nor immune to water leakage. In case of loading beyond the cracking strength, it is expected that flexural cracks will develop near the connection and water leakage became inevitable. This is an issue in both cast-in-place deck slabs and precast deck slabs with connections.

Figure 1.4-16 Testing of UHPC shear key joints between deck panels (Graybeal 2006)

The possible need for transverse post-tensioning (TPT) to secure the UHPC shear key connections in decked bulb T beams has not been investigated. Based on earlier studies performed on side-by-side box beam bridge (Grace et al. 2008), it was determined that TPT arrangement prevents differential deflection between the adjacent precast beams and also guarantees uniform distribution of live loads among the beams. TPT also helps in preventing the development of longitudinal cracks, which usually occurs along the joints between the precast units. If steel strands are used to apply the TPT forces, grouting must be used in the ducts to protect the steel strands. This hinders the ability to perform maintenance on the bridge. For instance, if a beam is damaged, the TPT cannot be removed in order to replace the damaged beam. Therefore, in a new approach which is followed by the Michigan Department of Transportation (MDOT), TPT strands are replaced with CFRP strands in order to avoid grouting of the ducts.

1.5 Fiber reinforced polymer (FRP) in bridge construction

1.5.1 Need for FRP reinforcement

The Prestressed Concrete Institute (PCI) design guidelines identify corrosion of steel reinforcement as one of three major and current problems in the nation's bridge inventory. Although concrete provides steel with an ideal alkaline environment for protection from atmospheric attack, corrosion of steel reinforcement remains a primary issue in reinforced and prestressed concrete structures. Corrosion of reinforcement occurs even if the concrete section is uncracked. Corrosion happens as a result of concrete carbonation or chloride ions penetration in processes called carbonation-induced corrosion or chloride-induced corrosion, respectively. Steel is thermodynamically unstable and it always tends to revert back to its original state whether it is steel oxide or steel hydroxide by reaction with oxygen and water.

Steel in an alkaline environment such as concrete creates an insoluble form of a thin passive protective layer at the surface of the reinforcement by combining the FE^{+} and the OH^{-} anions, which inhibits any corrosion. However, this passive protective coating is not stable in solutions containing chloride ions or where the PH is around 9 or less. On the other hand, concrete in nature is permeable and allows the ingress of water and chloride—from deicing chemicals. When the protective coating is broken, active corrosion of reinforcement occurs at a rate as high as several mm per year. The mechanics of chloride attack usually starts with the CL^{-} ions competing with the OH^{-} on the bond with FE^{+} and thereby attacking the passive protection film. In addition, the overall PH of the concrete is reduced, which accelerates the corrosion rate. The most detrimental consequence of chloride-induced reinforcement corrosion is the build-up of voluminous, insoluble corrosion products in the concrete. This leads to high internal stresses and eventually to cracking and spalling of the concrete cover (Hansson et al. 2007).

Carbonation of the concrete is another issue. Carbon dioxide from the atmosphere reacts with the calcium hydroxide and other hydroxides in the cement paste to form a neutralized solution around the steel in a chemical reaction such as [$Ca(OH)_2 + CO_2 \rightarrow CaCO_3 + H_2O$]. Carbonation starts at the surface of the concrete and can be detected by measuring the reduction in the PH at the surface. The PH on the surface can be 8 compared to 13 inside the concrete. The carbonation depth slowly increases with time until it reaches the reinforcement. Once the concrete around the reinforcement is neutralized, the protective coating of the steel is broken and corrosion starts at a

high rate. Unlike corrosion from chloride ions, corrosion due to carbonation is uniform and is extended over a wide area with no signs of spalling or concrete cracking at the earlier stages. However, rust stain may appear at the surface of the concrete as corrosion product dissolves in the water and migrates to the surface. Carbonation rate is usually at its maximum at moderate relative humidity (around 50 to 70 %). However, steel corrosion does not occur at that humidity range. Therefore, carbonation can be detrimental in the durability of concrete in hot climates where the concrete is easily dried out and periodically subjected to saturation by rainstorms. Chloride attack and carbonation can work together to induce a harsher scenario of steel corrosion and concrete deterioration (Hansson et al. 2007).

Several techniques were implemented in bridge construction to mitigate the problem of steel corrosion, which included providing adequate concrete cover, using epoxy coated reinforcement, or galvanizing the steel reinforcement. These corrosion-fighting techniques, though improve the durability of steel reinforcement, do not eliminate the corrosion problem. Sooner or later, steel reinforcement will undergo the process of corrosion, which imposes a threat to the structural element.

The recent development in the science of composite materials and their applications lured researchers and engineers to explore the option of replacing steel reinforcement with such non-corrosive materials. During the last few decades, extensive research efforts have be dedicated to evaluate the adequacy of replacing steel reinforcement with FRP materials in bridge construction. FRP is a composite material that is formed from an organic epoxy matrix reinforced with strong fibers such as glass, aramid, or carbon fibers and can be produced in different shapes such as bars, strands, wires, sheets, or plates. Depending on the strength of the epoxy matrix and the type of the reinforcing fibers, the overall physical and mechanical properties of FRP can be determined. For structural applications, carbon fiber reinforced polymer (CFRP) materials has favorable properties and better economic impact over both glass and aramid fiber reinforced polymer materials. CFRP is characterized by its exceptional high strength, high modulus of elasticity, and resistance to environmental conditions. Filaments of the carbon are produced by oxidation and heat pyrolysis of polyacrylonitrile (PAN) and recently from petroleum pitch delivered from oil processing. These fibers contain around 85 % carbon.

1.5.2 Recent field applications of FRP in bridge construction

FRP reinforcement has been successfully employed in several bridge construction projects all over the world and currently, there are various manufacturers fulfilling the need of the global market with FRP materials. In Japan, for instance, the production of FRP materials has shown significant increase since the 1990s with seven groups of FRP producers, construction, and design firms. Table 1.5-1 shows some of the companies and their products in civil engineering applications, while Table 1.5-2, 3, 4, and 5 show a few of the field applications of FRP materials in the bridge industry in Canada, Japan, USA, and Europe, respectively.

Table 1.5-1 FRP manufacturers and main products

Manufacturer	Country	Product
CFCC Group (Tokyo Rope Mfg. Co. Ltd.)	Japan	Carbon fibre cables and bars
Arapree Group (Nippon Aramid Co., Ltd. And Kajima Corp.)	Japan	Aramid prestressing elements
Technora Group (Teijin, Ltd., and Sumitomo Construction Co., Ltd)	Japan	Aramid bars/cables
Fibra Group (Shinko Wire Co., Ltd)	Japan	Woven bars and cables (Aramid)
Leadline group (Mitsubishi Chemical Co.)	Japan	Carbon fibre bars and cables
NACC Group (Nippon Steel Corp., Suzuki Metal Industry Co., Ltd)	Japan	Carbon fibre cables
NEFMAC group (Shimizu Corp.)	Japan	Mesh reinforcement
Marshal Composite Technologies LCC	USA	C-Bar

Table 1.5-2 Reinforced or prestressed FRP bridges in Canada

Bridge	Province	Year	System	FRP Component
Beddington Trail Bridge	Alberta	1993	CFCC Leadline	Prestressing of main beams (first application)
Catham Bridge	Ontario	1996	NEFMAC nets (carbon)	Slab cantilevers
Joffre Bridge	Quebec	1997	C-bar carbon	Slab reinforcement (partially)
Taylor Bridge	Manitoba	1997	CFCC, Leadline, C-bar (glass)	Prestressing of main beams, slabs and stirrup reinfocement, connections to guide rails
Crowchild Trail Bridge	Alberta	1997	C-bar glass	Slab reinfocement over columns and for canilevers
Bishop Grandin Boulevard	Manitoba	1998	GFRP dowels	Bridge deck joints

Table 1.5-3 Reinforced or prestressed FRP bridges in Japan

Bridge	Location	Year	System	FRP Component
Shinmiya Bridge	Ishikawa	1988	CFCC	Prestressing of main beams
Birdie Bridge	Ibaraki	1989	CFCC, Arapree, Leadline	Formwork elements, prestressing or ribbon, ground anchors
Bachiawa Minami Bridge	Fukuoka	1989	Leadline	Prestressing of main beams
Sumitomo Bridge (1)	Tochigi	1989	Technora	Prestressing of main beams, transverse prestressing
Talbus Bridge	Tochigi	1990	FiBRA	Prestressing of beams
Sumitomo Bridge (2)	Tochigi	1991	Technora	Prestressing of main beams
Hishinegawa Bridge	Ishikawa	1992	CFCC	Prestressing of main beams, stirrup reinforcement
Hisho Bridge	Aichi	1993	CFCC	Prestressing of main beams
Yamanaka Bridge	Tochigi	1996	FiBRA	Prestressing of main beams
Stress Ribbon Bridge	Nagasaki	1993	FiBRA	Prestressing of ribbon
Rainbow Bridge	Tokyo	1993	FiBRA	Prestressing of slabs
Mukai Bridge	Ishikawa	1995	CFCC	Prestressing of main beams

Table 1.5-4 Reinforced or prestressed FRP bridges in USA

Bridge	State	Year	System	FRP Component
McKinleyville Bridge	West Virginia	1996	C-Bar	Bridge deck, first use of reinforcing bars in the USA
Kentucky Boubon County Bridge	Kentucky	1997	C-Bar	Bridge deck
Route 668 Bridge over Gills creek	West Virginia	2003	GFRP	Bridge deck
Salem Ave. Bridge	Ohio	1999	GFRP	Bridge deck
Sierrita de la Cruz Creek Bridge	Texas	2001	GFRP	Bridge deck
53rd Avenue Bridge	Iowa	2001	GFRP	Bridge deck
Bridge Street Bridge	Michigan	2001	CFCC, Leadline	Bridge deck, first use of FRP prestressing
Penobscot Narrows Cable Stayed Bridge	Maine	2007	CFCC	Cable stayed system

Table 1.5-5 Reinforced or prestressed FRP bridges in Europe

Bridge	Country	Year	System	FRP Component
Lunen's Gasse Bridge Dusseldorf	Germany	1980	Polystal (12 cables each with 19 bars)	Slab prestressing
Ulenbergstrasse Bridge Dusseldorf	Germany	1986	Polystal (59 cables each with 19 bars)	Parabolic slab prestressing, degree of prestress 50%
Marienfelde Bridge Berlin	Germany	1988	Polystal (7 cables each with 19 bars)	External prestressing
Schiessbergstrasse Bridge Leverkusen	Germany	1991	Polystal (27 cables each with 19 bars)	Parabolic slab prestressing, degree of prestress 50%
Oststrasse Bridge	Germany	1991	CFCC	Prestressing of main beams
Notsch Bridge Karnten	Austria	1992	Polystal (41 cables each with 19 bars)	Slab prestressing
Fidgett's Bridge	England	1995	Eurocrete glass fibre bars	Slab reinforcement
Oppengaard Bridge	Norway	1996	Eurocrete glass fibre bars, Parafil cables	Slab reinforcement ties
Herning Bridge	Denmark	1999	CFCC	Stay cables, slab prestressing, slab reinforcement

1.5.3 Experimental investigations in CFRP reinforcement

Grace et al. (1999) developed a technology to combine bonded internal CFRP tendons with unbonded externally draped CFRP tendons in bridge construction. This technology was successfully implemented in the construction of Bridge Street Bridge, the first bridge built in the United States with CFRP as the main reinforcement (Grace et al. 2002). The design, fabrication, erection, long-term monitoring program, and load-distribution behavior of this concrete bridge was presented by Grace et al. (2003 and 2005).

Grace et al. (2003) presented the response of a newly developed two-span continuous double T bridge system with internal and external prestressing using CFRP leadline tendons. The effect of pre- and post-tensioning on the overall strain distribution was examined by first subjecting the bridge to 15 million cycles of repeated load at a constant amplitude equal to the service load, and then by loading the bridge to failure.

Fam et al. (1997) conducted reduced scale tests on beams constructed to represent the beams of Taylor Bridge in Manitoba, Canada. Two types of CFRP reinforcements for shear and prestressing were provided in the 30.5 ft long I-girders, which were compared to similar girders

with conventional steel strands and stirrups. Various web reinforcement ratios were used for each type of CFRP reinforcements. Steel and CFRP beams showed similar flexural behavior from zero loading to cracking. In the post-cracking stage, the CFRP beams showed nearly linear load-deflection relationship until failure while steel beams showed ductile behavior near failure. The effect of the CFRP stirrup configuration and size on the shear behavior and their performance in providing the dowel action between the girder and top slab was also analyzed.

Abdelrahman and Rizkalla (1999) investigated the flexural performance of beams partially prestressed with CFRP tendons. The focus of the investigation was on prestressing ratio and degree of prestressing. Eight specimens were prestressed with CFRP (Leadline) tendons and two specimens were prestressed with steel strands (control specimens). The CFRP tendons had a modulus of elasticity of 21,300 ksi, ultimate strength of 285 ksi, and a corresponding ultimate strain of 1.3 %. Horizontal cracks at the level of prestressing reinforcement were observed at failure. These cracks were attributed to the release of elastic strain energy when the bars ruptured. Traditionally, with steel reinforcement, under-reinforced beams yield more deflection than over-reinforced beams. However, this study showed that the maximum deflection of specimens which failed by bar rupture (under-reinforced) was less than the maximum deflection of the specimens which failed due to concrete crushing. In addition, beams prestressed with CFRP tendons had less cracks than beams prestressed with conventional steel strands due to a lower flexural rigidity. However, the average crack widths of the beams reinforced with CFRP tendons were larger. Overall, it was observed that specimens prestressed with CFRP tendons were significantly affected by the level of prestress. A higher level of prestress resulted in higher breaking load and a lower corresponding deflection.

Abdel-Rahman and Rizkalla (1999) proposed partial prestressing at low-jacking stresses to design concrete members prestressed with CFRP reinforcement. This technique is capable of reducing the cost and improving deformability by changing parameters such as prestressing ratio, level of prestressing, and distribution of the CFRP bars in the tension zone.

The arrangement of vertical reinforcement across the depth is a critical factor in flexural capacity, particularly in AASHTO beams and T beams. To maximize eccentricity which inherently increases the flexural capacity of the beam, it is advantageous to locate the prestressing

tendons as far from the neutral axis of the beam as possible. In decked bulb T sections, the designer should locate the longitudinal reinforcement based on strength requirements.

Progressive tendon fracture may occur in FRP prestressed concrete beams when tendons are vertically distributed throughout the section (Dolan and Swanson 2002). When straight prestressing tendons are distributed vertically throughout the section, the tendons farthest from the neutral axis are subjected to the highest strain. In conventional steel reinforced prestressed sections, the layer farthest from the neutral axis yields first. However, the strands do not rupture and the beam continues to sustain the applied loads. When the extreme layers of FRP strands reach the ultimate strain capacity, the strands rupture and the load carrying capacity of the beam is reached. As a result, the strength requirements for steel prestressed beams are not valid for under-reinforced FRP prestressed beams.

Naaman et al. (1993) experimentally and theoretically investigated partially prestressed concrete T beams with carbon fiber composite strands. Progressive failure was achieved in a T beam reinforced with 2#4 Grade 60 steel bars in the bottom layer, two non-prestressing carbon fiber composite cable (CFCC) seven-wire strands just above the steel bars, and two CFCC prestressing strands (1×7) directly above the CFCC non-prestressing strands. The post-peak load-deflection behavior was characterized by step-like decrease corresponding to the rupture of CFCC tendons.

Morais and Burgoyene (2003) proposed step layering of FRP reinforcement to develop a progressive failure and to improve ductility. However, the ultimate load capacity of the beam is achieved once and cannot be maintained after the first failure. Therefore, under real loading applications, the beam will initially fail unless the load can be distributed to other structural elements away from the failed beam. In the case of under-reinforced FRP sections, ACI 440.1R-06 guidelines suggest reserving strength in the FRP members to compensate for the lack of ductility. Otherwise, the FRP flexural elements shall be designed as over-reinforced. Various studies show that over-reinforced FRP beams exhibit a moderate amount of ductility before crushing of the concrete.

Ductility is the ability of a structure to sustain inelastic deformation without reduction in its load-carrying capacity prior to failure. Grace et al. (1998) proposed a new methodology to evaluate ductility of CFRP prestressed beams and bridges with both rectangular and skewed geometries. It

was observed that the CFRP reinforced bridges exhibited a reasonable amount of absorbed energy. Several loading/unloading cycles were applied to the bridge model to separate the elastic energy from the inelastic energy. The elastic energy ($E_{elastic}$), inelastic energy ($E_{inelastic}$), and additional inelastic energy ($E_{inelastic,addl}$) were quantified from the load-deflection response. The ductility was represented by the energy ratio. The energy ratio was defined as the ratio of absorbed inelastic energy to total energy, where the total energy was the summation of the elastic and the inelastic energies (Grace et al. 1998). The energy ratio can be expressed as:

$$\text{Energy ratio} = \frac{E_{inelastic}}{E_{Total}} = \frac{E_{inelastic}}{E_{elastic} + E_{inelastic} + E_{inelastic,addl}}$$

The failure mode of a bridge can be classified as ductile for energy ratios greater than 75 %, semi-ductile for energy ratios between 70 and 74 %, and brittle for energy ratios less than 69 %.

Jo et al. (2004) evaluated ductility of concrete beams prestressed with CFRP tendons. The ductility index was expressed as the ratio of the elastic energy at failure to the total energy of the beam. It was reported that concrete beams prestressed with CFRP tendons had sufficient ductility when compression failure took place by crushing of concrete or when unbonded tendons were used. To achieve increased ductility, a compression-controlled failure and unbonded tendons were recommended for CFRP reinforced beams.

Mutsuyoshi et al. (1993) put forth a strategy to improve ductility of prestressed concrete members reinforced with FRP tendons by improving the quality of the concrete. It was confirmed that compressive stress-strain behavior of confined concrete greatly improved the ductility.

Hassan et al. (1999) performed experimental investigations on full-scale models representing a portion of a highway bridge slab reinforced with CFRP and GFRP reinforcement. The static load-deflection behavior, crack patterns, strain distribution, and failure mode were reported and compared with the results obtained from nonlinear finite element analysis. Numerical models were generated and used to examine the influence of various parameters including the type of reinforcement, boundary conditions, and reinforcement ratio. Recommendations were made for CFRP and GFRP reinforcement based on the strength and serviceability results. Stroll et al. (2000) designed, fabricated, and tested two full-scale high-strength concrete bridge beams reinforced with FRP products for prestressing and shear reinforcement.

Abdel-Rahman and Rizkalla (1999) proposed a simplified method to calculate the deflection of beams prestressed with CFRP reinforcement under short-term and repeated loading. Throughout the experimental program, bond factors were introduced to account for tension stiffening of concrete beams prestressed with CFRP tendons and to determine the location of the neutral axis of cracked prestressed sections. Design guidelines were proposed to predict the deflection of beams partially prestressed with CFRP reinforcement.

El-Sayed et al. (2006) reported experimental data on the flexural performance and shear strength of high-strength concrete slender beams reinforced with FRP bars and conventional steel reinforcement. The authors conducted shear tests on large-scale reinforced concrete beams without stirrups using high-strength and normal-strength concrete with varying reinforcement ratios and modulus of elasticity of the longitudinal reinforcing bars. The experimental shear strengths of the FRP (carbon and glass) and steel reinforced concrete beams were compared to theoretical predictions provided by ACI 440.1R-03. It was concluded that the high-strength concrete beams exhibited slightly lower relative shear strength when compared to normal-strength concrete beams. The predicted shear strengths using ACI 440.1R-03 were found to be conservative.

Zou and Shang (2007) investigated the long term performance of FRP prestressed beams. The long term effects on curvature, deflection, strains, cracking, loss of prestress, and transfer length of FRP were all investigated. The experimental investigations also addressed the level of prestressing force, the level of sustained service loading, and concrete strength. The results showed that the creep of the CFRP was less than 0.2 %. In addition, the transfer length ranged from 11 to 31 in. It was concluded that the strength of the concrete at transfer was one of the major factors affecting the transfer length of the CFRP. A factor accounting for the concrete strength was proposed for estimating the transfer length of the CFRP tendons. Despite the creep and shrinkage of concrete and the relaxation of the tendon itself, the range for transfer length did not vary with time. It was also concluded that the performance of concrete beams prestressed with CFRP tendons meets the serviceability criteria in terms of deflection and cracking. The long-term performance was comparable to the performance of beams prestressed with steel tendons. Serviceability performance was improved with an increase in the concrete strength. The researchers defined a deformability index for prestressed concrete beams in terms of deflection and strength factors. The deflection factor represented the ratio of the deflection at failure to the deflection at first cracking,

while the strength factor represented the ratio of the ultimate moment (or load) to the cracking moment (or load).

1.5.4 Analytical representation for design of FRP sections

Grace et al. (1999) developed a mathematical solution for CFRP prestressed concrete skew bridges based on a closed-form series function. The bridge was assumed to behave as an orthotropic plate and membrane theory was used to simulate the effect of internal and external prestressing forces in the longitudinal and transverse directions. Flexural and torsional rigidity formulae were derived and implemented in the solution to determine deflections, induced stresses, and strains during various stages of construction. The results were validated by experimental results and finite element analysis using ABAQUS. The results of the mathematical solution matched the results of the experimental investigations and the results of the finite element analysis which validated the proposed rigidity formulae and the developed mathematical solution.

Grace and Abdel-Sayed (1999) experimentally investigated the design and construction techniques of CFRP prestressed concrete skew bridges. The results indicated that the repeated load has no adverse effect on the dynamic and static characteristics of CFRP reinforced skew bridges and had an insignificant effect on the load-distribution in the transverse direction. All the externally draped prestressing tendons remained intact under repeated and ultimate loads. The transverse load-distribution exhibited the same characteristics for bonded and unbonded transverse post-tensioning tendons.

Grace and Singh (2003) introduced a combined design approach based on strain compatibility for beams prestressed with bonded prestressing and unbonded post-tensioning CFRP tendons arranged in multiple vertical layers. The authors stated that this approach is applicable to various beam cross sections such as double T, box, or AASHTO I beam sections (Figure 1.5-1). The failure mode was determined by comparing actual reinforcement ratio (ρ_f) with the balanced reinforcement ratio (ρ_{fb}). The actual reinforcement ratio is obtained from the equilibrium of forces and compatibility of strains in the cross-section. The balanced reinforcement ratio and the actual reinforcement ratio can be calculated as follows:

$$\rho_{fb} = 0.85\beta_1 \frac{f_c^{'}}{f_{fu}} \frac{\varepsilon_{cu}}{\varepsilon_{cu} + \varepsilon_{fu} - \varepsilon_{pbmi}}$$

$$\rho_f = \frac{\sum_{j=1}^{m} F_{pi} + f_{pbb}A_{pb} + f_{pnbb}A_{pn} + F_{pui} + f_{pub}A_{fu} - f_{pnfb}A_{pnf}}{bd_m f_{fu}}$$

Where:

β_1 Depth of an equivalent rectangular stress block divided by the distance from the extreme compression fiber to the neutral axis (ACI-318 2005)

$f_c^{'}$ Specified compressive strength of the concrete

f_{fu} Specified tensile strength of bonded prestressing tendons

ε_{pbmi} Initial prestressing strain in bonded tendons

A_{pb} Total cross-sectional area of bonded tendons

A_{pn} Total cross-sectional area of non-prestressing rods

A_{fu} Total cross-sectional area of unbonded tendons

A_{pnf} Total cross-sectional area of non-prestressing rods located in the compression flange

F_{pi} Incremental initial jacking pretensioning force

F_{pui} Total initial post-tensioning force

f_{pbb} Flexural stress in the equivalent bonded tendon at the balanced condition

f_{pnbb} Flexural stress in equivalent non-prestressing tendon at the balanced condition

f_{pub} Flexural stress in equivalent unbonded tendons at the balanced condition

f_{pnfb} Flexural stress in equivalent non-prestressing tendon located in the compression flange at the balanced condition

b Flange width of the beam

d_m Distance from centroid of the bottom prestressing tendons to extreme compression fibers

Recently, Youakim et al. (2007) introduced a simple method to calculate the long-term prestress loss and change in concrete stresses in continuous prestressed concrete members with either CFRP tendons. The authors concluded that the prestress loss in FRP tendons was significantly less than that of steel strands. This was primarily due to the lower modulus of elasticity of FRP tendons. The long-term change in concrete stresses and deflection could either be smaller or greater than those of comparable girders prestressed with steel tendons. This is dependent on the type of FRP tendons and the initial stress profile of the cross-section under consideration.

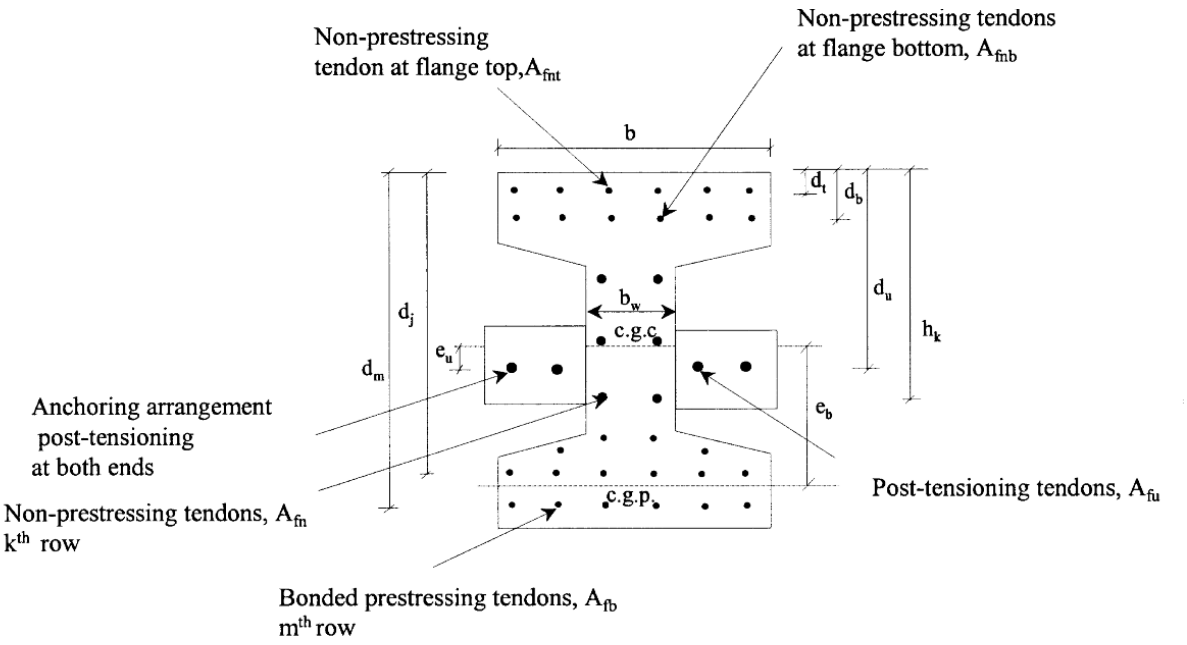

Figure 1.5-1 Typical AASHTO beam section used for design approach (Grace and Singh 2003)

In summary, it was concluded that while FRP reinforced/prestressed beams may not exhibit the same amount of ductility exhibited by steel beams, there are different warning signs such as excessive deflection and dense crack pattern that can serve as a clear visual warning sign before failure. In addition, concrete crushing is marginally more desirable than the rupture of FRP reinforcement because of the pseudo-plastic behavior of concrete members before rupture. However, both failure modes are acceptable in governing the flexural design of FRP reinforced/prestressed concrete members as long as strength and serviceability criteria are satisfied.

1.6 Skew angle in bridges

Bridges have to overcome natural obstacles such as rivers and mountain terrains along with manmade obstacles such as complex intersections (Huang et al. 2004). Therefore, bridges are often skewed to overcome these obstacles. Ebeido and Kennedy (1996) experimentally investigated the effect of the skew angle on the applied moment and moment-distribution factors. The experimental program included the construction and experimental testing of three I-beam bridges models. One bridge model had no skew and two bridge models had a skew angle of 45°. In addition, a parallel finite element analysis using ABAQUS was conducted to evaluate different span lengths in skewed bridge models. It was observed that the beam moment reduced due to the effect of the skew angle. It was also observed that skew angles less than 30° had an insignificant effect on the moment-distribution factor whereas skew angles more than 30° increased the moment-distribution factor (Figure 1.6-1).

Khaloo and Mirzabozorg (2003) conducted a finite element study on load-distribution factors in skewed bridges. The bridge models were examined with; no transverse diaphragms, transverse diaphragms parallel to the support, and transverse diaphragms perpendicular to the longitudinal beams. These diaphragm arrangements were analyzed under skew angles of 0°, 30°, 45°, and 60°. The authors noted that transverse diaphragms parallel to the support yielded the lowest load-distribution factor in skew bridges. The authors also indicated that AASHTO calculations of load-distribution factors are conservative.

Badwan and Liang (2007) performed a grid analysis to determine an optimum post-tensioning stress for a multi-beam deck. The effect of different skew angles on the transverse post-tensioning stresses was also studied in detail. The study revealed that skew angles more than 30° has a significant effect on post-tensioning stresses. The study also showed that AASHTO specifications are adequate or conservative for highly skewed bridges.

Several other investigations (Khaloo and Mirzabozorg 2003) were conducted to evaluate the distribution of truck wheel loads on multi-beam bridges. The wheel loads were placed at various locations on the bridge. The investigations addressed the performance of various beam connections including grouted shear keys and welded steel connectors and extended to include the effect of different diaphragm arrangements, transverse post-tensioning levels, girder spacing, and skew

angles. Findings of the research showed that transverse diaphragms were effective in distributing live loads on bridges.

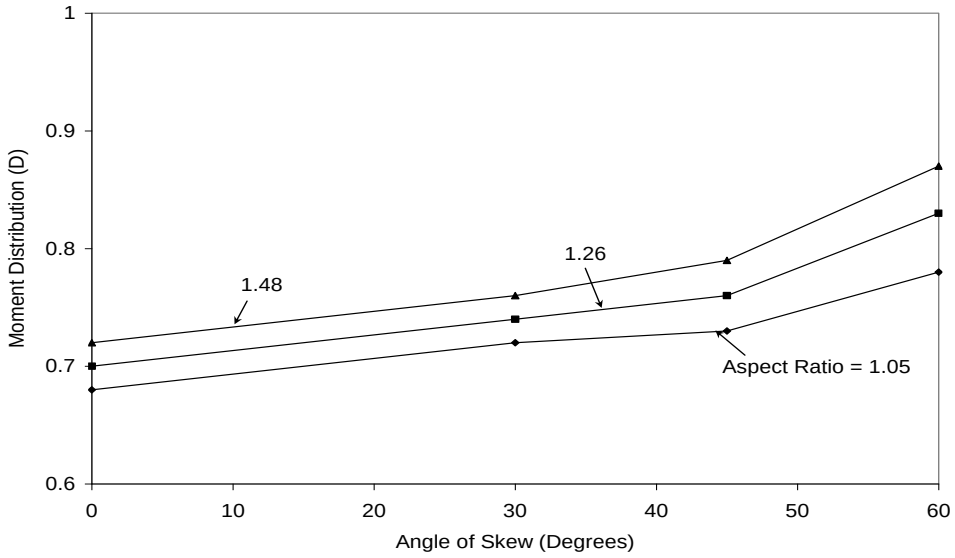

Figure 1.6-1 Effect of skew angle on the moment-distribution factor for an external girder (Ebeido and Kennedy 1996)

CHAPTER 2: EXPERIMENTAL INVESTIGATION

2.1 Introduction

An experimental investigation was initiated and executed to validate the performance of decked bulb T beam bridge system with CFCC reinforcement and to address all underlying technical and construction issues. The experimental investigation included the construction and testing of five one-half-scale control decked bulb T beams in addition to a complete one-half-scale bridge model. The bridge model consisted of five decked bulb T beams connected together with UHPC shear key joints and seven equally-spaced transverse diaphragms. The control beams and the bridge model had a total length of 41 ft, an effective span of 40 ft, a depth of 16 in., and initial prestressing force of 132 kip/beam. One control beam was tested to failure under shear loading and four beams were tested to failure under flexural loading. On the other hand, the bridge model was exposed to different loading configurations through three states: service limit state, where the applied load was not enough to induce flexural cracks, post-cracking limit state, where the applied load was larger than the cracking load of the bridge model, and strength limit state, where the load was applied to induce failure of the bridge. The following sections provide the details of specimens, sequence of construction, order of testing, observed performance and failure modes, and the main outcomes of the experimental investigation.

2.2 Details of control beams

The control beams (Figure 2.2-1) were identical in cross section dimensions with a top flange width of 18 in., a depth of 16 in. and a bottom flange width of 12 in., but varied in the reinforcement configuration. A summary of the reinforcement is shown in Table 2.2-1, where the acronym of the beams is composed of four letters. The first letter refers to the type of longitudinal reinforcement (S for steel and C for CFCC). The second letter refers to the type of transverse reinforcement (S for steel stirrups and C for CFCC stirrups). The third letter refers to the type of loading (F for flexural loading and S for shear loading). The last letter refer to the reinforcement ratio (U for under-reinforced section, B for balanced section, and O for over-reinforced section). As shown in the table, four beams including one beam with steel reinforcement were tested under flexural loading, while the fifth beam was provided with CFCC stirrups and was tested under shear loading.

Table 2.2-1 Details of reinforcement in control beams

	Longitudinal Reinforcement	Transverse reinforcement	Type of loading	Reinforcement ratio (Anticipated failure mode)
S-S-F-U	Steel	Steel	Flexural	Under reinforced (Steel yield, tension failure)
C-S-F-U	CFCC	Steel	Flexural	Under reinforced (CFCC rupture, tension failure)
C-S-F-B	CFCC	Steel	Flexural	Balanced reinforcement (Conc. Crushing & CFCC rupture)
C-S-F-O	CFCC	Steel	Flexural	Over-reinforced (Conc. crushing, compression failure)
C-C-S-B	CFCC	CFCC	Shear	Balanced reinforcement (concrete web crushing, shear failure)

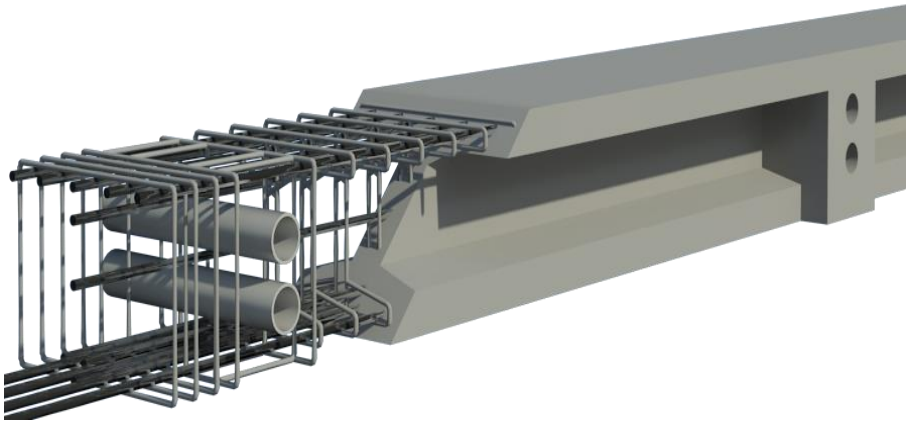

Figure 2.2-1 Configuration of control beams

As shown in Figure 2.2-2, Beam S-S-F-U was prestressed with four 7-wire low-relaxation steel strands with a diameter of 0.6 in. Each strand was prestressed with an initial prestressing force of 33 kip. In addition, three No. 5 Grade 60 steel deformed bars were provided as additional non-prestressed bottom reinforcement. The top flange was reinforced with five deformed steel bars No. 5 and two additional No. 5 bars were provided through the depth of the beam. In the transverse direction, the beam was provided with No. 3 steel stirrups with a center-to-center spacing of 4 in.

Beam C-S-F-U, shown in Figure 2.2-3, was prestressed with four steel strands with a diameter of 0.6 in. Similar to beam S-S-F-U, each strand was prestressed with an initial prestressing force of 33 kip. No non-prestressed reinfrocement was provided at the bottom flange. The reinformecent

of the top flange and the web was similar to other control beams where five non-prestressed CFCC strands with a diamter of 0.6 in. were provided as top flange reinforcement and two strands of the same diameter were provided in as web reinforcement.

Designed with a balanced reinforcement ratio, Beam C-S-F-B, shown in Figure 2.2-4, contained the same reinforcement as beam C-S-F-U with the exception that three additional non-prestressed steel strands with a diamter of 0.6 in. were provided at the bottom flange to increase the reinforcement ratio and approach the balanced failure. On the other hand, to satisfy the requirement for an over-reinforced section, Beam C-S-F-O, shown in Figure 2.2-5, included five non-prestressed strands in addition to the original four prestressed strands in the bottom flange. The physical and mechanical properties of all reinforcement are given in Table 2.2-1. During the course of the study, the research team received two lots of CFCC (Lot #1 and 2, shown in the table) strands with a slight difference in the ultimate strength, strain, and elastic modulus.

While all previously mentioned beams were reinforced with steel stirrups, the fifth beam, Beam C-C-S-B, was reinforced with CFCC stirrups with a diameter of 0.4 in. and a center-to-center spacing of 4 in. As shown in Figure 2.2-6, this beam was reinforced in the longitudinal direction with four prestressed CFCC strands and three non-prestressed CFCC strands, which is similar to the reinforcement of Beam C-S-F-B. This amount of reinforcement would achieve the balanced failure for this section.

Table 2.2-2 Physical and mechanical properties of reinforcement

	Diameter (in.)	Area ($in.^2$)	Yield strength (ksi)	Ultimate strength (ksi)	Elastic modulus (ksi)	Failure strain (%)
CFCC strands, Lot #1	0.60	0.179	-	375	23,061	1.6
CFCC strands, Lot #2	0.60	0.179	-	380	22,916	1.7
CFCC stirrups	0.44	0.090	-	384	22,625	1.7
CFCC (TPT)	1.00	0.472	-	384	22,625	1.7
Steel strands	0.60	0.217	230	279	28,400	5.4
Steel deformed bars	0.63	0.301	60	90	29,000	5.0
Steel stirrups	0.38	0.110	60	90	29,000	5.0

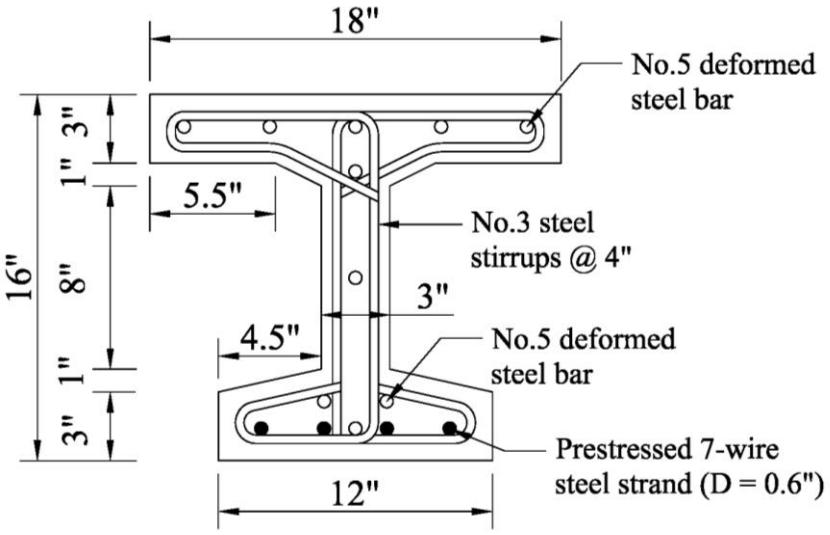

Figure 2.2-2 Details of Beam S-S-F-U

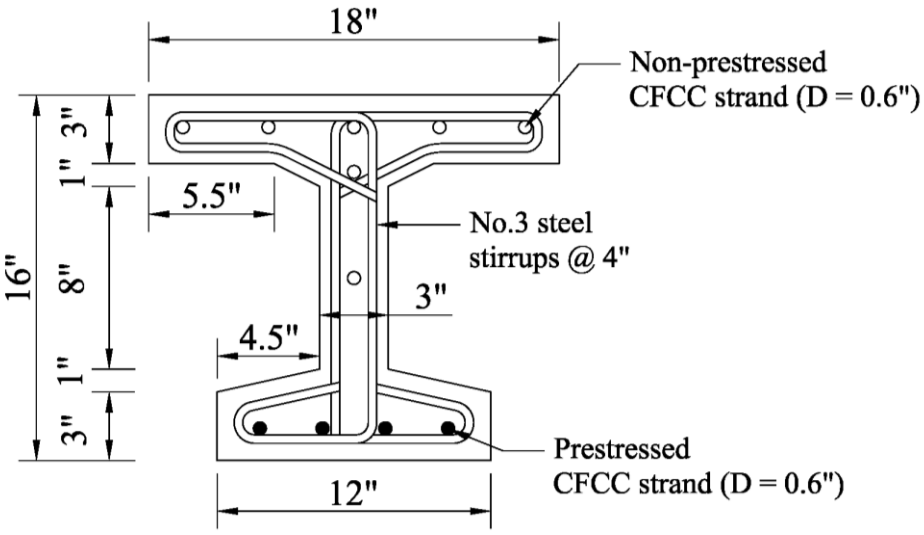

Figure 2.2-3 Details of Beam C-S-F-U

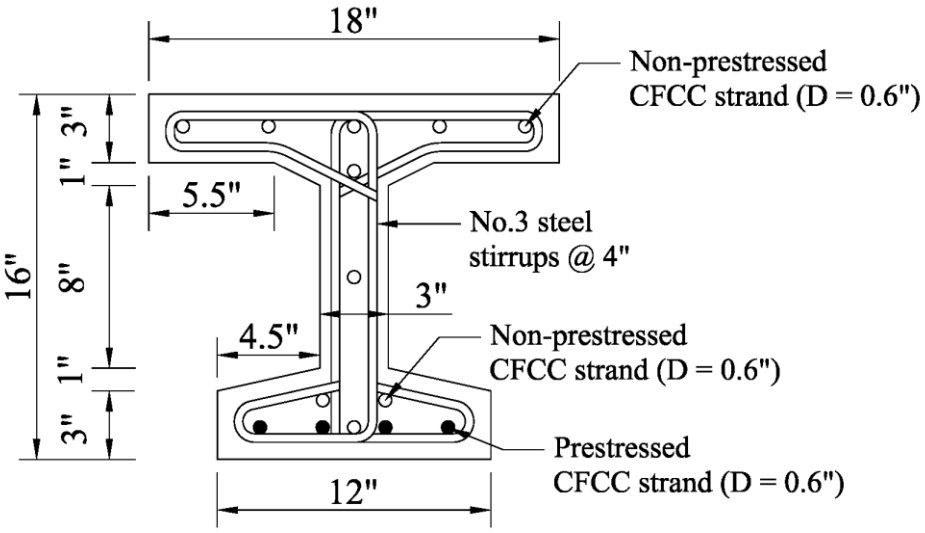

Figure 2.2-4 Details of Beam C-S-F-B

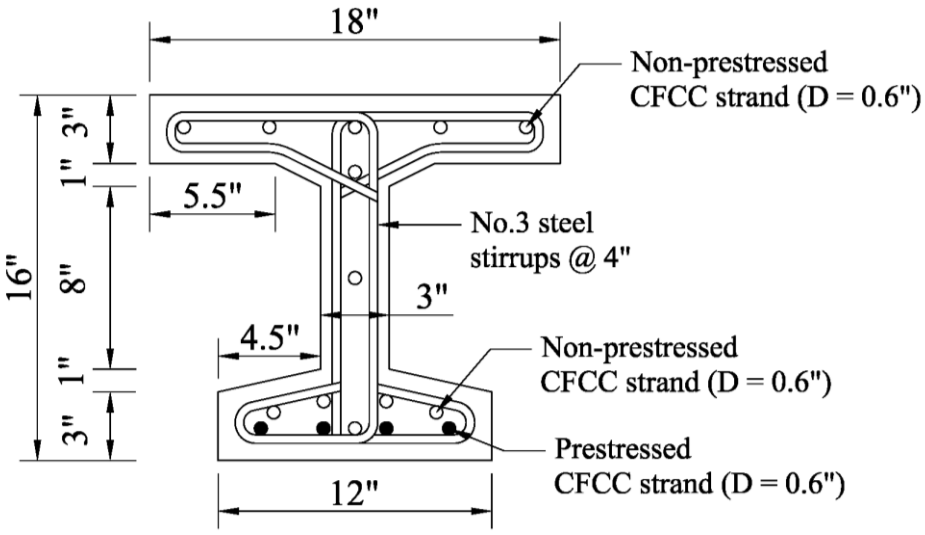

Figure 2.2-5 Details of Beam C-S-F-O

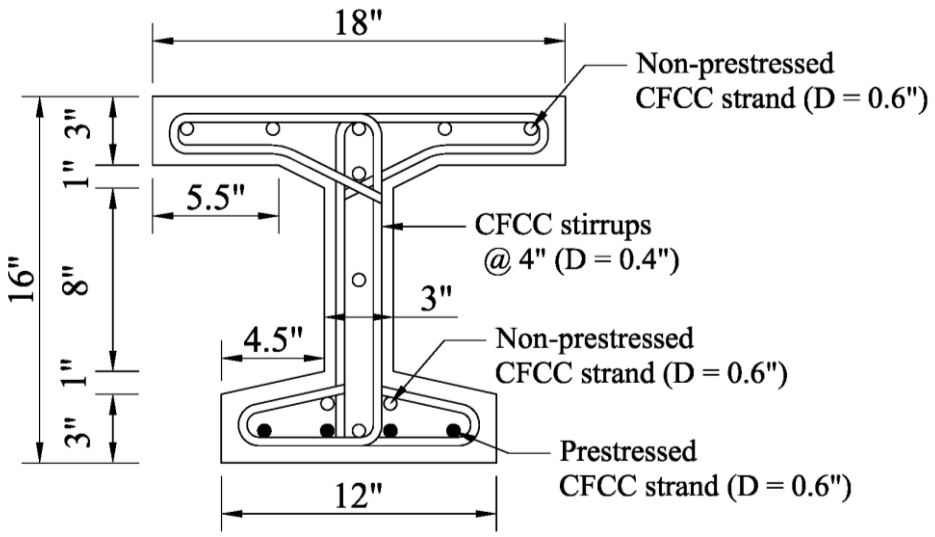

Figure 2.2-6 Details of Beam C-C-S-B

2.3 Details of bridge model

The bridge model consisted of five decked bulb T beams (Figure 2.3-1 and Figure 2.3-2). The beams were interconnected at their top flanges using UHPC shear key joints. In addition, seven full-depth equally spaced transverse diaphragms were provided through the span of the bridge model. Each diaphragm was provided with two 3.0-in. conduits to accommodate two transverse post-tensioning strands. The bridge model was simply supported over an effective span of 40 ft and had a total deck width of 8.5 ft. The reinforcement and prestressing of each beam was similar to those of Beam C-S-F-B. In addition, the transverse post-tensioning system consisted of a total of 14 CFCC strands with a diameter of 1.0 in. (two strands per diaphragm). Each strand was provided with two anchorage devices at its ends. The anchorage device consisted of a stainless steel threaded sleeve and a stainless steel locking nut. The anchorage was attached to the strand using highly expansive grout material (HEM).

The stirrups in the beams protruded for a distance of 3.0 in. from the side of the top flange to form the reinforcement for the shear key joints. Similarly, the transverse reinforcement of the diaphragms extended beyond the concrete surface and was spliced using additional reinforcement crossing the space between the beams.

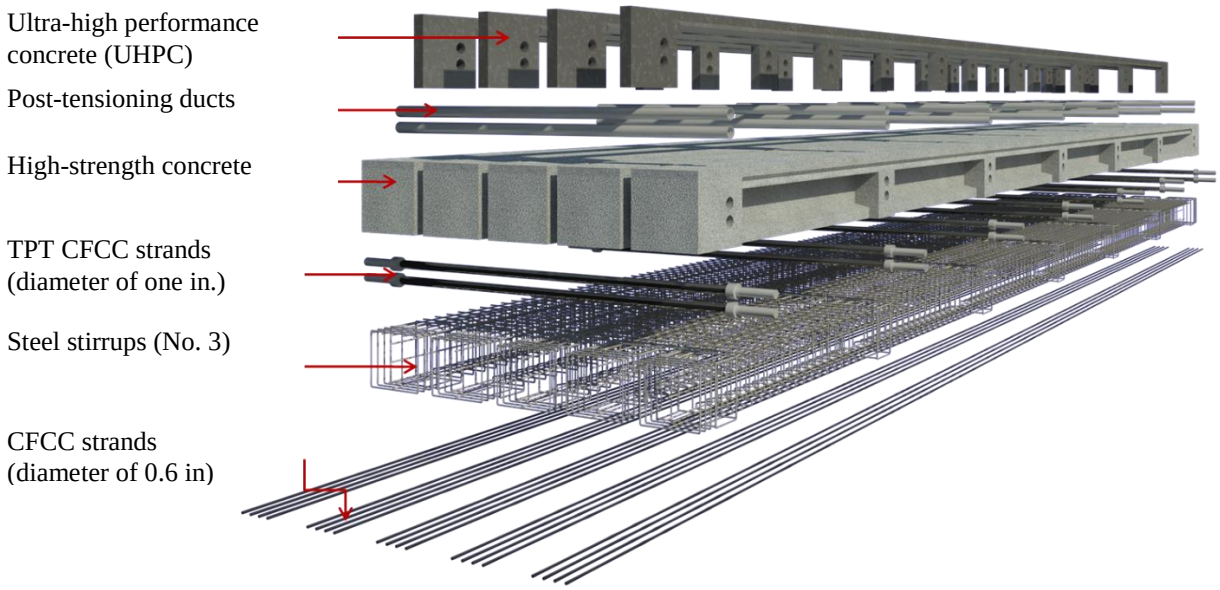

Figure 2.3-1 Components of bridge model

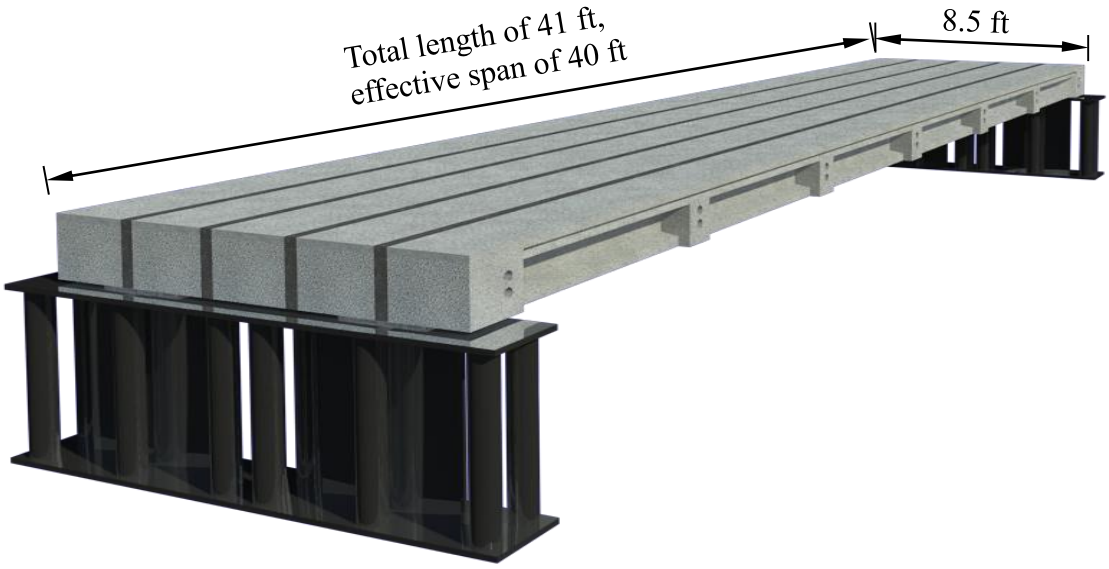

Figure 2.3-2 Layout of the bridge model

2.4 Details of construction of control beams

2.4.1 Construction & testing facility

The construction and testing of the specimens took place inside the structural engineering research facilities at Lawrence Technological University. The research facilities includes the Center for Innovative Materials Research (CIMR) and the Structural Testing Center (STC).

2.4.1.1 Center of Innovative Material Research (CIMR)

CIMR, Figure 2.4-1, is a 7,000 square feet testing facility that is equipped with a full-scale testing frame, two 330,000 lb pre-tensioning beds, an environmental/loading chamber with a testing frame, and a fire/loading chamber with a testing frame. The full-scale testing frame in CIMR has plan dimensions of 52 ft x 17 ft and is composed of three bays, each supporting a 250,000 lb MTS hydraulic testing actuator. With this particular testing facility, the research team was capable of testing the control beams and the bridge model as it can host specimens of spans up to 100 ft and widths up to 12 ft. The pre-tensioning beds are capable of supporting the prestressing forces for pre-tensioned beam specimens of spans up to 61 feet. Figure 2.4-1 shows the testing frame (1) and one of the pre-tensioning beds (2).

Figure 2.4-1 Center of Innovative Materials Research (CIMR).

2.4.1.2 Structural Testing Center (STC)

The Structural Testing Center (STC) contains two testing frames that are used to induce service and strength load conditions to bridge beams. One frame, (Figure 2.4-2), supports two 150,000-lb MTS hydraulic testing actuators. The other frame supports two 100,000-lb MTS hydraulic testing actuators. Two 300,000-lb prestressing beds which are approximately 61 ft. long are used for the production of various prestressing beams. The STC was also used to conduct the current investigation. The loading frame (1) in Figure 2.4-2 was used to test four control beams. The pretensioning bed (2) in Figure 2.4-2 was used during the construction and prestressing of the control and the bridge beams. The prestressing bed is composed of 8-ft-deep reinforced concrete bed with two steel bulk heads (3) secured to the concrete foundation using high-strength anchorage bolts.

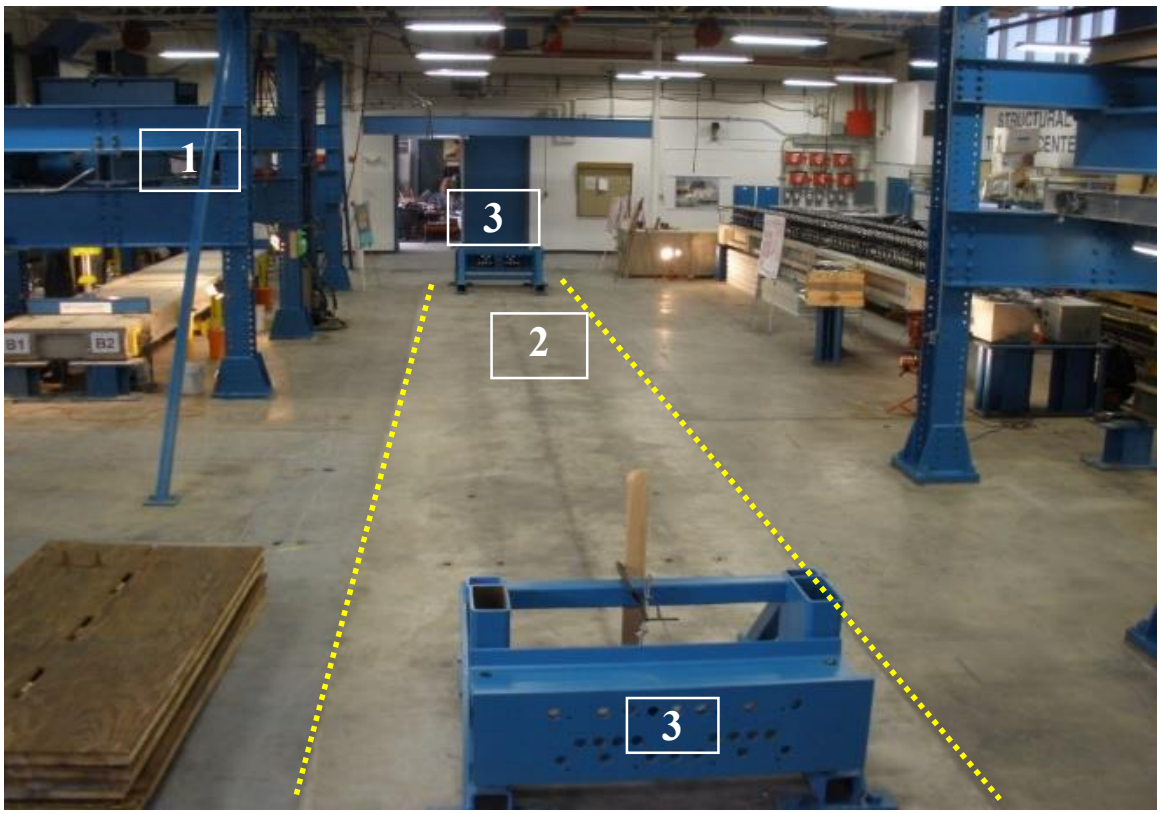

Figure 2.4-2 Structural Testing Center (STC) overview

2.4.2 Construction of formwork

As shown in Figure 2.4-3, each decked bulb T beam had a total length of 41 ft and was provided with seven equally spaced diaphragms at a spacing of 6.5 ft. The decked bulb T beams were cast side-by-side within the two prestressing beds in the STC and CIMR. Figure 2.4-4 shows the general layout for two beams during construction. The formwork for the beams included a wood platform decking system and the sides of the formwork. The decking platform was constructed of plywood and dimension lumber. Figure 2.4-5 shows the decking system. A laser level was used to level the entire platform, which had a total length of 42 ft and a total width of 4 ft to accommodate two decked bulb T beams. The sides of the formwork were constructed from layers of plywood and polystyrene (Styrofoam) to form the required bulb T shape and accommodate the diaphragms. This construction approach allowed for flexibility in creating any shape desired within the constraints of the wood support system. Deforming was another concern for choosing the polystyrene, due to the ease of removing after casting concrete. The extruded polystyrene was replaced with every beam constructed, while the wood support structure was reused throughout the entire experimental phase. Figure 2.4-6 shows the polystyrene layers adhered together and attached to the plywood. These layers of polystyrene were pre-cut to shape using a table saw and attached to the plywood using adhesive and wood screws.

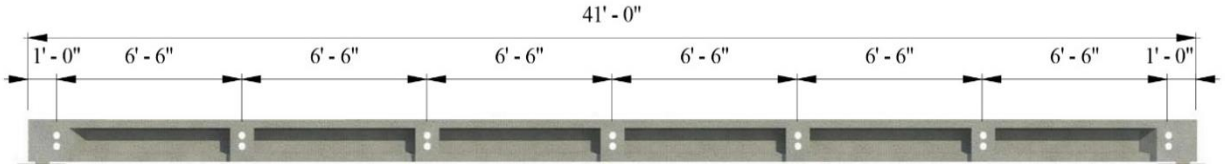

Figure 2.4-3 Longitudinal view of a decked bulb T beam

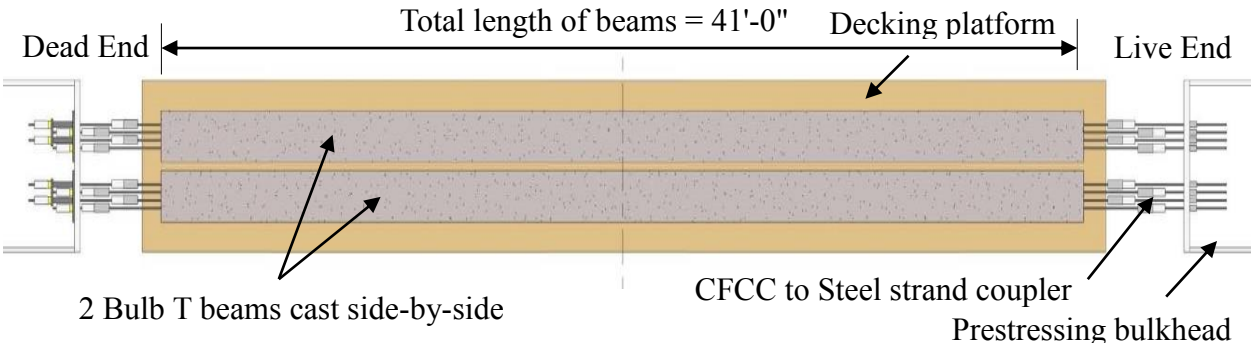

Figure 2.4-4 General layout of decked bulb T beam during construction

Figure 2.4-5 Wood platform decking system

Figure 2.4-6 Construction of formwork using layers of polystyrene and plywood

2.4.3 Reinforcement cages

The reinforcement cages were made of the stirrups and the non-prestressed strands/reinforcement. As mentioned earlier, all control beams other than C-C-S-B included steel stirrups, while Beam C-C-S-B included CFCC stirrups. The steel stirrups were made of two pieces welded together with tack welds as shown in Figure 2.4-7. Similarly, CFCC stirrups were made of two pieces tied together with heavy-duty plastic ties as shown in Figure 2.4-8.

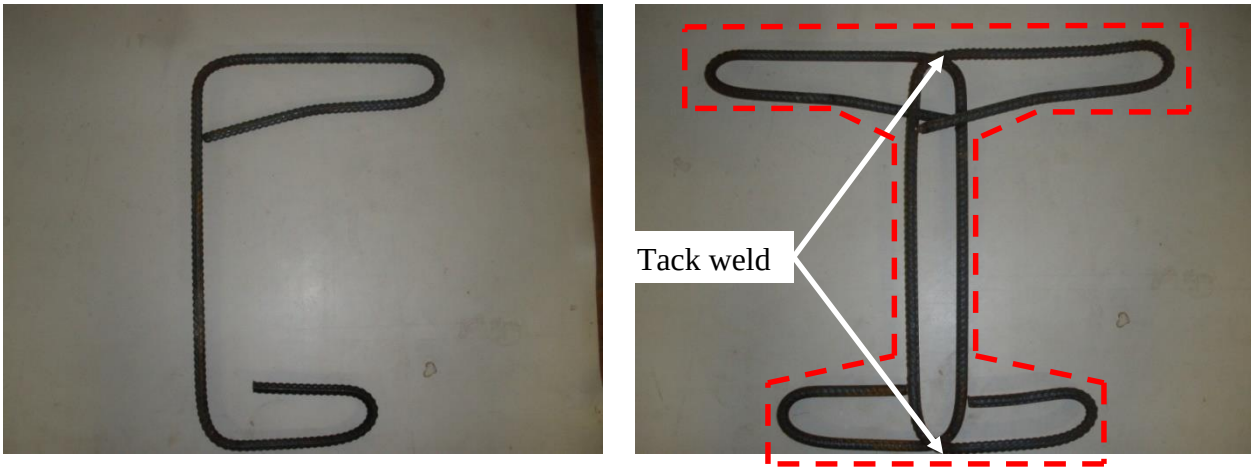

Figure 2.4-7 Steel stirrups of control beams other than Beam C-C-S-B

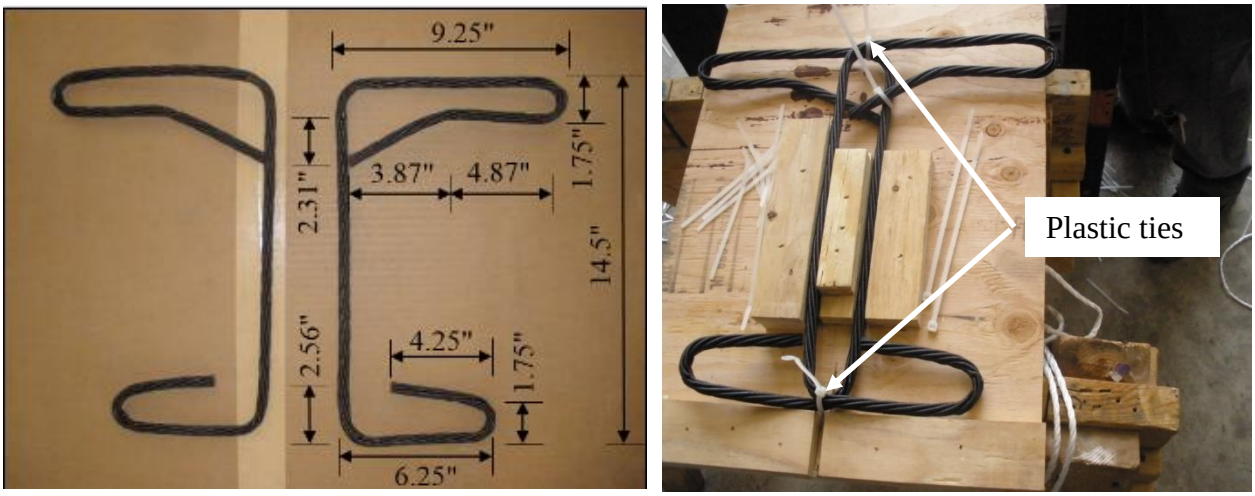

Figure 2.4-8 CFCC stirrups for Beam C-C-S-B

Similar to steel strands, CFCC strands came in rolls as shown in Figure 2.4-9. The research team cut the strands to the required length using air-powered cutting tools or a grinder. The strands were secured to a mount where the stirrups were attached and tied at a spacing of 4 in. as shown in Figure 2.4-10. The transverse diaphragms had additional longitudinal and transverse rectangular stirrups. Similarly, the end blocks were provided with rectangular stirrups every 2.0 in. to resist the bursting force at prestess release. Once reinforcement cages were completed, they were moved to the platform decking, where prestressing strands were passed through the cages as shown in Figure 2.4-11.

Figure 2.4-9 Cutting CFCC strands and constructing reinforcement cages

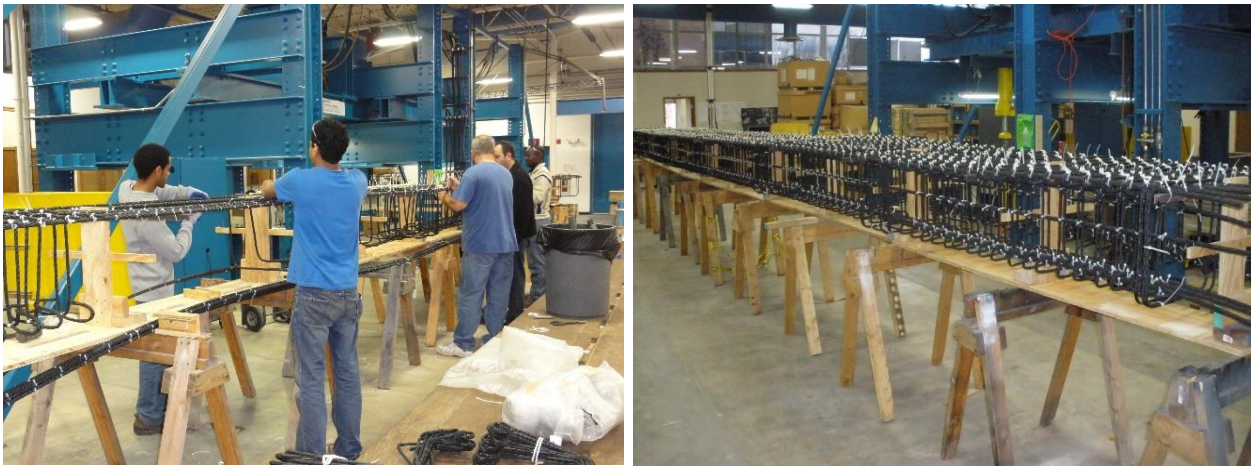

Figure 2.4-10 Building reinforcement cages for control beams

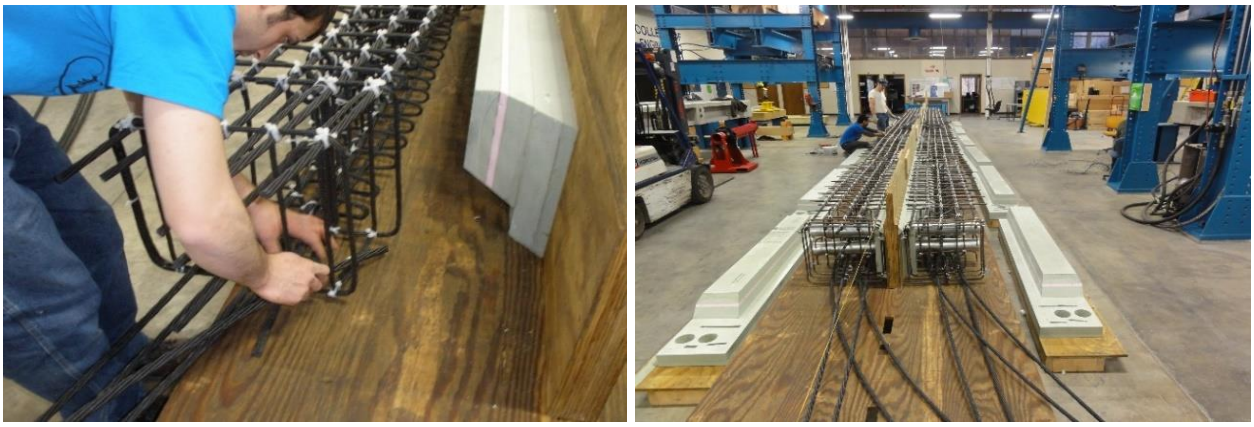

Figure 2.4-11 Moving reinforcement cages to platform decking and passing prestressing strands inside completed cages

2.4.4 Internal instrumentation

All the longitudinal reinforcement including prestressing and non-prestressing reinforcement was instrumented with strain gages at the mid-span for beams tested under flexural loading and under the loading point in Beam C-C-S-B which was tested under shear loading. In addition, each stirrup within the shear span of Beam C-C-S-B was provided with two strain gages. The shear span is defined as the distance from the center line of the support to the loading point. A protective layer was provided around the strain gages to ensure their workability after concrete casting and to prevent moisture penetration to the gage. The used protective layer was either a thick layer of silicon for stirrups or a heat shrink sleeve for longitudinal strands (Figure 2.4-12).

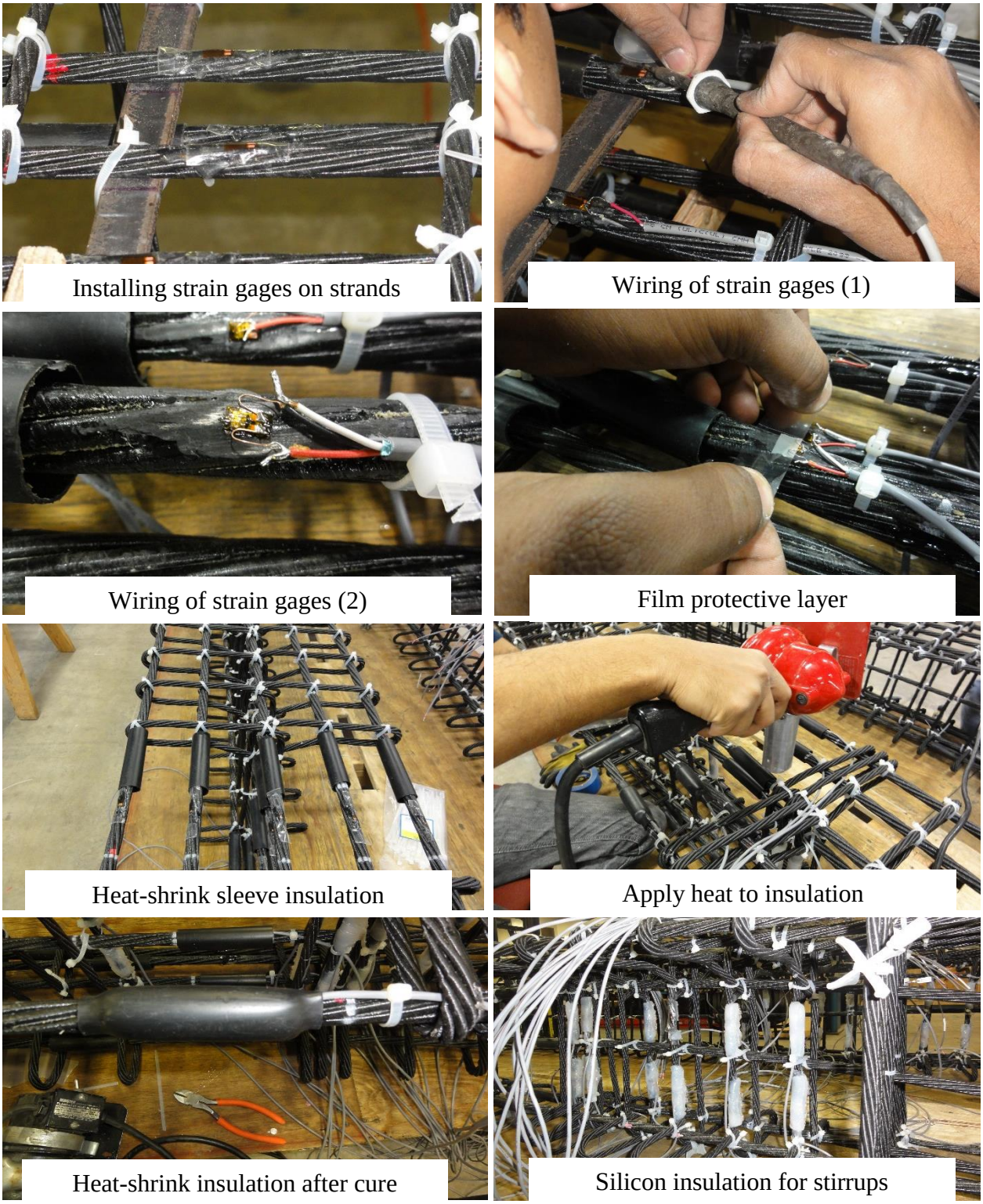

Figure 2.4-12 Internal instrumentation of control decked bulb T beams

2.4.5 Prestressing

To facilitate the process of prestressing and avoid damaging the CFCC strands, a special coupler system (Figure 2.4-13) was developed, tested, and used to connect the prestressing CFCC strands with conventional 7-wire 0.6 in. low relaxation steel strands. The couplers were provided on both the live and dead ends. Therefore, conventional steel anchorage was used at both bulkheads and the prestressing was executed by tensioning the steel strands. The coupler system consisted of two parts (Parts A and B). Part A of the coupler consisted of a high-strength steel barrel encasing a four-steel-wedge system, while Part B consisted of a high strength steel barrel with enough room to accommodate conventional anchorage for steel strands. The CFCC strand was attached to Part A, while the steel strand was attached to Part B. As shown in Figure 2.4-14, to attach the CFCC strand to Part A of the coupler, a buffer material with a steel braided-wire sleeve enclosed the strand to enhance the friction with the four-wedge-steel system. Part A was then fastened to the second barrel (Part B) with a steel strand anchored to it.

Figure 2.4-13 Completed coupler system for prestressing CFCC strands

Attaching buffer material to CFCC strands

Steel braided mesh to increase friction

Four-wedge system inside barrel

Fastening Parts A and B of the coupler

Figure 2.4-14 Coupling CFCC strands with steel strands for prestressing

After completing the installation of the coupler system, the prestressing stage started by tensioning the steel strands at the live end of the prestressing bed. The dead end included load cells to monitor the force. The prestressing was executed by a hydraulic pump and a jacking system, shown in Figure 2.4-15. The strands were prestressed in a predetermined sequence to avoid generating a significant eccentricity of the bulkhead. The initial prestressing force was set to 33 kip/strand. The elongation of each strand was measured and recorded (Figure 2.4-16). The force in each prestressing strand was measured using the reading form the load cell (Figure 2.4-17), the strain gage, the hydraulic pump and the elongation. As shown in Table 2.4-1, at a prestressing level of 33 kip, the elongation of CFCC strands averaged 6 in. while the elongation of steel strands averaged 4 in. A seating loss of 1.5 kip per strand (4.5%) was observed immediately after prestressing. An additional 1.0 kip loss was observed from time of jacking to placement of concrete 24 hours later.

Figure 2.4-15 Prestrssing CFCC strands by tensioning coupled steel strands

Figure 2.4-16 Measuring elongation of strands after prestressing

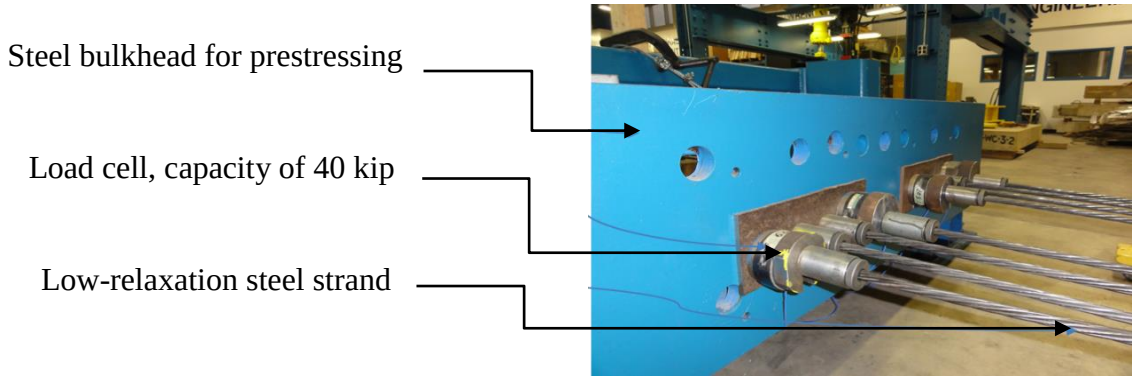

Figure 2.4-17 Load cells on the dead end of prestressing strands

Table 2.4-1 Measured elongation of strands immediately after prestressing

Beam	Elongation (in.)			
	Strand 1	Strand 2	Strand 3	Strand 4
C-S-F-B	6.38	6.38	6.50	6.50
S-S-F-U	4.00	4.00	3.94	4.00
C-C-S-B	6.25	6.25	6.00	6.13
C-S-F-U	6.25	6.13	6.25	5.75
C-S-F-O	6.00	6.00	6.00	5.88
Bridge Beam 1 (exterior)	5.75	5.94	6.38	6.38
Bridge Beam 2 (interior)	6.31	6.38	6.38	5.88
Bridge Beam 3 (intermediate)	5.75	5.75	6.00	6.00
Bridge Beam 4 (interior)	6.25	6.63	6.63	6.50
Bridge Beam 5 (exterior)	6.38	6.13	6.25	5.94

2.4.6 Concrete casting

All the beams were cast using a ready-mix concrete provided by Mc-Coig Concrete Inc. The concrete mix (shown in Table 2.4-2) was designed to achieve a 28-day compressive strength of 7000 psi. The maximum aggregate size was limited to 0.75 in. and a slump of at least 8 in. was imposed on all concrete batches. This concrete mix is a typical concrete mix used in highway bridge beams. Casting of the concrete was performed in CIMR and STC. The concrete was placed in the formwork using a half-cubic-yard hopper's chute and concrete vibrators. Typical casting time for two beams was around 20 minutes. Float troweling, edging, and finish troweling was performed to give a smooth surface finish on top of the beams. Figure 2.4-18 to Figure 2.4-20 show the process of concrete casting.

Figure 2.4-18 Slump test

Table 2.4-2 Concrete mix design

Component	Quantity per cubic yard
Coarse aggregate (L26A-GL)	1710 lb
Fine aggregate (2NS-WLB)	1290 lb
Cement (CMT1-HOL)	534 lb
Cement (CMGS-HOL)	288 lb
Water	31.8 gal
Water reducing agent (0WRA-BA)	24 oz
Medium-range water reducing agent	74 oz

Figure 2.4-19 Casting of concrete into the formwork of two beams

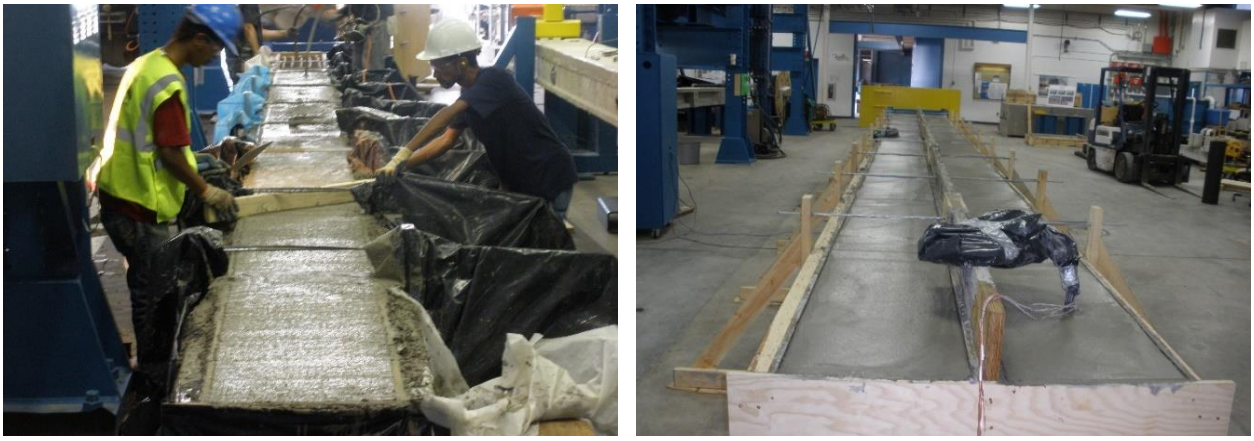

Figure 2.4-20 Leveling and finishing concrete surface

After concrete casting, the beams were covered with wet burlap and plastic sheets to prevent moisture escape and allow for proper curing. The burlap was soaked with water twice a day for seven days (Figure 2.4-21).

Figure 2.4-21 Wet curing of concrete beams

Concrete cylinders with a diameter of 6 in. and a length of 12 in. were also cast from every batch of concrete (Figure 2.4-22). The cylinders were allowed to cure under the same conditions of the concrete beams and were tested under uni-axial compressive stress according to ASTM C39/C39M-12a (2012), Standard Test Method for Compressive Strength of Cylindrical Concrete Specimens, to determine the compressive strength of concrete after 3, 7, 14, 21, and 28 days. In addition, at least three cylinders were reserved and tested on the same day as the corresponding beam testing. Table 2.4-3 gives the average compressive strengths, obtained from testing at least three cylinders, for the batches of concrete used during this investigation.

Table 2.4-3 Average concrete compressive strength at different ages

Beam	Compressive Strength (psi)			
	7 Day	14 Day	21 Day	28 Day
C-S-F-B	6580	7302	7598	7684
S-S-F-U	5728	6248	8404	8746
C-C-S-B	7356	7685	8623	8648
C-S-F-U & C-S-F-O	6866	7566	8869	9438
Bridge Beams 1, 2, 3, 4	7085	7448	8569	8995
Bridge Beam 5	6563	7617	8296	8780

Figure 2.4-22 Concrete cylinders and uni-axial compression test

2.4.7 Prestress release

Transfer of prestressing forces into concrete beams took place 10 days after casting of concrete and after verifying that the concrete had achieved more than 60 % of its 28-day compressive strength. The prestress release was executed by slowly heating the steel strands using an acetylene/oxygen torch as shown in Figure 2.4-23. The exterior strands of each beam were released before the interior strands. A heavy duty wooden cover was placed over the CFCC anchors to eliminate any hazards to the anchors and the person holding the torch. The camber of the beams was measured at the mid-span of the beam at prestress release. Figure 2.4-24 shows the camber of the beams measuring approximately 0.75 in. After prestress release, the beams were removed from the formwork and sent to either the testing facility or to indoor storage until a testing facility was available. While moving, the beams were simply supported as shown in Figure 2.4-25.

Figure 2.4-23 Prestress release using acetylene/oxygen torch

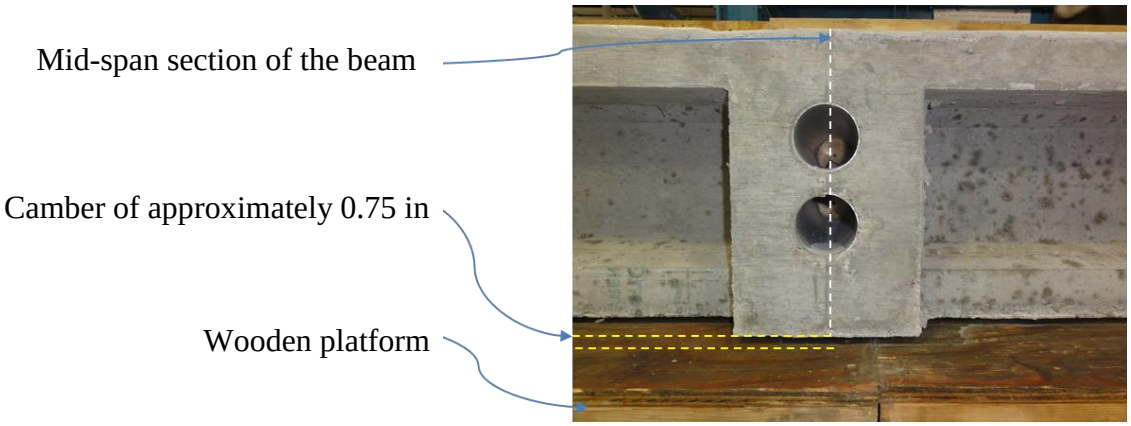

Figure 2.4-24 Camber of beam at mid-span immediately after prestress release

Figure 2.4-25 Moving the beams from the formwork to the loading facility

2.5 Construction details of bridge model

The main two phases of the bridge model construction were:

1. Construction of the individual decked bulb T beams
2. Assembling the bridge model from the individual beams using shear key connections.

As shown in Figure 2.5-1, Figure 2.5-2, and Figure 2.5-3, the bridge model consisted of five decked bulb T beam with two end diaphragms and five intermediate diaphragms. Part of the diaphragms was cast along with the beams and then the diaphragms were connected together using UHPC. Each intermediate diaphragm was reinforced with 4 No.3 reinforcing bars. These bars were spliced before pouring the UHPC. The end diaphragms and the intermediate diaphragms were also provided with galvanized steel conduits with a diameter of 3 in. to accommodate the transverse

post-tensioning strands. The following subsections provide a summary for the stages of construction of the bridge model.

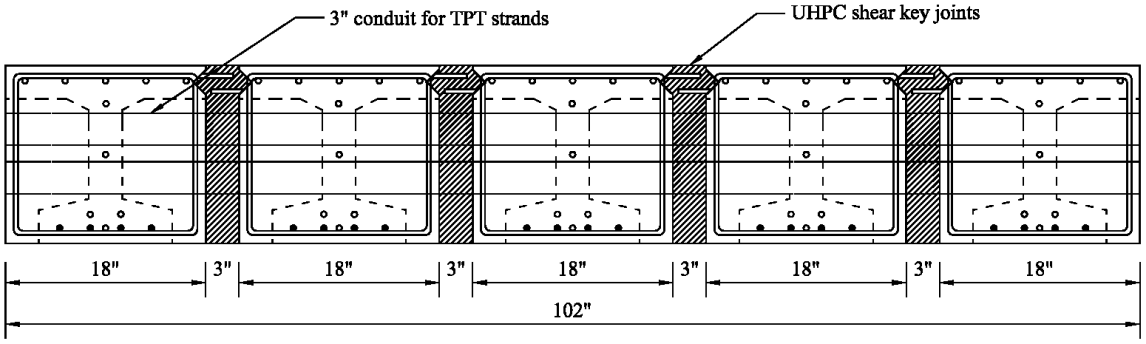

Figure 2.5-1 Cross section of bridge model at end diaphragms

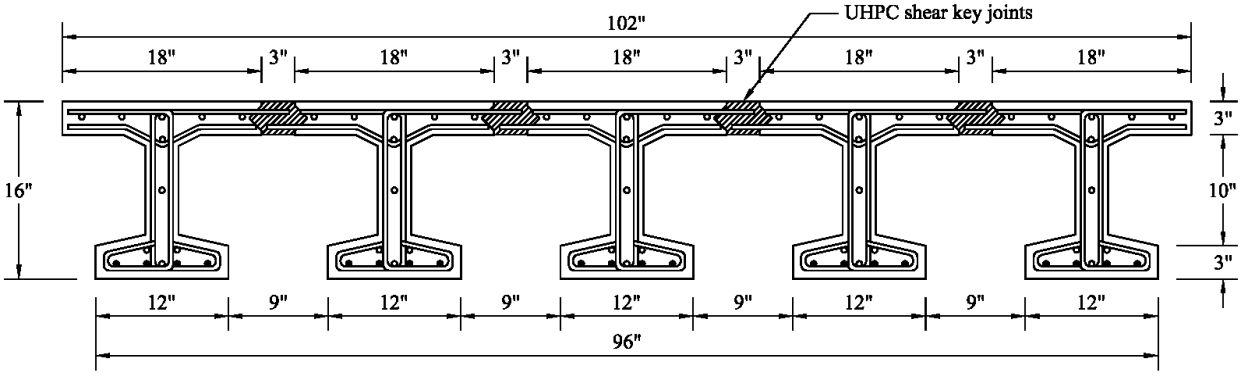

Figure 2.5-2 Cross section of bridge model between diaphragms

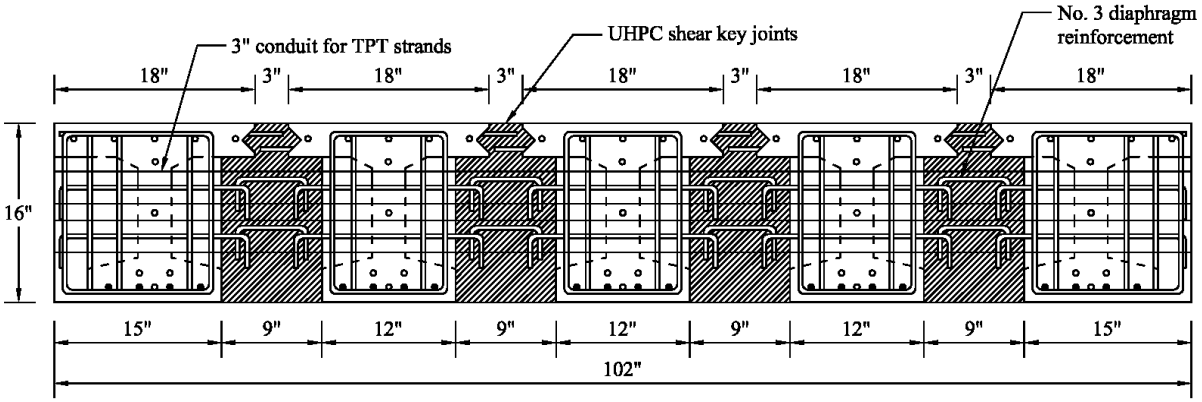

Figure 2.5-3 Cross section of bridge model at intermediate diaphragms

2.5.1 Construction of individual beams

The beams of the bridge model were identical in reinforcement to Beam C-S-F-B, with four bottom prestressed CFCC strands and three bottom non-prestressed CFCC strands in addition to five top non-prestressed CFCC strands and two web CFCC strands. In the transverse direction, the beams were also reinforced with steel stirrups at a center-to-center spacing of 4 in. However, the stirrups protruded the top flange of the beams and extended to a distance of 2.5 in. to form the required reinforcement of the shear key joints. The exterior beams had the protrusion from the interior side only while the interior beams had the protrusion from both sides as shown in Figure 2.5-4 and Figure 2.5-5.

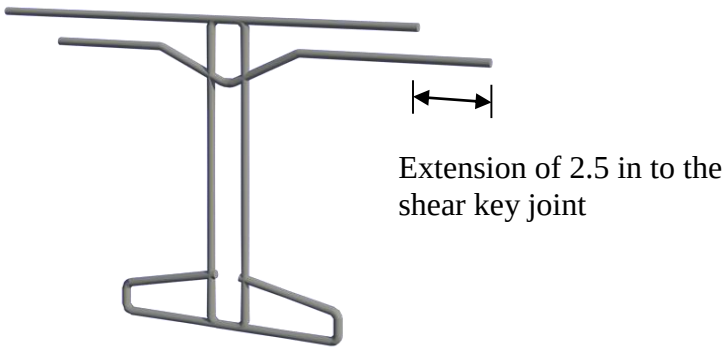

Figure 2.5-4 Steel stirrup for interior beams in bridge model

Figure 2.5-5 Sides of the formwork showing protrusion of steel stirrups for form shear key reinforcement in bridge beams

This protrusion of stirrups was accommodated during the construction of the sides of the formwork by drilling holes in the polyethylene and plywood layers as shown in Figure 2.5-5. In addition, the transverse reinforcement of the diaphragms also protruded of the concrete, mainly to facilitate the splice of reinforcement while assembling the bridge model. This protrusion was also accommodated during the construction of the formwork. Apart from this modification in the formwork, the construction of the individual beams of the bridge model went through the same construction stages of the control beams. Therefore, it will not be repeated in this section. The elongation of the prestressing strands at the time of prestressing is provided in Table 2.4-1, while the compressive strength of concrete at different ages was provided in Table 2.4-3.

2.5.2 Construction of shear key joints

2.5.2.1 Material testing

Prior to the construction of the shear key joints in the bridge model, small-scale specimens of UHPC joints were prepared and tested to failure. Eight specimens were prepared and tested according to ASTM C78-10 (Flexural strength of concrete using simple beam with third-point loading); ten specimens were prepared and tested according to ASTM C882-05 (Bond strength of epoxy-resin systems used with concrete by slant shear); and four specimens were prepared and tested according to ASTM C1583-04 (Tensile strength of concrete surfaces and the bond strength by direct tension, pull-off method). The standard tests were slightly modified to fit the intended application of UHPC in shear key joints. Figure 2.5-6 to Figure 2.5-8 show the configuration of the test specimens. The ASTM C78 specimens were prepared by connecting two 8 in. × 6 in. × 12 in. concrete blocks using a 3.0 in. wide flat or notched UHPC shear keys. The ASTM C882 specimens were prepared by casting 3 in. × 6 in. cylinders of concrete/UHPC. The ASTM C1583 specimens were prepared by connecting two 4 in. × 8 in. cylinders with an UHPC joint.

All test specimens were prepared by: first, pouring the concrete components; second, allowing enough time for curing; third, sand blasting and water saturating the surfaces; and finally, mixing and pouring the UHPC joints between concrete components. After pouring the UHPC joints, the test specimens were allowed to cure for 28 days before testing. On the day of the test, the concrete achieved an average compressive strength of 6 ksi, while the UHPC achieved a compressive strength of 21 ksi.

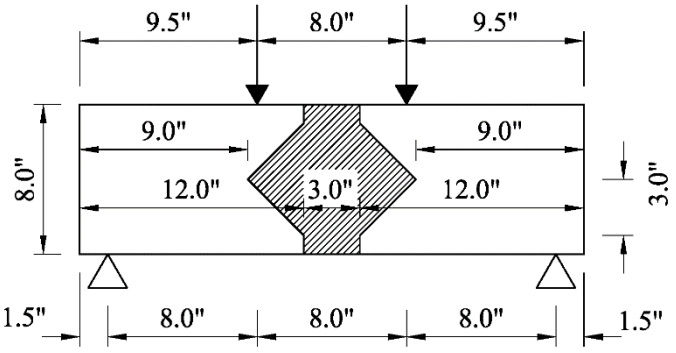

Figure 2.5-6 Details of test specimens for ASTM C78 with notched joint

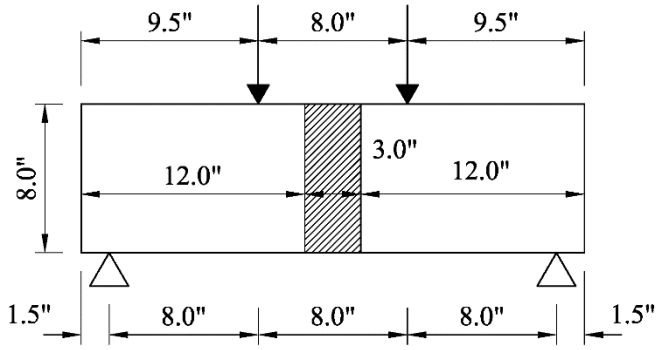

Figure 2.5-7 Details of test specimens for ASTM C78 with flat joint

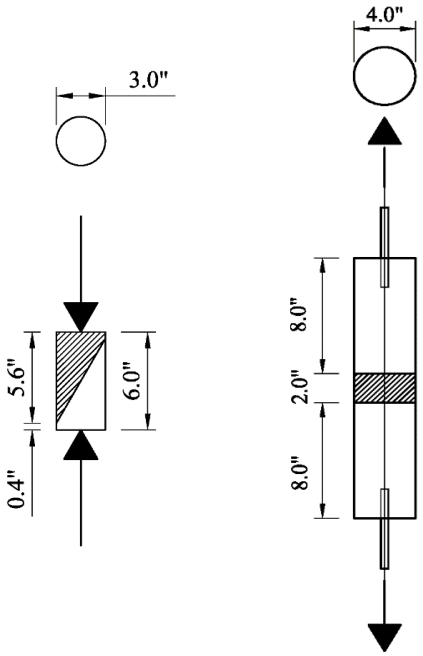

Figure 2.5-8 Details of test specimens for ASTM C882 (left), and ASTM C1583 (right)

Specimens tested under ASTM C78 with flat shear keys achieved an average failure load of 12.3 kip with an average flexural stress of 768 psi at the bottom surface of the specimens. Specimens tested under ASTM C78 with notched shear key achieved an average failure load of 16.4 kip with an average flexural stress of 1,027 psi. It should be noted that the apparent increase in the failure load in specimens with notched shear key was associated with the shift of the failure plane from the central region of the specimen toward the end of the specimens as shown in Figure 2.5-9.

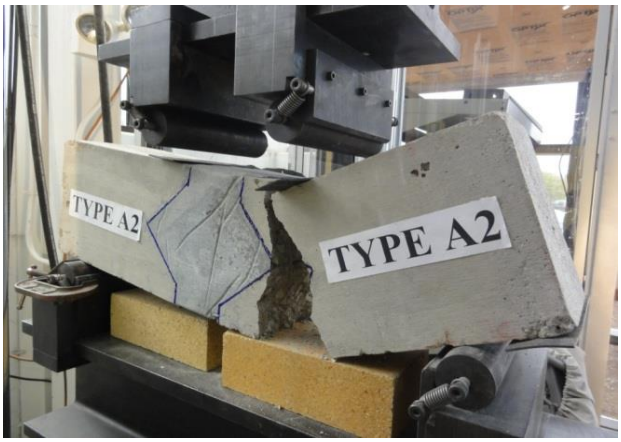

ASTM C78 with notched joint

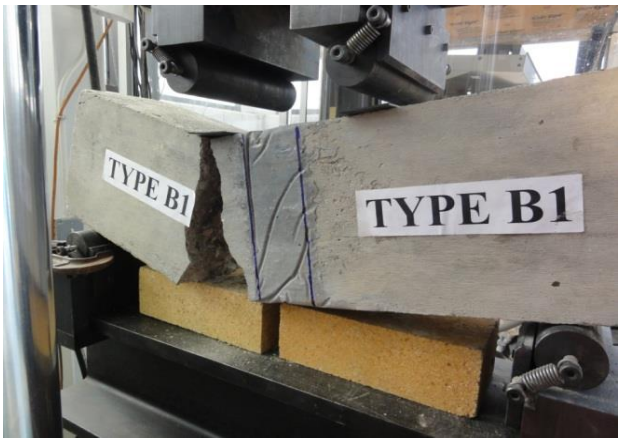

ASTM C78 with flat joint

ASTM C882

ASTM C1583

Figure 2.5-9 Failure and failure planes of UHPC joints under ASTM tests

Specimens tested under ASTM C882 achieved an average failure load of 71.5 kip with average bond strength at the concrete/UHPC interface of 5.1 ksi, considering an elliptical interface with an area of 14.13 in.^{2} according to ASTM C882. On the other hand, specimens tested under C1583

achieved an average failure load of 5.4 kip with an average direct tensile stress of 426 psi. As shown in Figure 2.5-9, the failure plane in all test specimens was always on the concrete side. Therefore, the provided stress values represented the maximum strength of the concrete and not the UHPC or the interface between the concrete and the UHPC. Consequently, it was concluded that the bond strength at the concrete/UHPC interface exceeded the strength of the concrete material. Accordingly, the research team gained confidence in the strength of the UHPC joints and proceeded with using the UHPC to form the shear key joints in the bridge model.

2.5.2.2 Surface preparation

The surface preparation for the decked bulb T beams included sandblasting the surface of the shear key joints and the face of the transverse diaphragms. The sandblasting was performed by spraying fine sand using air-powered spray nozzle as shown in Figure 2.5-10.

Figure 2.5-10 Sandblasting surfaces of the shear key joints

2.5.2.3 Placing UHPC Shear keys

After completing the sandblasting, the beams were set in position over the supports with a 3.0-in. gap between the beams as shown in Figure 2.5-11. Next, the differential camber of the beams was evened out using two steel beams connected together with steel threaded rods as shown in Figure 2.5-12. This process was necessary to create a smooth riding surface for the bridge. It should be noted that the differential camber between beams measured less than 0.1875 in. These steel beams were removed after casting and curing of UHPC shear-key joints.

After leveling the beams, the research team constructed the formwork for the shear key joints. The formwork extended beneath the shear keys and around the transverse diaphragms (Figure 2.5-13). In addition, to prevent the UHPC from seeping into the ducts of the transverse post-tensioning, galvanized steel pipes with a diameter of 2.5 in. was inserted inside the 3.0-in. pipes that passed through the body of the beams (Figure 2.5-14).

Figure 2.5-11 Setting beams over the supports with 3.0-in. gap for shear keys

Figure 2.5-12 Beam leveling to eliminate differential camber

Figure 2.5-13 Formwork for shear key joints and around transverse diaphragms

Figure 2.5-14 Continuous steel pipe to prevent UHPC leakage into transverse ducts

The UHPC was prepared at CIMR by mixing together: 3700 lb of Ductal premix, 219.1 lb of water, 50.6 lb of superplasticizer (Premia 150), and 262.9 lb of brass-coated steel fibers as shown in Figure 2.5-15. A centrifugal concrete mixer was used to mix the components for at least 25 minutes until the mix became homogeneous (Figure 2.5-16). The mixing of Ductal was executed by feeding the pre-mix powder to the mixer and then adding the water and the water reducing agent. The steel fiber was the last component added to the mix.

Each batch of UHPC provided by Lafarge was tested to ensure quality control throughout the casting. Figure 2.5-17 shows the setup for cylinder casting and flow table testing of batches. A count of 25 blows was performed according to ASTM C1437, Standard Test Method for Flow of Hydraulic Cement Mortar. The diameter of the sample after the 25 blows was approximately 9.0 in., which fell within the acceptable range of workability for the material.

Pouring the UHPC to the shear key joints was performed manually as shown in Figure 2.5-18. As the UHPC is characterized with its flowing and self-leveling ability, there was no need to use a vibrator or float the surface.

After pouring, the shear key joints were covered with plastic sheets and allowed to cure at ambient temperature for 72 hours (Figure 2.5-19). After curing, the surface of the joints was grinded using a drum grinder to achieve an even bridge surface as shown in Figure 2.5-20.

Pre-mix powder for UHPC

Water reducing agent

Coated steel fibers

Concrete mixer

Figure 2.5-15 Items used to prepare UHPC

Figure 2.5-16 Mixing UHPC

Figure 2.5-17 Flow test for UHPC according to ASTM C1437

Figure 2.5-18 Pouring UHPC shear key joints

Figure 2.5-19 Curing of shear key joints using plastic sheets

Figure 2.5-20 Grinding the surface of UHPC shear key joints

2.5.3 Transverse post-tensioning

The bridge model was provided with seven transverse diaphragms. Each diaphragm hosted two transverse ducts to accommodate two CFCC transverse post-tensioning strands. The anchorage devices (threaded sleeve and lock nut) for the strands were already attached by the manufacturer (Figure 2.5-21). However, to distribute the post-tensioning force over the diaphragm area and eliminate the concentration of the stress, steel bearing plates with a thickness of 2 in. were attached to the exterior sides of the diaphragms. The post-tensioning strands were passed through the transverse ducts and had their lock nuts bearing against the steel plates. The post-tensioning force was applied using a hydraulic pump and a jacking system. To monitor the post-tensioning force, load cells were sandwiched between two steel plates as shown in Figure 2.5-22.

Figure 2.5-21 Transverse post-tensioning system with pre-attached sleeve-and-nut anchorage

Figure 2.5-22 Load cells to monitor the transverse post-tensioning force

2.6 Sensors and data acquisition system

The sensors used in the study included internal strain gages on CFCC strands, external strain gages on concrete, linear motion transducers (LMT) for deflection measurements, and load cells. All sensors were connected to a data acquisition system as shown in Figure 2.6-1 and Figure 2.6-2 . As shown in the figure, the sensors were connected to the central processing units, which transform the analog electrical pulses from the sensors to digital signals recorded and stored in a laptop computer equipped with the data acquisition software "Mars Labs".

The strain gages on the concrete had a length of 2.0 in. The length was selected to be larger than twice the maximum aggregate size of the concrete mix (0.75 in.). The gages were attached to the surface of the concrete using special epoxy adhesive after preparing the surface. Through the flexural testing of the control beams and the bridge model, the strain gages were attached to the top surface of the concrete at the mid-span and next to the two loading points of the four-point loading setup. The load was applied through a 220 kip MTS hydraulic actuator with a maximum stroke of 20 in. The actuator was programmed to deliver load by displacement control at a rate of 0.25 in/min. In addition, load distribution tests on the bridge model was performed using a 100-ton hydraulic cylinder with a stroke of 10 in. The LMTs performed as expected and were able to capture the deflection of the test specimens. In addition, Mitutoyo 3.0-in. dial gages with an accuracy of ± .005 in. (Figure 2.6-3) were also used in testing the bridge model under service loads. The dial gages accurately captured the small deflection of the bridge model under service loads without experiencing the electrical noise associated with using electrical sensors.

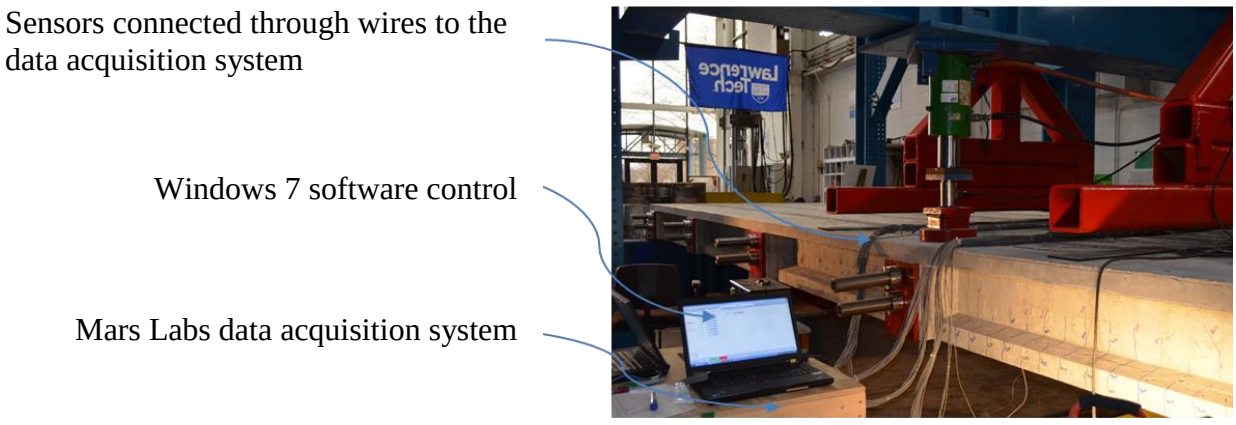

Figure 2.6-1 Data acquisition system wired into bridge model sensors

Figure 2.6-2 Mars Labs Titan model field pods for data acquisition

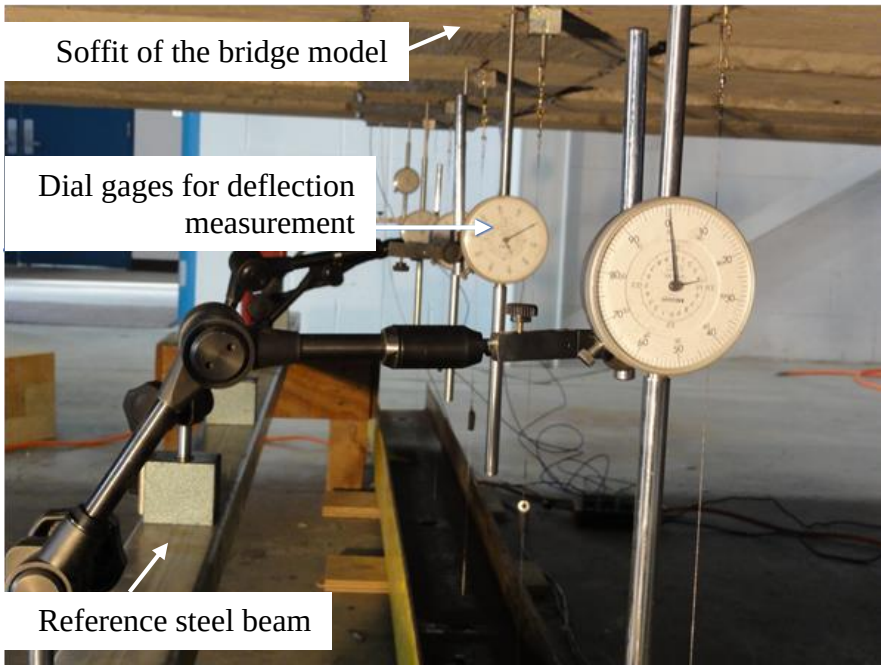

Figure 2.6-3 Dial gages to measure deflection under service loads

CHAPTER 3: TESTING & RESULTS

3.1 Introduction

This chapter presents the test methodology and the test results for the five control decked bulb T beams and the bridge model. The results are presented in the form of charts showing the relationship between the applied load and the response of the test specimens including deflection, strain of concrete, and strain in CFCC strands. In addition, for each test specimen, the ductility ratio was calculated to evaluate the failure mode analytically.

Four control beams were tested to failure under flexural loading, while one control beam was tested under shear loading to failure. The bridge model was exposed to several loading scenarios at the service limit state, post-cracking limit state, and strength limit state. While testing of the control beams was conducted to evaluate the flexural and shear response, testing of the bridge model was conducted to evaluate the integrity of the entire superstructure and the probability of developing longitudinal deck cracking especially with the absence of a cast-in-place deck slab.

3.2 Flexural testing of Beam C-S-F-U

Beam C-S-F-U had a total length of 41 ft and was constructed with four bottom prestressed CFCC strands in addition to five top non-prestressed CFCC strands, two web non-prestressed CFCC strands, and steel stirrups. The theoretical analysis for the cross section using force equilibrium and strain compatibility indicated a tension failure by rupture of CFCC prestressing strands. During the test, the beam was simply supported over two elastomeric bearing pads with an effective span of 40 ft. The bearing pads had a length of 12.0 in., a width of 6.0 in., and a thickness of 1.0 in. The load was applied to the beam using a steel spreader with two-point load as shown in Figure 3.2-1. The distance between the points of loading was 78 in. This distance was maintained through the testing of this control beam and other flexurally tested control beams.

The test was commenced by applying the load through load cycles. After every load cycle, the beam was inspected and marked for cracks. The load cycles were applied in increments of 2 kip until the first flexural crack was observed and in increments of 4 kip from cracking to failure. The deflection of the beam was recorded using two Linear Motion Transducers (LMTs) attached to the soffit of the beam as shown in Figure 3.2-2.

Figure 3.2-1 Typical four-point-loading test setup for control beams

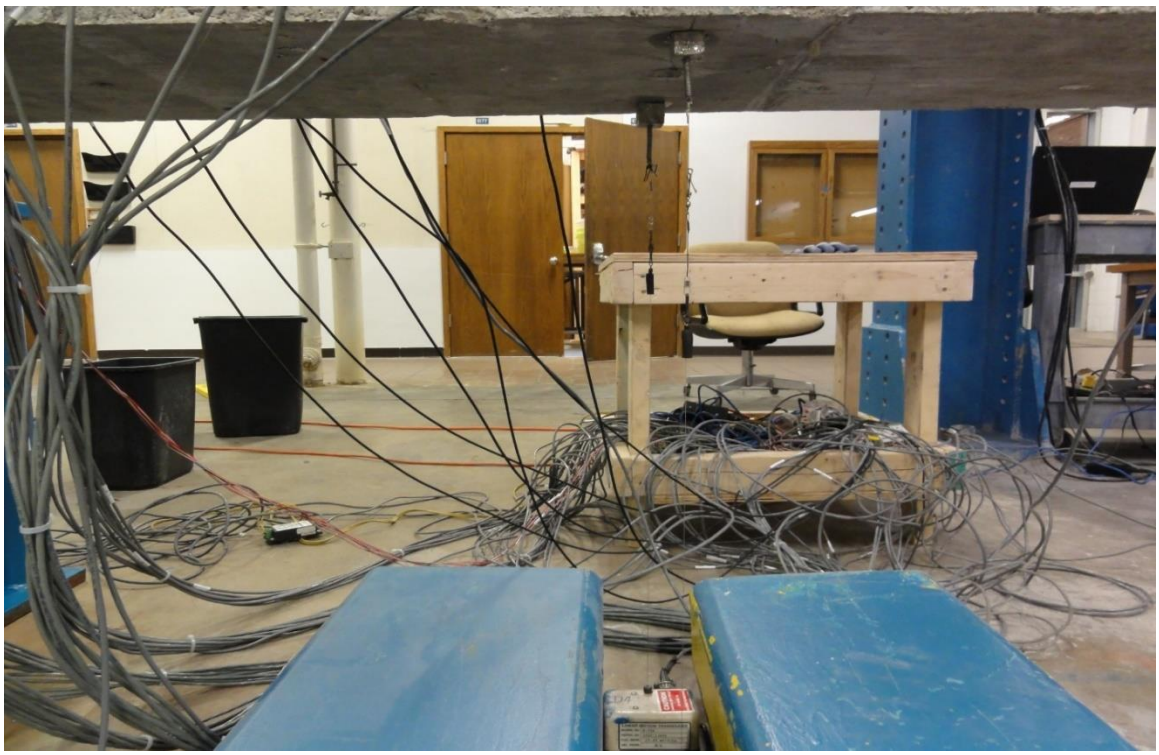

Figure 3.2-2 Linear motion transducers to evaluate deflection under different load levels

The first flexural crack was observed at a load level of 12.2 kip. This was confirmed from the recorded data as the load-deflection curves and the load-strain curves showed a remarkable change in the slope at nearly the same load level. After cracking, three strain gages were attached to the soffit of the beam near the first observed flexural crack and the load cycles were continued. The recoding from the three strain gages were used to estimate the average decompression load and consequently the average prestressing force in concrete after all losses. In subsequent load cycles, the applied load had to overcome the decompression in the beam due to prestressing before the flexural cracks can open again. Therefore, the strain gages around the crack provided strain readings until the decompression was overcome and the crack started to open. When the crack opened, the strain at the adjacent concrete ceased to increase and that marked the decompression load. The decompression load was also determined from the load deflection curves. In subsequent load cycles, an initial load was resisted by the pre-compressed section, which had the stiffness of a non-cracked gross section. Once the decompression load was reached, the stiffness dropped to that of a cracked section, and therefore, there was a remarkable change in the slope in the load-deflection curves at the decompression load in all post-cracking load cycles. The decompression load estimated using the readings from the soffit strain gages matched that estimated using the load-deflection curves and was approximately 9.9 kip, which represented a prestress loss of approximately 12 to 13 %.

The load cycles were continued and new cracks were marked after every load cycle as shown in Figure 3.2-3. The cracks were vertical and uniformly distributed under the loading spreader but they were inclined outside the loading points due to combined effect of shear and moment. As shown in Figure 3.2-4, this control beam was characterized with a dense crack map before failure. The cracks typically overlapped the stirrups and the average distance between the cracks was around 4 in., which matched the spacing between the stirrups. It should be also noted that the beam exhibited a significant deflection before failure. The deflection can be visually observed as shown in Figure 3.2-5. In practice, this deflection will be difficult to go unnoticed and it will be accompanied by cracking and collapse of non-structural components such as utility pipes, sidewalks, and barriers. Therefore, it serves as a significant visual warning sign before failure.

Figure 3.2-3 Crack mapping between load cycles

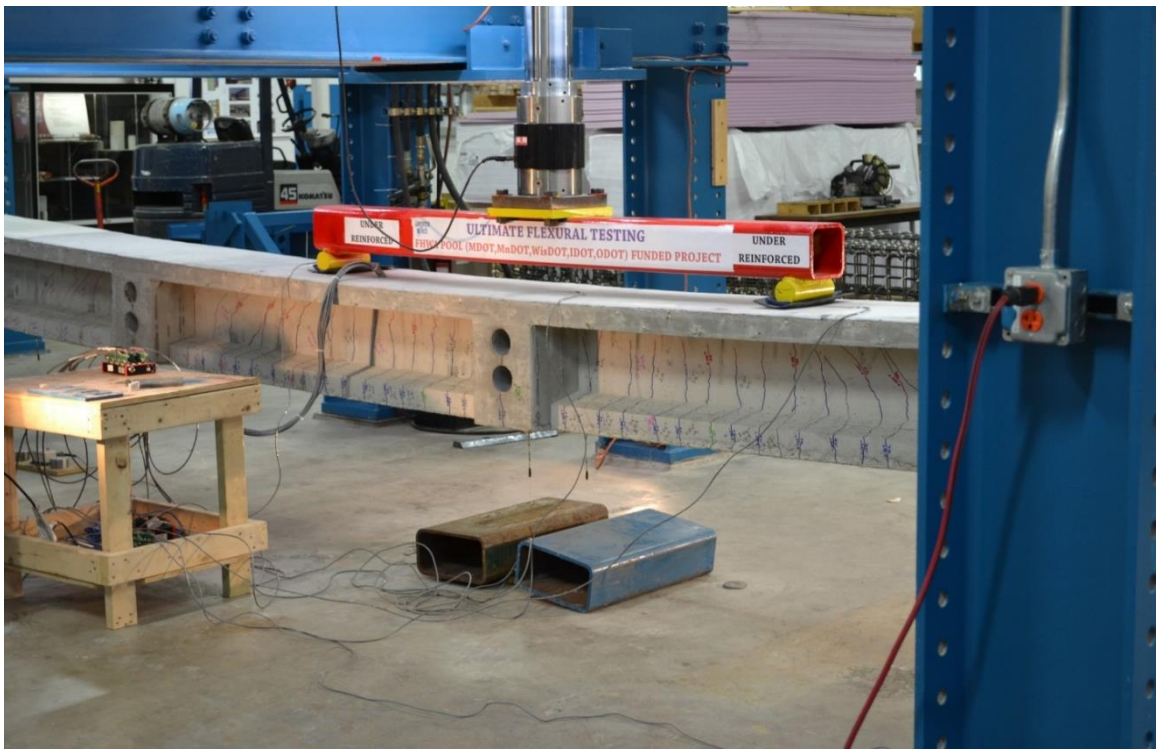

Figure 3.2-4 Load cycles of Beam C-S-F-U

Figure 3.2-5 Deflection of Beam C-S-F-U

The last load cycle before failure reached 24 kip with a corresponding deflection of 9.11 in. After unloading, the residual deflection from all load cycles was 0.82 in. as indicated in Figure 3.2-6. The last load cycle included loading the beam to failure. The failure of this control beam took place at a load level of 32.47 kip with a corresponding deflection of 14.42 in. (not including the residual deflection of 0.82 in.). At this load level, a popping sound was heard and the load slightly dropped to 31.72 kip with a corresponding deflection of 14.61 in. Then the beam continued to resist the load and the load level increased again to 33.19 kip with a corresponding deflection of 15.62 in. At that point, the popping sound was heard again and the load decreased to 31.55 kip with a corresponding deflection of 15.83 in. The beam however continued to take more load and approached a load level of 32.07 kip. Finally, multiple popping sounds were heard and the beam lost its structural integrity and sustained a permanent deformation as shown in Figure 3.2-7.

After failure, the beam was inspected and it was found that there was a spalling of the concrete cover at multiple locations (Figure 3.2-8). Failure in the CFCC strands was also observed and was linked to the concrete spalling (Figure 3.2-9). It was determined that the popping sounds that were heard during the test were the sound of CFCC strands rupture. However, it should be noted that

due to the configuration of the CFCC strand, which encompasses seven wires, the tensile failure usually occurs on the wire level and not the strand level. In other words, every popping sound heard could have represented the rupture of single wire in the CFCC strand.

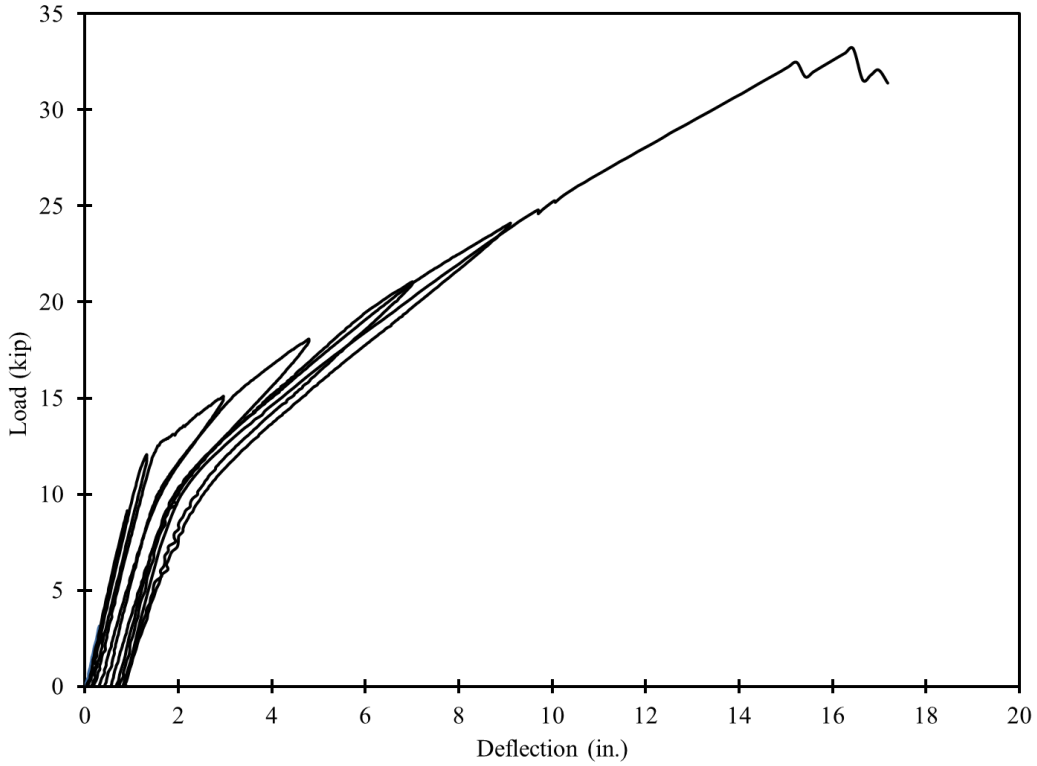

Figure 3.2-6 Load-deflection cycles of Beam C-S-F-U

Figure 3.2-10 and Figure 3.2-11 show the strain in the concrete top surface and the CFCC strands during the last load cycle. The maximum recorded concrete strain before failure was approximately 2,236 με, while the maximum recorded strain in the CFCC strands before failure was 18,233 με. The guaranteed ultimate strain in the CFCC as given by the manufacturer is 16,000 με. Therefore, it was evident that the failure took place in the CFCC strands (tension failure).

Finally based on the load-deflection curves from all load cycles including the ultimate load cycle, the ductility ratio was calculated according to Grace et al. (2000). The area under the load-deflection curve is divided into two areas of elastic and inelastic energies. The elastic energy is the energy that can be retrieved once the load is removed from the beam, while the inelastic energy is the energy dissipated in the formation of cracks and for high concrete strain, the energy dissipated by the plastic deformation of concrete. According to Figure 3.2-12, the total energy absorbed by beam C-S-F-U at failure was approximately 387 kip.in. By following the last un-loading curve and

estimate the un-loading curve at failure, the total energy was divided into elastic energy of 259 kip.in. and inelastic energy of 128 kip.in. The ductility ratio was calculated as the ratio between the inelastic energy and the total energy and was estimated as 33%. It should be noted that the mode of failure slightly increased the ductility ratio.

As expected, the ductility ratio of the beam indicated a brittle failure (ductility ratio less than 70%, Grace et al. (2000)). However, the large deflection and the dense cracking patterns give a clear visual sign before failure. The failure mode by the consecutive rupture in the individual wires of the strands may also be regarded as a warning sign before complete failure.

Figure 3.2-7 Beam C-S-F-U at failure

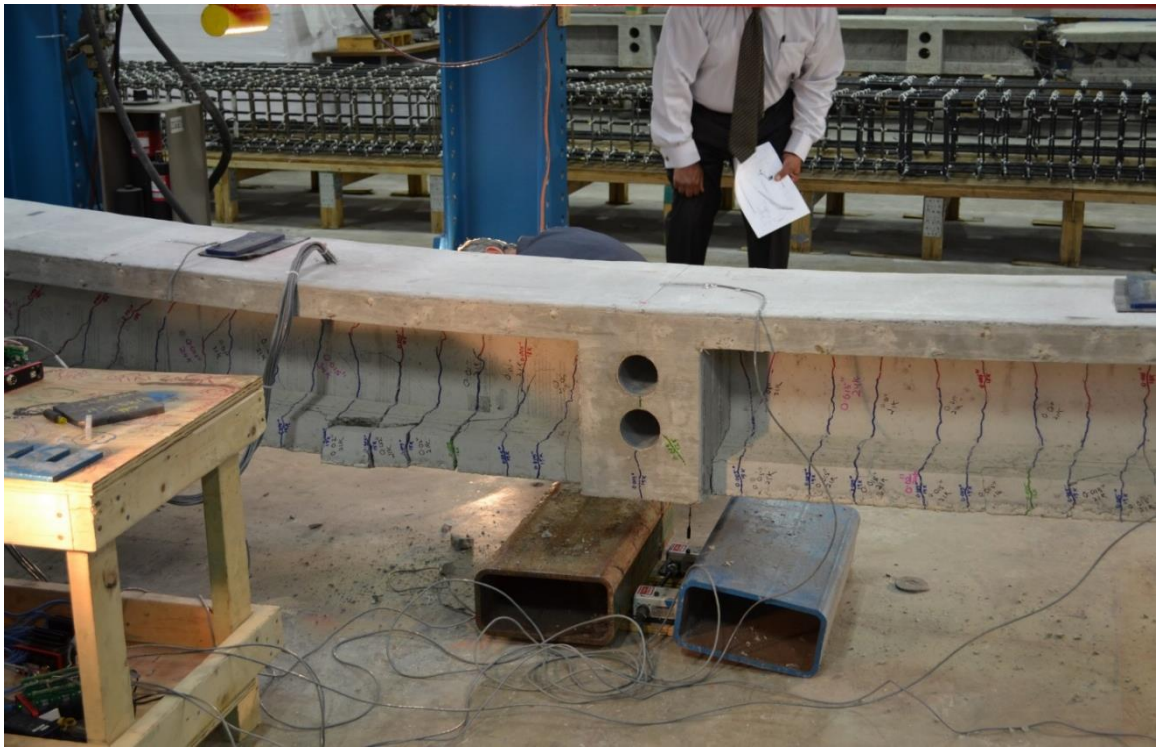

Figure 3.2-8 Spalling of concrete at failure in Beam C-S-F-U

Figure 3.2-9 Rupture of prestressing CFCC strands in Beam C-S-F-U

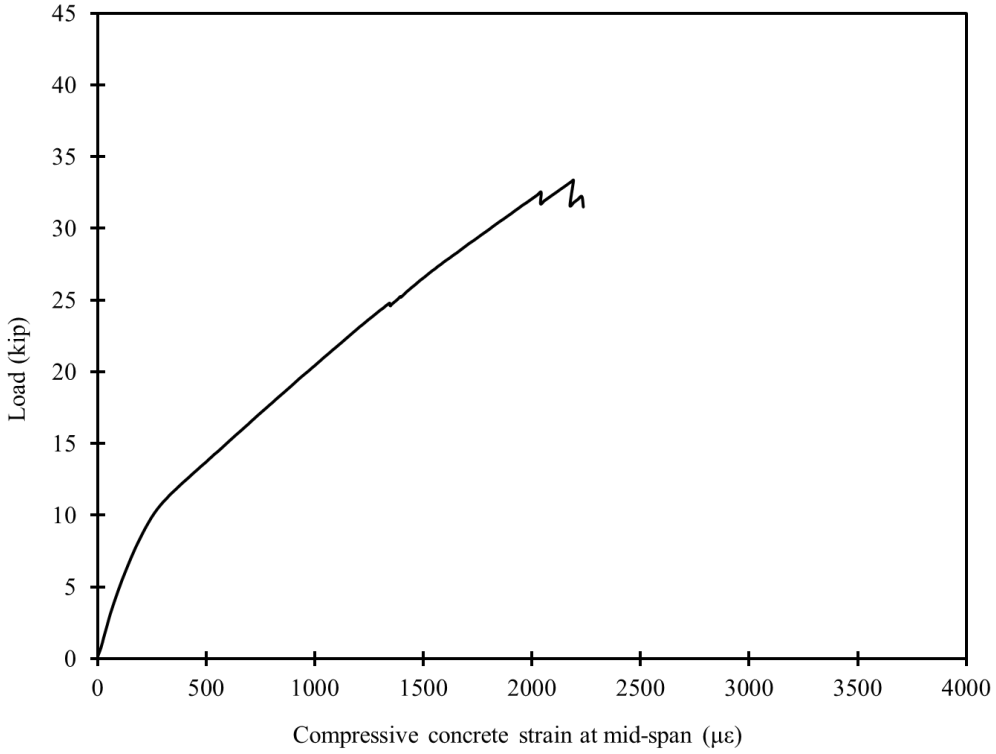

Figure 3.2-10 Load vs. concrete strain during last load cycle of Beam C-S-F-U

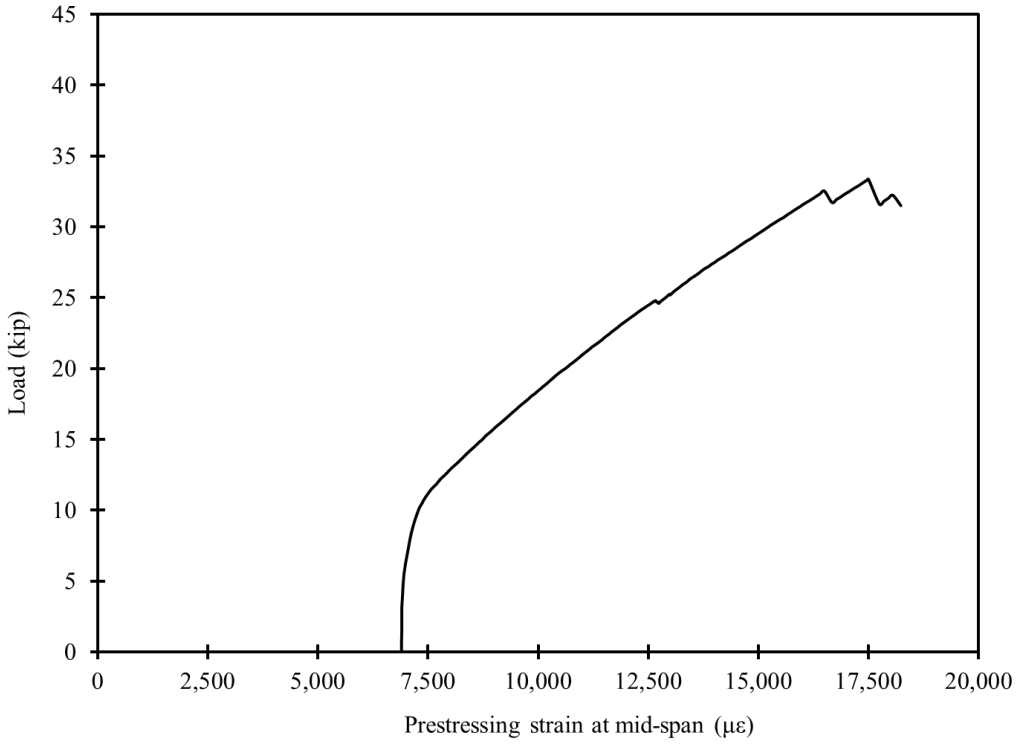

Figure 3.2-11 Load vs. strain of prestressing strands during last load cycle in Beam C-S-F-U

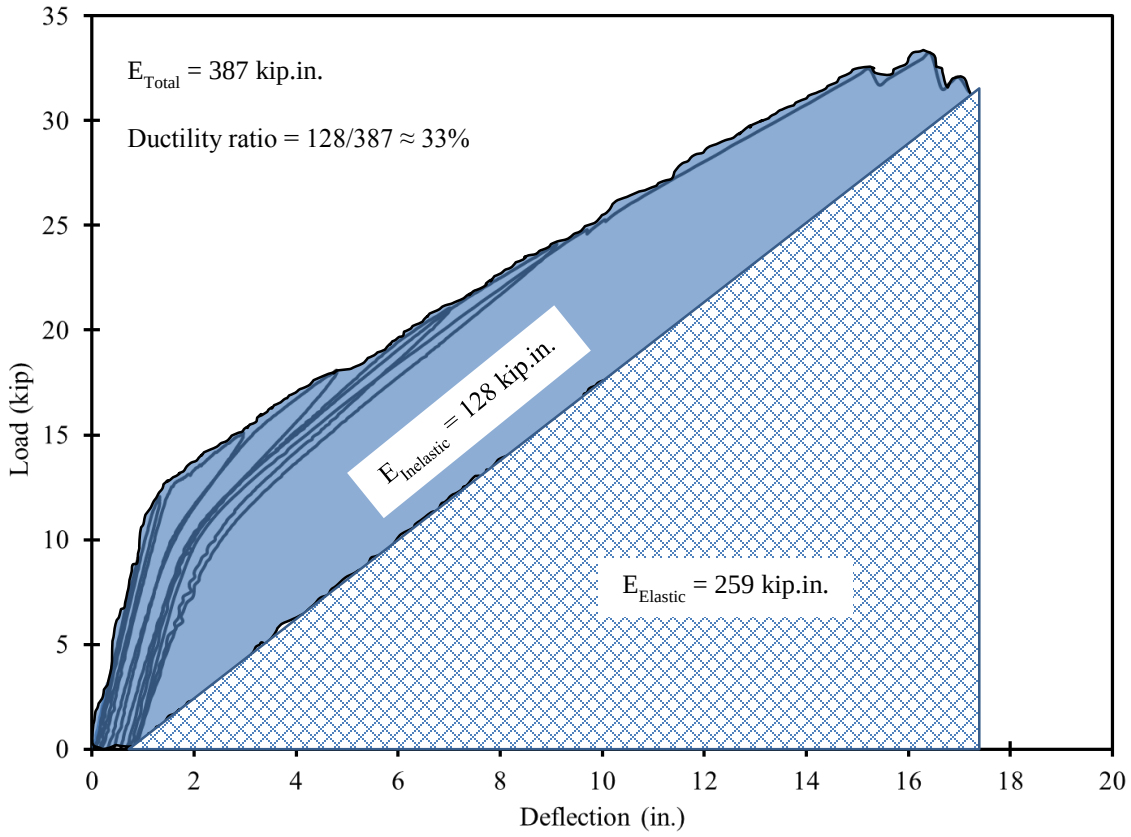

Figure 3.2-12 Ductility ratio in Beam C-S-F-U

3.3 Flexural testing of Beam C-S-F-B

This control beam was reinforced with four bottom CFCC prestressing strands and three bottom CFCC non-prestressing strands in addition to the top and web reinforcement. The beam was loaded under four-point flexural loading and the load was applied in cycles with a load increment of 2 kip before cracking and 4 kip after cracking. The last load cycle involved loading the beam to failure and as shown in Figure 3.3-1 and Figure 3.3-2, the failure resulted in breaking and total separation of the beam. The failure took place under one of the loading points, which represented the location of the maximum moment and maximum shear in the beam.

Similar to beam C-S-F-U, the observed cracking load was approximately 12 kip and the decompression load was estimated from strain readings and load-deflection curves as 9.5 kip. As shown in Figure 3.3-3, the last load cycle before failure reached 24 kip with a corresponding deflection of 8.24 in. After unloading, the remaining deflection from all load cycles was

approximately 0.95 in. The load cycles before cracking were characterized by a mono-slope load-deflection curves, while load cycles after cracking were characterized by a bilinear load-deflection curve. The decompression load marked the change of slope in all load-deflection curves performed after cracking.

The failure took place at a load level of 40.79 kip with a corresponding deflection of 16.98 in. or 17.94 in. after adding the residual deflection from previous load cycles. The concrete strain at failure reached 3,272 με. The strain in the concrete matched the theoretical analysis and indicated a balanced failure. Due to strain gages malfunctioning, the recording of the strain in prestressing strands was interrupted early at the test.

The total energy stored in the beam before failure (area under load-deflection curve) was approximately 447 kip.in. as shown in Figure 3.3-4. The elastic and inelastic energies were estimated (graphically and analytically) as 321 and 126 kip.in., respectively. The ductility ratio for this beam was estimated as 28%.

Figure 3.3-1 Balanced failure of Beam C-S-F-B

Figure 3.3-2 Balanced failure resulting in complete separation of Beam C-C-F-B

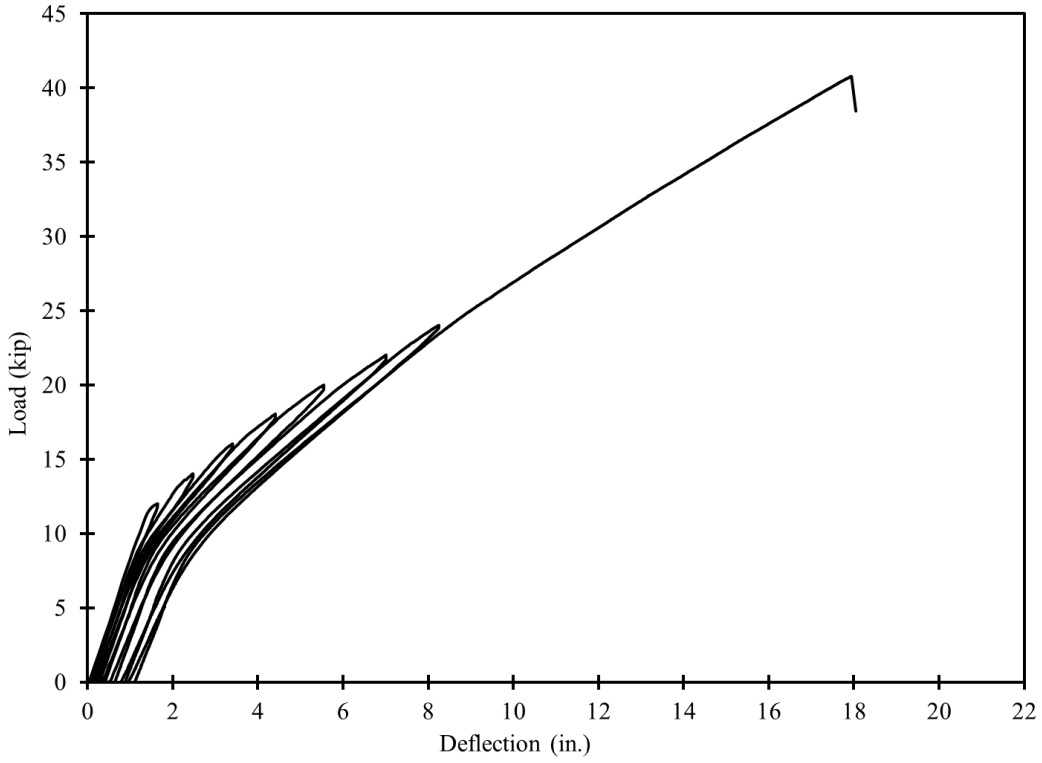

Figure 3.3-3 Load-deflection curves for Beam C-S-F-B

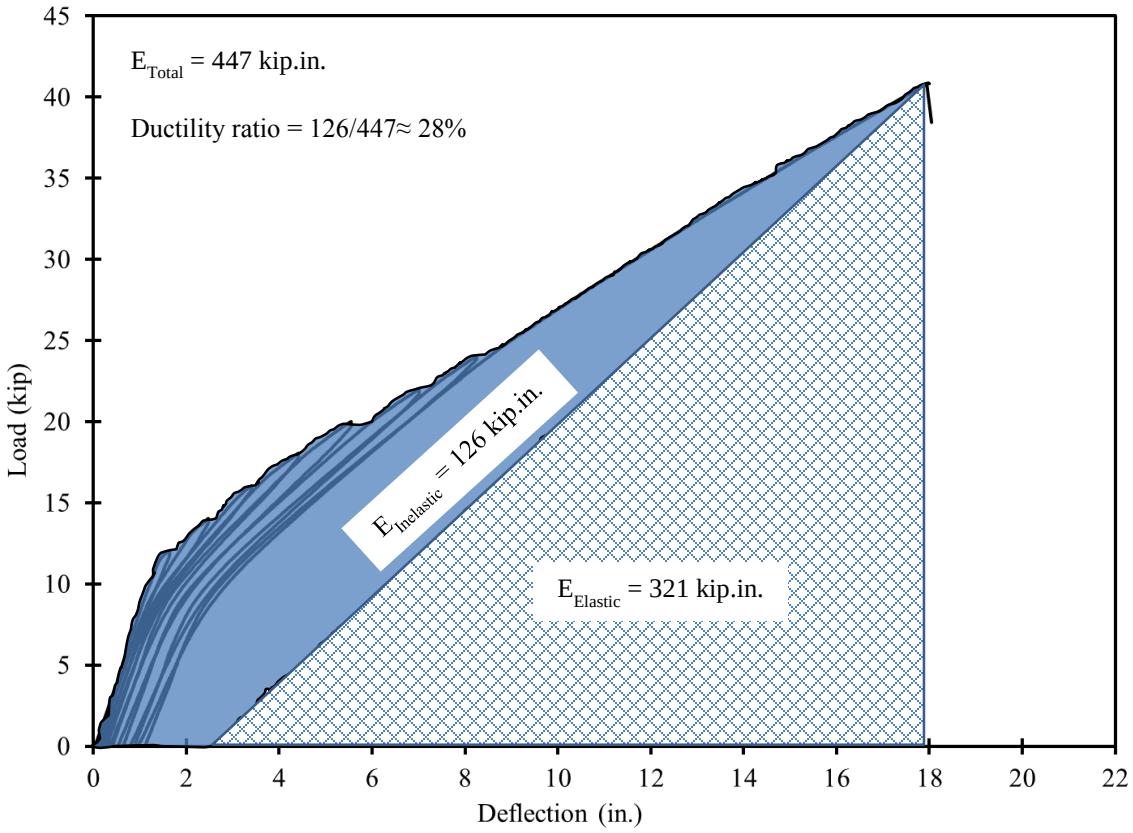

Figure 3.3-4 Ductility ratio in Beam C-S-F-B

3.4 Flexural testing of Beam C-S-F-O

This control beam was provided with four bottom prestressing CFCC strands and five bottom non-prestressing CFCC strands. This amount of bottom reinforcement guaranteed the compression failure mode. As shown in Figure 3.4-1 through Figure 3.4-3, the failure of this beam was characterized by the crushing of the concrete in the top flange followed by shearing and rupturing of both prestressing and non-prestressing CFCC strands and breaking of the beam into two pieces.

The failure of the beam took place at a load level of 43.6 kip with a corresponding deflection of 14.89 in. or 15.59 in. with the added residual deflection from previous load cycles. The maximum recorded concrete strain in the top flange before failure was approximately 2,951 με, while the maximum recorded strain in the prestressing strands at failure was approximately 13,665 με.

Figure 3.4-4 shows the load-deflection curves obtained from all load cycles. Similar to previous beams, mono-slope linear curves were obtained before cracking, while bilinear curves

were obtained after cracking with the decompression load marking the change in slope. The cracking load was around 12.3 kip, while the decompression load was estimated as 9.5 kip. The last load cycle before failure reached 34 kip with a corresponding deflection of 11.01 in. After unloading, the residual deflection from all load cycles was approximately 0.7 in.

Figure 3.4-5 highlights the elastic and inelastic energy absorbed by the beam before failure. The elastic energy was approximately 280 kip.in., while the inelastic energy was approximately 123 kip.in. with a total energy of 403 kip.in. and a ductility ratio of 31%. Similar to previous beams with CFCC reinforcement, from the aspect of ductility ratio, the failure of the beam falls under the brittle failure category but from a deflection and cracking perspective, the failure was accompanied by enough warning signs that indicated the overstressing.

Figure 3.4-1 Beam C-S-F-O at failure

Figure 3.4-2 Compression failure followed by rupture of strands in Beam C-S-F-O

Figure 3.4-3 Close view showing the failure section of Beam C-S-F-O

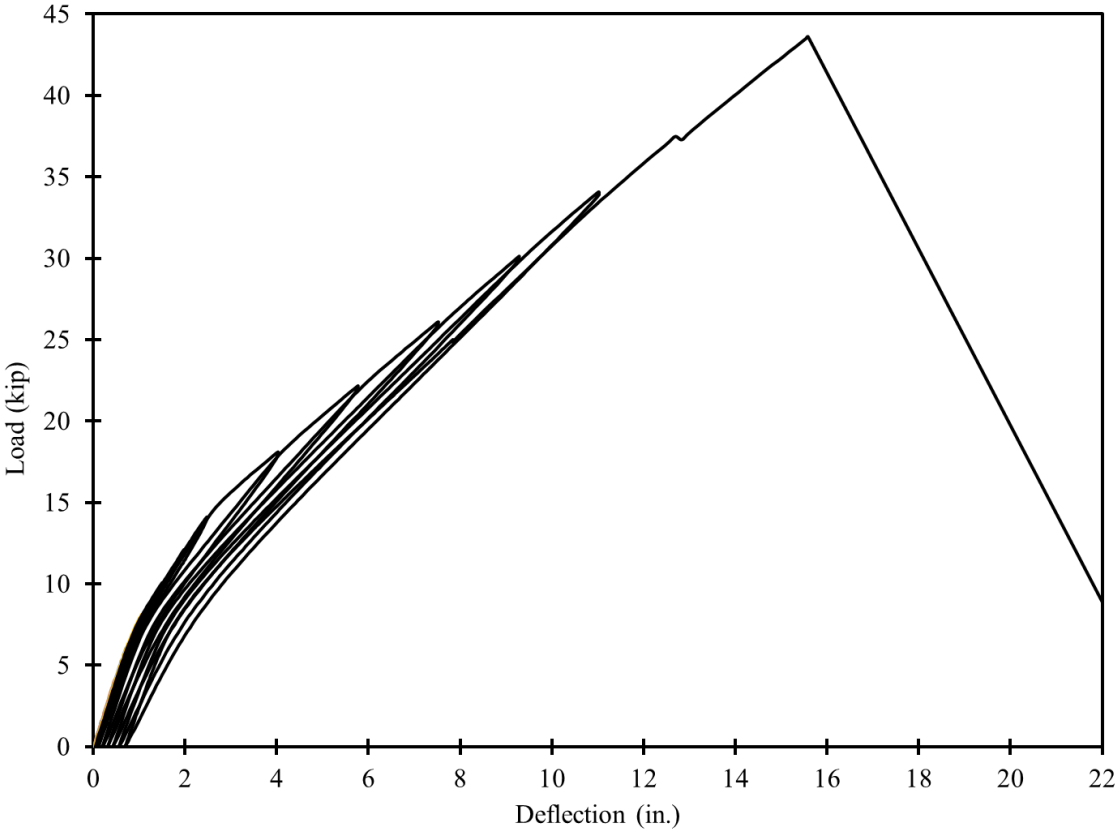

Figure 3.4-4 Load-deflection curves for Beam C-S-F-O

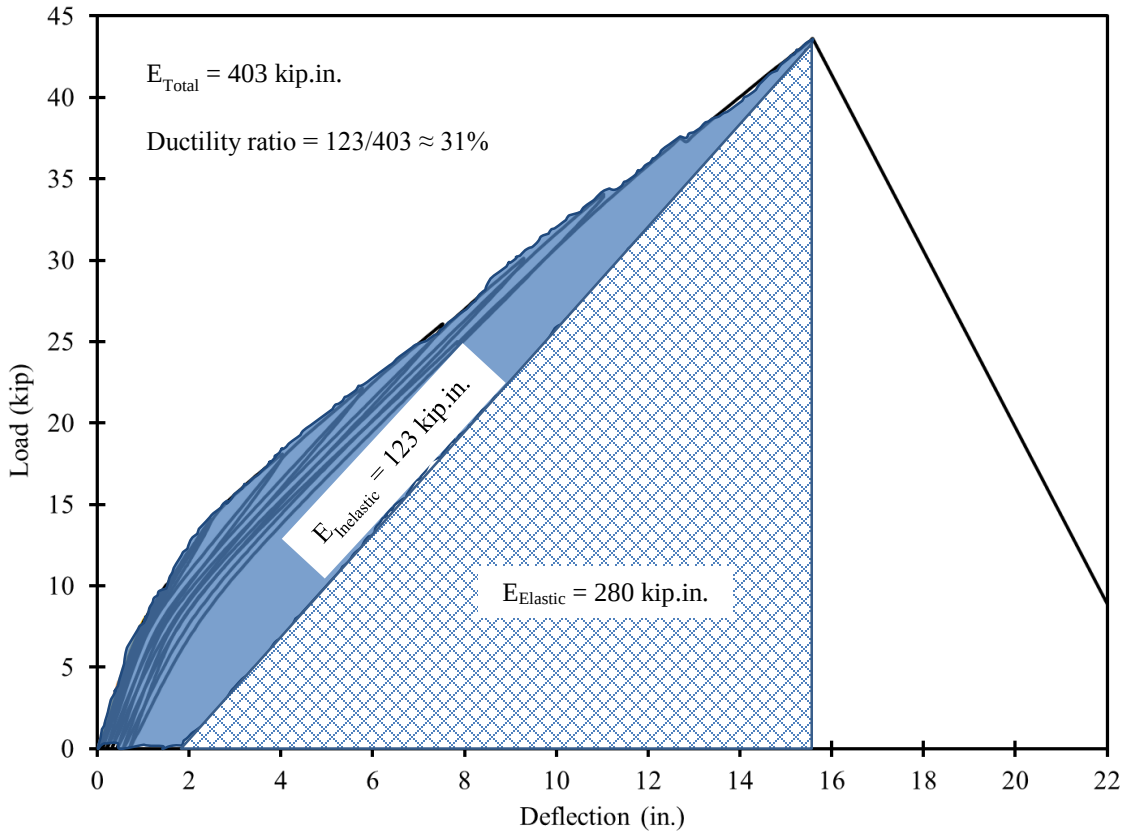

Figure 3.4-5 Ductility ratio of Beam C-S-F-O

3.5 Flexural testing of Beam S-S-F-U

This beam was prestressed with four bottom low-relaxation steel prestressing strands in addition to three non-prestressed deformed steel bars. The configuration of reinforcement was similar to that of the balanced CFCC beam, Beam C-S-F-B. However, because of the difference in material properties between steel and CFCC, this beam was expected to fail in tension by yielding of prestressing strands. Similar to other control beams, this beam was tested under four-point loading applied through cycles of loading and unloading. The cracking load and the decompression load were around 12 kip and 9.5 kip, respectively. The last load cycle before failure reached 30 kip with corresponding deflection of 7.03 in. After unloading, the residual deflection was approximately 0.74 in.

During the last load cycle, the beam exhibited yielding of strands at a load level of 30.6 kip with a corresponding deflection of 7.52 in. (including the residual deflection). After yield, the deflection of the beam increased successively with a smaller increase in the applied load. The

failure took place at a load level of 39.37 kip with a corresponding deflection of 20.17 in. (including the residual deflection). At failure, the concrete in the top flange crushed and the top reinforcement showed signs of buckling as shown in Figure 3.5-1 through Figure 3.5-3. The maximum recorded concrete strain before failure averaged 2,615 με, while the strain in the prestressing steel strands averaged 18,784 με. From the results and as shown in Figure 3.5-4, it can be seen that approximately 12.65 in. of deflection was obtained between steel yield and concrete crushing with a corresponding load increase of approximately 8.77 kip.

Due to the yielding of prestressing strands, this control beam exhibited a high ductility ratio. As shown in Figure 3.5-5, the total energy absorbed before failure was estimated as 613 kip.in. The elastic energy was estimated as 185 kip.in, while the inelastic energy was estimated as 428 kip.in. Therefore, the ductility ratio was calculated as 70%, which places this failure within the ductile failure boundaries.

Figure 3.5-1 Flexural failure of Beam S-S-F-U

Figure 3.5-2 Failure of Beam S-S-F-U showing crushing of concrete after yield

Figure 3.5-3 Buckling of top reinforcement in Beam S-S-F-U at failure

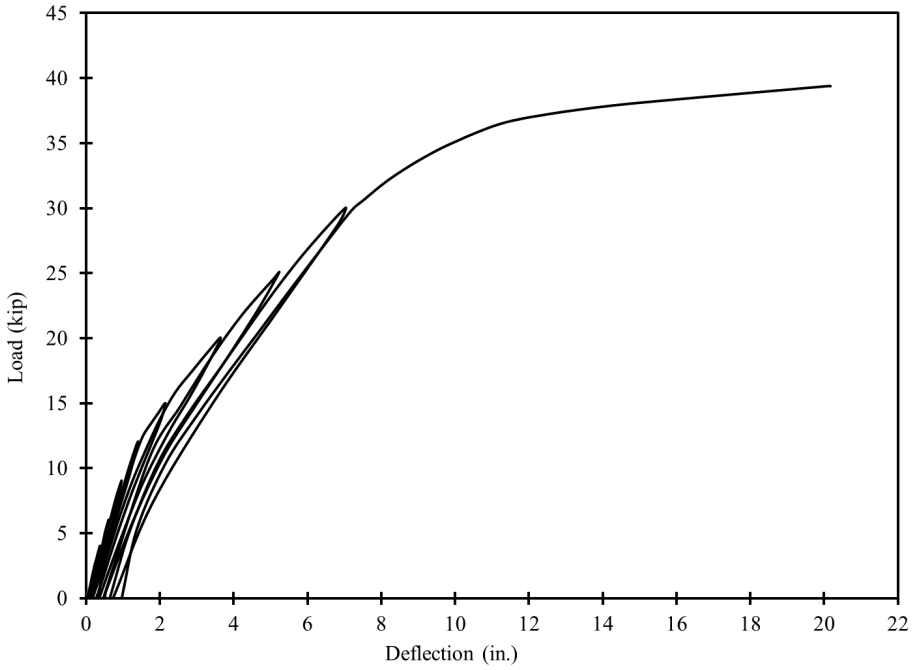

Figure 3.5-4 Load-deflection curves for Beam S-S-F-U

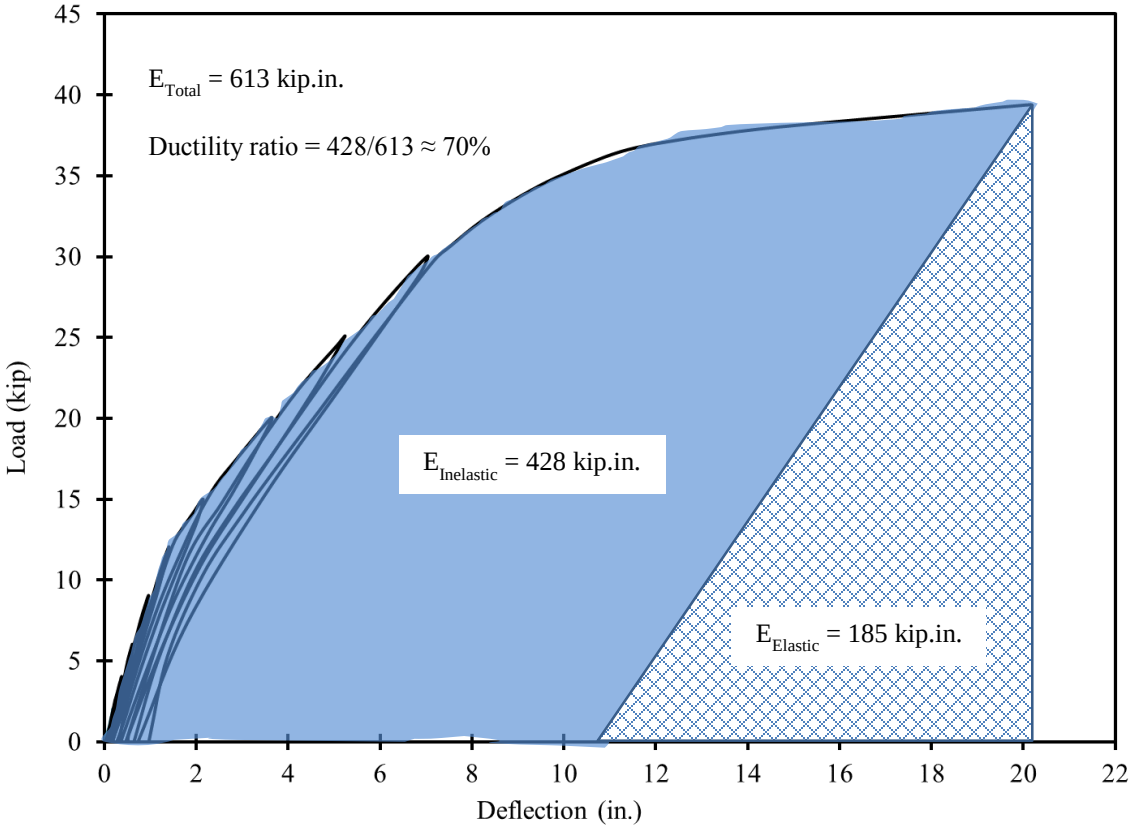

Figure 3.5-5 Ductility ratio in Beam S-S-F-U

3.6 Comparison between flexural control beams

The load-deflection curves during the ultimate-load cycle for all control beams are plotted in Figure 3.6-1 with elimination for the residual deflection from previous load cycles. All the beams had the same stiffness before reaching the decompression load. After the decompression load, Beam S-S-F-U with steel strands had the highest stiffness followed by Beam C-S-F-O, Beam C-S-F-B, and finally Beam C-S-F-U. The difference in bending stiffness between control beams with CFCC reinforcement was attributed to the difference in reinforcement ratio, while the difference in stiffness between Beam S-S-F-U and other control beams was attributed mainly to the difference in material properties between steel and CFCC.

The recorded concrete strain in all beams at the mid-span during the ultimate load cycle is shown in Figure 3.6-2. Strain readings in beam S-S-F-U were significantly less than those in other control beams until yielding. After yielding the concrete strain in beam S-S-F-U increased rapidly and approached those of beams C-S-F-B and C-S-F-O. It should be noted that the recorded strain does not necessarily represent the maximum strain in the concrete flange as it only represents the strain at the location of the gages. However, it can be seen that the concrete crushing in beams S-S-F-U, C-S-F-B, and C-S-F-O occurred at approximately 3000 $\mu\varepsilon \pm 400\ \mu\varepsilon$. Figure 3.6-3 shows the average strain readings in the prestressing strands in all control beams during the last load cycle. As mentioned earlier, the prestressing strain recoding in Beam C-S-F-B was interrupted and stopped early at the test. The ultimate load and maximum strain and deflection readings for all beams are presented in Table 3.6-1, which also shows the design factored load for each beam when including all strength reduction factors.

The design factored load was analytically calculated by estimating the theoretical nominal capacity of each beam and multiplying this nominal capacity by the appropriate strength reduction factor according to available design guides. A strength reduction factor of 0.65 (ACI 440.4R-04) was included in case of CFCC prestressed beam with compression failure and a strength reduction factor of 0.85 was implemented in case CFCC prestressed beam with tension failure. Beam S-S-F-U with prestressing steel strands was designed with a strength reduction factor of 1.0 (AASHTO LRFD 2012). In addition, a CFCC guaranteed strength of 339 ksi was used in the design and it was further reduced to 304.9 ksi to account for the exposure to environmental conditions (ACI 440.1R-06).

Table 3.6-1 Summary for the ultimate-load testing of control beams

Beam	Crack/ service load (kip)	Decomp. load (kip)	Ultimate load (kip)	Defl. at failure (in.)	Concrete strain at failure (με)	Prestress strain at failure (με)	Design factored load (kip)
C-S-F-U Under-Reinf. CFCC	12.2	9.9	33.19	15.62	2,236	18,233	23.0
C-S-F-B Balanced CFCC	12.0	9.5	40.79	17.00	3,272	-	28.1
C-S-F-O Over-Reinf. CFCC	12.3	9.5	43.6	14.89	2,951	13,665	30.5
S-S-F-U Under-Reinf. steel	12.0	9.5	39.37	19.43	2,615	18,787	34.6

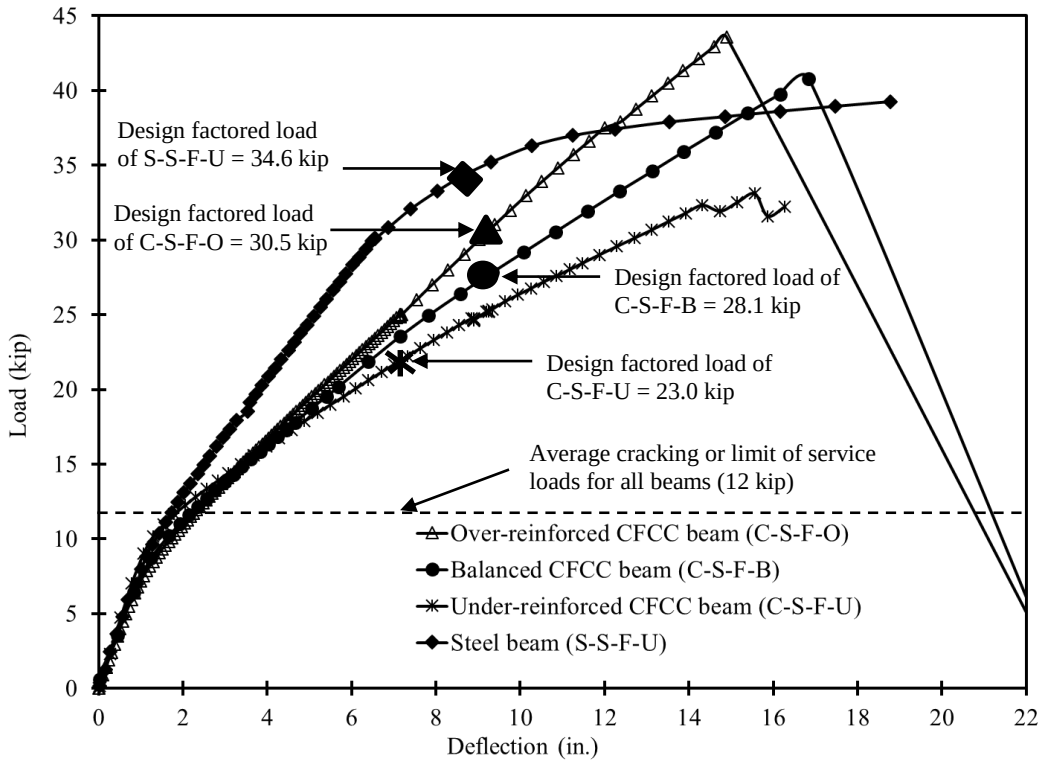

Figure 3.6-1 Load-deflection curves for all control beams tested in flexure

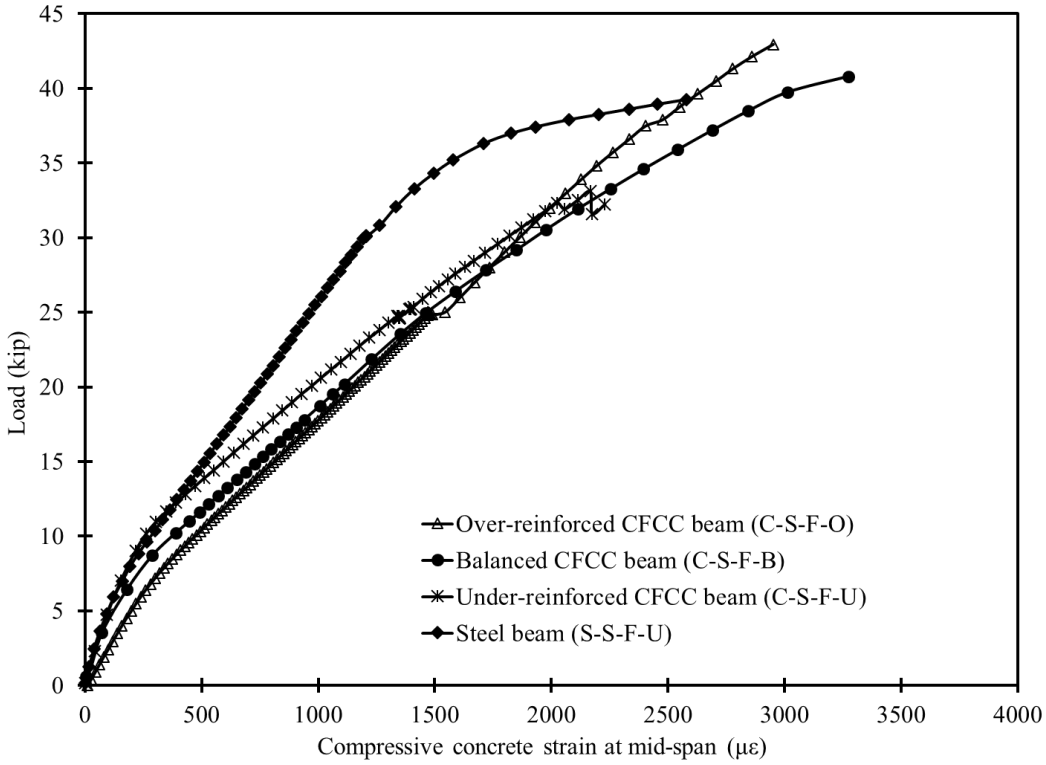

Figure 3.6-2 Load-concrete-strain curves for all control beams tested in flexure

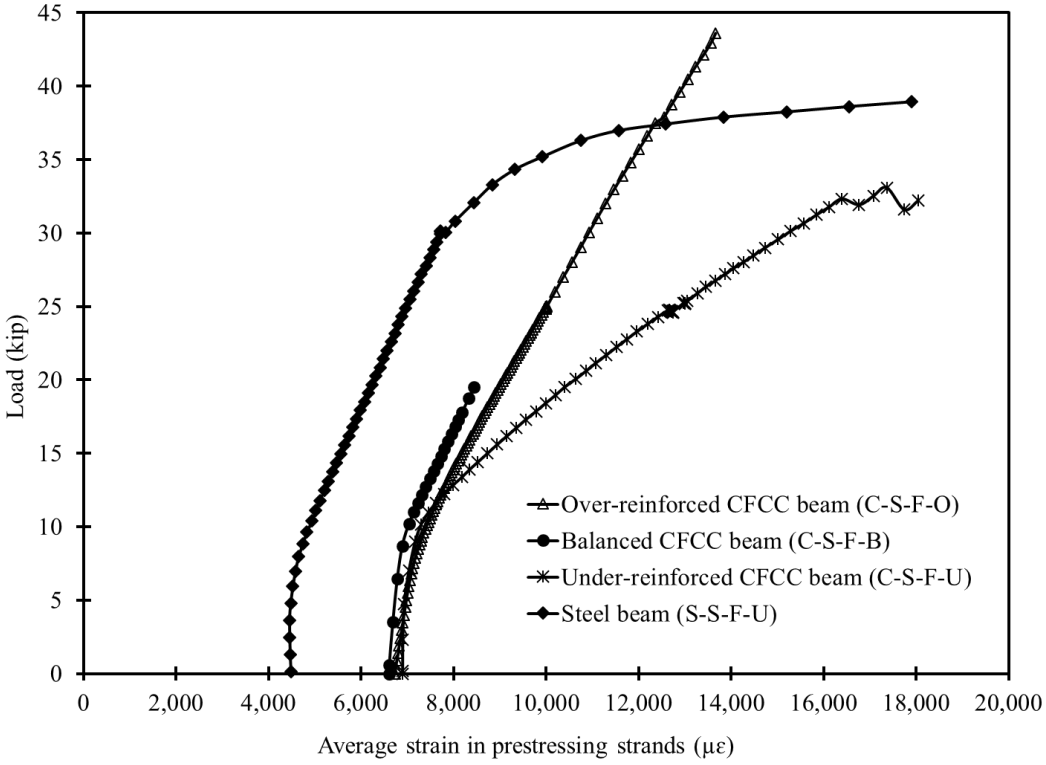

Figure 3.6-3 Load-prestressing-strain curves for control beams tested in flexure

3.7 Shear testing of Beam C-C-S-B

This control beam was reinforced with four bottom prestressing CFCC strands and three non-prestressing CFCC strands. In the transverse direction, the beam was provided with CFCC stirrups at a center-to-center spacing of 4.0 in. The beam had a total length of 41 ft and effective span of 40 ft and was simply supported over two elastomeric bearing pads.

In shear testing, the shear loading mechanism is affected by the distance from the applied load to the nearest support, or the shear span distance. If the shear span distance is very small, the load is typically transferred to the support through arch action and the shear reinforcement does not participate in the shear load carrying mechanism. If the shear span is long, the failure is usually a combination between the shear and flexural failure. Previous studies (Tuchscherer et al. 2011 and Zsutty 1971), uses the shear-span-to-depth ratio as a means of evaluating the failure mode. For instance, it was observed that arch action failure is the dominant failure mode in beams with shear-span-to-depth ratio less than 2.5, while shear failure dominate beams with shear-span-to-depth ratios ranging between 2.5 to 6.0, and flexural failure dominates beams with shear-span-to-depth ratios larger than 6.0.

As shown in Figure 3.7-1, the load was applied near the end of the beam with an effective shear span of 45 in., which resulted in a shear-span-to-depth ratio of 3.0 and consequently promoted the shear failure in this control beam. To capture the shear loading mechanism and the shear failure mode, the beam was instrumented with multiple LVDTs to record the slippage of CFCC strands at the end of the beam as shown in Figure 3.7-2. The beam was also provided with a series of linear strain gages, rosette strain gages, and LVDTs through the shear span as shown in Figure 3.7-3 and Figure 3.7-4. In addition, strain gages were provided on the top flange near the loading point to record the strain in the concrete. LMTs were attached to the beam under the point of loading and under the mid-span section.

Internally, each stirrup through the shear span was provided with two strain gages as shown in Figure 3.7-5. The stirrups were labeled from S1 near the support to S8 just under the load. In addition, all the internal reinforcement including the prestressing CFCC strands was provided with strain gages at the section under load.

The testing of the beam started with applying the load in cycles of loading and unloading. After each loading cycles, the beam was inspected for cracks. The first observed crack was a shear crack that developed through the web of the beam. The readings from the rosette strain gages confirmed the developed crack as the cracking stress of the web was exceeded at the development of the first shear crack at a shear force level of 25.64 kip. The shear force is equal to the reaction at the near support. After cracking, the readings from the strain gages did not represent the exact stress and strain distribution at the shear span and therefore was not presented here to avoid confusion. However, these readings were analyzed to evaluate the compression stress in the concrete struts between shear cracks. Figure 3.7-6 and Figure 3.7-7 show the development of the shear cracks during different loading stages until just before failure.

On the other side of the beam, the LVDTs recorded significant relative displacements only after cracking. As the LVDTs crossed the shear cracks, the average crack width was determined by analyzing the readings from the LVDTs in three different directions 0, 45, and 90 degrees according to Shehata (2000).

With increasing the load, the existing shear cracks propagated and new shear cracks developed. In addition, some shear cracks developed into flexural cracks. The first flexural crack was observed at a shear force level of 41 kip.

The failure of the beam took place at a shear force level of 41.24 kip. The failure was explosive in nature (Figure 3.7-8). The only warning sign was the development of a main diagonal shear crack extending from the support after the diaphragm and across the shear span to the loading point. The failure was characterized by the crushing of the concrete strut in the web and subsequently in the deck flange as shown in Figure 3.7-9. After failure, the stirrups were exposed and inspected for failure but no rupture of CFCC stirrups was observed (Figure 3.7-10).

As shown in Figure 3.7-11, the maximum recorded compressive concrete strain in the top flange under the load was approximately 2,668 με, while the maximum record strain in the web at 45° was approximately 1,935 με. On the other hand, the maximum deflection under load and at mid-span at failure was approximately 3.29 in. and 5.71 in., respectively. As shown in Figure 3.7-12, both deflection curves under load and at mid-span were bilinear curves with the decompression load marking the change of the slope between the two linear segments of each curve.

Figure 3.7-13 shows the strain in selected stirrups during the ultimate load cycles. It should be noted that during initial load cycles, the strain in the stirrups was negligible until the development of first flexural crack. On crack development, stirrups intercepted by the crack showed a sudden increase in the strain, while stirrups not intercepted by cracks did not show any significant strain reading. The readings shown in Figure 3.7-13 represent the maximum recorded strain in stirrups as those stirrups were intercepted by shear cracks in previous load cycles. The maximum recorded strain in the stirrups at failure was that recorded by the bottom strain gage in S3 and was approximately 3,720 με. By looking at Figure 3.7-5, it can be seen that there was a major shear crack crossing near that particular strain gage and that shear crack developed to be the failure plane as shown in Figure 3.7-8 and Figure 3.7-9. Finally, Figure 3.7-14 shows the average shear crack width as calculated based on the readings from the LVDTs. The maximum recorded shear crack width was approximately 0.09 in. It should be noted that the maximum limit of the LVDTs was exceeded near failure and that was the reason for the constant crack width reading near the failure.

Figure 3.7-1 Test setup of Beam C-C-S-B

Figure 3.7-2 Monitoring slippage of prestressing CFCC strands using end LVDTs

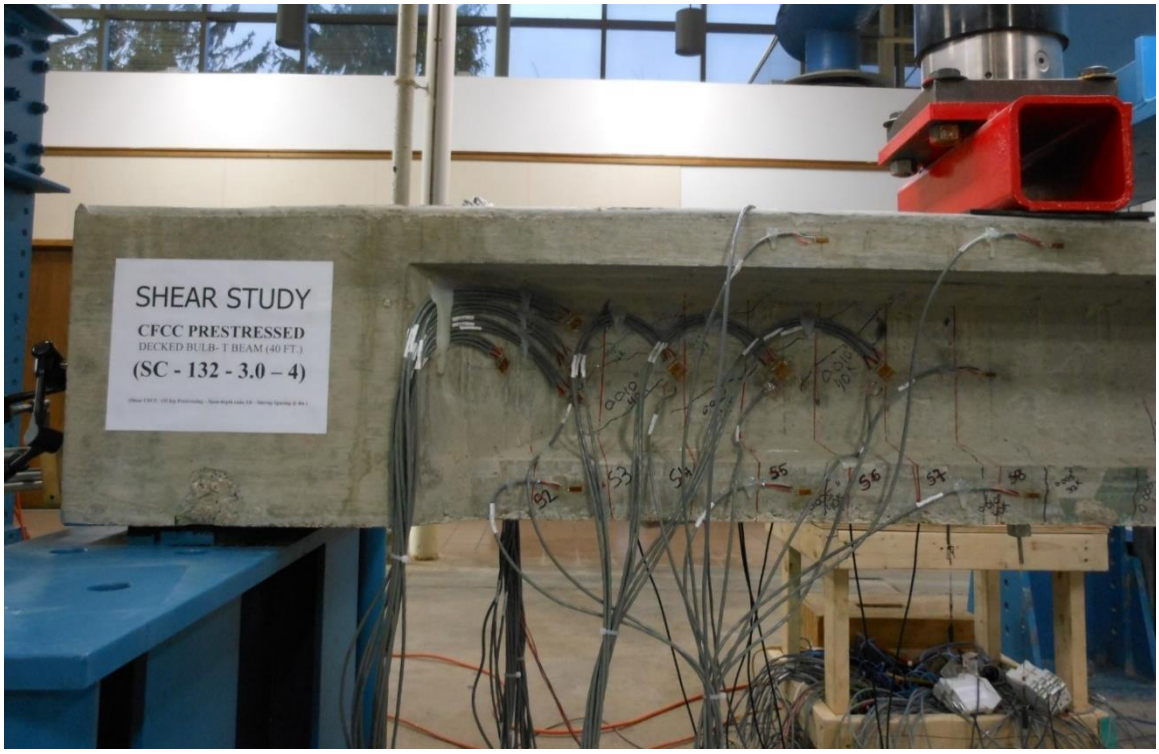

Figure 3.7-3 Strain gages through shear span of Beam C-C-S-B

Figure 3.7-4 LVDTs at 0, 45, and 90° to evaluate shear cracking

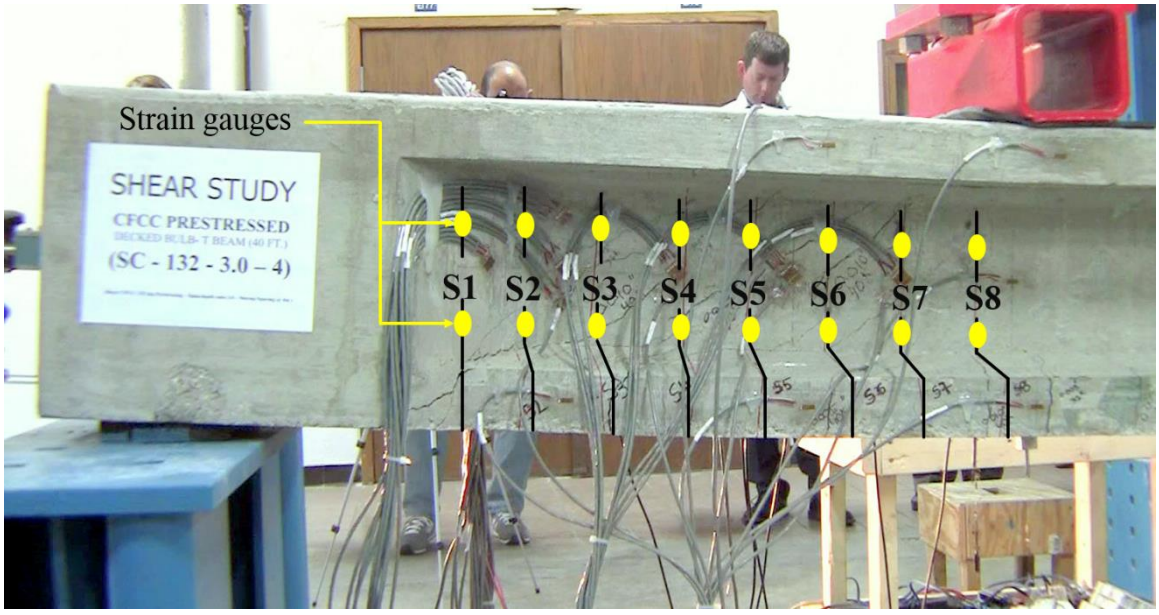

Figure 3.7-5 Location of internal strain gages on CFCC stirrups of Beam C-C-S-B

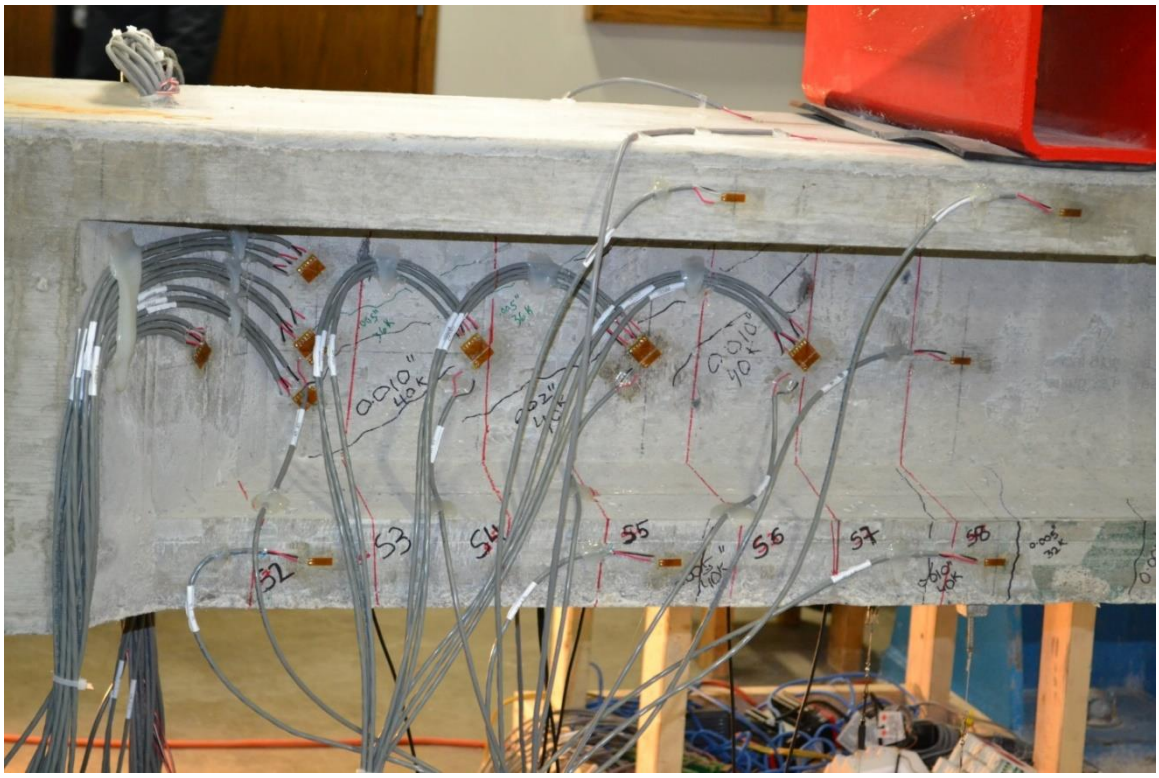

Figure 3.7-6 Crack development in shear span of Beam C-C-S-B

Figure 3.7-7 Development of main shear crack just before failure in Beam C-C-S-B

Figure 3.7-8 Explosive failure of Beam C-C-S-B

Figure 3.7-9 Beam C-C-S-B after failure

Figure 3.7-10 No rupture of CFCC stirrups was observed in Beam C-C-S-B

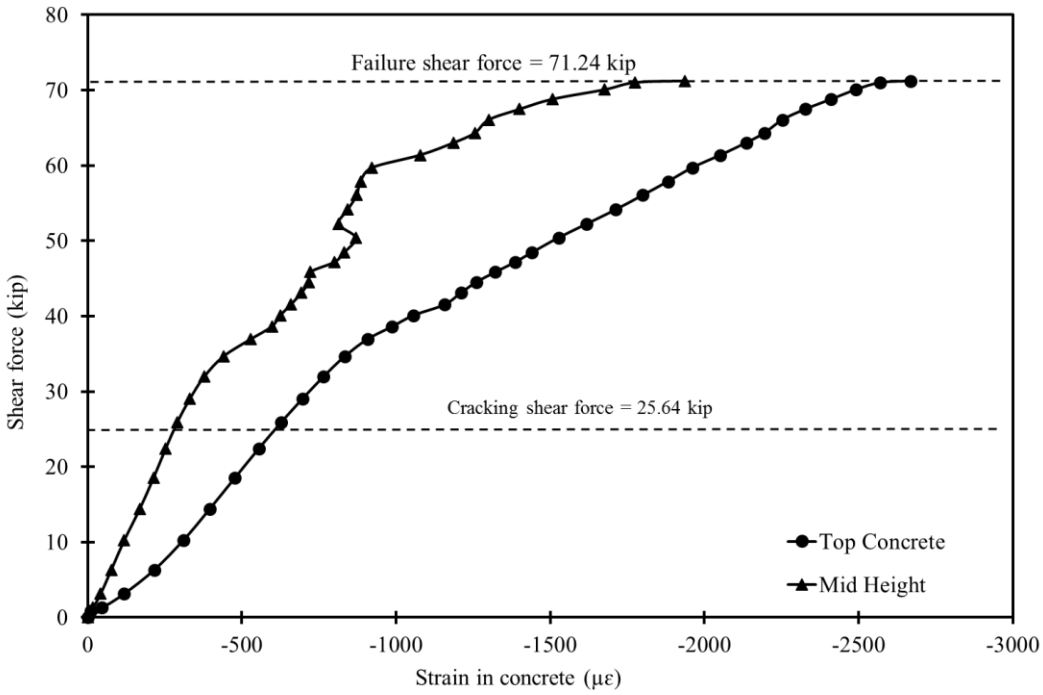

Figure 3.7-11 Recorded concrete strain under loading point of Beam C-C-S-B

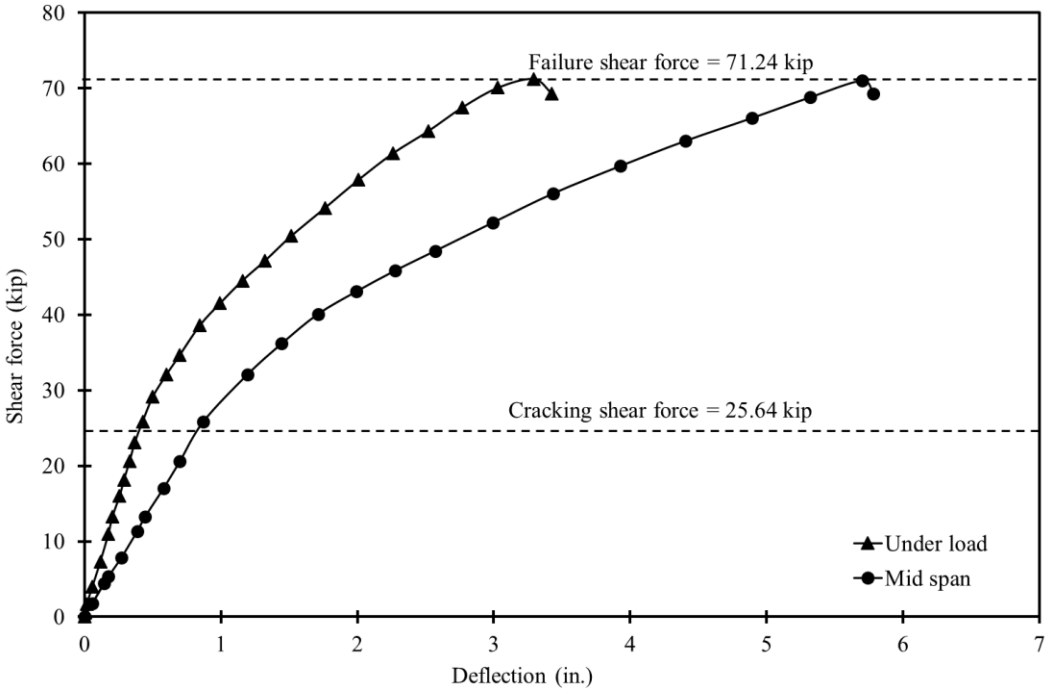

Figure 3.7-12 Recorded deflection under load and at mid-span of Beam C-C-S-B

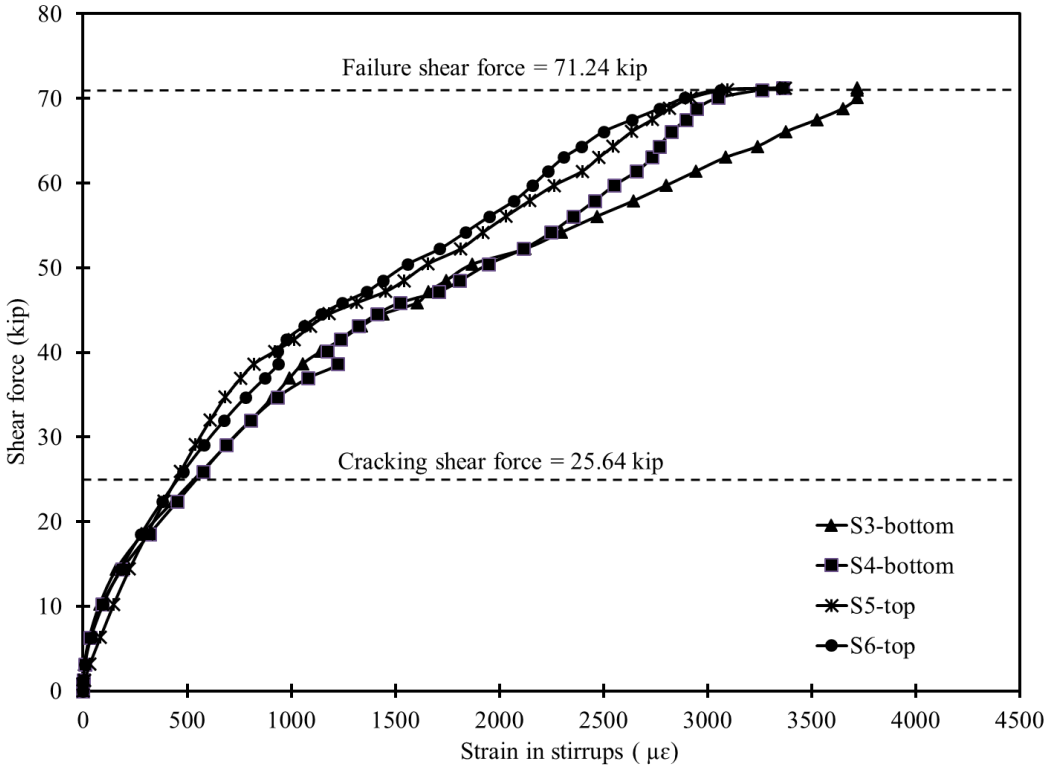

Figure 3.7-13 Shear force vs. stirrup strain in Beam C-C-S-B

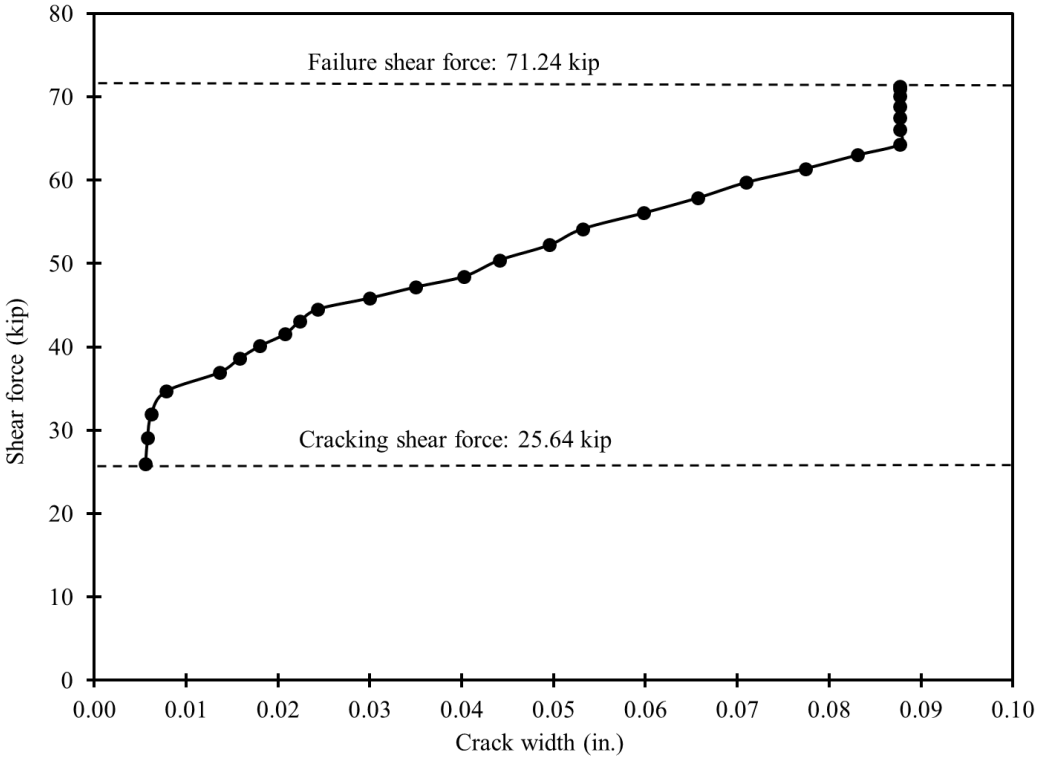

Figure 3.7-14 Shear force vs. calculated crack width in Beam C-C-S-B

3.8 Testing of bridge model

The bridge model was subjected to several testing scenarios. The first testing scenario included applying a service point load at the mid-span of each beam. This test represented the service limit state of the bridge model, where the applied load is not enough to induce flexural cracks in the model. The second testing scenario included applying a post-cracking service load at the mid-span of each beam. The post-cracking service load level was higher than the cracking load but was not enough to induce a failure in any of the bridge components. The third testing scenario included loading the exterior beam under a four-point loading with the objective of stressing the shear key joint to evaluate it performance. The fourth testing scenario included loading the entire bridge model under four-point loading to evaluate it overall performance and ductility. Finally, the last testing scenario included loading the bridge model to failure to evaluate its strength limit state. The following sections present a detailed discussion for the testing scenarios along with the obtained results and observations.

3.8.1 Service limit state testing

As shown in Figure 3.8-1, the bridge model was provided with seven equally spaced diaphragms. Each diaphragm accommodated two transverse post-tensioning un-bonded CFCC strands with an allowable prestressing force of 60 kip per strand. This transverse post-tensioning system was evaluated during the service limit state testing of the bridge model.

As shown in Figure 3.8-2, a single point load of 15 kip was applied at the mid-span of each beam in the bridge model. The test was executed with three configuration of TPT. First, the service load was applied with a TPT force of 120 kip per diaphragm in all seven diaphragms. Second, the service load was applied with a TPT force of 120 kip in three diaphragms (the two end diaphragms and the middle diaphragm). Third, the service load was applied with no TPT force in any of the diaphragms. In addition, the entire test with various levels of TPT force was repeated using a service load of 30 kip instead of the originally applied force of 15 kip.

Figure 3.8-3 shows the test setup. The load was applied using a 200,000-lb hydraulic cylinder connected to a hydraulic pump. A load cell was provided to monitor the applied load and as shown in Figure 3.8-4, the load was applied first to the exterior beam followed by the interior beam, the intermediate beam, the second interior beam, and finally the second exterior beam. It should be noted that the response of the bridge model when the load was applied on one side was a mirror image to that when the load was applied on the opposite side. To avoid repetition, only the deflection curves obtained from loading one side (exterior, interior, and middle beams) are presented in the discussion.

The response of the bridge model under service loads of 15 kip and 30 kip for different loaded beams and at various levels of TPT force is presented in Figure 3.8-5 through Figure 3.8-7. As shown in these figures, the TPT system does not appear to have any influence of the distribution of the load or the recorded deflection. In addition, no cracks or signs of shear key distress were observed during the test. Therefore, it is reasonable to conclude that TPT force is not mandatory at service limit state and non-prestressed transverse diaphragms along with UHPC shear key joints may be sufficient to distribute the load among the adjacent beams without any crack development.

An effective method of evaluating the response of the bridge model under service loads is to calculate the distribution factors among the beams and compare them for different load levels. The

distribution factor for a beam can be calculated by dividing the deflection of the beam by the sum of deflection of all five beams. Table 3.8-1 and Table 3.8-2 show the deflection and distribution factors under service loads of 15 and 30 kip, respectively.

Figure 3.8-1 Schematic diagram showing the location of the transverse post-tensioning forces

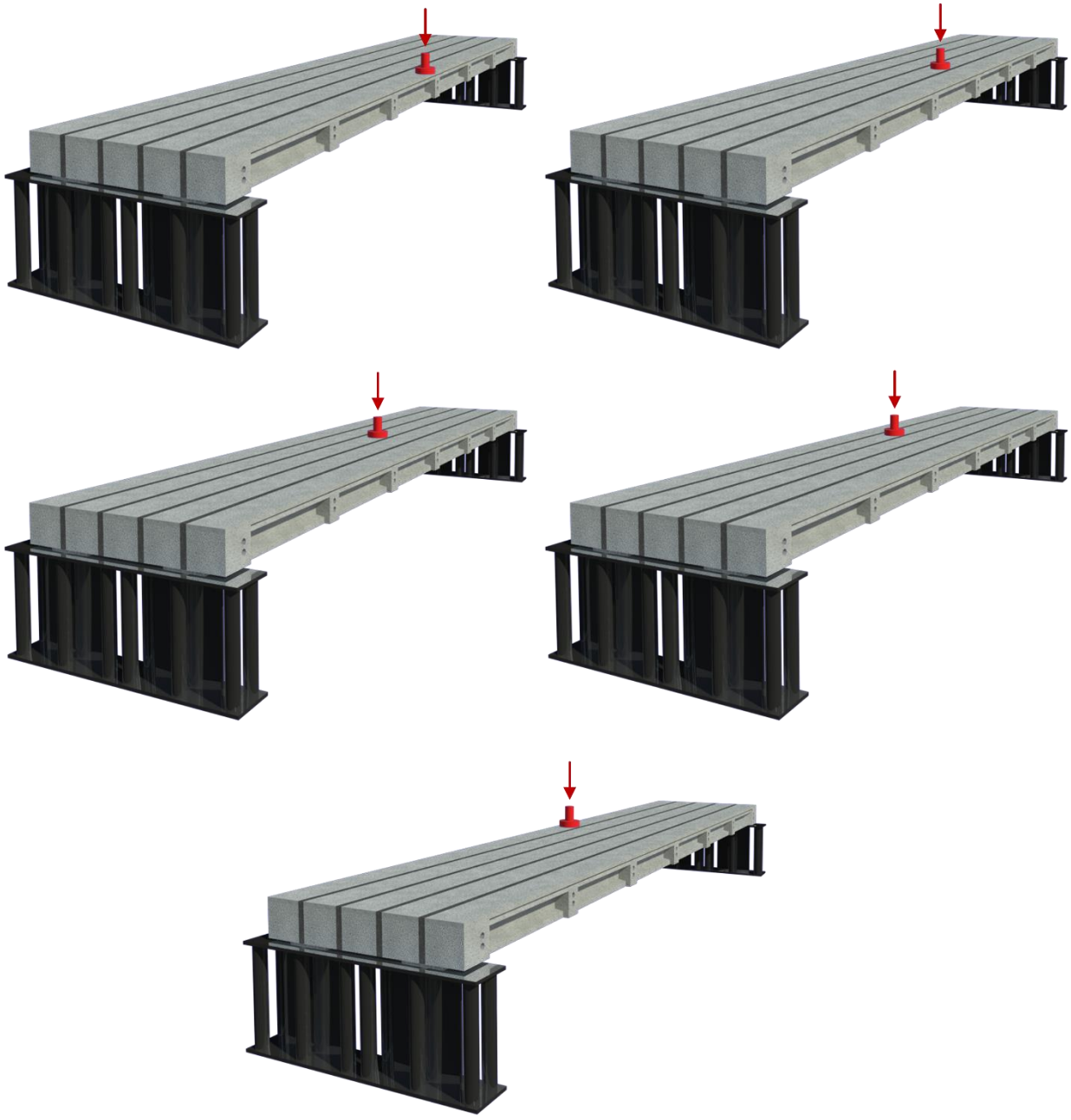

Figure 3.8-2 Sequence of service load application with/without TPT force

Figure 3.8-3 Service limit state testing of the bridge model

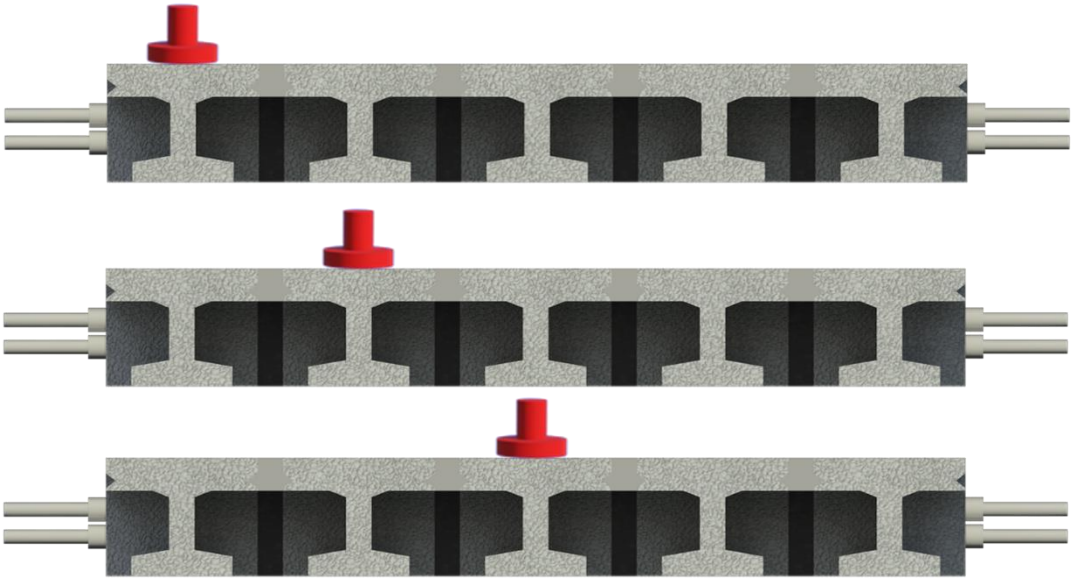

Figure 3.8-4 Sequence of application of service loads in bridge model on: exterior beam, first interior beam, and intermediate beam

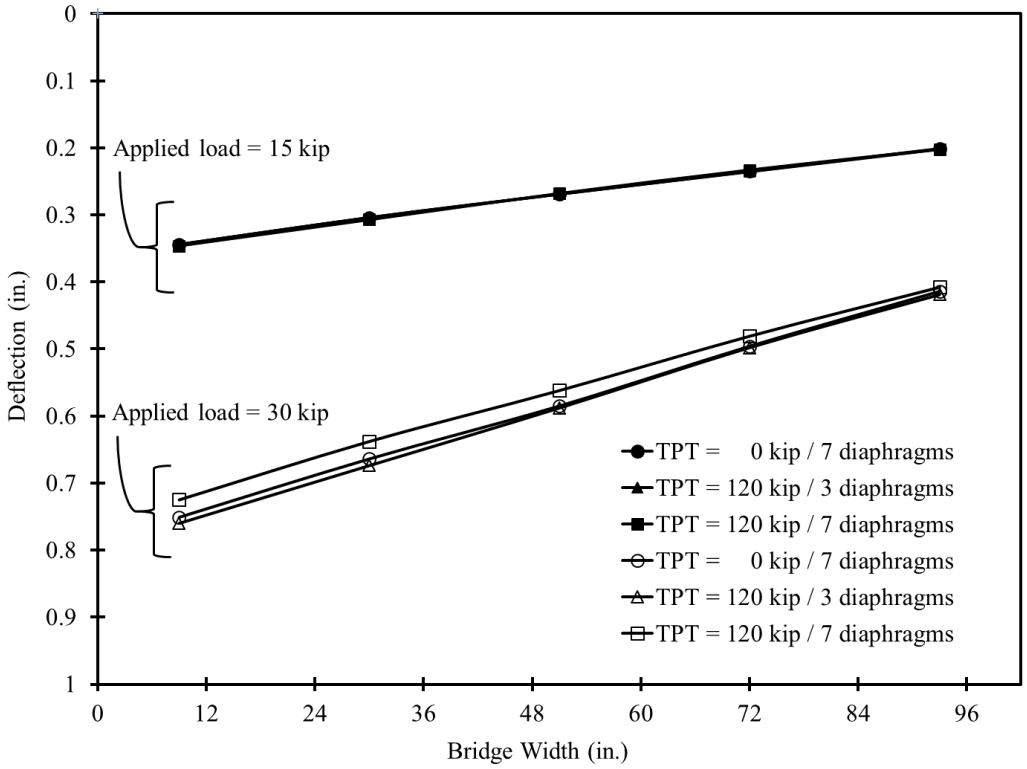

Figure 3.8-5 Deflection curves due to service loads on exterior beam

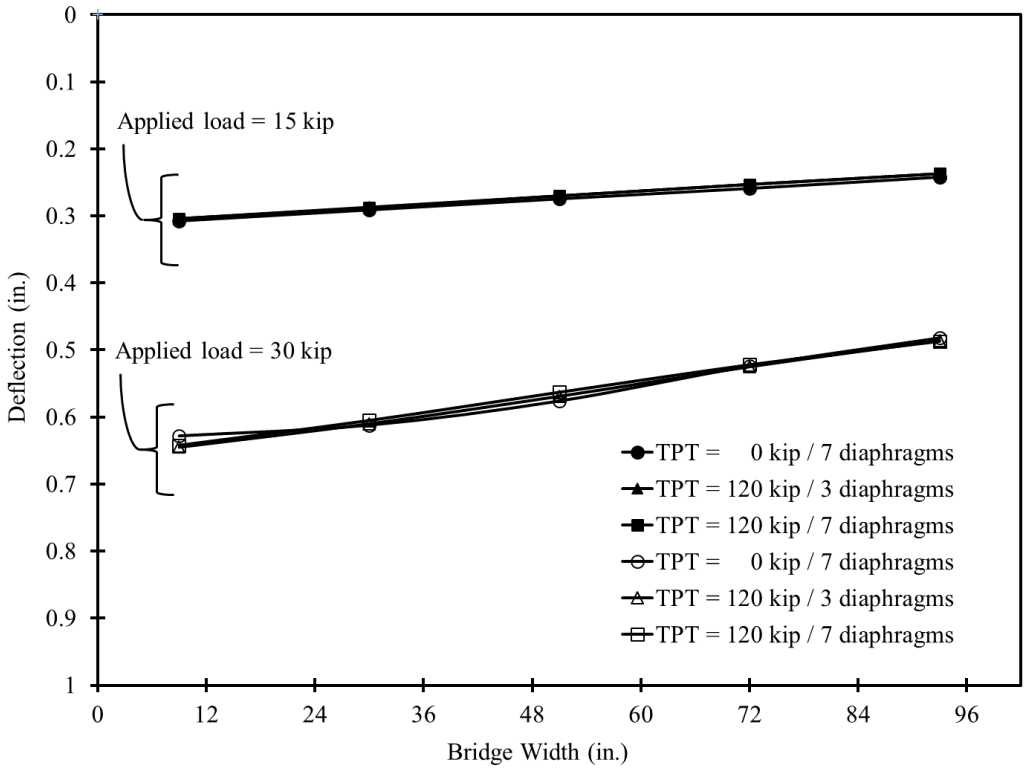

Figure 3.8-6 Deflection curves due to service loads on first interior beam

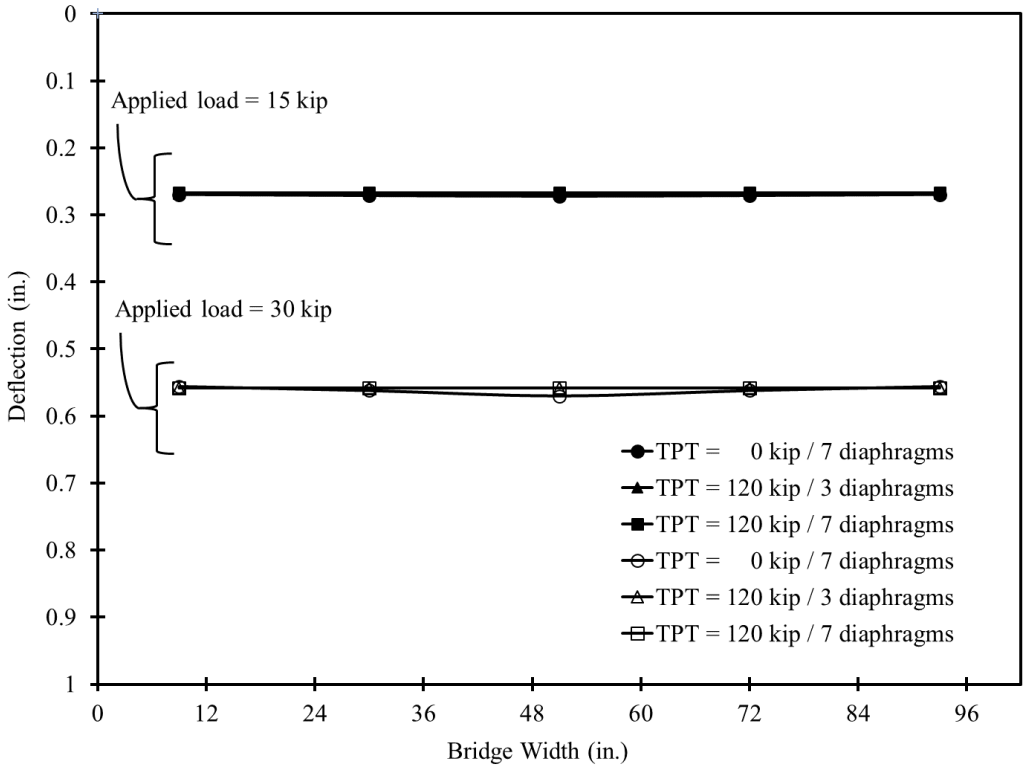

Figure 3.8-7 Deflection curves due to service loads on intermediate beam

Table 3.8-1 Load distribution factors under a point load of 15 kip, no TPT force

	Loaded beam					
	Exterior I beam		Interior I beam		Intermediate beam	
	δ (in.)	D.F.	δ (in.)	D.F.	δ (in.)	D.F.
Exterior I beam	0.344	0.254	0.308	0.224	0.270	0.199
Interior I beam	0.304	0.225	0.291	0.212	0.271	0.200
Intermediate beam	0.269	0.199	0.275	0.200	0.272	0.201
Interior II beam	0.235	0.174	0.259	0.189	0.271	0.200
Exterior II beam	0.201	0.149	0.242	0.176	0.270	0.199

Table 3.8-2 Load distribution factors under a point load of 30 kip, no TPT force

	Loaded beam					
	Exterior I beam		Interior I beam		Intermediate beam	
	δ (in.)	D.F.	δ (in.)	D.F.	δ (in.)	D.F.
Exterior I beam	0.751	0.258	0.628	0.223	0.556	0.198
Interior I beam	0.664	0.228	0.612	0.217	0.562	0.200
Intermediate beam	0.585	0.201	0.576	0.204	0.570	0.203
Interior II beam	0.496	0.170	0.524	0.186	0.562	0.200
Exterior II beam	0.414	0.142	0.482	0.171	0.556	0.198

3.8.2 Post-cracking limit state testing

At the beginning of this state, the bridge model was loaded until flexural cracks developed. Then, a load distribution test using a single point load of 60 kip was performed to evaluate the response of the cracked bridge model. In addition, the exterior beam of the bridge model was loaded under four-point loading without TPT force until signs of shear key distress were recorded. Furthermore, the entire bridge model was loaded under four-point loading to approximately 80% of its ultimate load carrying capacity to evaluate the residual deformation and the absorbed energy near failure.

3.8.2.1 Cracking of bridge model

To induce the flexural cracks, the bridge model was loaded in a four-point loading setup as shown in Figure 3.8-8 and Figure 3.8-9. The distance between the points of load was adjusted to 78 in. The load was applied through cycles of loading and unloading with a load increment of 10 kip between cycles. After each loading cycle, the bridge model was inspected for cracks. The first flexural crack was observed during the 60 kip load cycle (Figure 3.8-10). After evaluating the load-deflection curves, it was determined that the first crack developed at a load level of 53.2 kip with a corresponding deflection of 1.23 in. The development of cracks marked a rapid change in the slope of the load-deflection curve.

Once the first flexural crack developed, a series of strain gages were attached to the soffit of the beams near the crack as shown in Figure 3.8-10. The reading from these strain gages were used later on to evaluate the decompression load of the bridge model and back calculate the effective prestressing force.

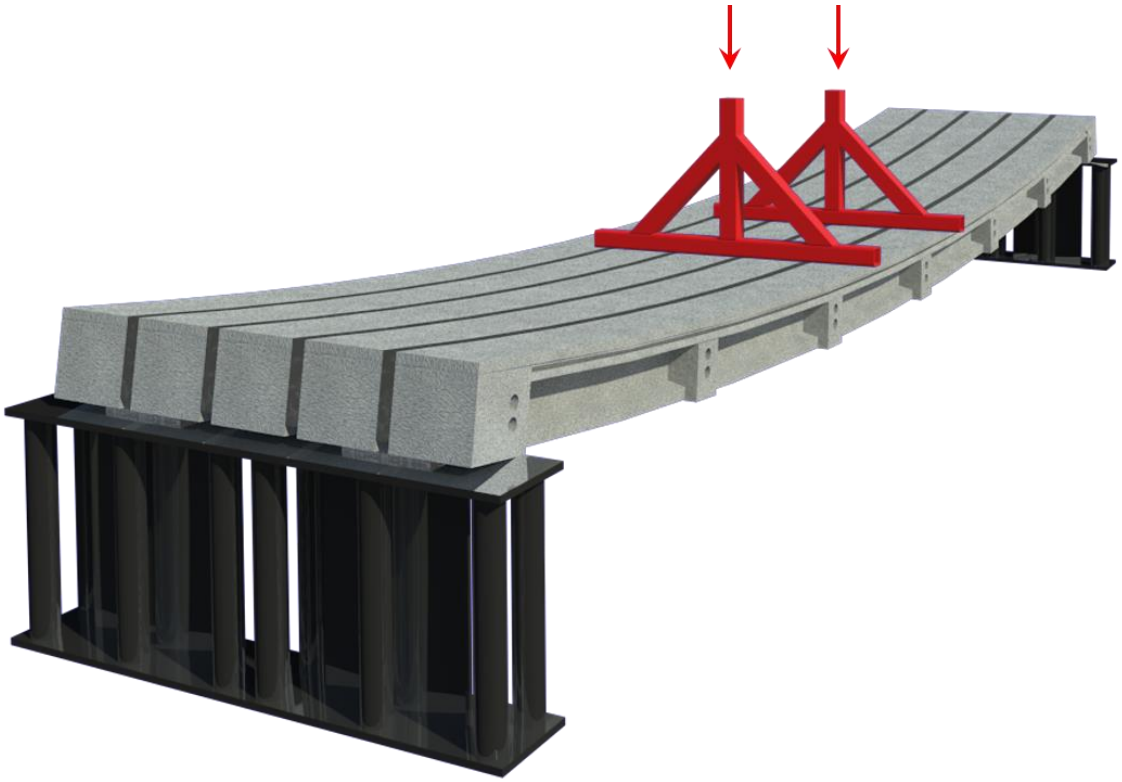

Figure 3.8-8 Four-point-loading setup for inducing flexural cracks

Figure 3.8-9 Four-point loading of bridge model

Figure 3.8-10 Development of first flexural crack in bridge model under four-point loading

3.8.2.2 Load distribution

After cracking the bridge model, the load distribution test was performed again (Figure 3.8-11) with a point load of 60 kip. Based on the results from un-cracked service limit state testing, it was decided to eliminate the TPT force from all the diaphragms.

Similar to the service limit state testing, the deflection of the bridge model was recorded and presented in Figure 3.8-12. As shown in the figure, the deflection curves indicated a uniform load distribution with no observed cracks or shear key distress. In addition, the distribution factors were calculated based on the deflection values as shown in Table 3.8-3 and compared with those obtained from service loads of 15 and 30 kip as shown in Table 3.8-4. As shown in the tables, the distribution factor did not significantly change even when the load increased from 15 to 60 kip. It should be noted that the recorded deflection values at service load of 30 kip are nearly double the values recorded at 15 kip. However, the deflection values at 60 kip is more than double the values at 30 kip. This is due to the cracking and loss of stiffness of the bridge model.

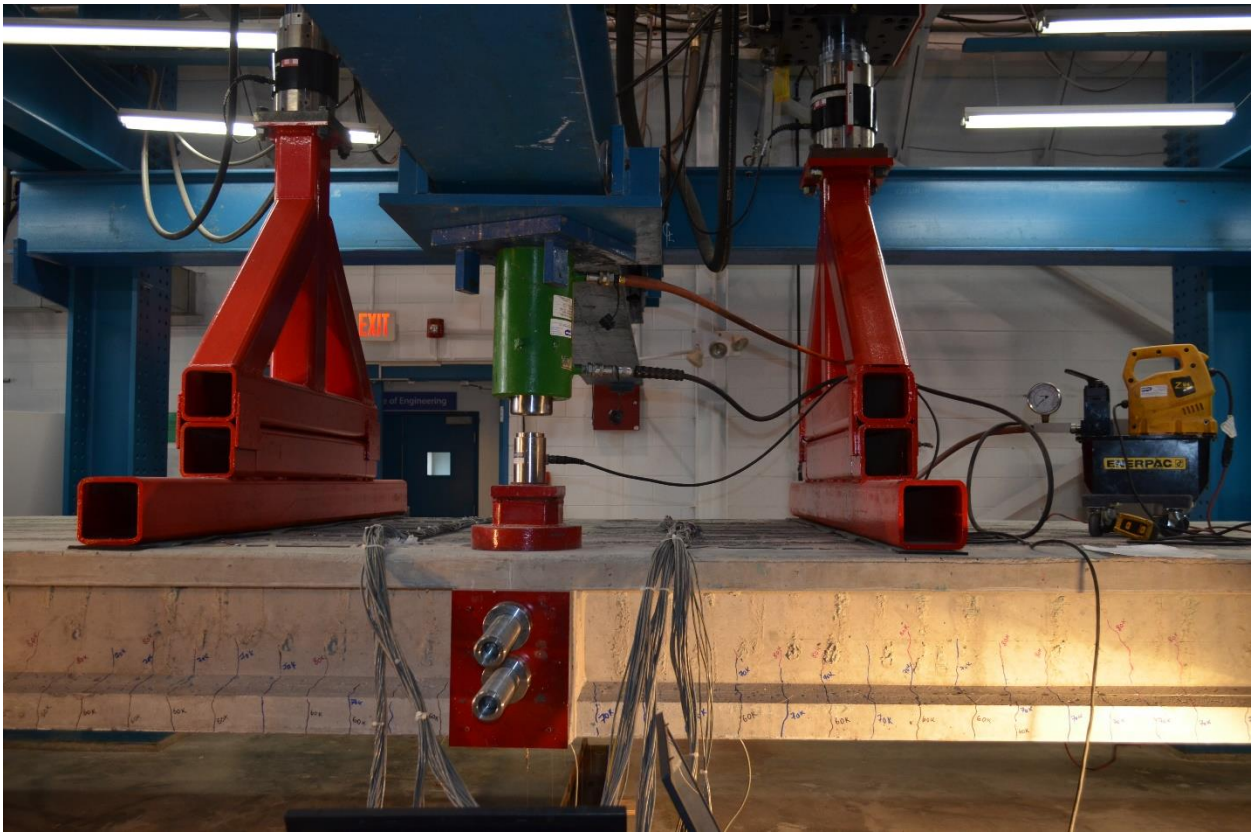

Figure 3.8-11 Post-cracking load distribution test

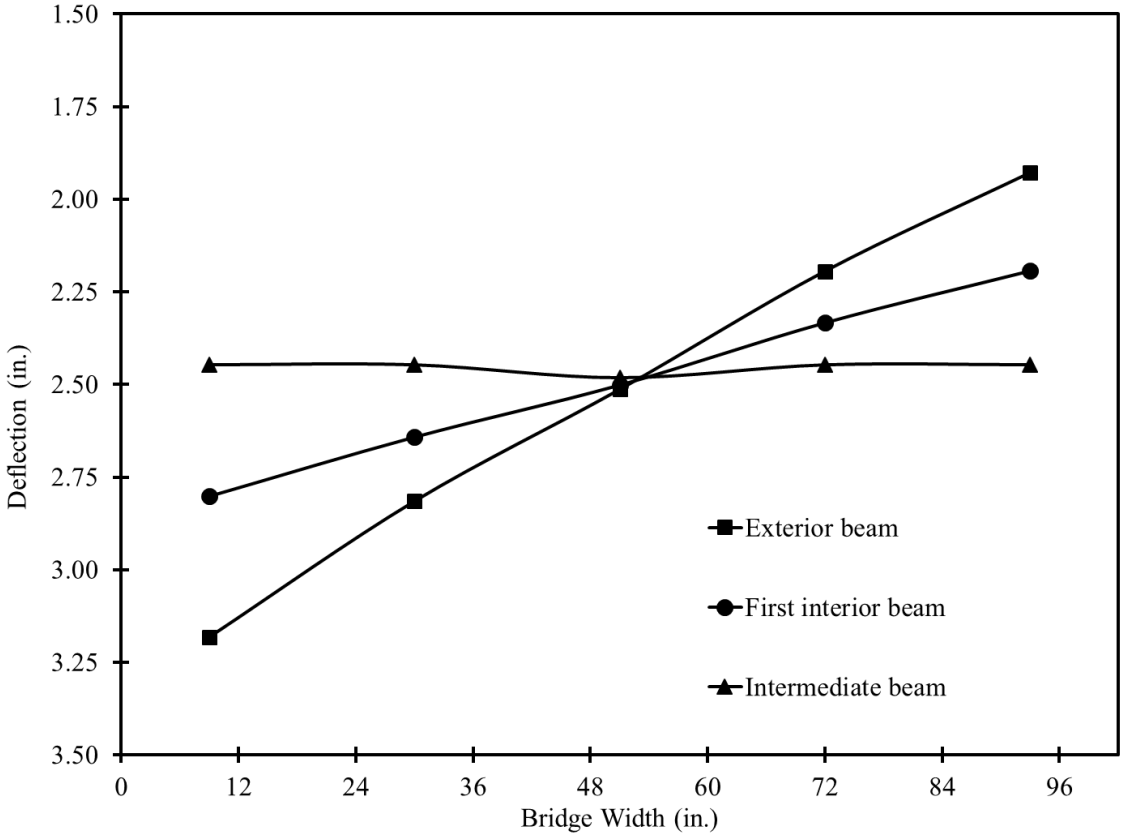

Figure 3.8-12 Deflection curves of bridge model due to post-cracking service load of 60 kip

Table 3.8-3 Load distribution factors under a point load of 60 kip, no TPT force

	Loaded beam					
	Exterior I beam		Interior I beam		Intermediate beam	
	δ (in.)	D.F.	δ (in.)	D.F.	δ (in.)	D.F.
Exterior I beam	3.18	0.251	2.80	0.225	2.45	0.199
Interior I beam	2.81	0.222	2.64	0.212	2.45	0.199
Intermediate beam	2.51	0.199	2.50	0.200	2.48	0.202
Interior II beam	2.19	0.174	2.33	0.187	2.45	0.199
Exterior II beam	1.93	0.153	2.19	0.176	2.45	0.199

Table 3.8-4 Comparison of distribution factors (DF) under point loads of 15, 30, and 60 kip

	Loaded beam								
	Exterior I beam			Interior I beam			Intermediate beam		
	15 kip	30 kip	60 kip	15 kip	30 kip	60 kip	15 kip	30 kip	60 kip
Exterior I beam	0.254	0.258	0.251	0.224	0.223	0.225	0.199	0.198	0.199
Interior I beam	0.225	0.228	0.222	0.212	0.217	0.212	0.200	0.200	0.199
Intermediate beam	0.199	0.201	0.199	0.200	0.204	0.200	0.201	0.203	0.202
Interior II beam	0.174	0.170	0.174	0.189	0.186	0.187	0.200	0.200	0.199
Exterior II beam	0.149	0.142	0.153	0.176	0.171	0.176	0.199	0.198	0.199

3.8.2.3 Shear key testing

The testing scenario was developed to directly evaluate the performance of UHPC shear joints along with the transverse diaphragms. An exterior beam of the bridge model was loaded until localized shear key cracks were developed. As shown in Figure 3.8-13 and Figure 3.8-14, the exterior beam was loaded through a four-point loading setup with 78-in. distance between the two points of load. No TPT force was applied at any of the transverse diaphragms. The load was applied in cycles starting from 60 kip with an increment of 10 kip. The bridge model was inspected for cracks after each load cycle.

No cracks developed at a load level of 70 kip. At a load level of 80 kip, minor cracks developed around the three intermediate diaphragms in addition to a limited hairline crack at the shear key joint near the applied load as shown in Figure 3.8-15 through Figure 3.8-17. All cracks developed on the concrete side of the joint and not on the UHPC side. In addition, when the load increased to 90 kip, the cracks seemed to slightly propagate.

By taking into consideration that failure load of any of the bridge beams was approximately 40.79 kip, it can be concluded that the shear key joint resisted approximately twice the load carrying capacity of a single beam before cracking. In case of interior beam, the load is distributed through two shear key joints instead of one and it is expected that higher resistance would be achieved before cracking the shear key. Since the purpose was not to destroy the shear key joint,

the test was terminated after reaching a load level of 90 kip. Figure 3.8-18 shows the deflection of the bridge model while the load was applied on the exterior beam.

Figure 3.8-13 Schematic diagram showing testing of shear key joint

Figure 3.8-14 Shear key testing of bridge model

Figure 3.8-15 Bottom view of bridge model showing development of cracks at diaphragm

Figure 3.8-16 Localized shear key cracks at load level of 80 kip

Figure 3.8-17 Cracks under a load of 80 kip near intermediate diaphragm

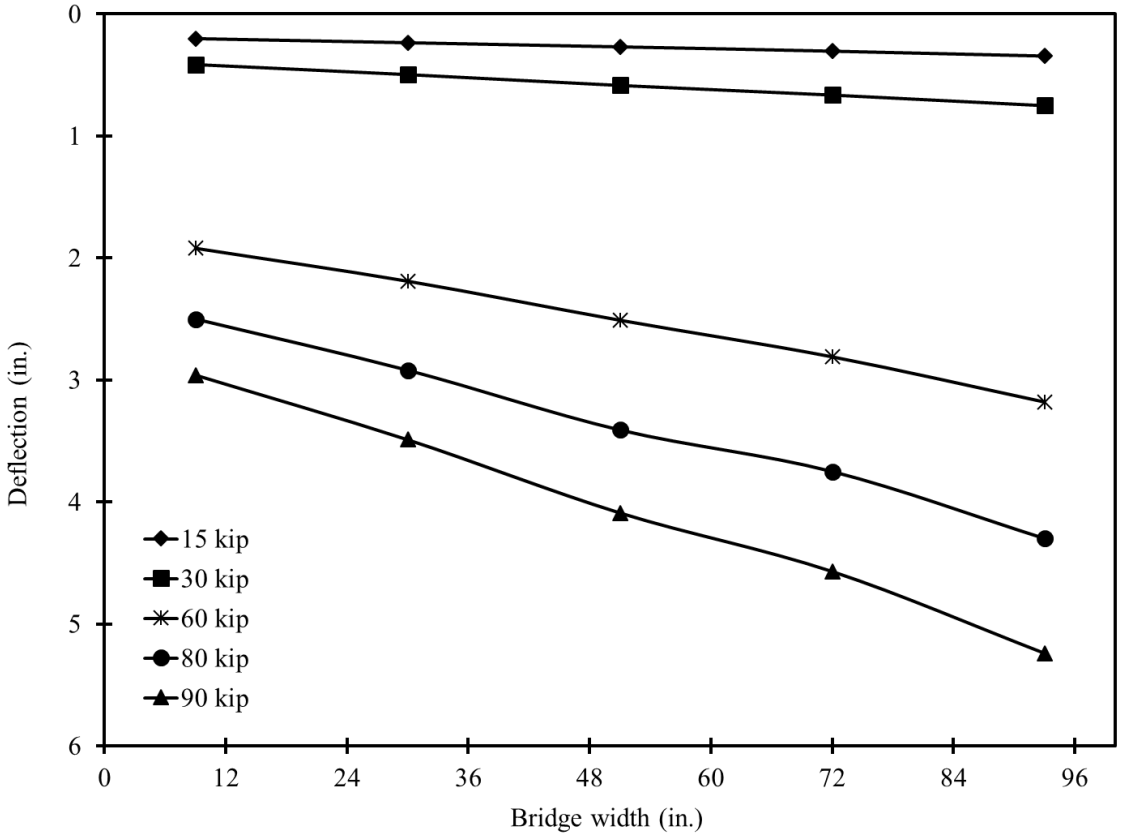

Figure 3.8-18 Deflection curves of bridge model while loading exterior beam

3.8.2.4 Load cycles

After completing the testing scenario for the shear key joint, the test setup was revised back to the four-point loading across the entire width of the bridge model as shown in Figure 3.8-19. At this stage of loading, it was necessary to perform load cycles to separate the elastic energy of the bridge model from the inelastic energy and to determine the decompression load. The loading of the bridge model was applied through cycles of loading and unloading with an increment of 10 kip until a load level of 160 kip. This load level represented approximately 80% of the anticipated ultimate load carrying capacity. The load-deflection curves for all load cycles including those executed while cracking the bridge model are presented in Figure 3.8-20. As shown in the figure, the corresponding deflection for a load of 160 kip was approximately 11.75 in. By the end of the unloading phase, the residual deflection from all loading cycles was approximately 0.95 in.

The decompression load was estimated using the readings from the soffit strain gages and from the load-deflection curves. Figure 3.8-21 shows a typical reading from the soffit strain gage near the crack. As shown in the figure, the strain gage captured positive strain until the flexural crack started to open. With crack opening, the reading from the strain gage did not increase with the load and eventually decreased after further increasing the load. The decompression load can be determined from the maximum strain reading or from the corresponding load that caused the maximum reading.

On the other hand, Figure 3.8-22 shows the method of calculating the decompression load from the load-deflection curves. As shown in the figure, every load-deflection curve had two distinct linear segments. Those segments represented the un-cracked and cracked states of the bridge model. The un-cracked state was achieved when the prestress forced the cracks to close. The cracked state was achieved when the applied load overcame the effect of prestressing and caused the flexural cracks to open. Therefore, the two segments of the curve connected at the decompression load.

The average decompression load from both methods of calculation was approximately 45.97 kip. When back calculating the prestressing force, it was determined that the average prestress loss was approximately 14.8% .

Figure 3.8-19 Load cycle test of bridge model

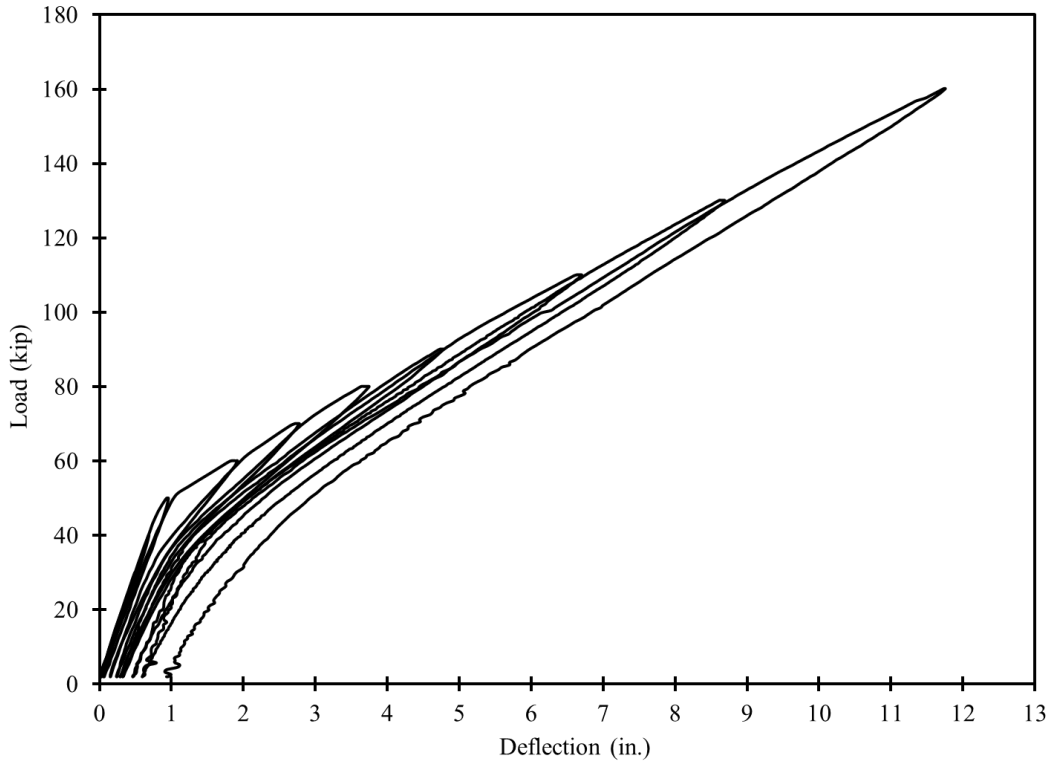

Figure 3.8-20 Load-deflection curves of bridge model under flexural load cycles

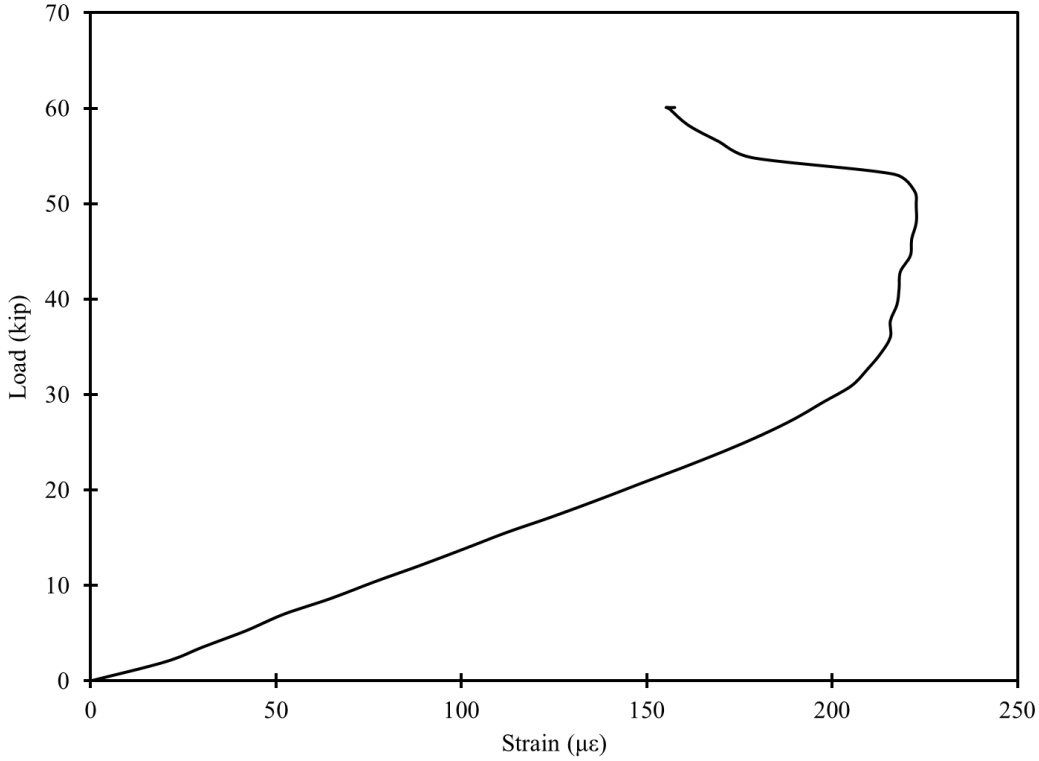

Figure 3.8-21 Load vs. strain at the soffit of the beam after crack initiation

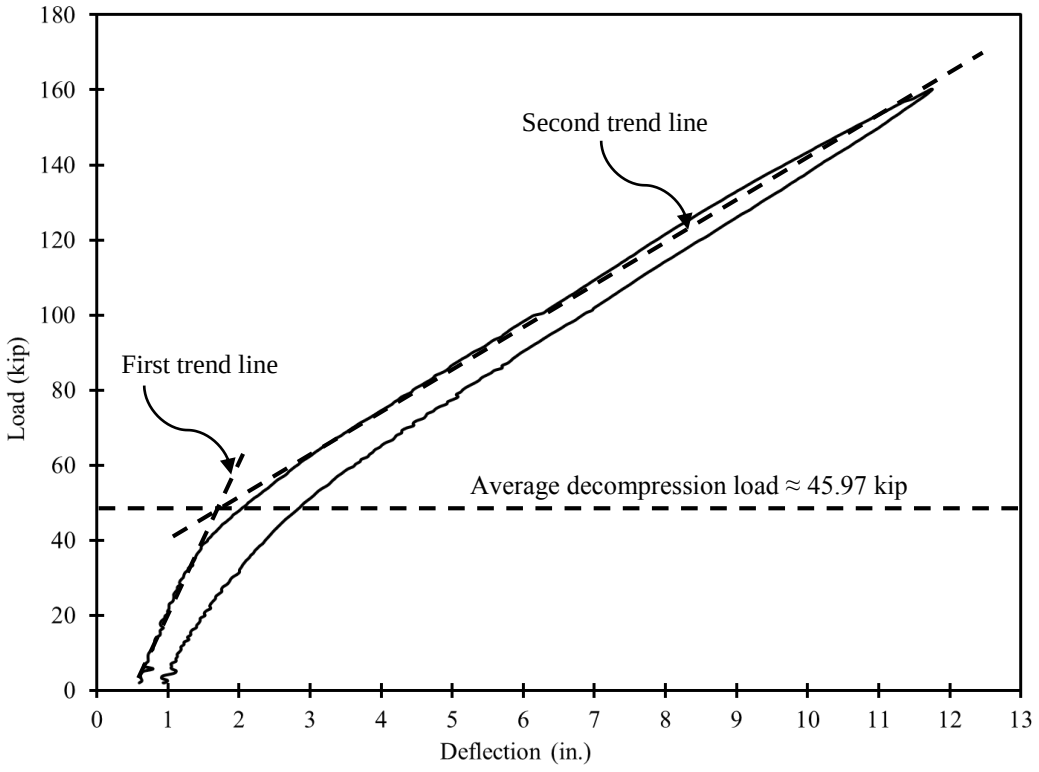

Figure 3.8-22 Estimating decompression load from load-deflection curves

3.8.3 Strength limit state testing

The strength limit state testing of the bridge model included loading the intermediate beam under four-point loading as shown in Figure 3.8-23. The distance between the two points of load was maintained at 78 in. Therefore, no TPT was applied through any of the diaphragms and the TPT strands were removed from the bridge model. One of the main objectives of this test setup was to determinate the efficiency of UHPC shear key joints along with non-prestressed transverse diaphragms on distributing the applied load.

The loading rate was maintained at 4 kip per minute and was applied through two MTS actuators with a maximum capacity of 250 kip, each. The load was applied through a force control module in one continuous phase of loading to failure. Deflection and strain measurements were recorded through a series of LMTs and strain gages, while the load was recorded through two loads cells attached to the actuators. All sensors were connected to the data acquisition system.

The bridge model experienced a significant deflection before failure. As shown in Figure 3.8-24 and Figure 3.8-25, the deflection was noticeable with a naked eye and was accompanied by a dense cracking pattern. The cracks were distributed evenly at a 4.0-in. spacing and was overlapping the location of the stirrups at the mid-third region of the bridge model.

The bridge model achieved a load level of 220 kip with a corresponding deflection of 18.14 in. With further increasing the load, a popping sound corresponding to rupture of CFCC strands was heard. With every strand rupture, spalling of concrete and sudden drop in the load were observed. Initially, the concrete in the top flange did not show any signs of crushing but after the rupture of a few CFCC strands, signs of partial concrete crushing at the exterior beam were observed (Figure 3.8-26 and Figure 3.8-27).

Even with strand rupture, the bridge model continued to support some load at a decreased rate. That was due to the distribution of the load from the intermediate loaded beam to the adjacent beams along with the increased deflection, which allowed a brief relief of the load before the actuators stressed the bridge model again. As shown in Figure 3.8-28 and Figure 3.8-29, the spalling of the concrete and rupture of the CFCC strands took place mainly in the intermediate loaded beam. The adjacent beams were also stressed but to a slightly lesser degree and therefore, they continued to support additional load and did not immediately fail. This observation proved

that the shear key joints and the transverse diaphragm continued to function even after the failure of the intermediate beam.

Through visual inspection, the shear key joints appeared to be in a sound condition until the bridge model reached it maximum load carrying capacity of 220 kip. Based on previous test results, shear key hairline cracks were suspected but it was not possible to check during the loading of the bridge model. After the failure of the intermediate beam, it was visually apparent that the shear key joints next to the intermediate beam were over-stressed with a clear sign of separation and longitudinal cracks at the points of loading. As shown in Figure 3.8-30, equal deflections were recorded under all five beams of the bridge model until the maximum load of 220 kip was reached. After the maximum load, the deflection curve of the loaded beam substantially departed from the rest of the curves of the other beams. This indicated the failure and separation of the loaded beam along with the adjacent shear key joints.

Figure 3.8-31 and Figure 3.8-32 show the load vs. concrete strain and prestressing strain, respectively. Since the beams were constructed with a balanced reinforcement, the strain in the concrete at failure was well within the range of 2,500 to 3,000 με and at the same time the strain in the prestressing strands was within the range of 16,000 με. The strain in the concrete and the prestressing strands in the intermediate beam showed the highest values with the strain in the concrete approximately 3,000 με and the strain in the prestressing strands approximately 16,570 με. The failure however geared toward the tension failure because the added strength in the compression zone by the UHPC shear key joints.

To calculate the ductility ratio of the bridge model, the load deflection curve of the limit state testing was added to those from previous load cycles as shown in Figure 3.8-33 and the area under the curves were calculated and divided into elastic and inelastic zones by estimating the un-loading path from the ultimate load as shown in Figure 3.8-34. Based on the calculations for the areas, the elastic energy was estimated as 2,002.4 kip.in., while the inelastic energy was estimated as 604.4 kip.in. By dividing the inelastic energy by the total energy, the ductility ratio of the bridge model was estimated as 23%. Similar to beams with CFCC reinforcement, the ductility ratio indicated a brittle failure. However, this brittle failure was accompanied by a significant deflection that was enough warning sign that the bridge was over-stressed.

Figure 3.8-23 Four-point loading of intermediate beam at strength limit state testing

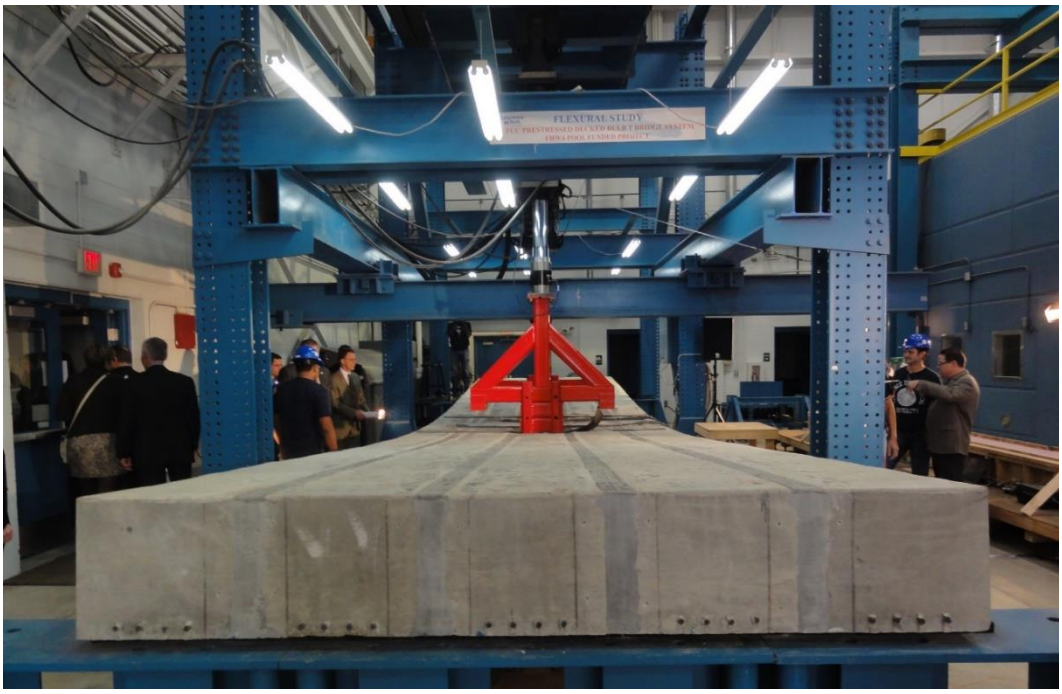

Figure 3.8-24 Deflection of bridge model during strength limit state testing

Figure 3.8-25 Overview of bridge model during strength limit state testing

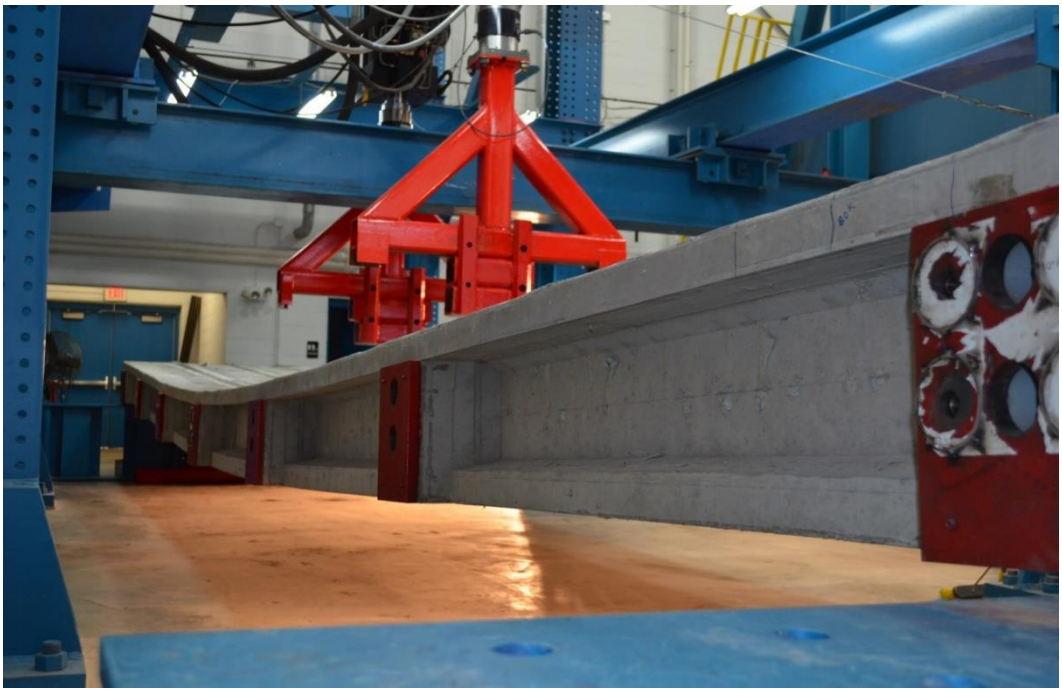

Figure 3.8-26 Bridge model at failure

Figure 3.8-27 Partial concrete crushing in top flange after failure

Figure 3.8-28 Spalling of concrete from bottom of loaded intermediate beam at failure

Figure 3.8-29 Rupture of prestressing CFCC strands in bridge model in intermediate beam

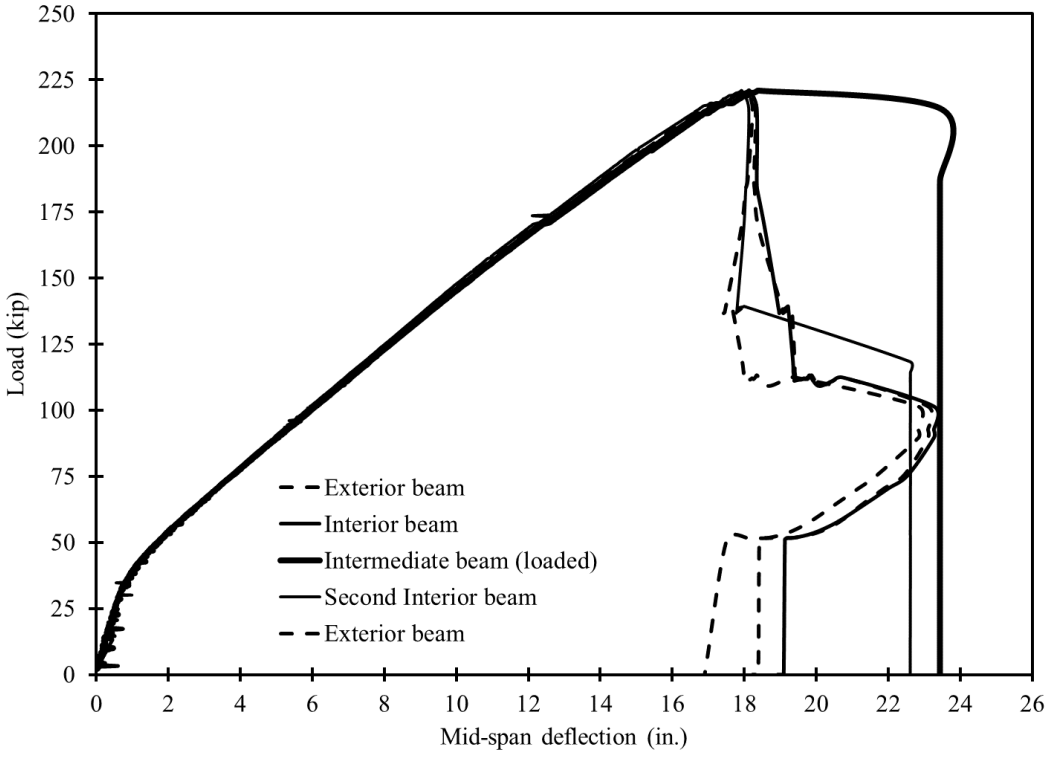

Figure 3.8-30 Load-deflection curves for all beams during ultimate load cycle

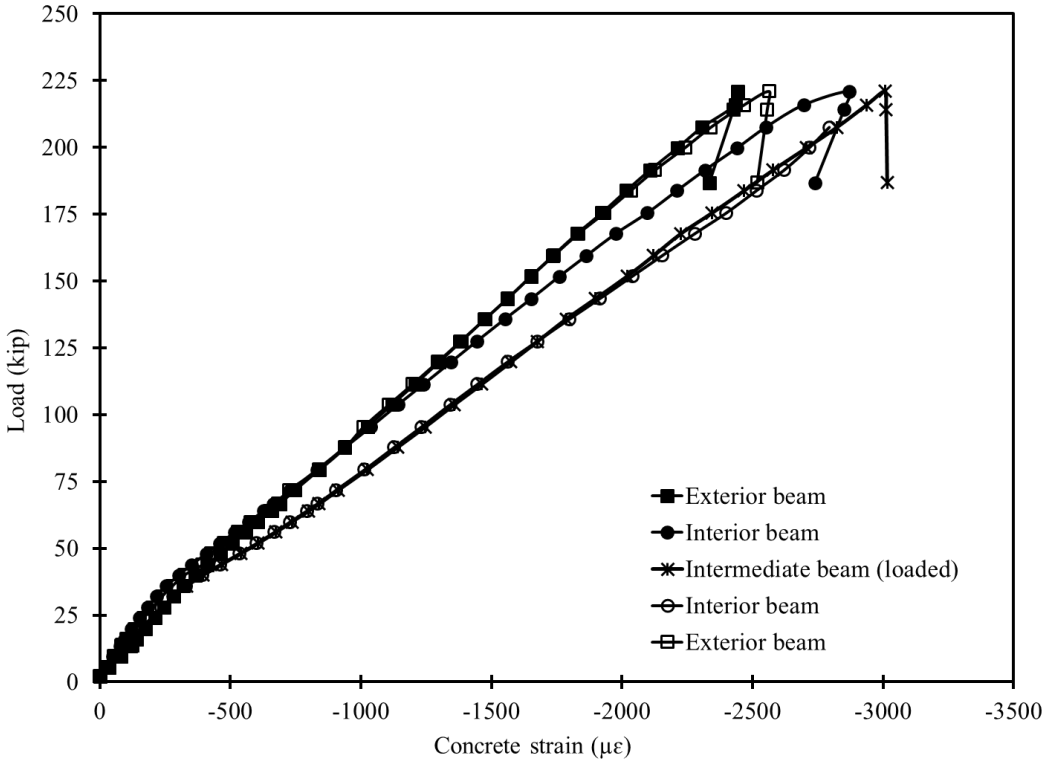

Figure 3.8-31 Load vs. average beam concrete strain during ultimate load cycle

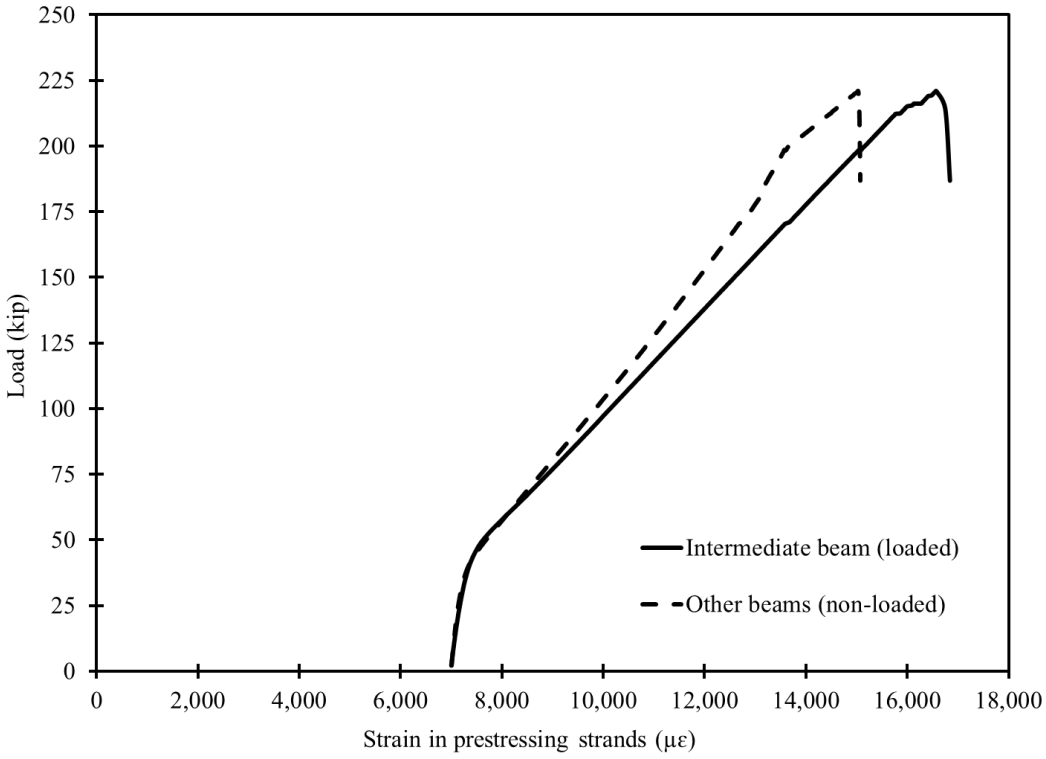

Figure 3.8-32 Load vs. average strain in prestressing strands during ultimate load cycle

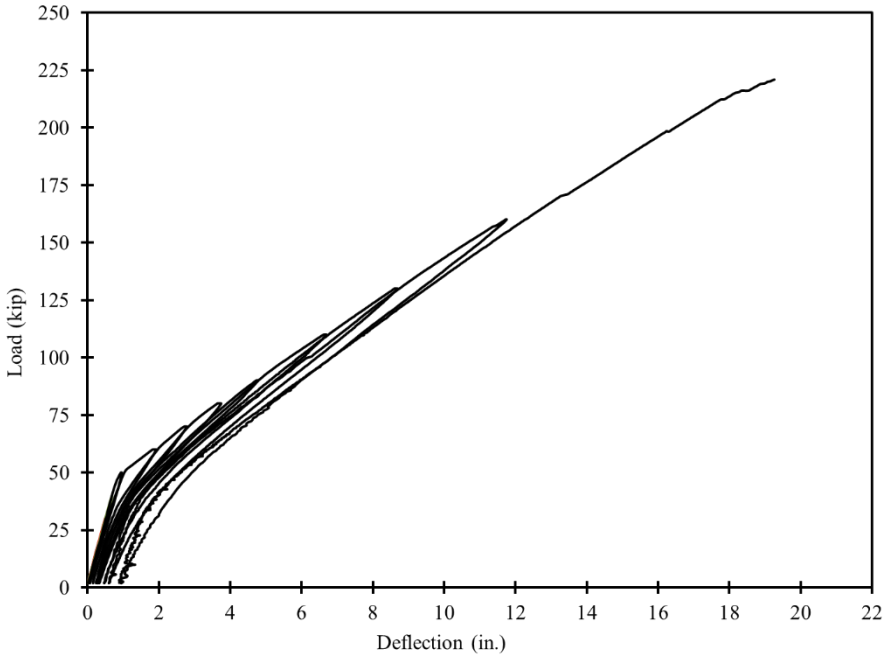

Figure 3.8-33 Combined load-deflection curves for all load cycles to failure of bridge model

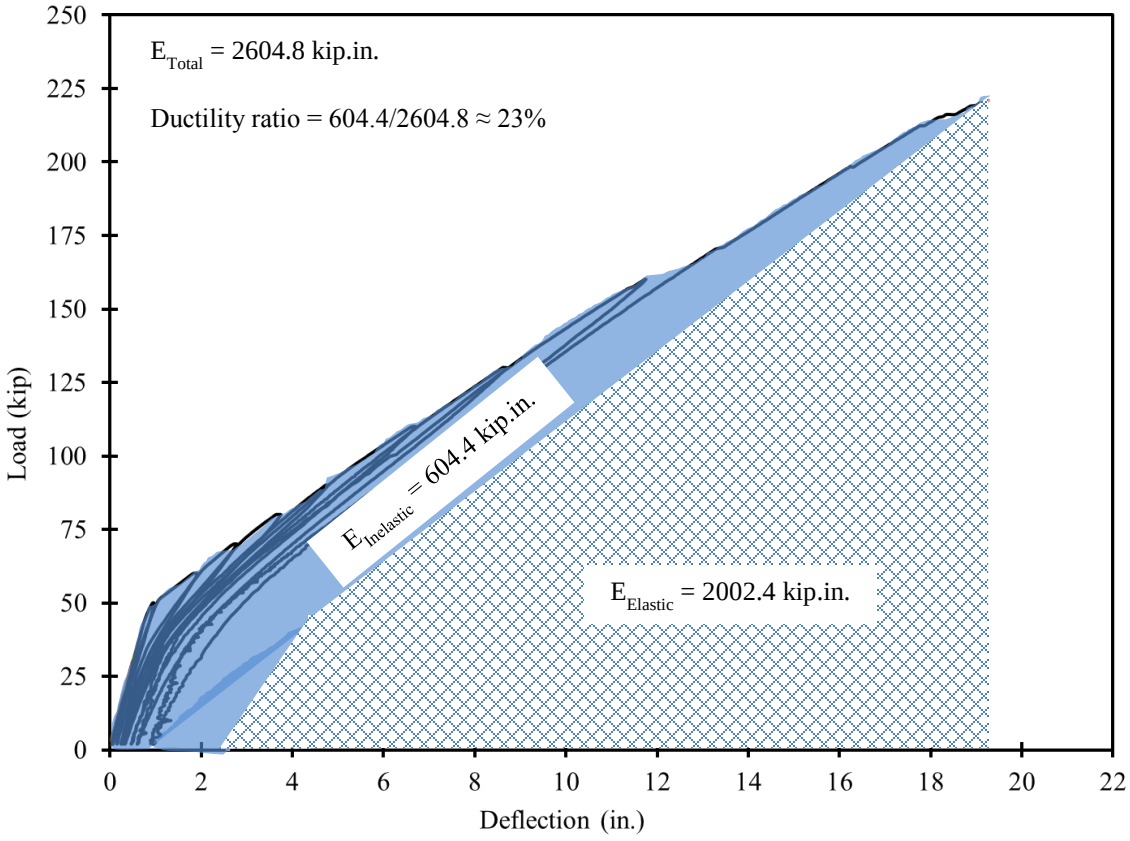

Figure 3.8-34 Ductility ratio of bridge model

CHAPTER 4: NUMERICAL INVESTIGATION

4.1 Introduction

This numerical investigation was conducted to establish an adequate transverse system in decked bulb T beam bridges and to ensure the distribution of the traffic load without over-stressing or cracking the shear key joints between the beams. The numerical investigation was conducted using the commercial software package ABAQUS version 11.2.1. The investigated transverse post-tensioning (TPT) system in decked bulb T beam bridges consisted of a series of transverse diaphragms, which were either non-prestressed or prestressed with TPT force applied through un-bonded TPT CFCC strands.

This chapter is composed of four main sections. The first section offers a detailed explanation for: the components of the numerical models, material properties, elements types, boundary conditions, analysis steps, and all the assumptions that have been used through the process of modeling. The second section presents the verification of the numerical investigation. The verification was executed by generating and analyzing numerical models for the control beams and bridge model. The third section provides the results of a parametric study that was conducted on real-scale bridges. The fourth section summarizes the results of the numerical investigation and presents a guide specification for transverse post-tensioning systems in typical decked bulb T beam bridges.

4.2 Components of numerical models

All numerical models including verification models and those of the parametric study were composed of decked bulb T beams reinforced and prestressed longitudinally with CFCC strands and transversely with steel or CFCC stirrups. All beams and bridge models were simply supported over two reinforced neoprene pads at their ends. No deck slab was provided but the top flanges of the beams were connected together using UHPC shear key joints. In addition, transverse diaphragms made of UHPC and transverse elements representing TPT CFCC strands were provided in some of the numerical models. The following subsections represent the details of each bridge component.

4.2.1 Decked bulb T beams

The concrete of the decked bulb T beams was simulated using a brick element (C3D8R). This is a three dimensional element with eight nodes as shown in Figure 4.2-1. Each node has three transitional degrees of freedom (U_x , U_y , U_z,).

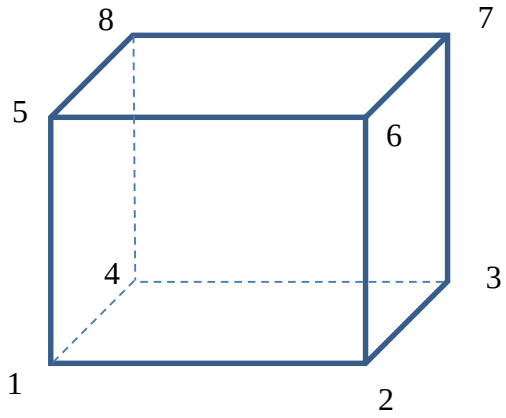

Figure 4.2-1 Illustration of C3D8R brick element used to mode decked bulb T beams (ABAQUS Manual 2011)

A continuum, plasticity-based, damage model for concrete was used to model the material behavior. The concrete damaged plasticity model uses concepts of isotropic damaged elasticity in combination with isotropic tensile and compressive plasticity to represent the inelastic behavior of concrete. It assumes that the main two failure mechanisms are tensile cracking and compressive crushing of the concrete material. Consequently, the concrete material was defined by its uni-axial compressive and tensile performance in addition to the elastic properties.

For compressive stress, the material model response is linear until the value of initial yield. The initial yield is assumed to occur at a stress equal to 60% of the concrete ultimate strength and then the material begins the plastic response, which is typically characterized by stress hardening followed by strain softening beyond the ultimate stress.

For tensile stress, the stress-strain response follows a linear elastic relationship until reaching the value of the cracking stress, which corresponds to the onset of micro-cracking in the concrete material. Beyond the cracking stress, the formation of micro-cracks is represented macroscopically with a softening stress-strain response, which includes strain localization in the concrete structure.

The elastic properties of the concrete including the modulus of elasticity, Poisson's ratio, and modulus of rupture were estimated according to AASHTO LRFD Sections 5.4.2.4, 5.4.2.5, and 5.4.2.6, respectively.

4.2.2 Reinforcement

The reinforcement cages of the decked bulb T beams were modeled using a two-node linear 3D truss element (T3D2) shown in Figure 4.2-2. Each node has three degrees of freedom (U_x , U_y , U_z,). Truss elements were embedded inside the host elements or concrete brick elements. The transitional degrees of freedom of the embedded element nodes were constrained to the interpolated values of the corresponding degrees of freedom of the host element nodes.

The behavior of CFCC reinforcement was assumed elastic to failure. The maximum strength and strain of the material was taken from the material data sheets provided by the manufacturer (Tokyo Rope Co.). It should be noted that there is a slight uncertainty in the ultimate strength and strain of CFCC material. The material data sheets showed a maximum strain within the range of 1.6 to 1.7%. Therefore, during the verification stage, the ultimate strain and corresponding strength was optimized based on the results from the experimental investigation. Losses were taken as 15% of initial prestressing force for all numerical models.

Besides CFCC strands, low-relaxation steel strands with a diameter of 0.6 in. were used in Beam S-S-F-U and steel stirrups were used through all the numerical models except for Beam C-C-S-B. The material properties of the reinforcing steel bars (assuming Grade 60 ksi) and steel strands were taken from AASHTO LRFD 2012 Sections 5.4.3 and 5.4.4, respectively.

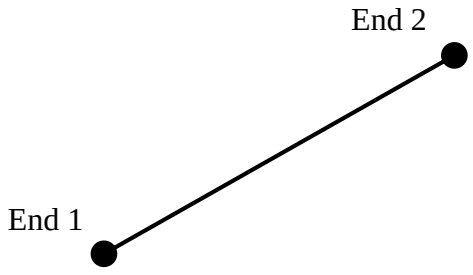

Figure 4.2-2 Two-node linear 3D truss element T3D2 for reinforcement (ABAQUS 2011)

4.2.3 Shear key joints

The shear key joints were modeled using the same three dimensional brick element C3D8R. The material properties were taken based on experimental test results of uni-axial compressive strength test preformed on UHPC cylinders and also with reference to previous studies (Graybeal 2006). The ultimate compressive strength was taken as 28 ksi. The modulus of elasticity was taken as 7000 ksi, while the cracking strength was taken as 1500 psi.

Based on the experimental investigation, the interface between the UHPC and the concrete is stronger than the concrete itself. Therefore, the cracking is likely to occur on the concrete side and not through the interface or the UHPC. Therefore, through the numerical analysis, a full bond was assumed through the interface between the UHPC and the concrete of the beams. The full bond was achieved by assigning a "TIE" element between the nodes of surfaces in contact. The TIE element is a virtual element that constrains the degrees of freedom of one node on one of the surfaces, called the slave surface, to the degrees of freedom of the nearest node on the other surface, called the master surface. The master surface was taken as the surface of the beam, while the slave surface was taken as the surface of the UHPC shear key joint.

4.2.4 Reinforced elastomeric bearing pads for supports

The end supports were provided for the decked bulb T beams as steel-reinforced elastomeric bearings. The bearings were composed of alternate layers of steel reinforcement and elastomer bonded together. The elastomer was defined in the numerical analysis as a hyper-elastic material of ultimate uni-axial tensile stress of 2500 psi and ultimate uni-axial tensile strain of 400% (complies with ASTM D412). Both the reinforcement and the elastomer layers were modeled with eight-node linear brick elements. However, the elements functioned differently during the analysis. The reinforcement layers were modeled with element type C3D8R. This element is controlled by the reduced integration during the analysis (identified by the letter R at the end of the name). The elastomer layers, on the other hand, were modeled with element type C3D8H. This element is controlled by hybrid formulations that can deal with the elastomer material behavior (identified by the letter H). The ABAQUS Manual (2011) for element types provides a detailed description for both elements and their functions.

The length, width, and thickness of the bearing pads were calculated according to AASHTO LRFD 14.7.5 (2012). The pads used in the experimental models had a length of 12 in., a width of 6 in. and a thickness of 1.0 in. The pad is composed of three elastomer layers with a thickness of 0.25 in. each and alternated with two steel layers with a thickness of 0.125 in. each. On the other hand, the pads assigned for the models in the parametric study had a length of 32 in., a width of 8 in. and a thickness of 2.075 in. divided into: three steel layers of thickness 0.125 in. each, two interior elastomer layers of thickness 0.6 in. each, and two exterior elastomer layers of thickness 0.25 in. each. It should be noted that due to their fine detailing, elastomeric bearing pads required a significantly large number of elements, which resulted in considerable CPU time delay in the analysis. Therefore, in models with a large number of elements, elastomeric bearing pads were replaced with steel plates of the same dimensions and boundary conditions were assigned as a roller support for one side and a pin support for the other side. This simplification was verified before implementation and the difference in the results were proven insignificant.

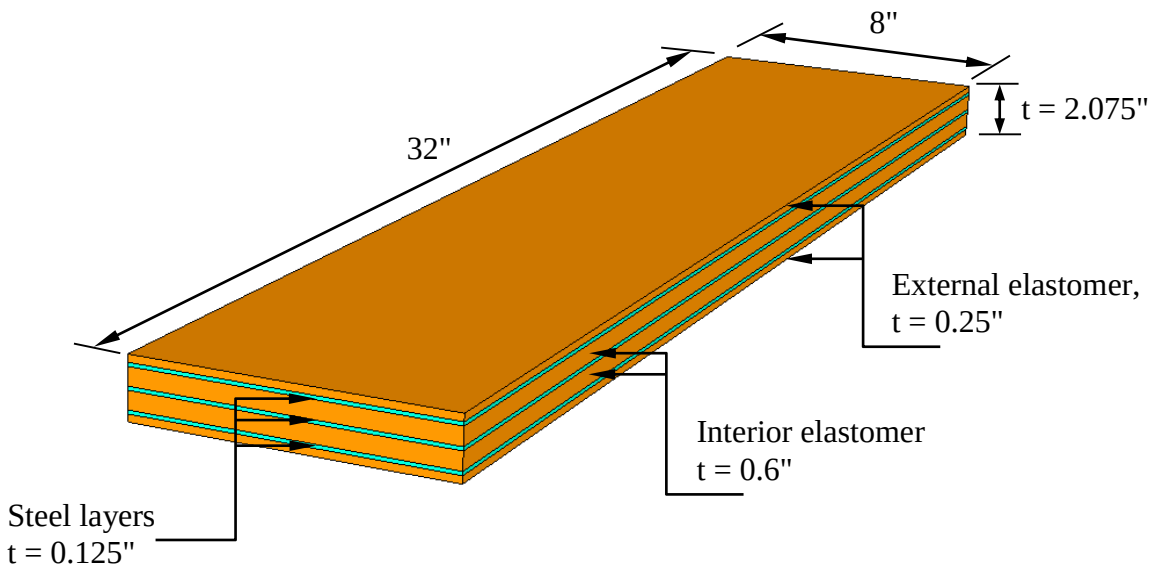

Figure 4.2-3 Elastomeric bearing pad for one beam

4.2.5 Transverse diaphragms

The transverse diaphragms were modeled using the brick element C3D8R with material properties of UHPC. It was assumed that the diaphragms will be cast in place along with the shear key joints from the same UHPC batch. It was also assumed that full bond is developed between the diaphragm and the sides of the decked bulb T beams. No slippage or separation was allowed between the diaphragms and the beams.

4.2.6 Transverse post-tensioning cables

The two-node truss element (T3D2) was used to model the transverse un-bonded post-tensioning strands which functioned as ties confining the decked bulb T beams transversely. The end nodes of the transverse strands were tied to steel plates acting as end bearing plates. The steel plates were tied to the exterior sides of the external box beams. The interior nodes of the post-tensioning strands were not tied to the surrounding objects. The steel plates in this connection were provided to distribute the post-tensioning force on the concrete surface and prevent any concrete crushing failure. The TPT strands were modeled with CFCC properties, where linear elastic behavior was assumed until failure of the strand.

4.3 Verification of numerical study

Through the verification study, finite element models were developed for the tested control decked bulb T beams and to the bridge model. Model response such as deflection, strain distribution in the concrete, strain in the reinforcement, and ultimate load were compared with those obtained experimentally. The following subsections provide a detailed discussion for the finding of the verification study.

4.3.1 Control beams

Numerical models were generated for all experimental control beams. As shown in Figure 4.3-1, the numerical models consisted of the body of the beam, diaphragms, longitudinal reinforcement, stirrups, and supports. Four models representing Beams C-S-F-U, C-S-F-B, C-S-F-O, and S-S-F-U were generated and analyzed in flexural loading as shown in Figure 4.3-2, while one model for Beam C-C-F-B was generated and analyzed under shear loading as shown in Figure 4.3-3.

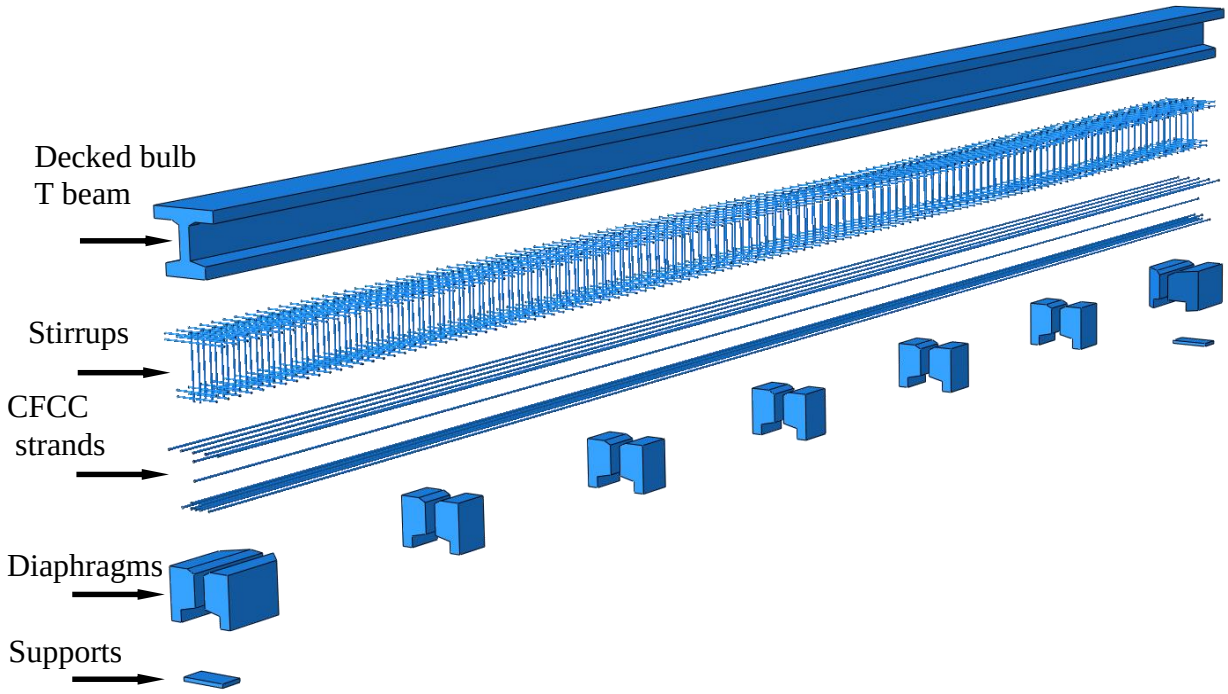

Figure 4.3-1 Details of numerical model

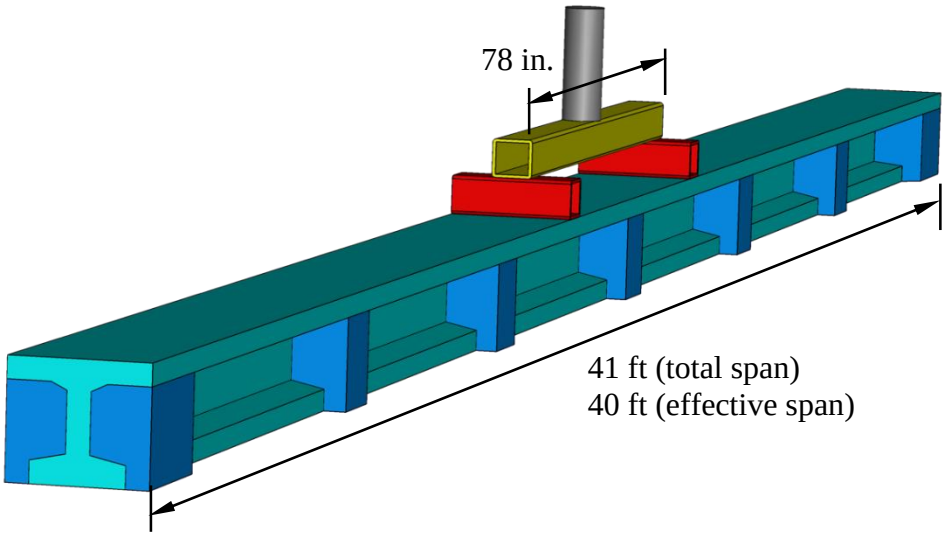

Figure 4.3-2 Models for control beams under flexural loading

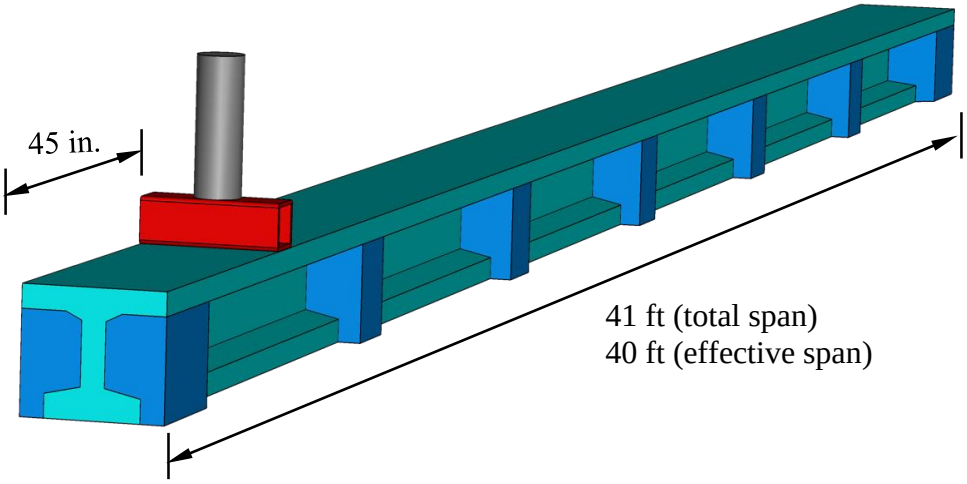

Figure 4.3-3 Model for a control beam with shear loading

4.3.1.1 Numerical model for Beam C-S-F-U

The concrete material in this control beam model was defined with a 28-day compressive strength of 9 ksi, tensile strength of 690 psi, and elastic modulus of 5,751 ksi. Both the modulus of elasticity and the tensile strength were adopted from AASHTO LRFD 2012 Sections 5.4.2.4 and C.5.4.2.7, respectively, while the compressive and tensile stress-strain curves (shown in Figure 4.3-5 and Figure 4.3-6) of the concrete were developed based on an analytical formula (Collins et al. 1993, Popovics et al. 1973, and Thorenfeldt et al. 1987). Normal-weight concrete was assumed with a self-weight of 0.15 kip/ft^3 and Poisson's ratio of 0.2. The beam was reinforced/prestressed with CFCC strands and steel stirrups every 4 in. The beam had a total span of 41 ft and effective span of 40 ft. The numerical model simulated the configuration and the reinforcement of the control beams with four bottom CFCC prestrssing strands and five top non-prestressing CFCC strands in addition to two non-prestressing strands through the depth of the web. The CFCC strands were defined in the model with an effective cross sectional area of 0.179 in.^{2}, a modulus of elasticity of 22,480 ksi, ultimate tensile strength of 375 ksi, and ultimate strain of 1.67%. Figure 4.3-4 shows the stress-strain curve for CFCC materials. The stirrups were modeled as truss elements with cross sectional area of 0.11 in.^{2} (No. 3 deformed steel bars) and were assigned the material properties of Grade 60 steel with a yield strength of 60 ksi, elastic modulus of 29,000 ksi, ultimate strength of 90 ksi, and ultimate strain of 0.05 as shown in Figure 4.3-7.

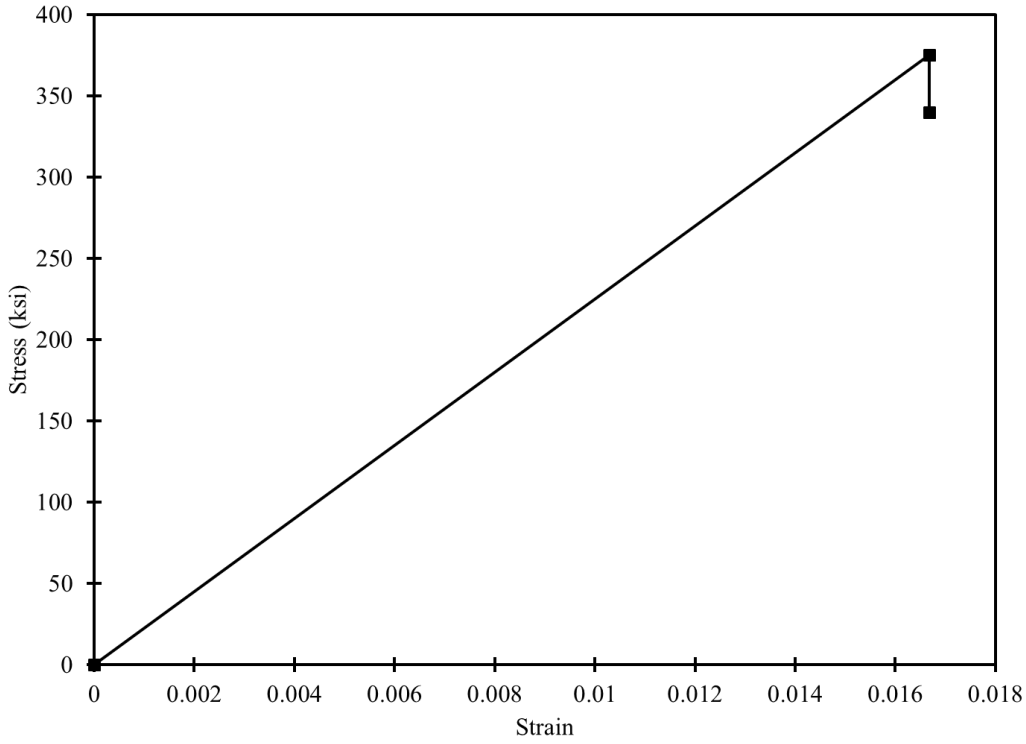

Figure 4.3-4 Stress-strain curve for CFCC strands

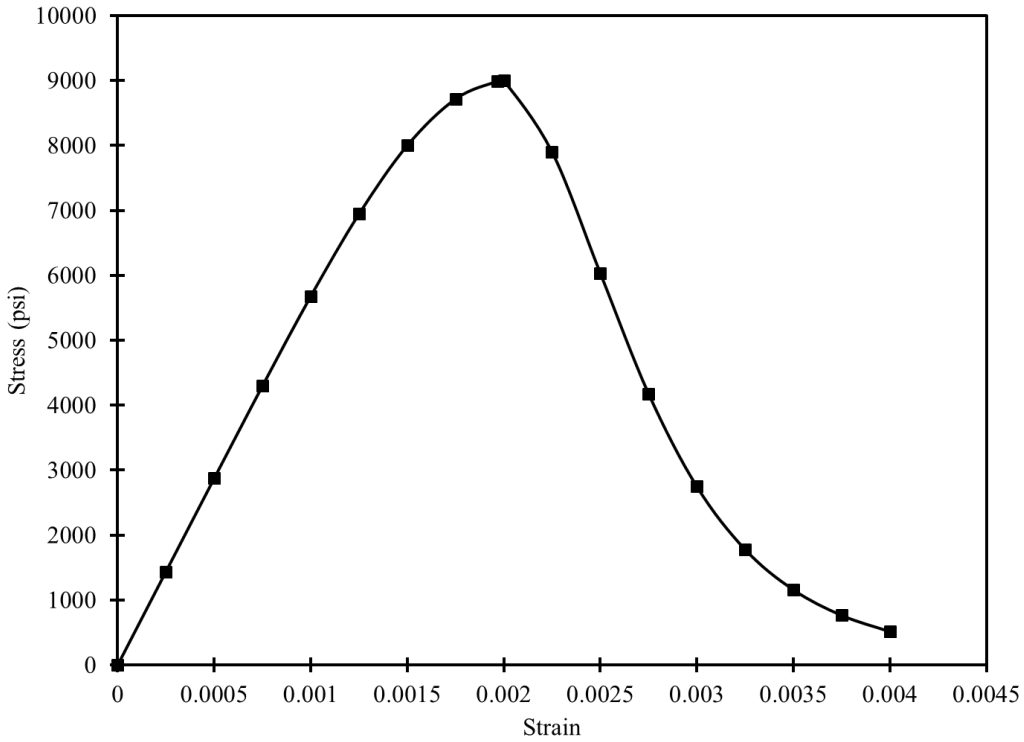

Figure 4.3-5 Compressive stress-strain curve for 9000-psi concrete

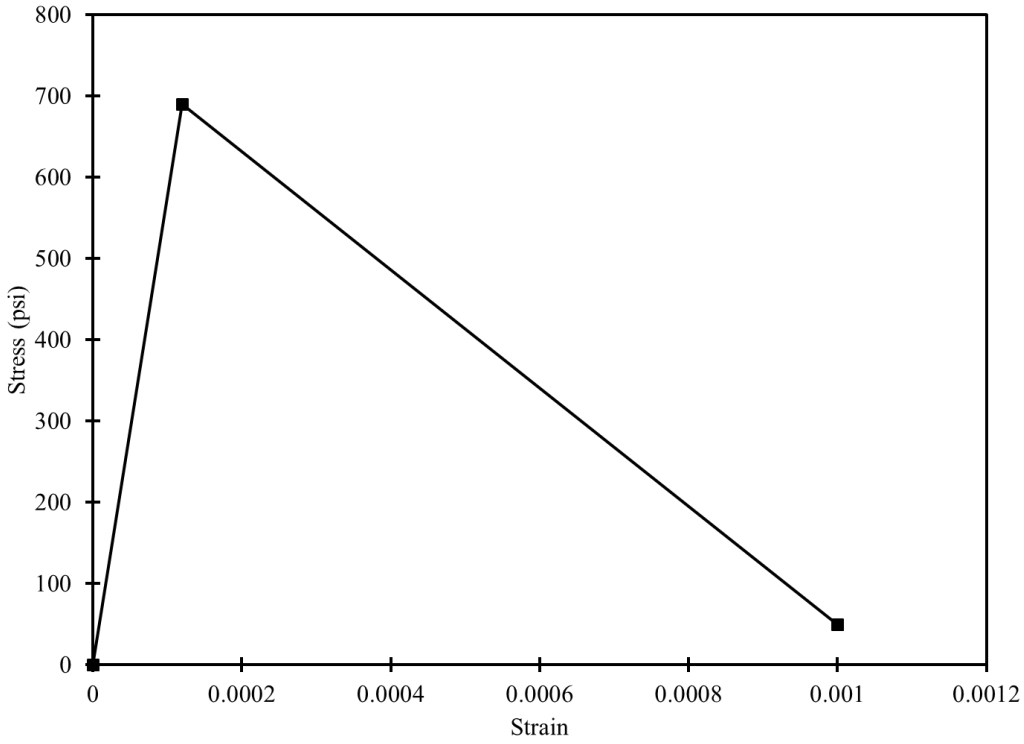

Figure 4.3-6 Tensile stress-strain relationship for 9000-psi concrete

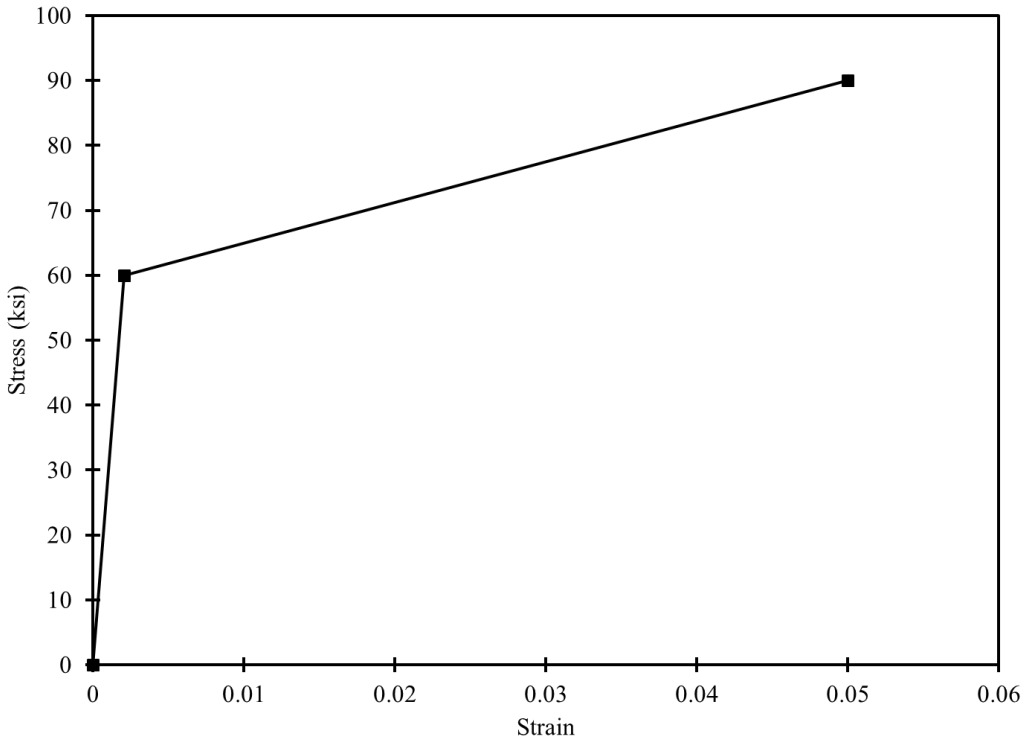

Figure 4.3-7 Idealized stress-strain curve for deformed steel bars, Grade 60

During the numerical analysis, the control beam is analyzed under flexural static load to failure. The load-deflection curves of the beam and the load-strain curves of the concrete and CFCC strands were compared with those obtained from the experimental study. The numerical model exhibited a cracking load of approximately 12.0 kip, which matched the cracking load of the experimental beam. The numerical model showed a maximum load carrying capacity of 33.5 kip with a corresponding deflection at failure of 15.86 in. However, the envelope of the experimental load cycles showed a maximum load 33.1 kip and then the load dropped to 31.4 kip with a corresponding deflection of 16 in. The difference between the numerical and experimental results was approximately 2%. Figure 4.3-8 shows the load deflection curves obtained numerically and experimentally. The experimental load-deflection curve is the envelope for all the load cycles. As shown in the figure, there is an overall fair agreement between the numerical and experimental responses of this control beam. The load-strain curves for the concrete and the CFCC strands are shown in Figure 4.3-9 and Figure 4.3-10, respectively. Close agreement was observed between the numerical and experimental strain reading with a difference of approximately 6 % in concrete strain readings and 9 % in CFCC strain readings at failure.

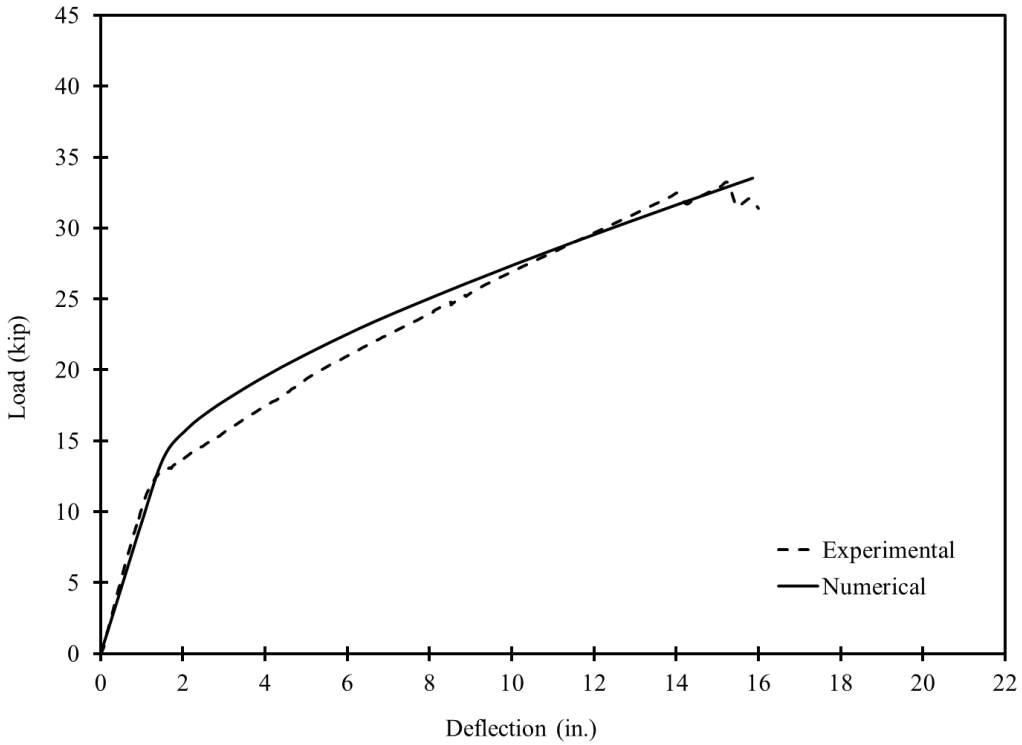

Figure 4.3-8 Numerical vs. experimental load-deflection curves of Beam C-S-F-U

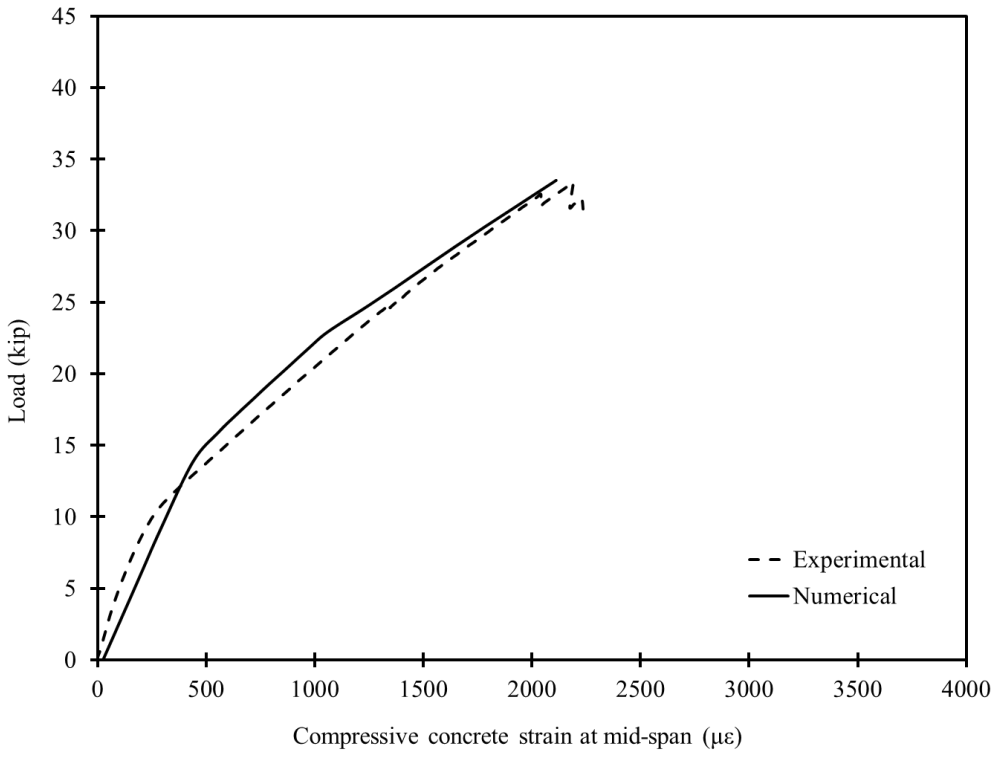

Figure 4.3-9 Numerical vs. experimental load-concrete-strain curves of Beam C-S-F-U

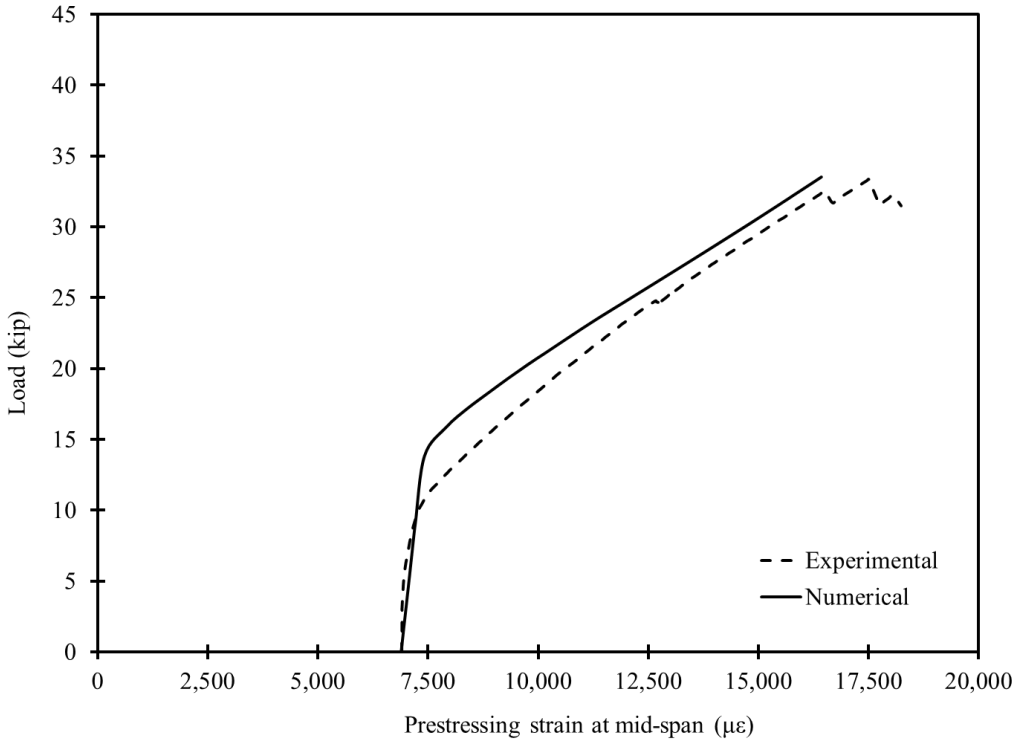

Figure 4.3-10 Numerical vs. experimental load-prestressing-strain of Beam C-S-F-U

4.3.1.2 Numerical model for Beam C-S-F-B

The modeling and analysis approach for this beam was similar to the previous beam with the exception that the concrete strength was slightly lower. Based on the 28-day uni-axial compressive strength, the concrete compressive strength averaged 7,684 psi, and on the day of the test, the concrete compressive strength slightly exceeded 8,000 psi. Therefore, the material properties and stress-strain curves for 8,000-psi concrete was adopted for this beam. It should be noted that this was the only beam that experienced a slightly lower concrete strength. All other beams including those for the bridge model experienced a concrete strength with the average of approximately 9,000 psi. The modulus of elasticity for the concrete was taken as 5,422 ksi, while the direct tensile strength was taken as 650 psi. Figure 4.3-11 shows the adopted compressive stress-strain relationship for the 8,000-psi concrete.

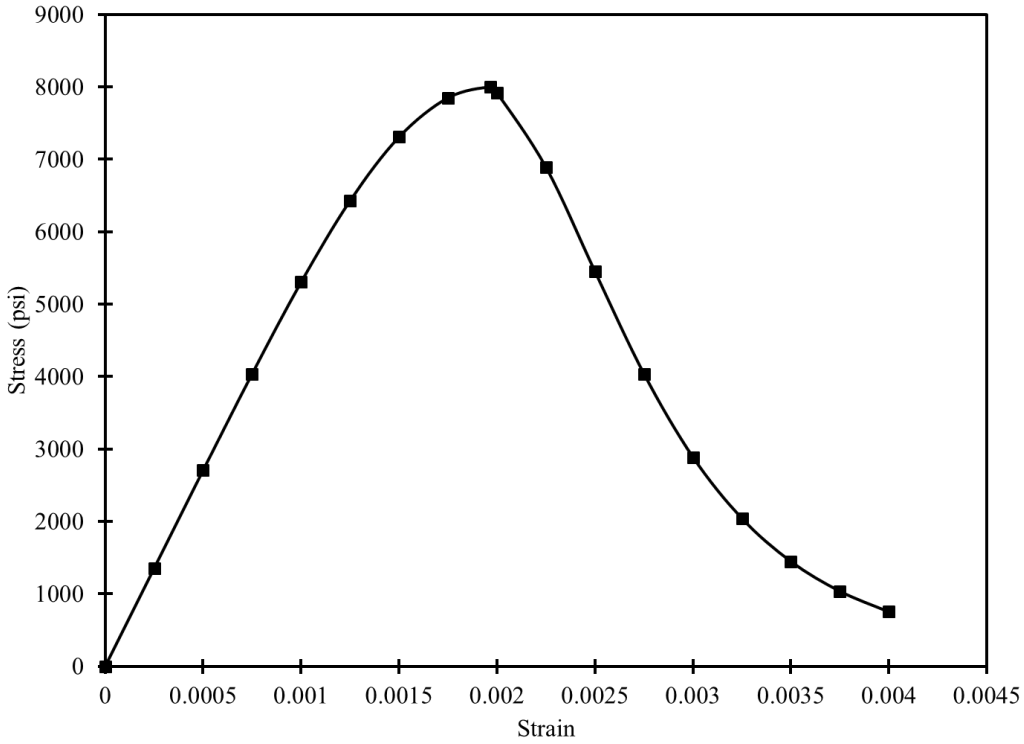

Figure 4.3-11 Compressive stress-strain curve for 8,000-psi concrete

The results from the numerical model are in good agreement with those from the experimental investigation. As shown in Figure 4.3-12, the numerical model predicted the failure at a load level of 41.31 kip with a corresponding deflection of 17.63 in. The experimental test showed an ultimate load of 40.81 kip with a corresponding deflection of 16.43 in. The difference between the

numerical and experimental failure load was approximately 1.2%, while the difference in the deflection at failure was approximately 7%.

Similarly, there is a good agreement between the numerically predicted concrete strain and the experimentally recorded strain as shown in Figure 4.3-13. The numerical model predicted the failure of the beam at a concrete strain of 2,900 με, while the maximum experimentally recorded strain was around 3,270 με. On the other hand, the recoding of the strain in the prestressing strands was interrupted early during the experimental testing but the data collected shows a good agreement with the numerically predicted prestressing strain as shown in Figure 4.3-14. The numerical analysis predicted the failure of the beam at prestressing strain of 16,143 με.

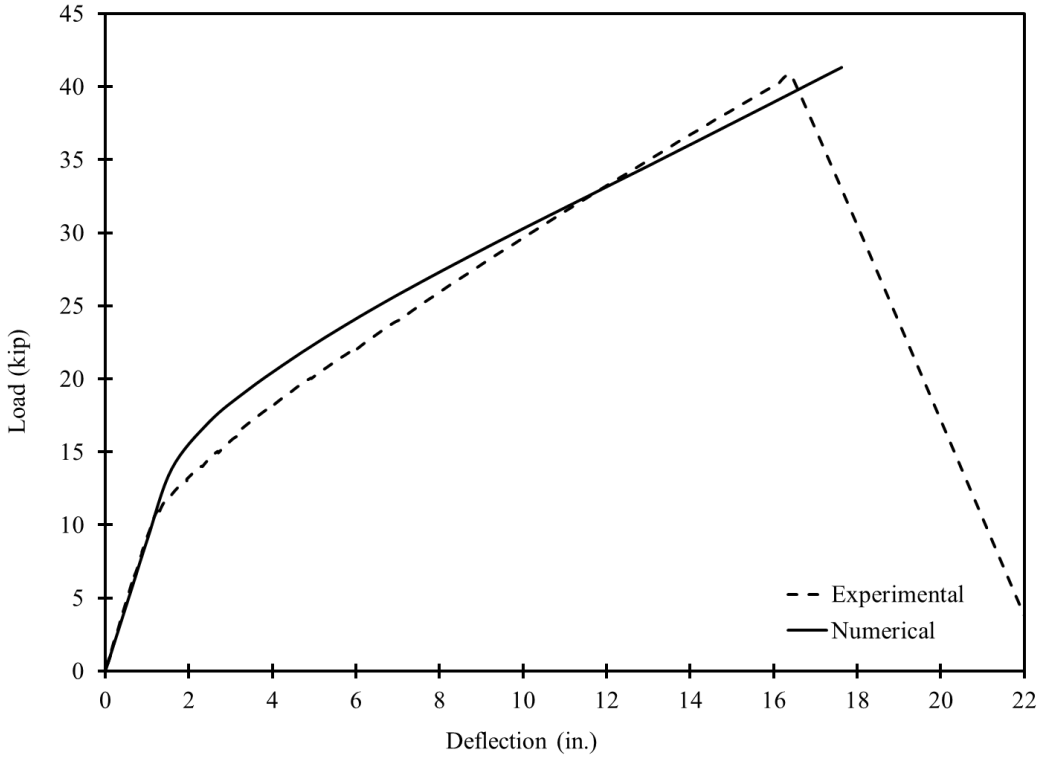

Figure 4.3-12 Numerical vs. experimental load-deflection curves of Beam C-S-F-B

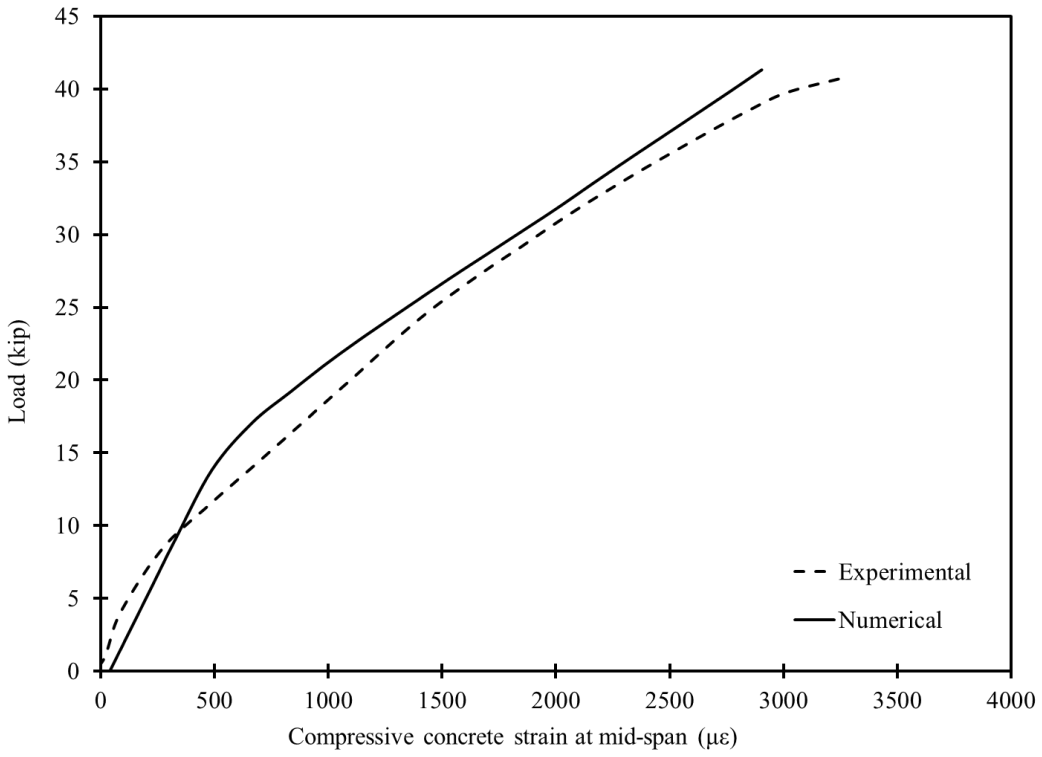

Figure 4.3-13 Numerical vs. experimental load-concrete-strain curves of Beam C-S-F-B

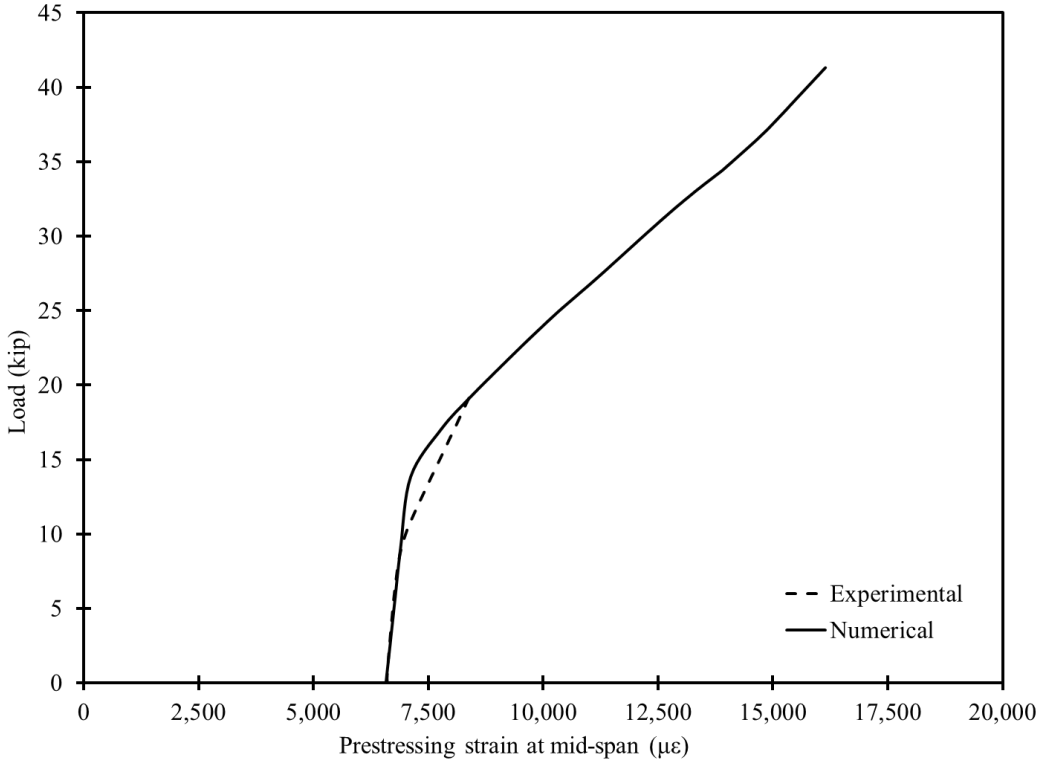

Figure 4.3-14 Numerical vs. experimental load-prestressing-strain curves of Beam C-S-F-B

4.3.1.3 Numerical model for Beam C-S-F-O

Similar to previous beams, a numerical model was generated for Beam C-S-F-O and analyzed under four-point loading. The results from the numerical analysis were compared with those obtained experimentally as shown in Figure 4.3-15 through Figure 4.3-17. The observed cracking load was approximately 12 kip, while the maximum load was approximately 43.7 kip with a corresponding deflection of 14.61 in. The concrete strain obtained numerically was slightly different from that recorded using strain gages, mainly because of the variation in the stress-strain behavior of the concrete. The concrete in the numerical analysis was defined with an ideal concrete stress-strain curve, where for a 9000-psi concrete, it was assumed that the strain corresponding to a stress of 9000 psi was approximately 2,000 με. After that, the concrete was assumed to lose strength with a gradual increase in strain until failure at a strain of 3,000 με. Therefore, the numerical load-strain relationship followed the pre-defined pattern exactly as shown in Figure 4.3-16. At the maximum load, the concrete strain was slightly higher than 2,000 με but it tended to increase with a slight decrease in the load until failure occurred at a concrete strain of 3,000 με. This exact behavior was not captured by the strain gages in the experimental investigation. On the other hand, Figure 4.3-17 shows the numerical vs. experimental prestressing strain in the CFCC strands. As shown in the figure, both the experimental and numerical results indicated a prestressing strain of approximately 13,600 με at failure, which confirmed the compression failure of the beam. Overall, there was good agreement between the numerical and experimental results. At failure, the differences in load, deflection, strain in concrete, and strain in prestressing strands were approximately 0.2, 1.9, 1.6, and 0.4%, respectively.

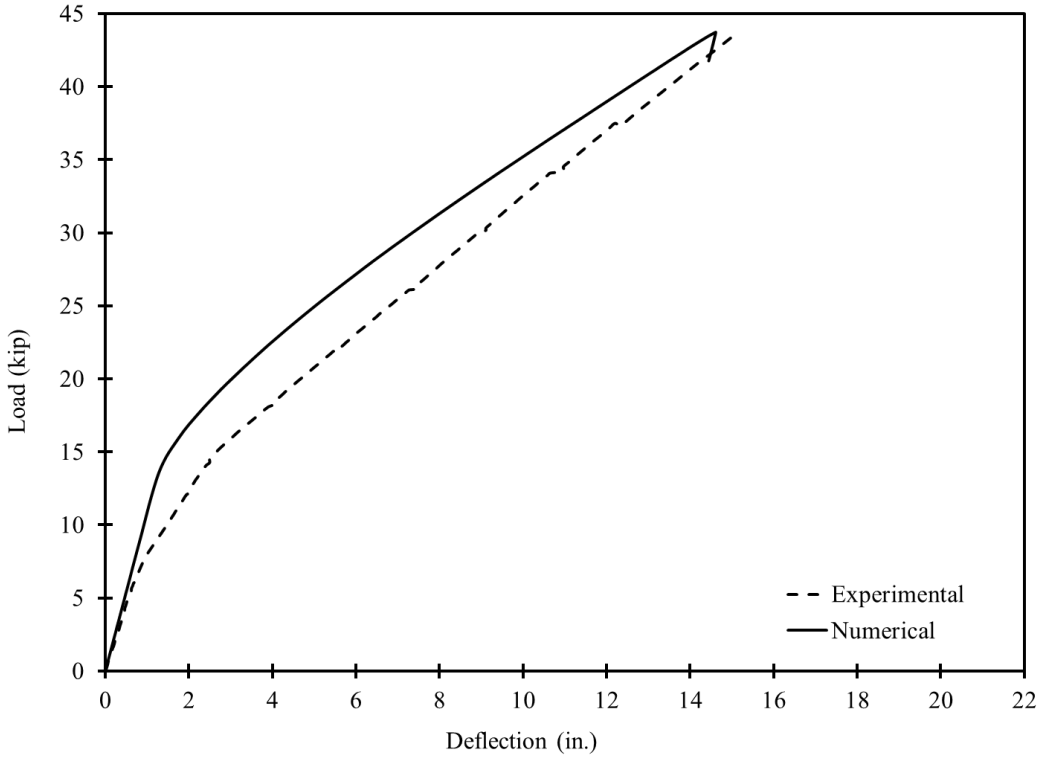

Figure 4.3-15 Numerical vs. experimental load-deflection curves of Beam C-S-F-O

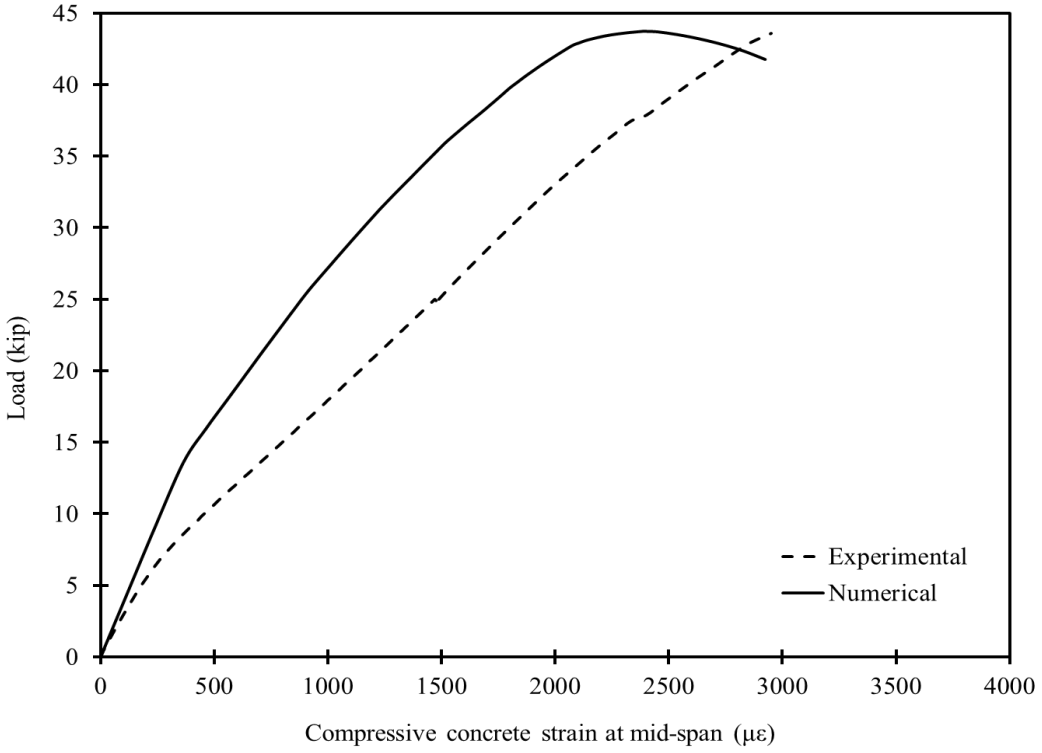

Figure 4.3-16 Numerical vs. experimental load-concrete-strain curves of Beam C-S-F-O

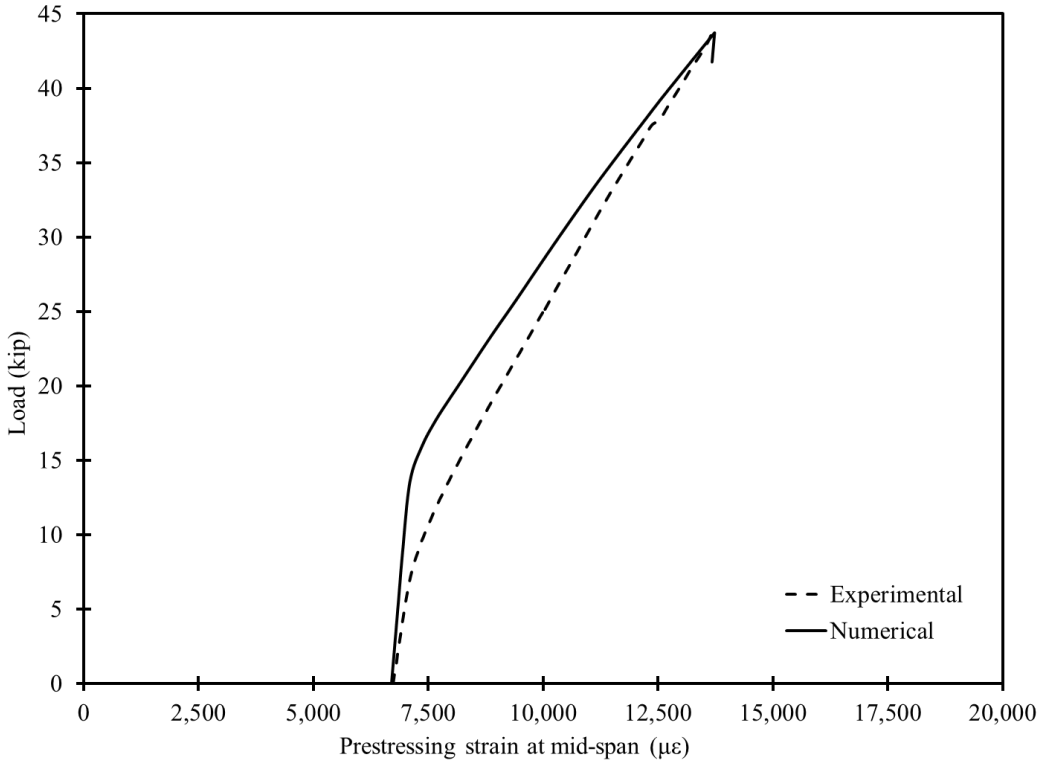

Figure 4.3-17 Numerical vs. experimental load-prestressing-strain curves of Beam C-S-F-O

4.3.1.4 Numerical model for Beam S-S-F-U

This control beam was reinforced with 7-wire low relaxation steel strands with a diameter of 0.6 in. The non-prestressed reinforcement was composed of deformed steel bars, Grade 60. Therefore, in the numerical modeling, the prestressing strands were assigned the material properties of steel strands with modulus of elasticity of 28,500 ksi, yield strength of 230 ksi, and ultimate strength of 270 ksi with a corresponding ultimate strain of approximately 5%. Figure 4.3-18 shows the idealized stress-strain curve for low-relaxation steel strands.

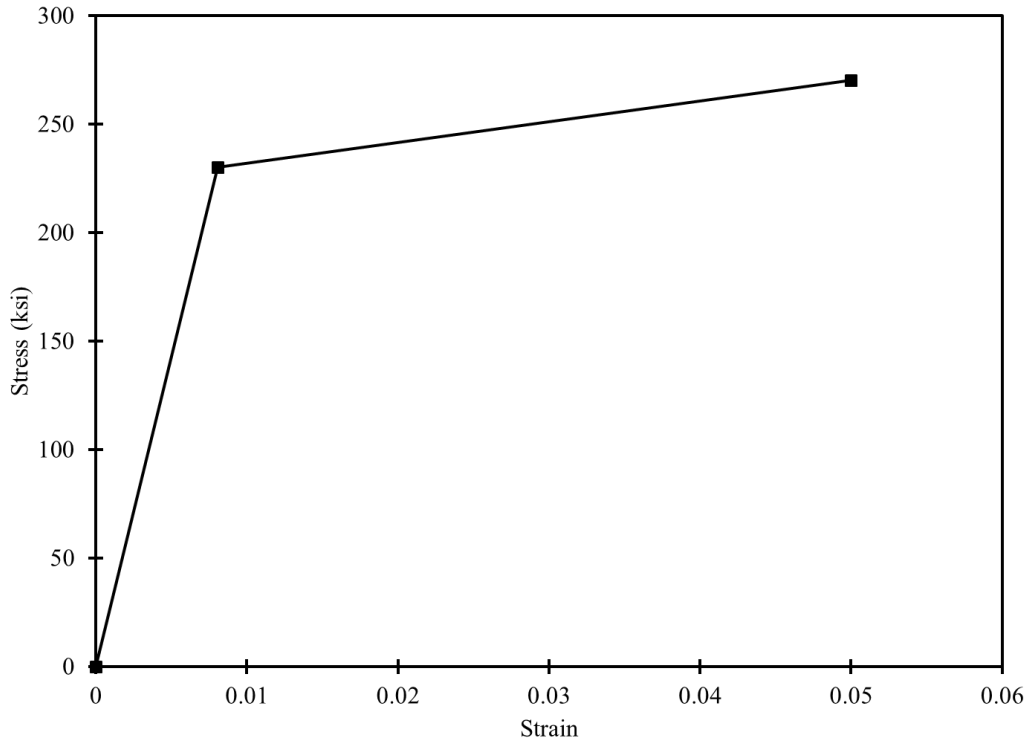

Figure 4.3-18 Idealized stress-strain curve for low-relaxation steel strands

As shown in Figure 4.3-19, Figure 4.3-20, and Figure 4.3-21, the deflection, concrete strain, and prestressing strain values from the numerical analysis are in good agreement with the values obtained experimentally. The numerical analysis shows a maximum load of 38.77 kip with a corresponding deflection at failure of 17.5 in, while the experimental testing shows a maximum load of 39.4 kip with a corresponding deflection of 19.14 in. The maximum experimental recorded strain in the concrete was approximately 2,615 με, which also matched the maximum numerically calculated concrete strain at failure. The experimental strain in the prestressing strands at failure was approximately 18,784 με, while the numerically predicted value is approximately 19,184 με.

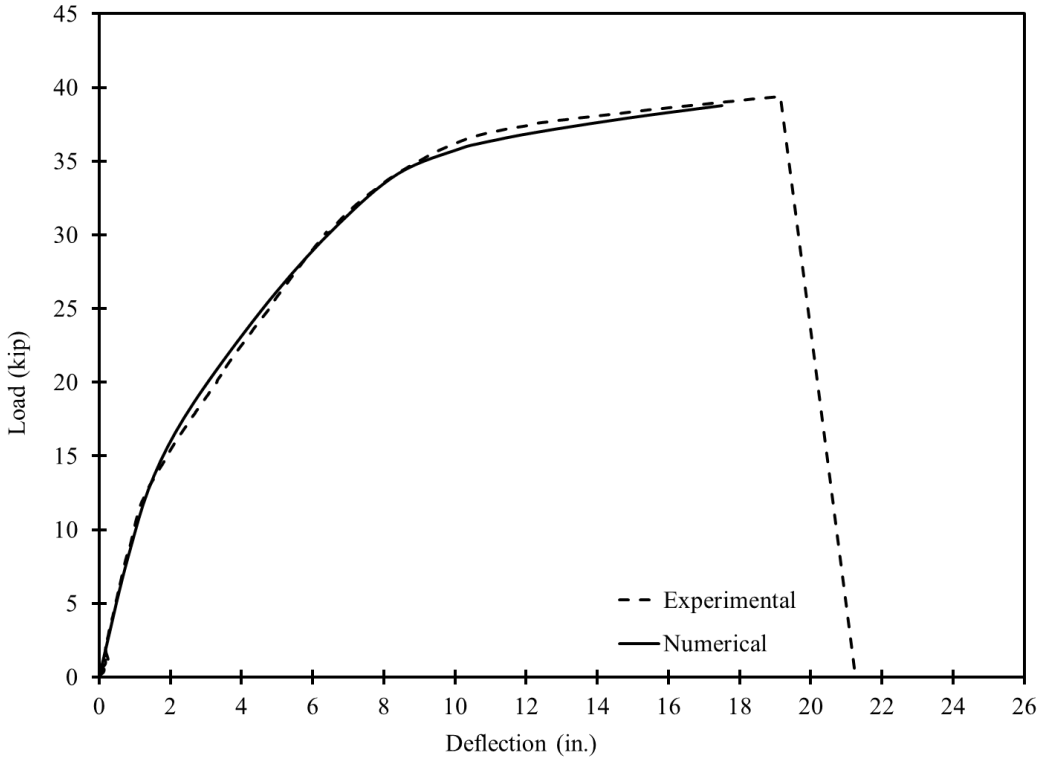

Figure 4.3-19 Numerical vs. experimental load-deflection curves of Beam S-S-F-U

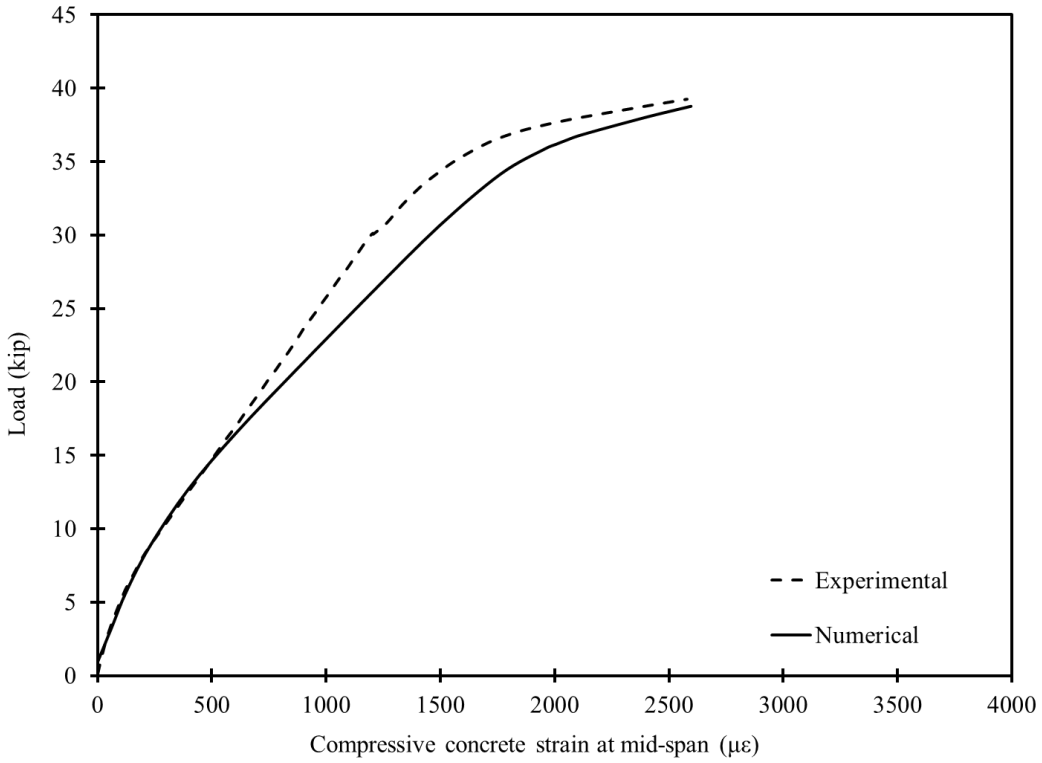

Figure 4.3-20 Numerical vs. experimental load-concrete-strain curves of Beam S-S-F-U

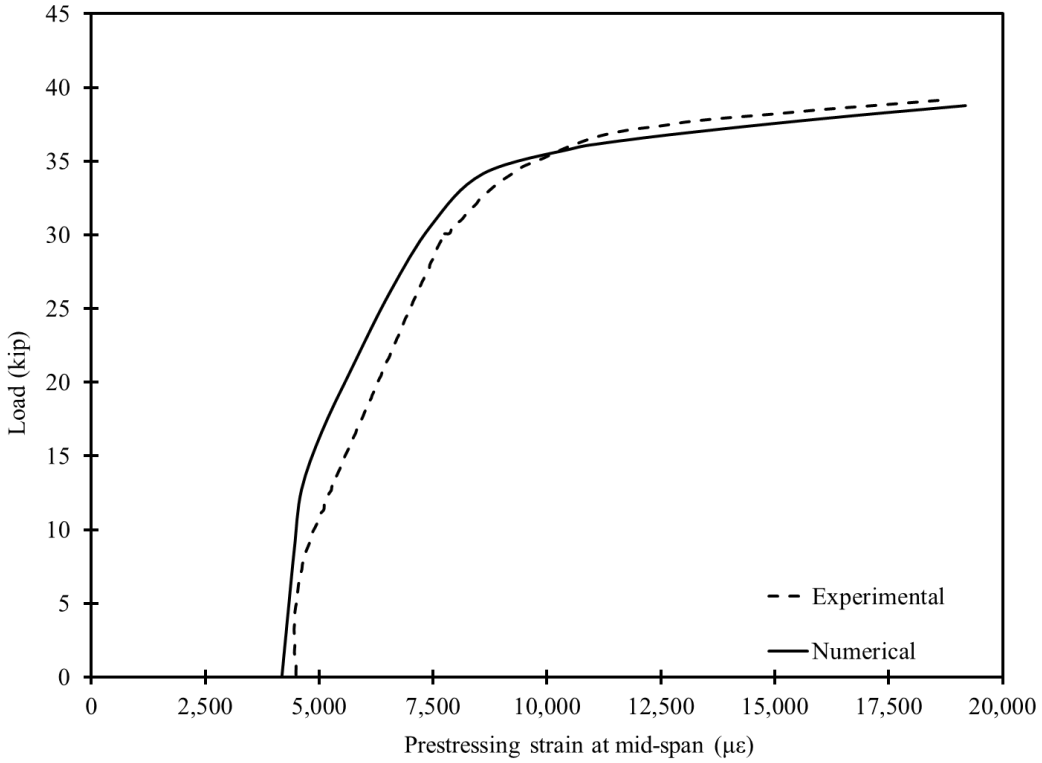

Figure 4.3-21 Numerical vs. experimental load-prestressing-strain curves of Beam S-S-F-U

4.3.1.5 Numerical model for Beam C-C-S-B

This numerical model for this control beam was analyzed under shear loading with a shear span of 45 in. The concrete elements were assigned the material properties of 9,000-psi concrete, while the stirrups were assigned the material properties of CFCC with an elastic modulus of 21,030 ksi and an ultimate strength of 400 ksi with a corresponding ultimate strain of 1.9%. Properties of CFCC stirrups were adopted from a material data sheet tested and provided by the manufacturer. The CFCC stirrups had a diameter of 0.41 in. with effective cross sectional area of approximately 0.09 in^2.

As shown in Figure 4.3-22 and Figure 4.3-23, the numerically-predicted deflection under the loading point and at the mid-span matches those recorded experimentally with a good agreement from the beginning of the loading to failure. The predicted failure load from the numerical analysis is around 80.88 kip with a corresponding deflection of 3.09 in. under the load and 6.08 in. at the mid-span. The experimental results showed that the ultimate load was around 78.4 kip with a corresponding deflection of 3.18 in. under the load and 5.77 in. at the mid-span.

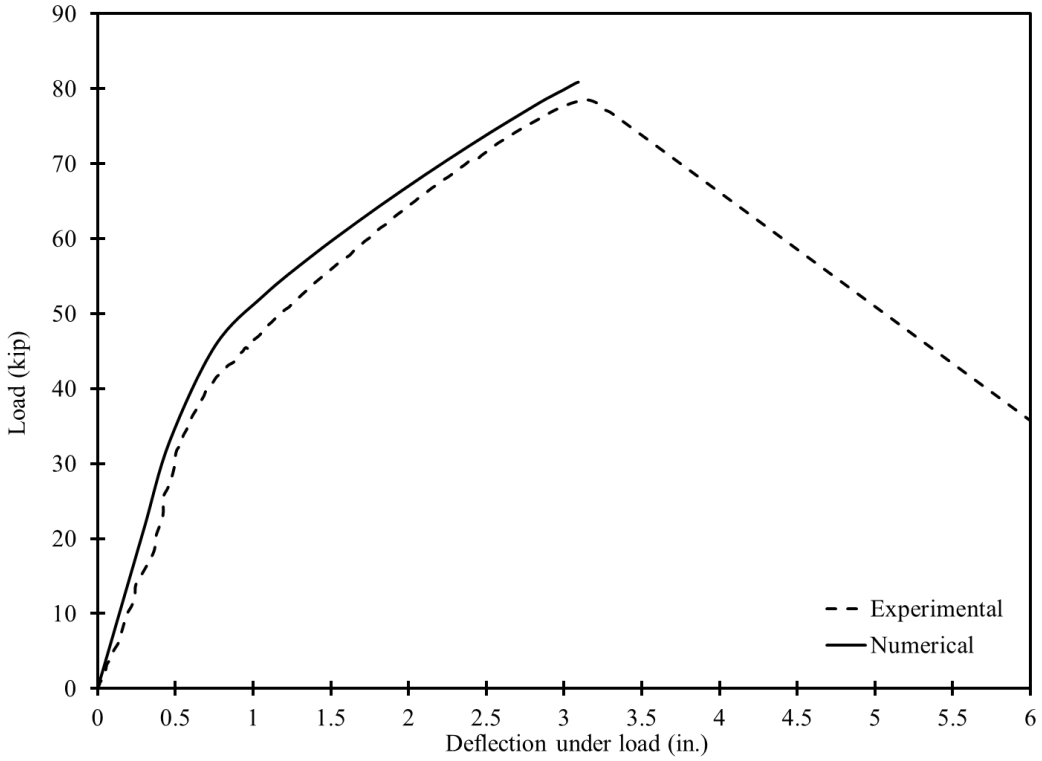

Figure 4.3-22 Numerical vs. experimental load-deflection curves of Beam C-C-S-B

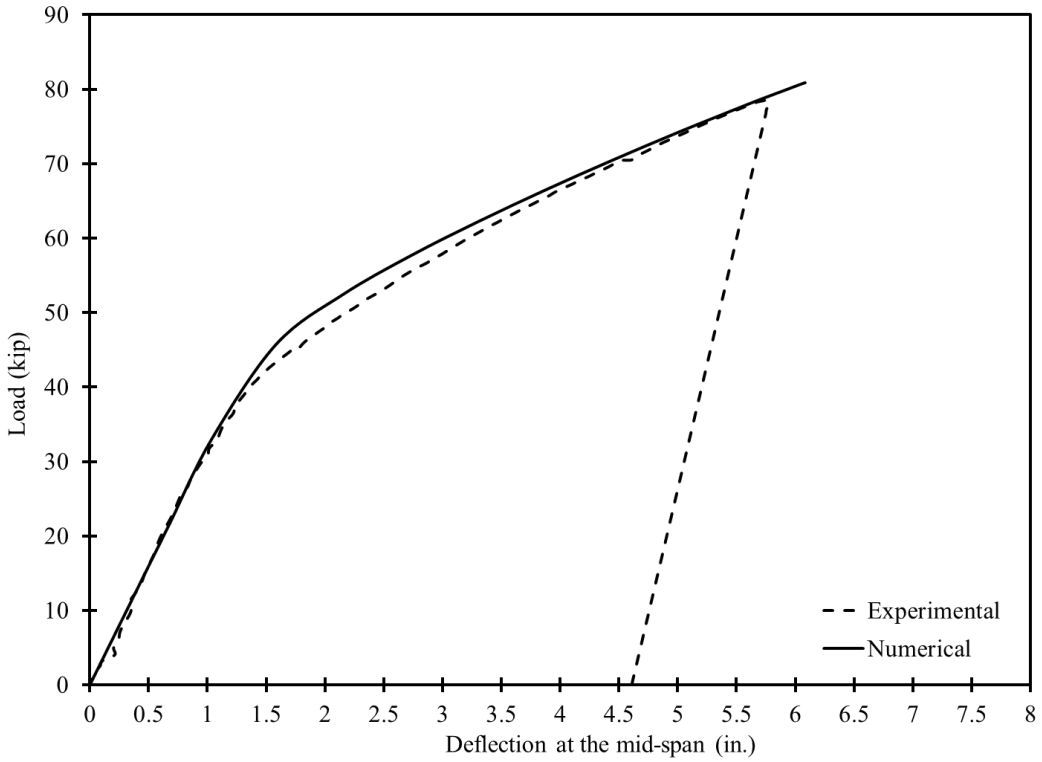

Figure 4.3-23 Numerical vs. experimental load-mid-span-deflection curves of Beam C-C-F-B

The numerical and experimental strain readings in the concrete top flange surface near the loading are compared in Figure 4.3-24. The numerical model predicted a concrete strain of 2,220 με at failure, while the maximum concrete strain that was recorded experimentally is approximately 2,670 με. Similarly, the numerical strain in the longitudinal prestressing strands was compared with that obtained experimentally as shown in Figure 4.3-25. Good agreement is observed in the strain readings with the numerical analysis predicting a maximum prestressing strain of 11,687 με and the experimental recording showing a maximum strain of 12,276 με.

The strain in the CFCC stirrups was obtained numerically and was plotted against the experimental strain in different stirrups. Figure 4.3-26 shows an example for the comparison between the numerical and experimental stirrup strain. As shown in the figure, two trends of experimental strain readings are observed; one trend represented stirrups intercepted by diagonal cracks for the first time (strain reading of S6-B), while the other trend represented the strain in stirrups intercepted by diagonal shear cracks during previous load cycles (strain reading of S3-T). The location of the strain gages on the stirrups is shown in Figure 4.3-27, where S3 is the third instrumented stirrup in the shear span from the left and S6 is the sixth instrumented stirrup. The letters T refers to the top strain gage and the letter B refers to the bottom strain gage on the stirrup. Since no load cycles were performed in the numerical analysis, the predicted strain in the stirrups is in close agreement with the strain in stirrups not intercepted by cracks during previous load cycles.

Finally, the numerical model accurately predicted the failure mode under the shear loading. As shown in Figure 4.3-28, the failure of the numerical model occurred due to excessive strain and deformation in the concrete elements of the web of the beam and to a lesser extent in the top flange, which matched the failure mode observed during the experimental test.

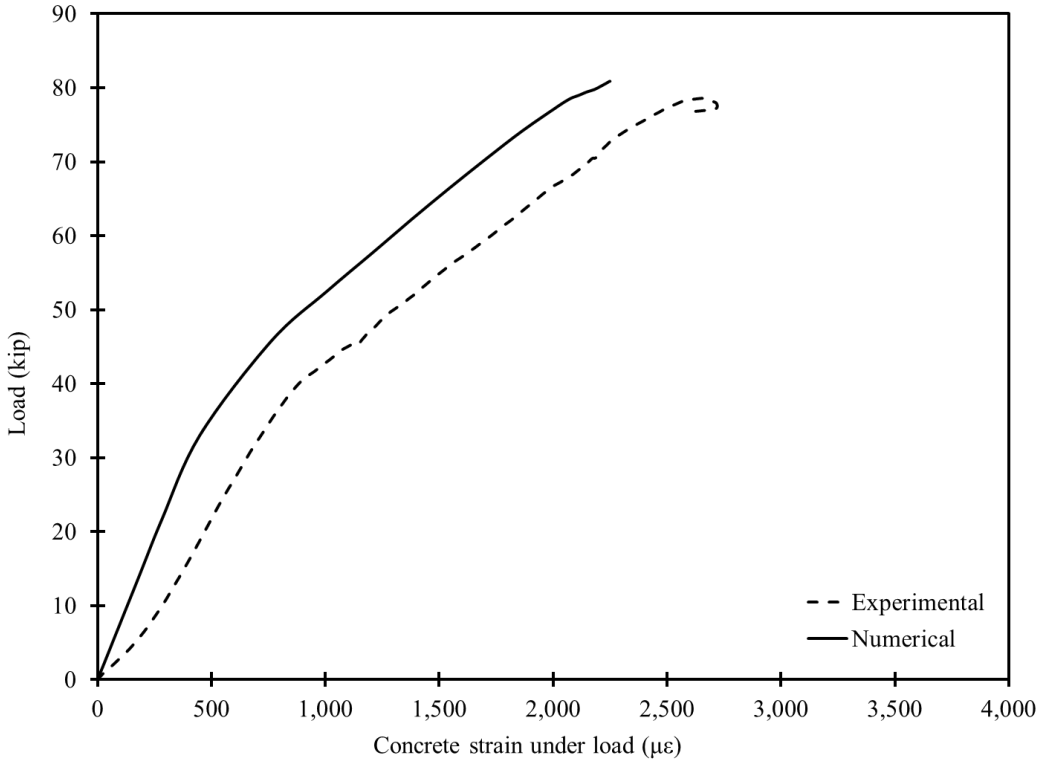

Figure 4.3-24 Numerical vs. experimental load-concrete-strain curves of Beam C-C-F-B

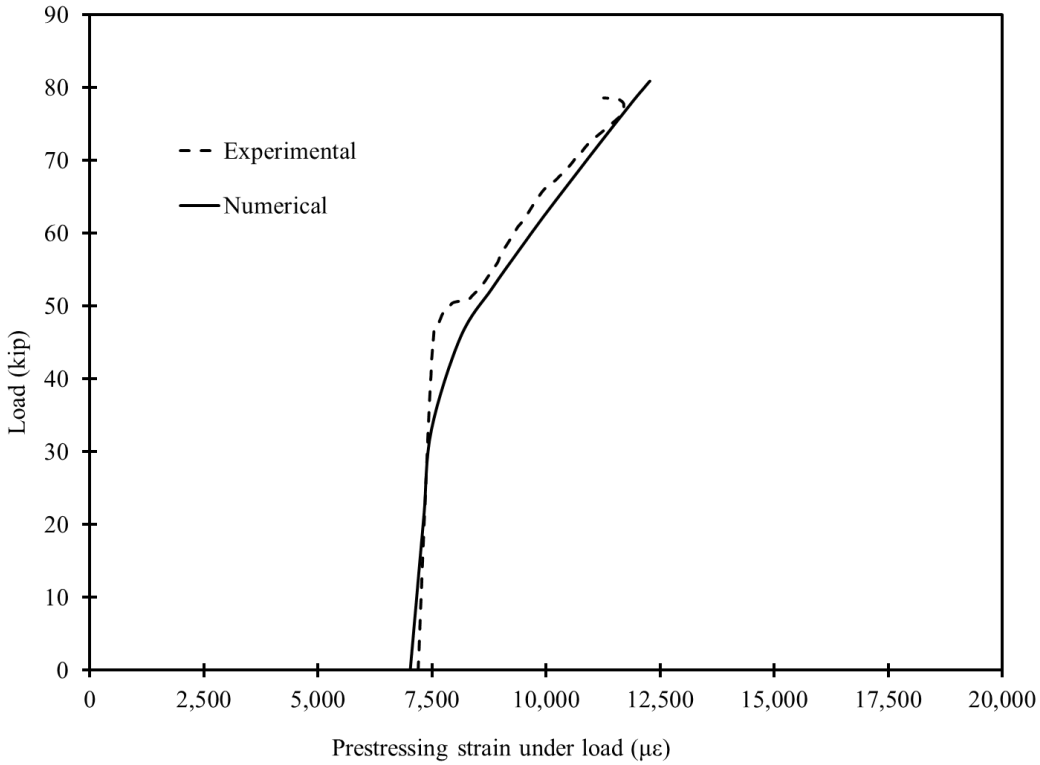

Figure 4.3-25 Numerical vs. experimental load-prestressing-strain curves of Beam C-C-F-B

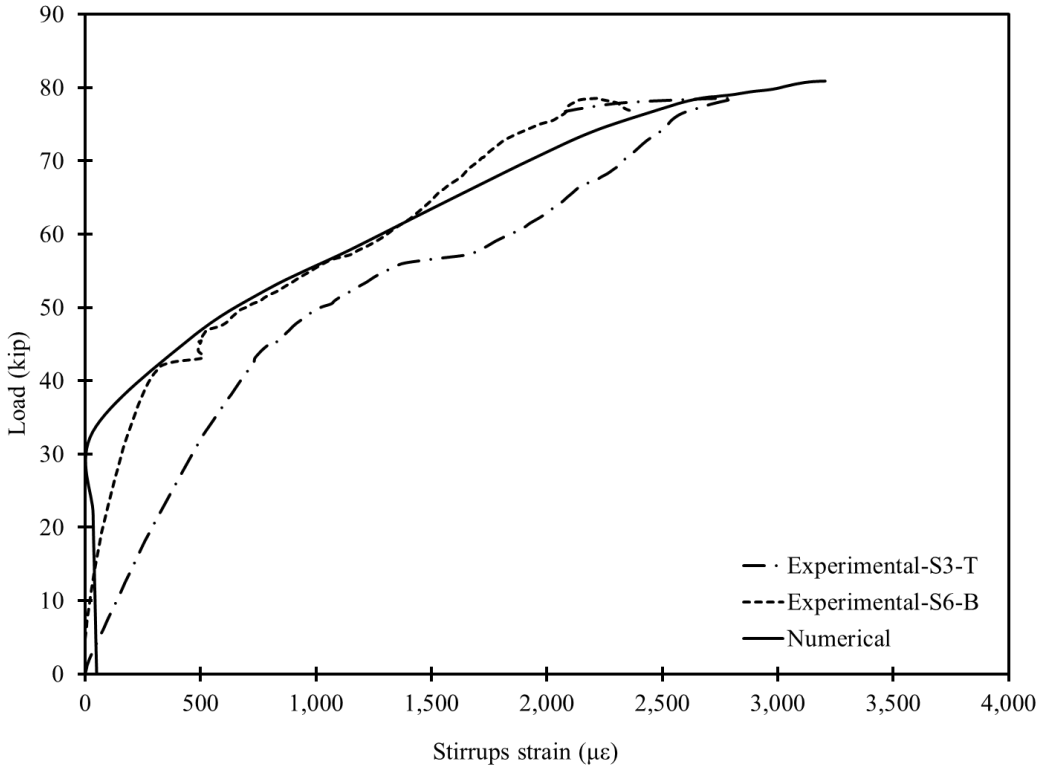

Figure 4.3-26 Numerical vs. experimental load-stirrup-strain curves of Beam C-C-F-B

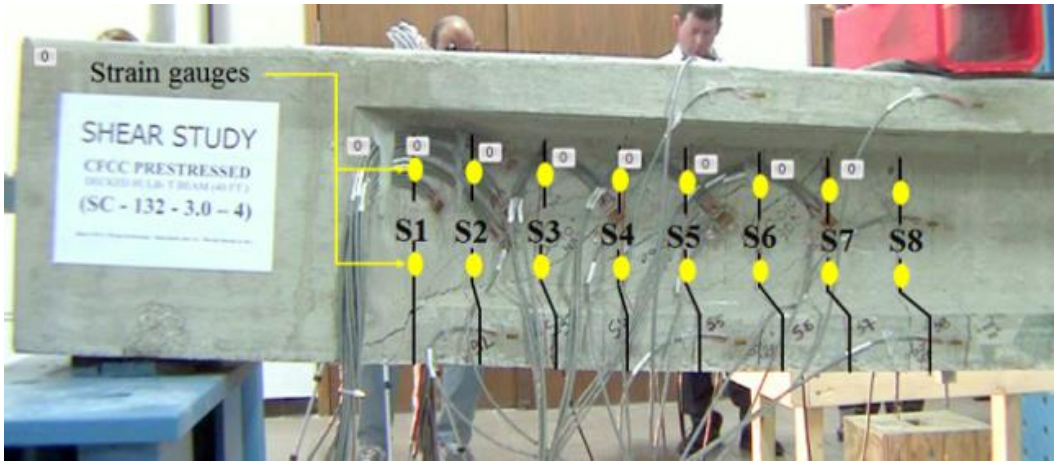

Figure 4.3-27 Nomenclature of strain gages in Beam C-C-S-B

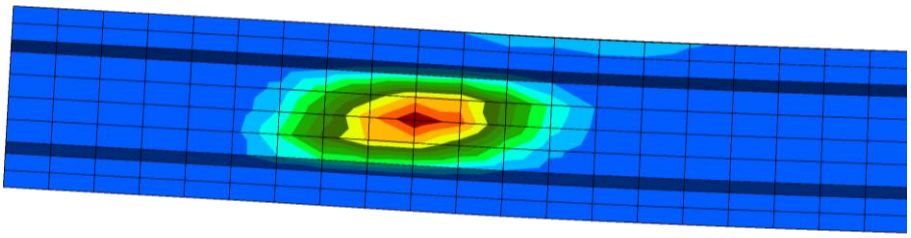

Figure 4.3-28 Shear failure simulation in the numerical model

4.3.2 Bridge model

A numerical model was generated and analyzed for the bridge model under service, post-cracking, and strength limit states. As shown in Figure 4.3-29 through Figure 4.3-31, the numerical analysis depicted with good accuracy the response of the bridge model under service loads of 15 and 30 kip at the mid-span of exterior, interior, and intermediate beams. In addition, and similar to the experimental loading scenario, the numerical model was analyzed under four-point loading until flexural cracks developed and then was analyzed under a single point load of 60 kip on the exterior, interior, and intermediate beams. The numerically obtained deflection values under the load of 60 kip were plotted against those recorded experimentally. The maximum difference between the numerical and experimental results was approximately 8%.

After completing the service and post-cracking limit states analysis, the numerical model was analyzed with the exterior beam loaded under four-point loading (shear key test). The deflection from this phase of analysis is also shown in Figure 4.3-29 at load levels of 80 and 90 kip. At both load levels, the numerical model exhibited a cracking pattern similar to that observed experimentally.

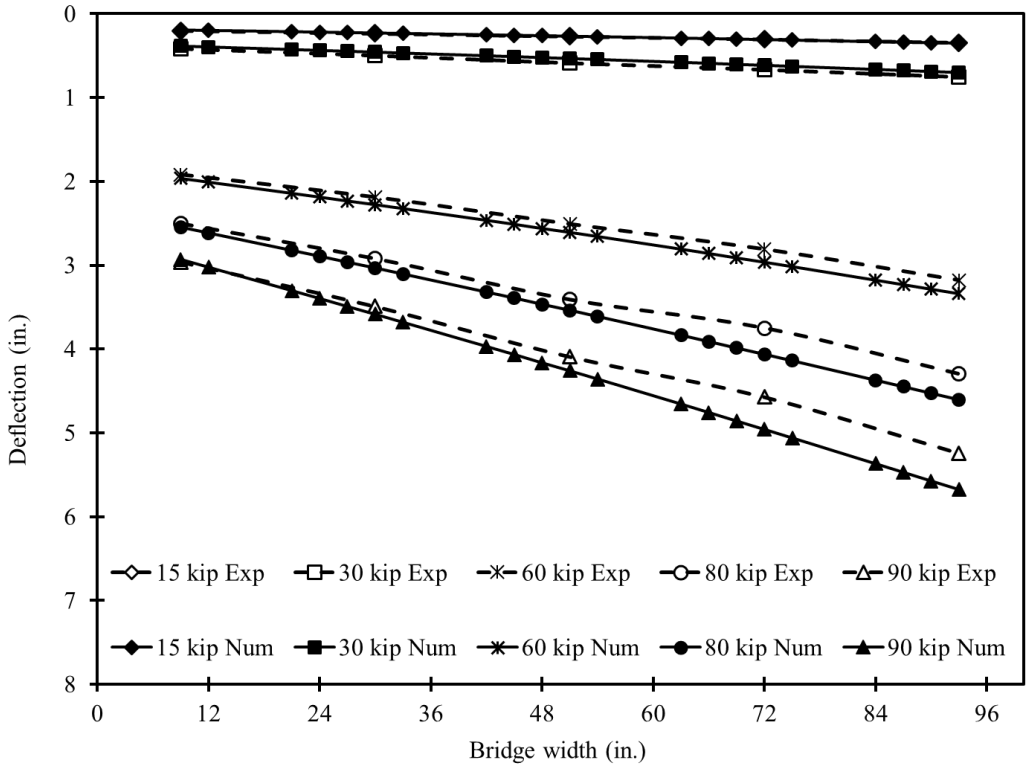

Figure 4.3-29 Numerical vs. experimental deflection curves with loads on exterior beam

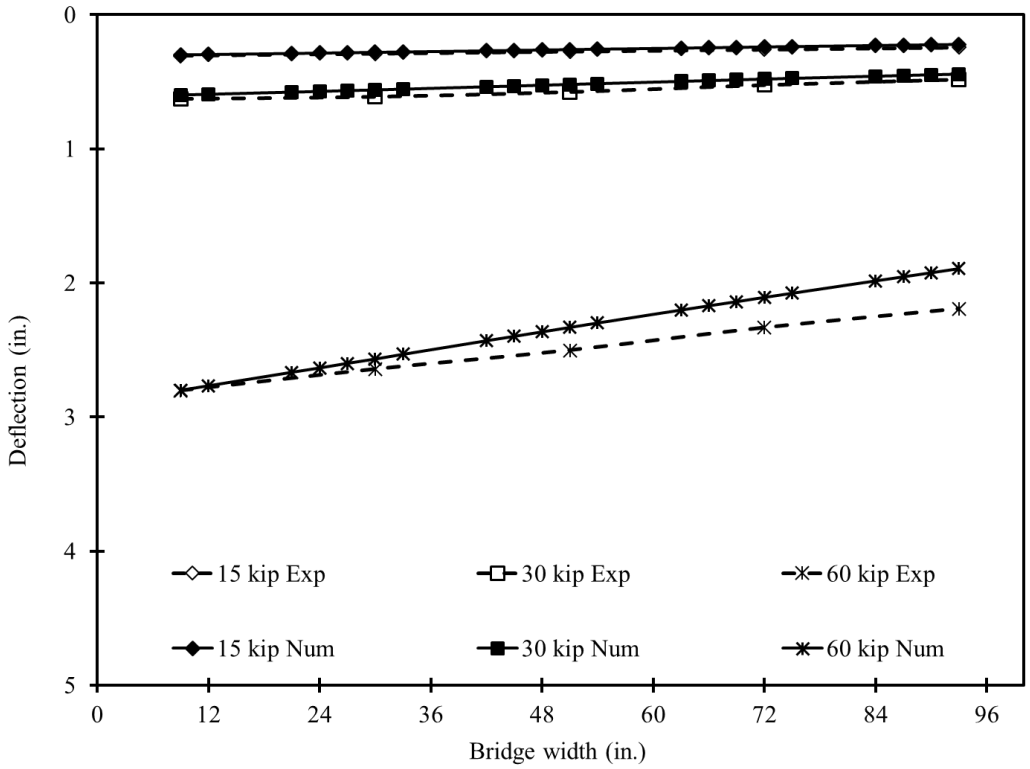

Figure 4.3-30 Numerical vs. experimental deflection curves with loads on interior beam

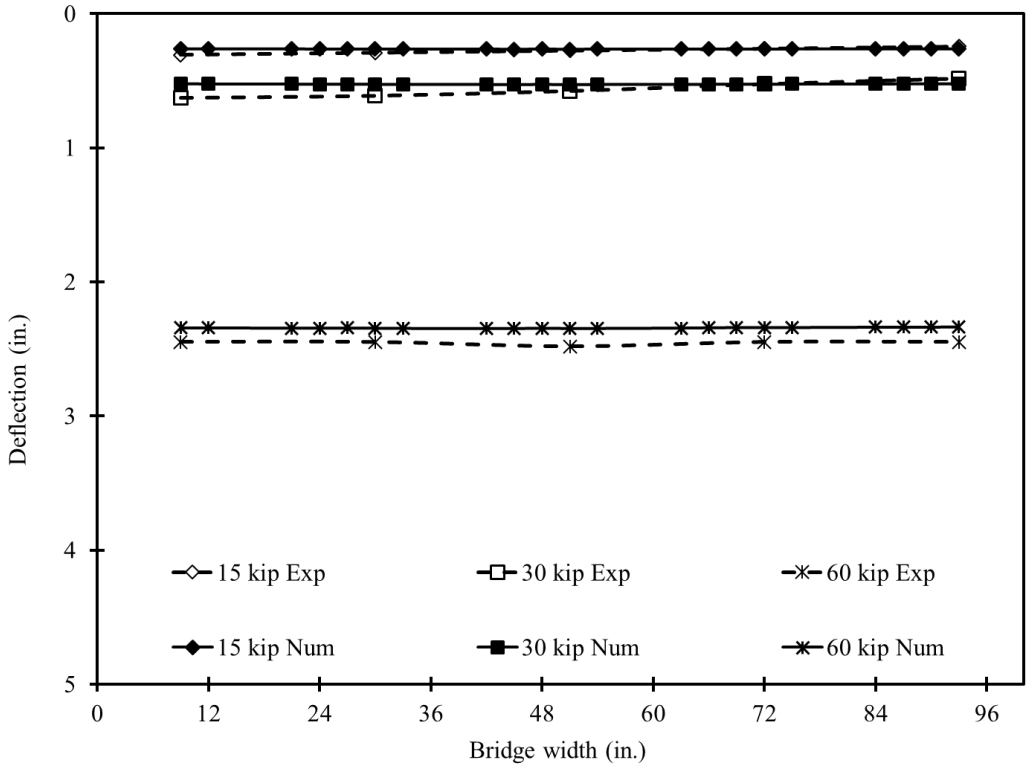

Figure 4.3-31 Numerical vs. experimental deflection curves with loads on intermediate beam

The final stage of the analysis included evaluating the response of the numerical model under strength limit state by performing the analysis with the intermediate beam loaded under a four-point loading setup to failure. Similar to control beams, the response of the bridge model was evaluated through the deflection, concrete strain, and prestressing strain. Figure 4.3-32 through Figure 4.3-34 show the response of the numerical model versus the experimentally recorded data. The numerical analysis showed a failure load of 219.6 kip with a corresponding deflection of 16.64, 16.61, and 16.56 in. under the intermediate, interior, and exterior beams respectively. At the intermediate beam, the concrete strain at the maximum load was approximately 2,800 με, while the strain in the prestressing strands reached the ultimate strain of 16,000 με.

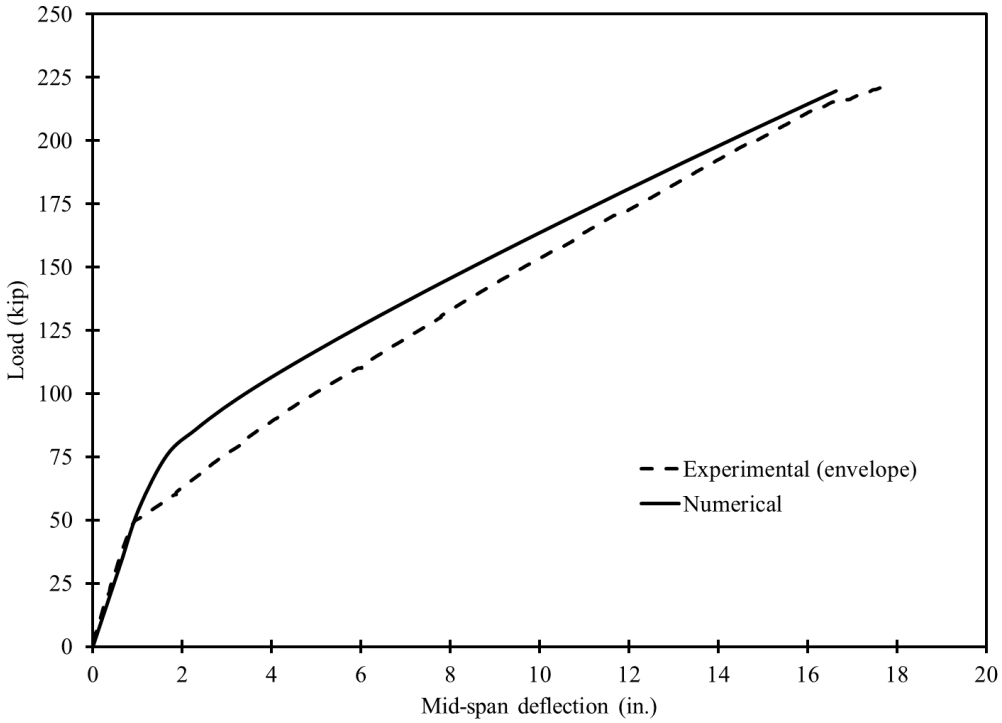

Figure 4.3-32 Numerical vs. experimental deflection curves with loads on intermediate beam during the ultimate load cycle

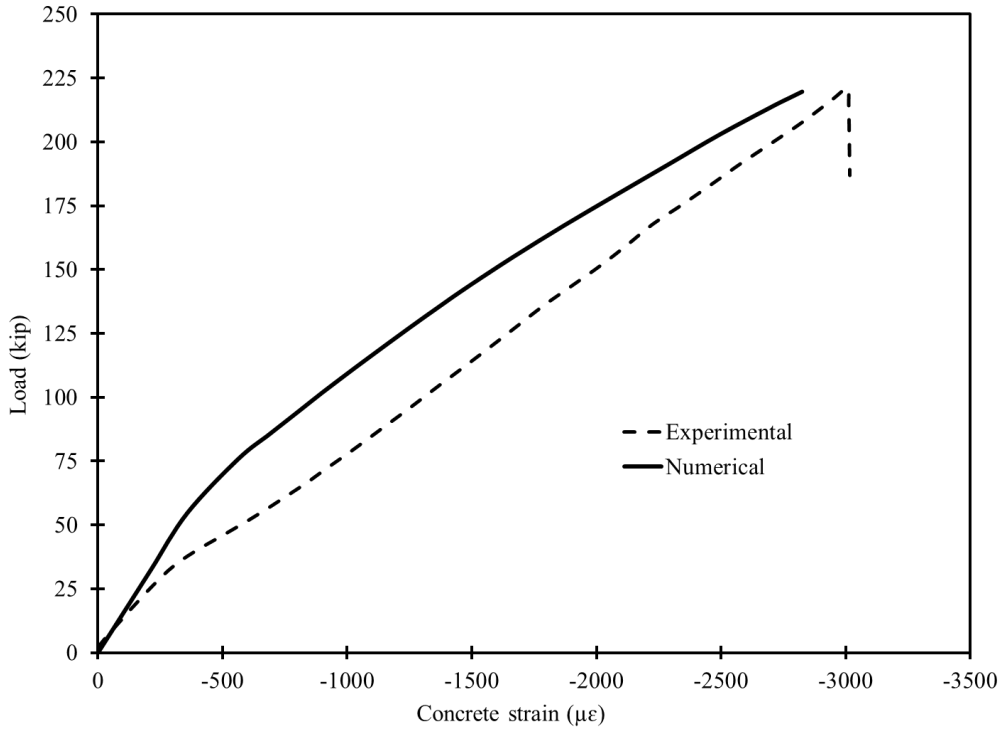

Figure 4.3-33 Numerical vs. experimental load-strain curves in concrete top surface of intermediate (loaded) beam in bridge model during ultimate load cycle

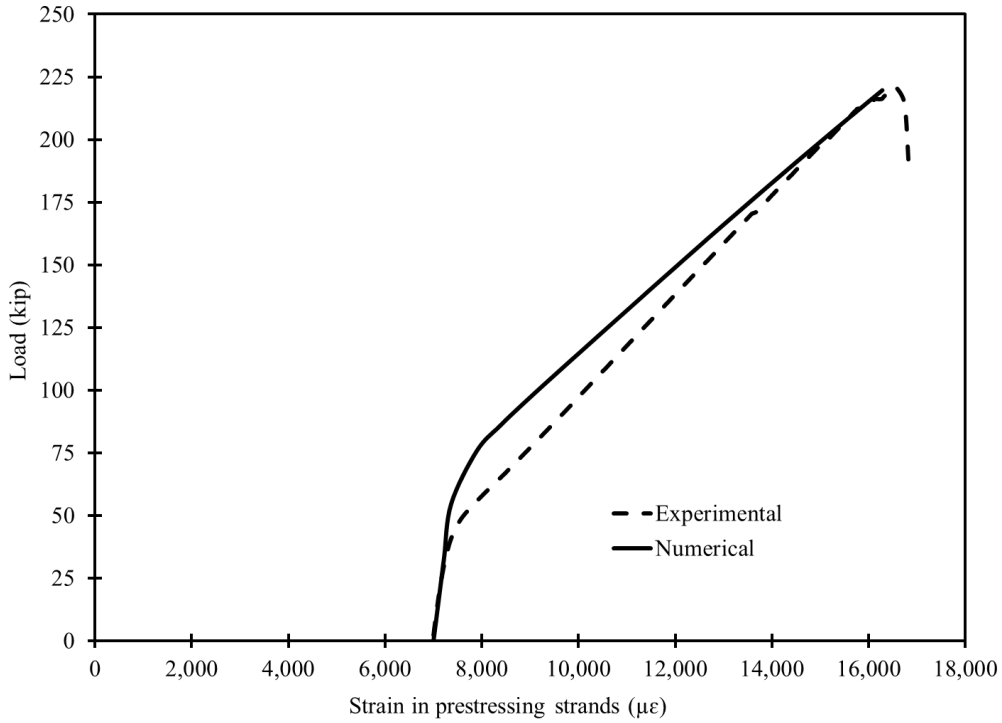

Figure 4.3-34 Numerical vs. experimental load-strain curves in prestressing strands of intermediate (loaded) beam in bridge model during ultimate load cycle

4.4 Parametric study

Through this parametric study, numerical models were generated for decked bulb T beam bridges with different spans and widths to evaluate the performance of the shear key joints and determine the need for a transverse post-tensioning system. The parametric study addressed bridges with spans of 50, 75, and 100 ft and deck widths of approximately 25, 52, and 78 ft. A general cross section for full-scale decked bulb T beam is shown in Figure 4.4-1, where the top flange width can range from 48 in. to 96 in. and the depth of the beam can range from 33 in. to 60 in. The top flange thickness is usually maintained at 9 in. and the bottom flange thickness is maintained at 8 in. with a bottom flange width of 36 in.

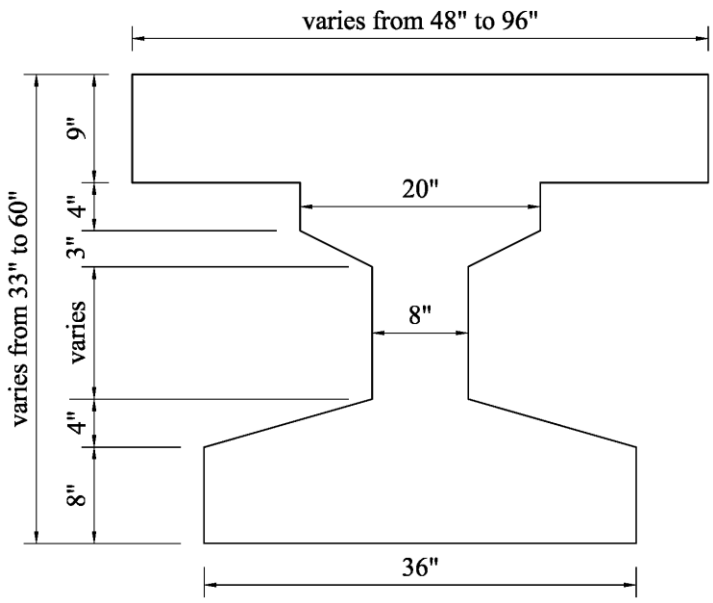

Figure 4.4-1 Typical cross section dimensions for full-scale decked bulb T beams

The choice of the cross section and the amount of reinforcement is dependent on both the span and the width of the bridge. To simplify the analysis and facilitate the choice of the appropriate cross section in the generated full-scale bridge models, a series of design charts were developed analytically to relate the span and flange width of the decked bulb T beam to the depth and the number of prestressing strands.

These design charts are developed based on the design HL-93 vehicular loading with impact allowance of 0.33 for CFCC prestressing strands with a diameter of 0.6 in, cross sectional area of 0.179 in.^{2}, guaranteed tensile strength of 339 ksi, initial prestressing force of 39.5 kip/strand (65% of guaranteed load), and average prestress loss of 15%. The 28-day concrete compressive strength was taken as 7,000 psi. It should be noted, however, that these charts are not a substitute for a detailed bridge design. Instead, they may serve as a rough estimate for the required depth of a decked bulb T beam and the required number of prestressing CFCC strands. The design charts are presented in Figure 4.4-2 through Figure 4.4-8 for decked bulb T beams with depths of 33, 36, 39, 42, 48, 54, and 60 in.

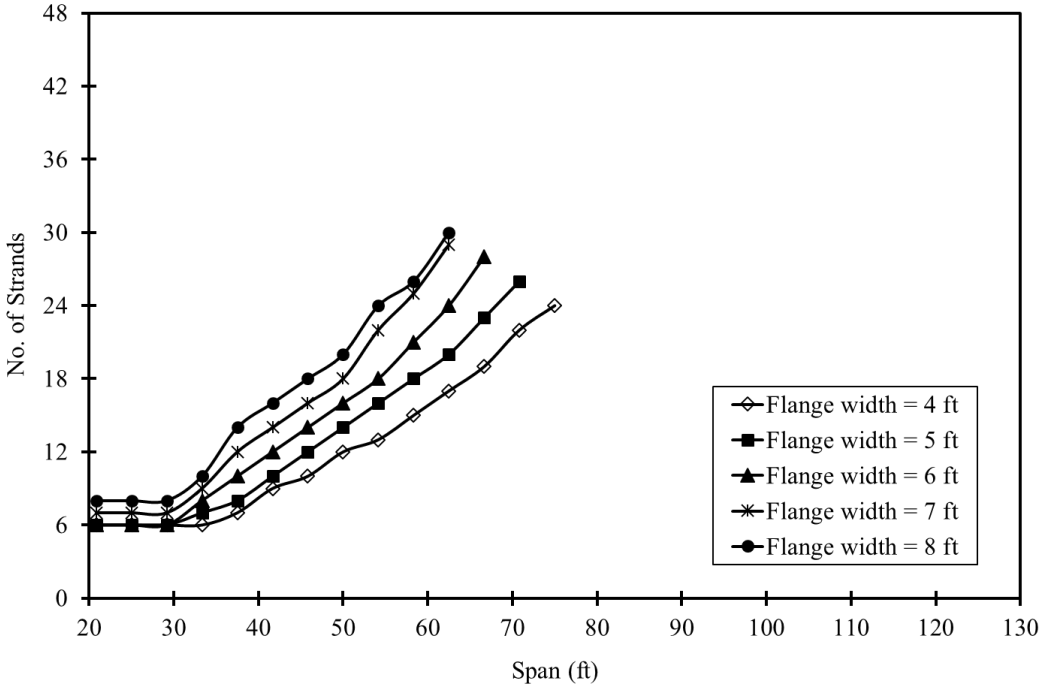

Figure 4.4-2 Design curves for 33-in.-deep decked bulb T beams

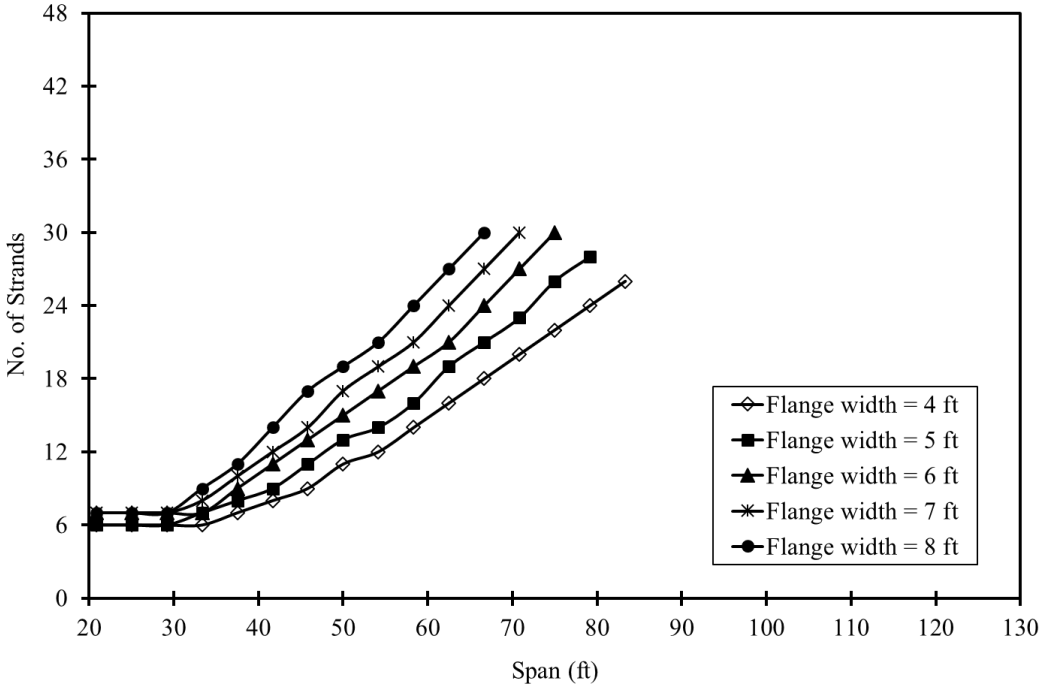

Figure 4.4-3 Design curves for 36-in.-deep decked bulb T beams

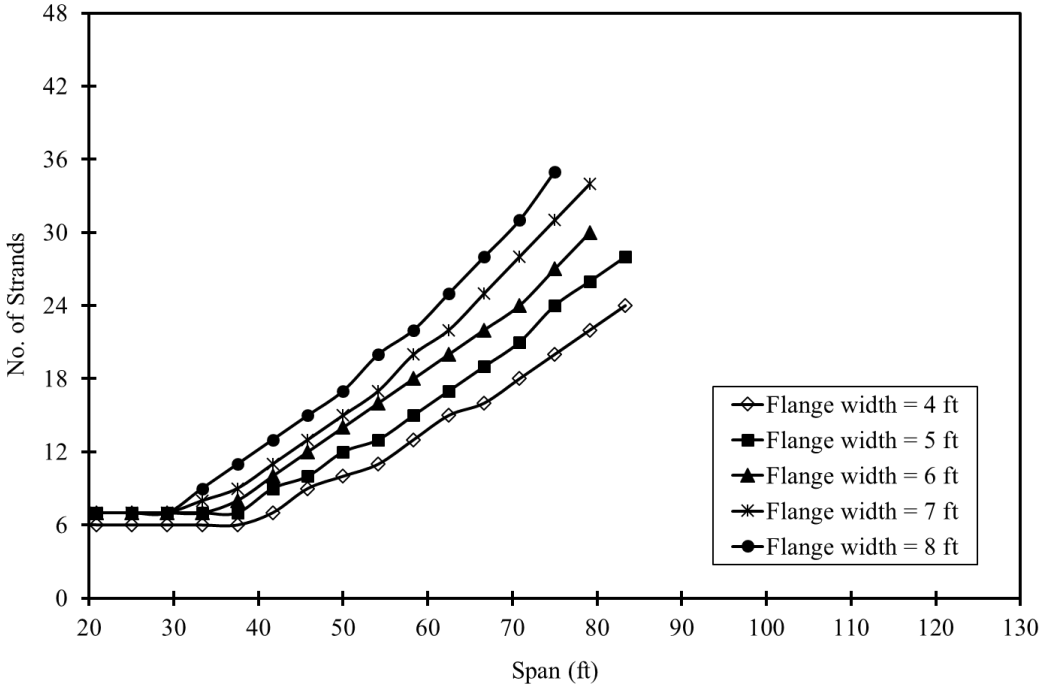

Figure 4.4-4 Design curves for 39-in.-deep decked bulb T beams

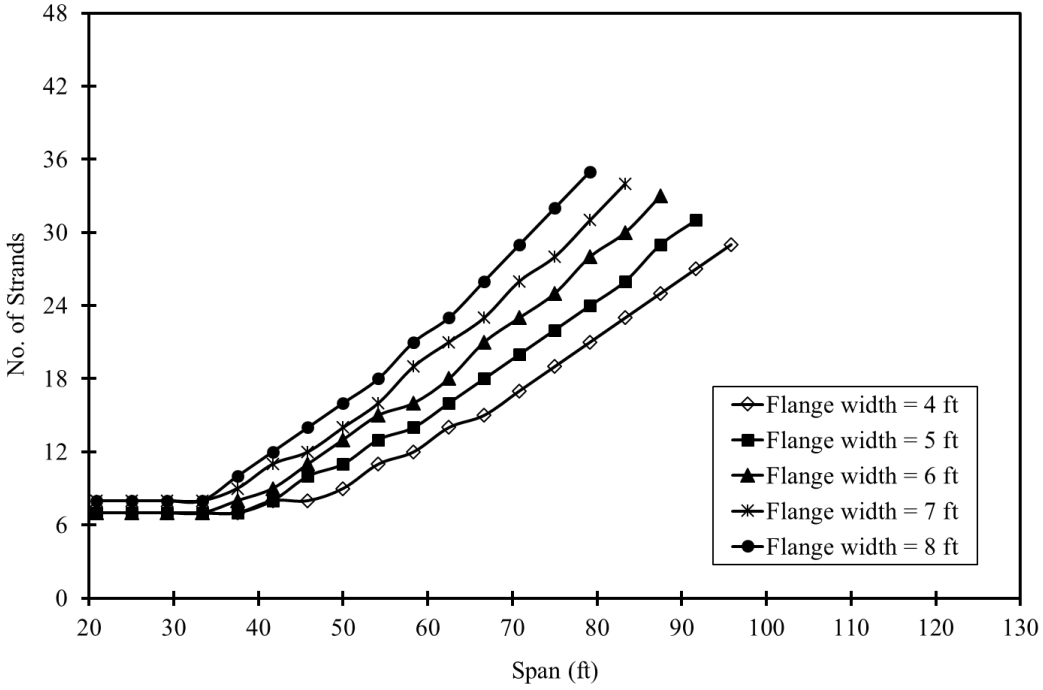

Figure 4.4-5 Design curves for 42-in.-deep decked bulb T beams

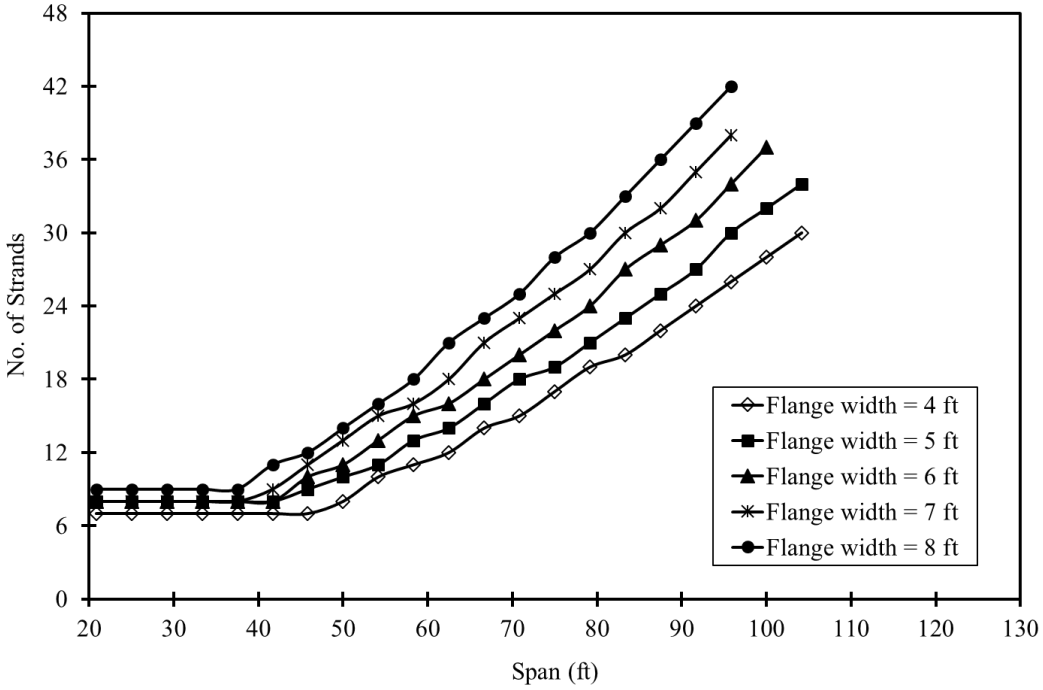

Figure 4.4-6 Design curves for 48-in.-deep decked bulb T beams

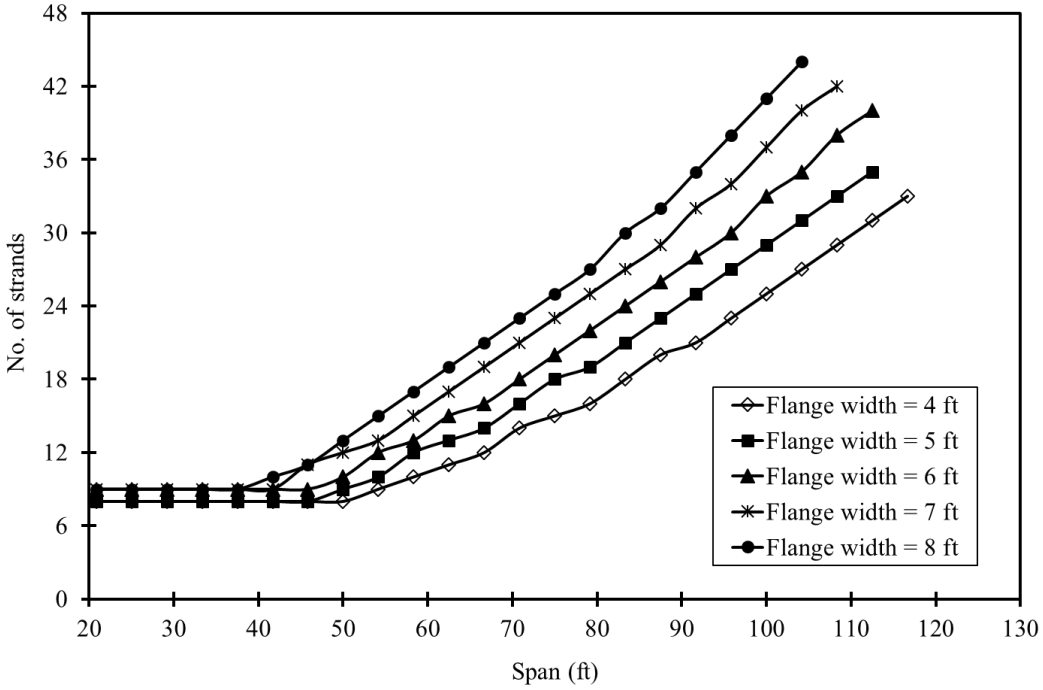

Figure 4.4-7 Design curves for 54-in.-deep decked bulb T beams

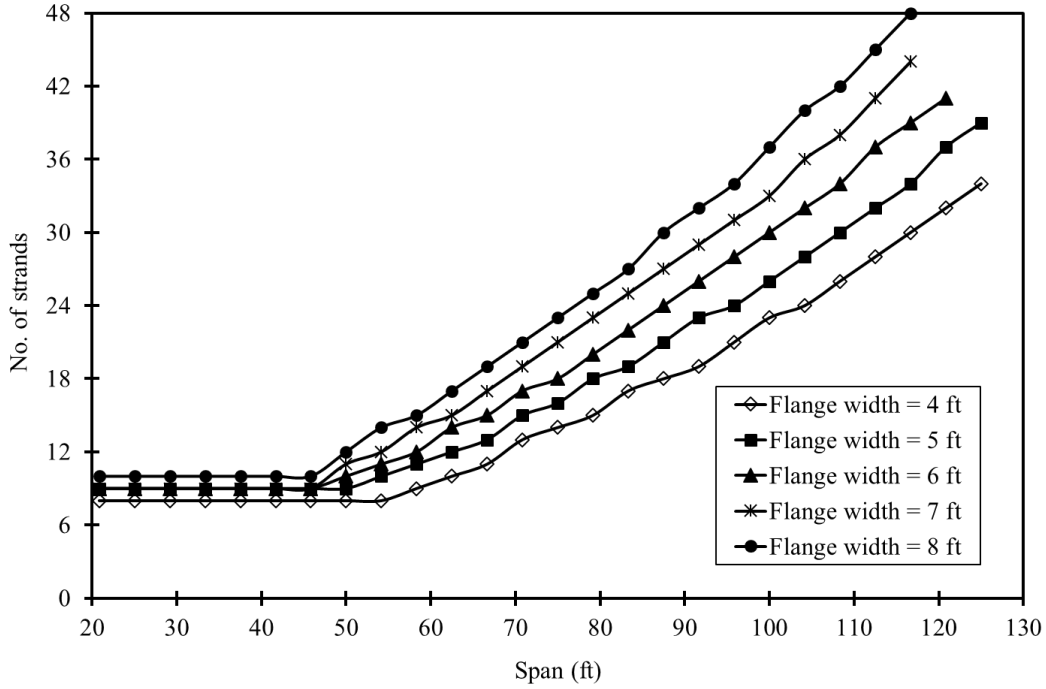

Figure 4.4-8 Design curves for 60-in.-deep decked bulb T beams

4.4.1 Loads and environmental conditions

The FEA bridge models in this parametric study were subjected to two groups of loads, construction loads and traffic loads in addition to a positive temperature gradient. Construction loads included the prestressing force, dead loads, transverse post-tensioning force, and superimposed dead loads, which included the self-weight of the parapet and the self-weight of a 2-in. wearing surface. The prestressing force and the self-weight of the beams were applied before adding the shear keys, and the diaphragms, to the bridge model. The self-weight of the shear keys and the superimposed dead loads were applied after integrating the shear keys to the bridge model. It should also be noted that the prestressing force was reduced from the initial prestressing value to the final prestressing value (85% of the initial value) after integrating the shear keys into the bridge models and before applying the superimposed dead loads.

The self-weight of the decked bulb T beams was calculated assuming a unit weight of 150 lb/ft^3 and was applied as a gravity load in the beams. The prestressing force was introduced as initial conditions in the prestressing strands with initial prestrssing force of 39.5 kip/strand and final prestressing force of 33.5 kip/strand. Superimposed dead loads included the weight of a

wearing surface (25 lb/ft^2) and the weight of the barriers. Barriers Type 4 with a weight of 475 lb/ft were provided at both sides of the bridge model.

Based on previous studies (Grace et al. 2008 and 2012), it was determined that shear key joints are most vulnerable to positive temperature gradient (+ve TG) and to a lesser extent the traffic loads. The worst situation, which usually results in shear key cracking is when positive temperature gradient is combined with traffic loads. Therefore, the application of the service loads in the current numerical investigation included applying positive temperature gradient followed by applying traffic loads. Both temperature gradient and traffic loads were taken according to AASHTO LRFD (2012) with the appropriate adjustment factors.

When exposed to sunlight during the daytime, the top fibers of the bridge experience higher temperatures than the bottom fibers, defined herein as positive gradient, and when the temperature drops down during the night in the winter, the top fibers experience lower temperatures than what the bottom fibers experience, defined herein as negative gradient. The variation of the temperature over the cross section of the bridge is usually highly nonlinear. For simplicity, AASHTO LRFD 3.12.3 provides a general bi-linear configuration for the positive temperature gradient, shown in Figure 4.4-9. The negative temperature gradient can be obtained from the same figure by multiplying the temperature values by -0.2 for decks with asphalt overlay and -0.3 for plain concrete.

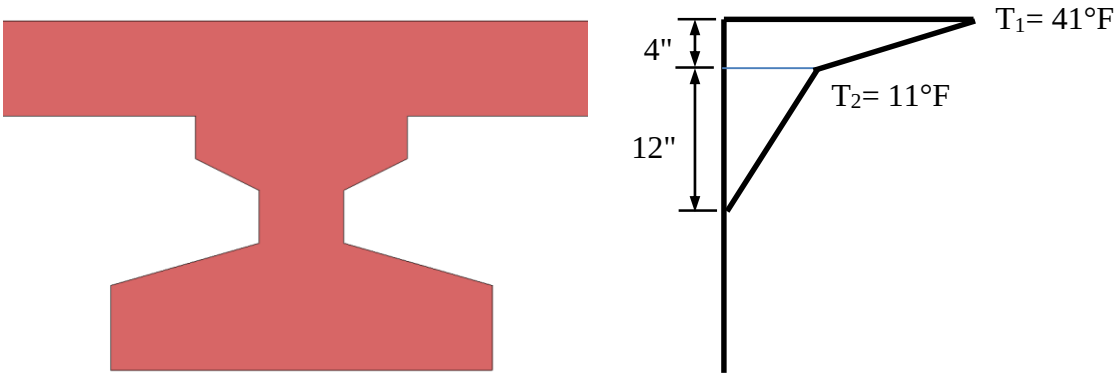

Figure 4.4-9 Positive temperature gradient (+ve TG) in MI according to AASHTO LRFD (2012)

Section 3.6.1.2 of AASHTO LRFD (2012) provides the common vehicular loading HL-93 (Figure 4.4-10), which consists of a combination of a design truck or tandem in addition to a design lane load. Each design lane under consideration shall be occupied by either a design truck or tandem, coincident with the lane load. The load shall be assumed to occupy 10.0 ft transversely within a design lane. Furthermore, the maximum live load effect shall be determined by considering each possible load combination of number of loaded lanes multiplied by the corresponding multiple presence factor as provided by Section 3.6.1.1.2 of AASHTO LRFD which account for the probability of simultaneous lane occupation by the HL-93 live load. The presence factors is highlighted in Table 4.4-1. Since the study accounts for the effect of positive temperature gradient and traffic load at the same time, a situation that may occur for a few hours during the day, it was not realistic to consider presence factor for average daily truck traffic (ADTT) more than 5,000. Instead, presence factors corresponding to ADTT between 100 and 1,000 were found appropriate for the current case of analysis.

To account for the dynamic effect of the moving loads, AASHTO LRFD 3.6.2 specifies a percentage of the static load of the truck or the tandem, but not the lane load, to be added to the original load as a dynamic allowance. The limit shall be taken as 75% for the purpose of designing the deck slab joints and 33% for designing other bridge components. It is not specified clearly in Section 3.6.2 whether 75% is applicable for the design of the transverse deck joints only or if it is applicable for the design of both transverse and longitudinal deck joints. In this numerical analysis, the impact allowance was taken equal to 75% based on the calibration of a full-scale bridge model (Grace et al. 2008).

The traffic load was positioned relative to the span of the bridge as to induce the maximum bending moment. In the transverse direction, the traffic load was positioned in three different locations named as Traffic Locations I, II, and III (TL#I, II, and III) as shown in Figure 4.4-11. In Traffic Location I, one lane (with a width of 10 ft) is occupied by the traffic load HL-93. This lane is the first lane immediately after the edge of parapet on either side of the bridge. In Traffic Location II, both side lanes of the bridge are occupied with traffic load HL-93 (each lane is loaded with HL-93 vehicular loading). In Traffic Location III, the two central lanes of the bridge are loaded with HL-93 vehicular loading. The central lanes are 10-ft-wide each measured from the mid-width of the bridge.

Table 4.4-1 Multiple presence factor, m, AASHTO LRFD 3.6.1.1.2 (2012)

Number of loaded lanes	Multiple presence factor (*m*)		
	ADTT[1] > 5000	100 ≤ ADTT ≤ 1000	ADTT < 100
1	1.20	1.14	1.08
2	1.00	0.95	0.90
3	0.85	0.81	0.73
> 3	0.65	0.62	0.59

1: Average Daily Truck Traffic

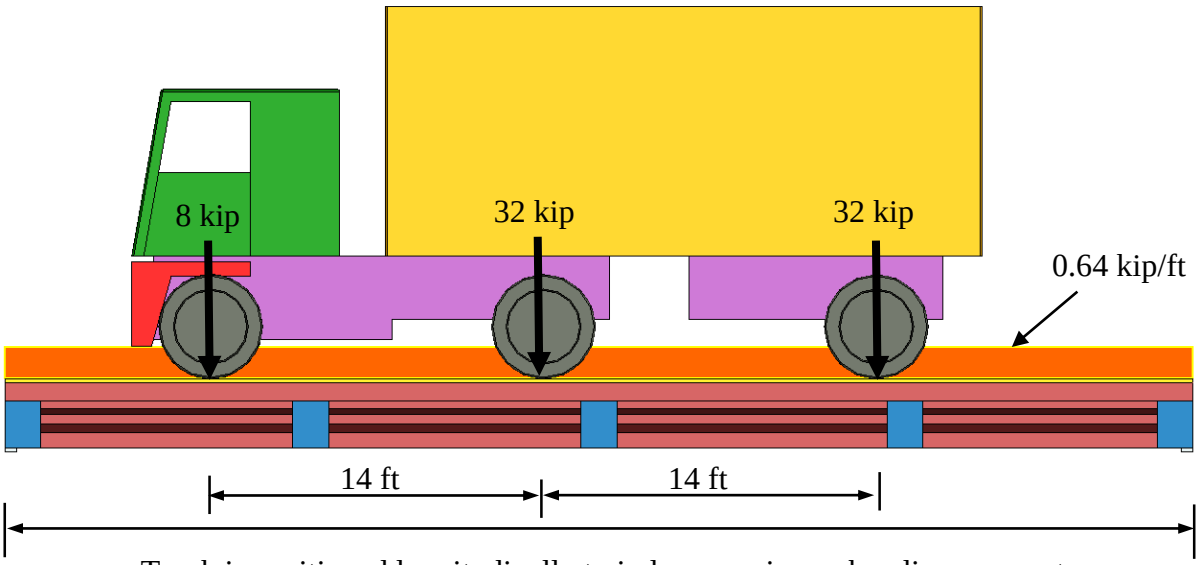

Truck is positioned longitudinally to induce maximum bending moment

Figure 4.4-10 AASHTO LRFD HL-93 vehicular loading

Traffic Location I
(TL#I)

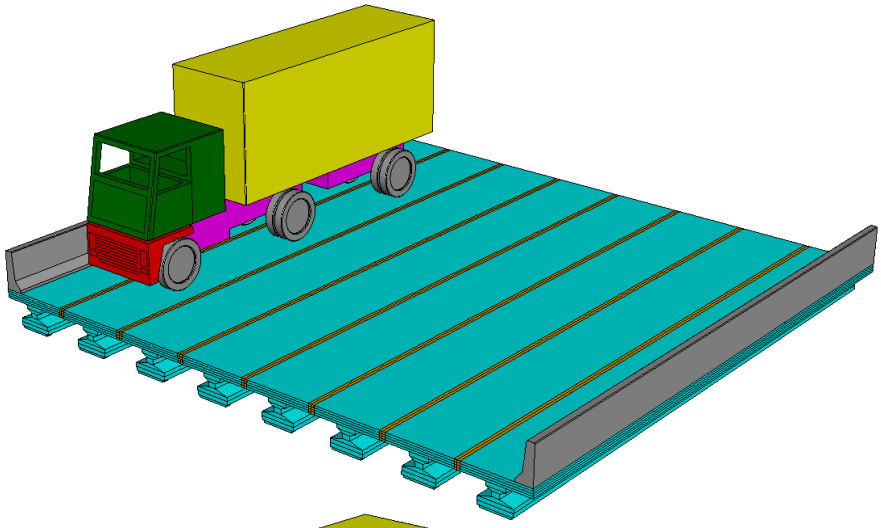

Traffic Location II
(TL#II)

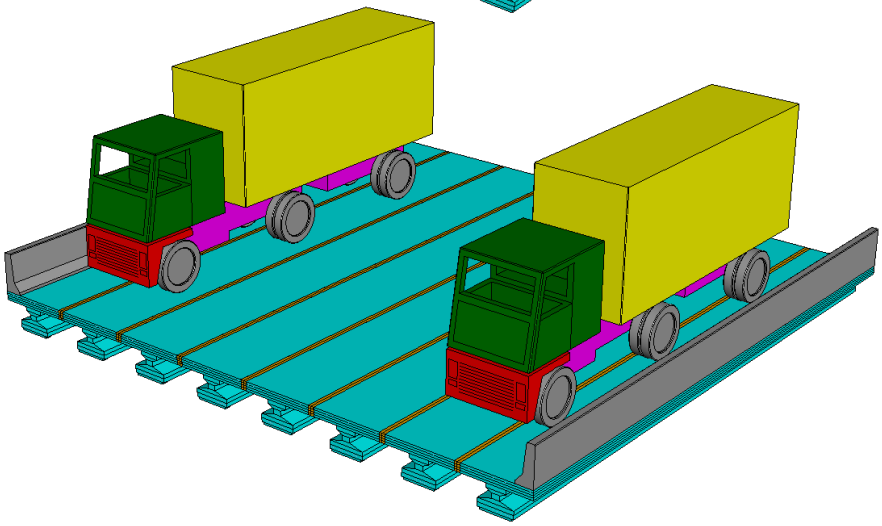

Traffic Location III
(TL#III)

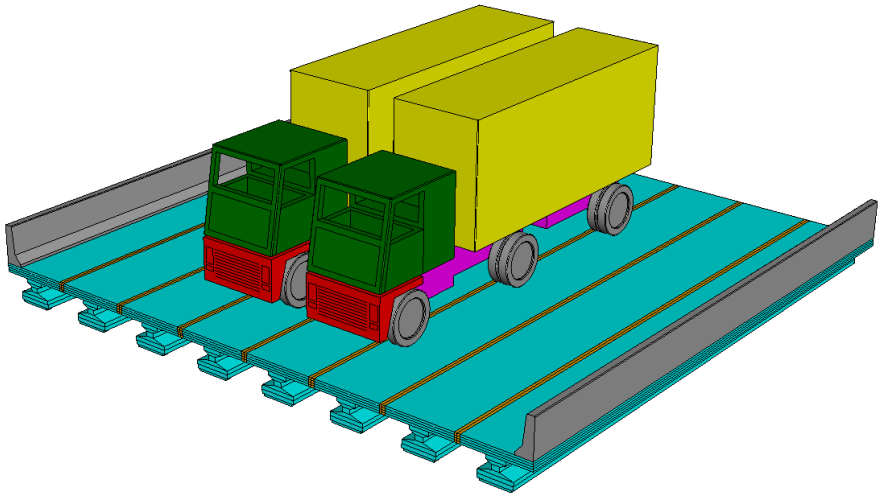

Figure 4.4-11 Truck locations across the width of the bridge models

4.4.2 Layout of parametric study

The main study was developed for decked bulb T beams with a flange width of 72 in. Later on, key models were generated for decked bulb T beams with flange widths of 48 in. and 96 in. to verify the results. The cross section dimensions and number of prestressing strands for the numerical models were selected based on the design graphs provided early in this section.

The general layout of the parametric study is presented in Figure 4.4-12. The steps of the analysis can be summarized as follows:

1. Decked bulb T beam bridge models with different span and widths were generated.
2. The bridge models were analyzed with no transverse diaphragms under positive temperature gradient and AASHTO LRFD vehicular loading with appropriate impact and presence allowances.
3. The models were checked for shear key cracks. When cracks were observed in the bridge model, the analysis was repeated with transverse diaphragms. The number of transverse diaphragms ranged from two, at the ends of the span, to five equally spaced diaphragms along the span.
4. This stage of analysis was performed for bridge models with:
    - Spans of 50, 75, and 100 ft.
    - Widths of 25, 52, and 78 ft.
    - Skew angles of 0, 30, 45, and 60°
5. When cracks persisted even with the increased number of diaphragm, TPT force was applied through the transverse diaphragms. The TPT force ranged from 50 to 200 kip/diaphragm.
6. The analysis ended when the bridge model was able to sustain the positive temperature gradient and the traffic loads with no shear key cracks.
7. Bridge models that exhibited shear key cracks even with using practical number of diaphragms and TPT force were labeled to avoid when using decked bulb T beam bridge system.

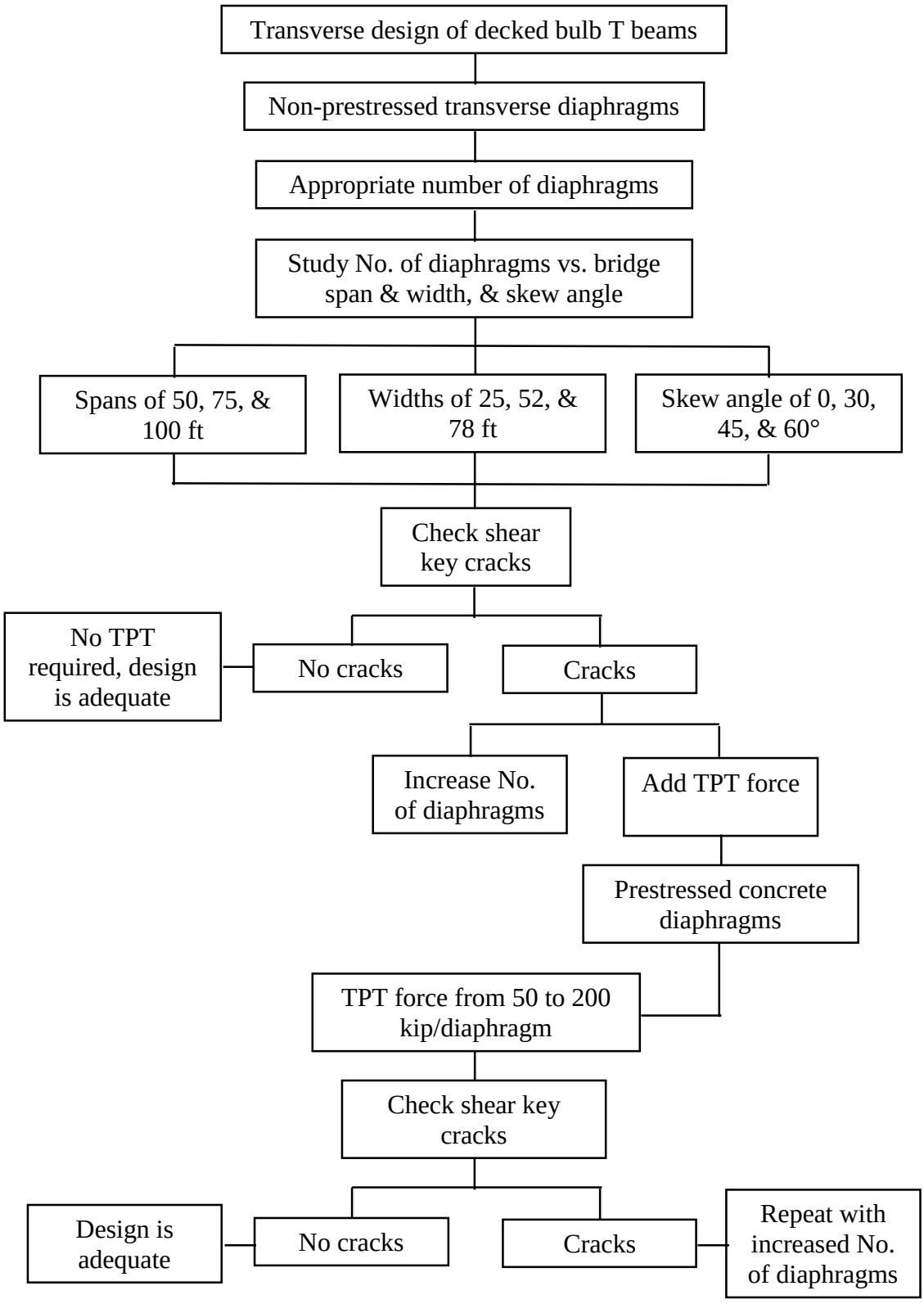

Figure 4.4-12 Flowchart of conducted parametric study

4.4.3 Configuration of numerical models

The numerical investigation included bridge models with spans of 50, 75, and 100 ft and widths of 25.5, 51.5, and 77.6 ft as shown in Figure 4.4-13. Since the main investigation was performed on decked bulb T beam with a flange width of 6 ft, bridge models with a deck width of 25.5 ft were assembled of four beams with three 6-in.-wide shear key joints. Bridge models with a deck width of 51.5 ft were assembled from eight beams with seven shear key joints and bridge models with a width of 77.5 ft were assembled from twelve beams and eleven shear key joints.

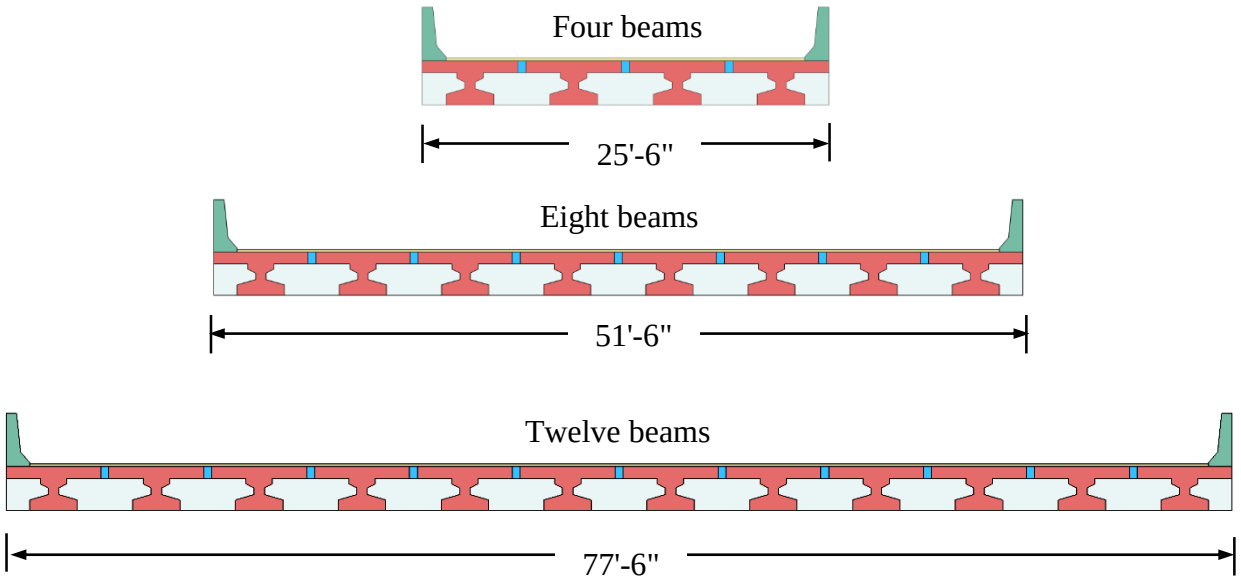

Figure 4.4-13 Widths of bridge models considered in the investigation

The cross section of the decked bulb T beam was dependent on the span. For bridge models with a span of 50 ft, 33-in-deep decked bulb T beams with 17 CFCC strands (diameter of 0.6 in.) were used through the analysis. For bridge models with a span of 75 ft, the depth of the decked bulb T beam was increased to 42 in. and the prestressing strands increased to 26 strands. Finally, for bridge models with a span of 100 ft, 54-in-deep decked bulb T beams with 34 prestressing CFCC strands were used in the analysis. The dimensions and reinforcement for the selected cross sections are shown in Figure 4.4-14.

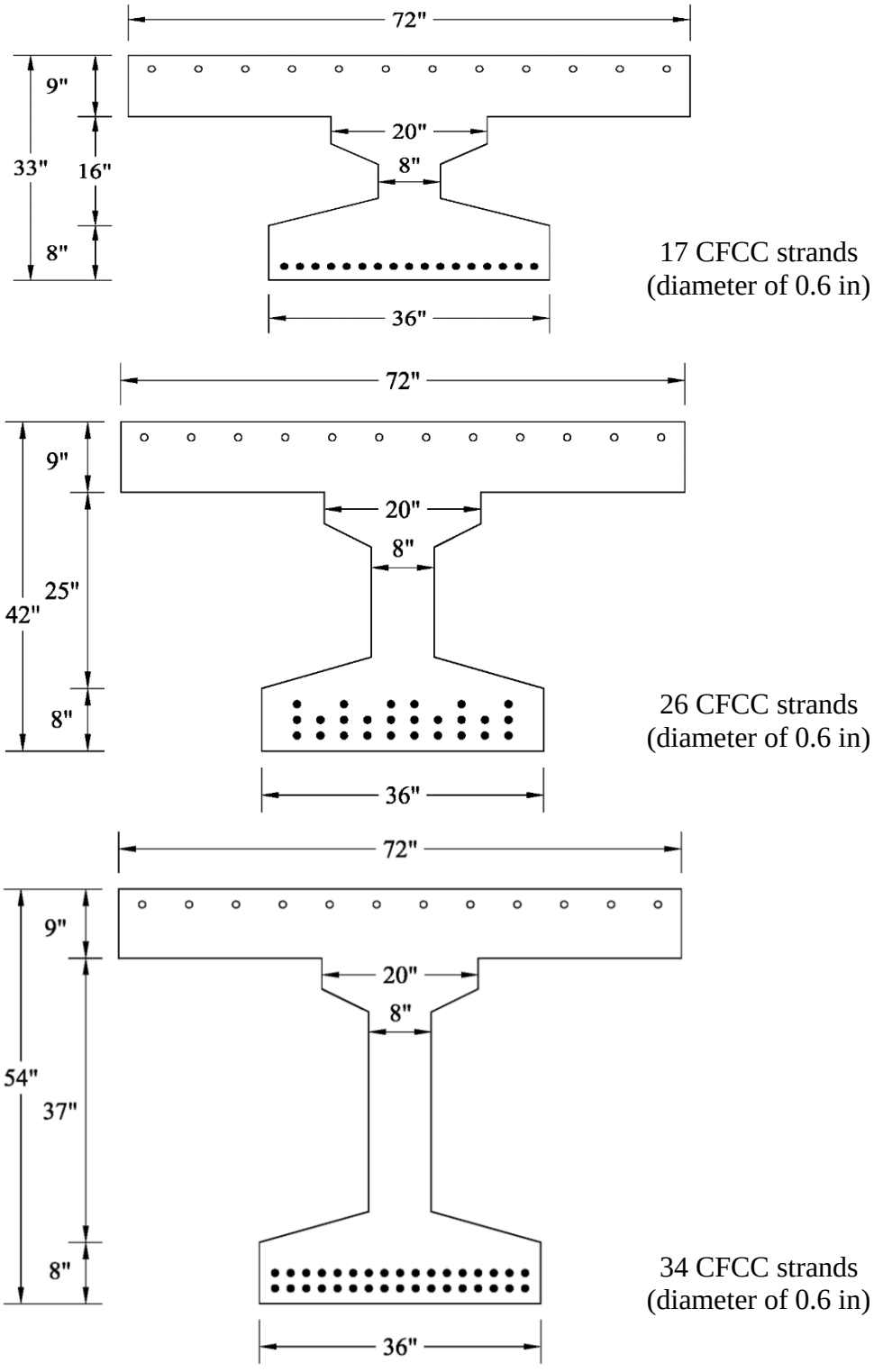

Figure 4.4-14 Configuration of cross sections used in main numerical investigation

4.4.4 Effect of number of diaphragms

The first step of the numerical analysis was to determine the appropriate number of diaphragms. All the numerical models were analyzed with:

1. No transverse diaphragms,
2. Two diaphragms at the ends,
3. Two diaphragms at the ends and one intermediate diaphragm at the mid-span
4. Five equally spaced diaphragms along the span

The general procedure for analysis and applying the loads consisted of five phases:

- Phase I included applying the self-weight of the beams and the prestressing force simultaneously. The self-weight of the beams and the prestressing force were applied to the individual beams as the shear key joints were not introduced into the model in this phase.
- The shear key joints and the joints between transverse diaphragms were integrated into the model through Phase II of analysis.
- Phase III of the analysis included applying the superimposed dead loads, the self-weight of the barriers and the weight of the wearing surface.
- Phase IV of the analysis included applying the positive temperature gradient.
- Phase V included applying the traffic loads in either Location I, II, or III.

4.4.4.1 Results of numerical models with a span of 50 ft

The maximum recorded principal, longitudinal, and transverse stresses in the deck flanges of bridge models with a span of 50 ft are shown in Table 4.4-2, Table 4.4-3, and Table 4.4-4, respectively. It should be noted that these stresses do not necessarily develop at the same location. As shown in the tables, the deck flange experiences tensile stresses during prestressing. With the current prestressing level, the longitudinal tensile stresses was approximately 392 psi and are developed near the ends of the beams. These longitudinal tensile stresses caused the maximum principal stresses at that location to reach 392 psi. There are also mild transverse tensile stresses of 125 psi due to prestressing. These transverse stresses are developed at the junction between the

web and the flange at the ends of the beams. They are not developed at the same location of the maximum longitudinal stresses of 392 psi.

Adding SIDL (self-weight of parapets and wearing service) slightly reduces the longitudinal tensile stresses and increases the transverse tensile stresses. The overall change in the maximum principal stresses does not exceed 20 psi.

A significant change in the map of stress distribution occurs when positive temperature gradient is applied to the bridge model. Concrete is considered a good thermal insulator and therefore, as the temperature of the top deck is elevated during the day, the temperature of the bottom of the deck remains substantially low. According to AASHTO LRFD (2012), this difference in temperature through the depth of the deck flange can reach 35 °F. The expansion of the top surface due to heating generates compressive stresses in the top fibers and tensile stresses in the bottom fibers of the deck flange.

Applying positive temperature gradient increased or decreased the maximum principal stresses as shown in the Table 4.4-2. A clear relationship cannot be established from the maximum principal stresses as the location of the maximum stresses changes with applying the positive temperature gradient. However, by examining the longitudinal and transverse stresses, it can be determined that applying positive temperature gradient resulted in reduction in the longitudinal tensile stresses but a significant increase in the transverse tensile stresses. The increase in transverse stresses is maximized in the case of no transverse diaphragms and decreases with the increase in the number of diaphragms. The same trend is noticed in bridge models with different widths.

The maximum transverse stresses due to positive temperature gradient are developed near the ends of the beams. Therefore, adding two end diaphragms seems to have the maximum influence on reducing the transverse stresses under positive temperature gradient. Adding intermediate diaphragms does not seem to have the same transverse stress reduction influence as that of the end diaphragms as shown in Figure 4.4-15.

The addition of traffic load at select locations seems to further increase the maximum principal stresses and the transverse tensile stresses in the deck flange. For instance, adding the traffic load in Location I in bridges with no transverse diaphragms results in cracking the deck flange (Figure

4.4-16). The cracks appeared in all bridge models regardless of the deck width. The cracks developed at the ends of the beams at the locations that showed high transverse tensile stresses under positive temperature gradient.

Adding end diaphragms to the bridge model eliminated the cracks at the ends of the beams and reduced the maximum principal stresses and the tensile transverse stresses in the deck. Intermediate diaphragms, while slightly reducing the tensile stress, did not seem to greatly influence the stress values in case of traffic loads at Location I.

The same trend was also noticed when adding traffic load in Location II. Cracks developed at the ends of the beams where there was no transverse diaphragms (Figure 4.4-17). After adding the end diaphragms, the maximum principal stresses and the transverse stresses in the deck reduced and the cracks were eliminated at the ends of the beams. Adding intermediate diaphragms did not seem to have a significant influence on the stress level under this loading case even though bridge models with five transverse diaphragms consistently exhibited slightly lesser tensile stresses than those observed in bridge models with two or three transverse diaphragms.

Unlike Locations I and II, traffic loads positioned in Location III showed a direct relationship to the number of intermediate diaphragms with no relationship to the end diaphragms. In case of bridge models with no diaphragms or with diaphragms at the ends only, the models with traffic loads at Location III always exhibited cracks at the mid-span of the bridge (Figure 4.4-18). When an intermediate diaphragm is added, the shear key cracks were eliminated but the transverse stresses and the corresponding maximum principal stresses remained critical. Increasing the number of diaphragms from three to five significantly reduced the transverse stresses by approximately 148 psi and 208 psi in case of bridge models with deck widths of 52.5 ft and 77.5 ft, respectively.

Table 4.4-2 Maximum principal stresses in deck flange for bridges with a span of 50 ft

Span (ft)	Width (ft)	No. Diaph.	Maximum principal stresses in deck (psi)					
			Prestress	SIDL	+ve TG	TL#I	TL#II	TL#III
50	25.5	0	392	379	569	crack	-	-
	25.5	2		386	356	482	-	-
	25.5	3		377	346	421	-	-
	25.5	5		374	332	395	-	-
	51.5	0		396	527	crack	crack	crack
	51.5	2		401	365	425	443	crack
	51.5	3		393	365	417	438	430
	51.5	5		388	347	416	407	309
	77.5	0		405	527	crack	crack	crack
	77.5	2		410	384	475	485	crack
	77.5	3		403	386	476	488	502
	77.5	5		399	353	431	441	322

Table 4.4-3 Longitudinal stresses in deck flange for bridges with a span of 50 ft

Span (ft)	Width (ft)	No. Diaph.	Longitudinal stresses in deck (psi)					
			Prestress	SIDL	+ve TG	TL#I	TL#II	TL#III
50	25.5	0	392	375	277	crack	-	-
	25.5	2		382	278	294	-	-
	25.5	3		375	268	283	-	-
	25.5	5		373	266	274	-	-
	51.5	0		393	288	crack	crack	crack
	51.5	2		397	292	315	305	crack
	51.5	3		391	294	314	300	242
	51.5	5		387	293	310	296	247
	77.5	0		403	293	crack	crack	crack
	77.5	2		407	301	314	325	crack
	77.5	3		401	302	311	323	267
	77.5	5		398	302	309	321	267

Table 4.4-4 Transverse stresses in deck flange for bridges with a span of 50 ft

Span (ft)	Width (ft)	No. Diaph.	Transverse stresses in deck (psi)					
			Prestress	SIDL	+ve TG	TL#I	TL#II	TL#III
50	25.5	0	125	153	565	crack	-	-
	25.5	2		144	337	406	-	-
	25.5	3		135	306	357	-	-
	25.5	5		129	288	339	-	-
	51.5	0		162	521	crack	crack	crack
	51.5	2		146	365	396	436	crack
	51.5	3		139	354	389	432	430
	51.5	5		137	334	389	399	282
	77.5	0		165	522	crack	crack	crack
	77.5	2		147	374	472	480	crack
	77.5	3		140	377	473	484	502
	77.5	5		138	342	427	435	294

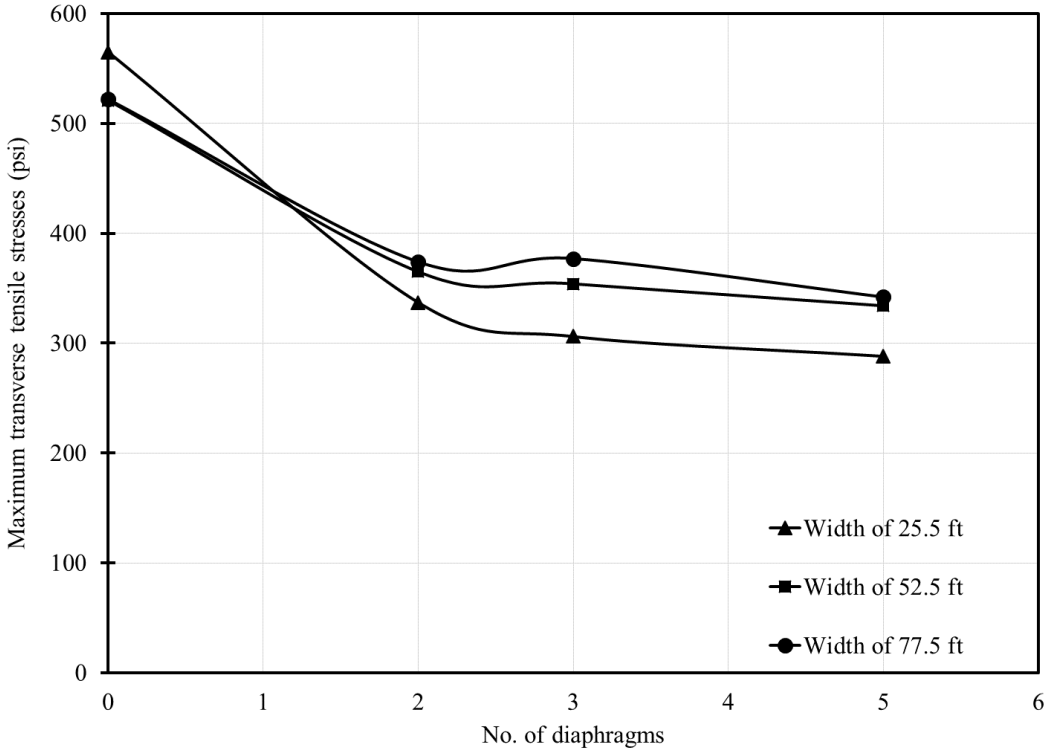

Figure 4.4-15 Effect of increasing number of diaphragms on transverse stresses under positive temperature gradient in bridges with a span of 50 ft

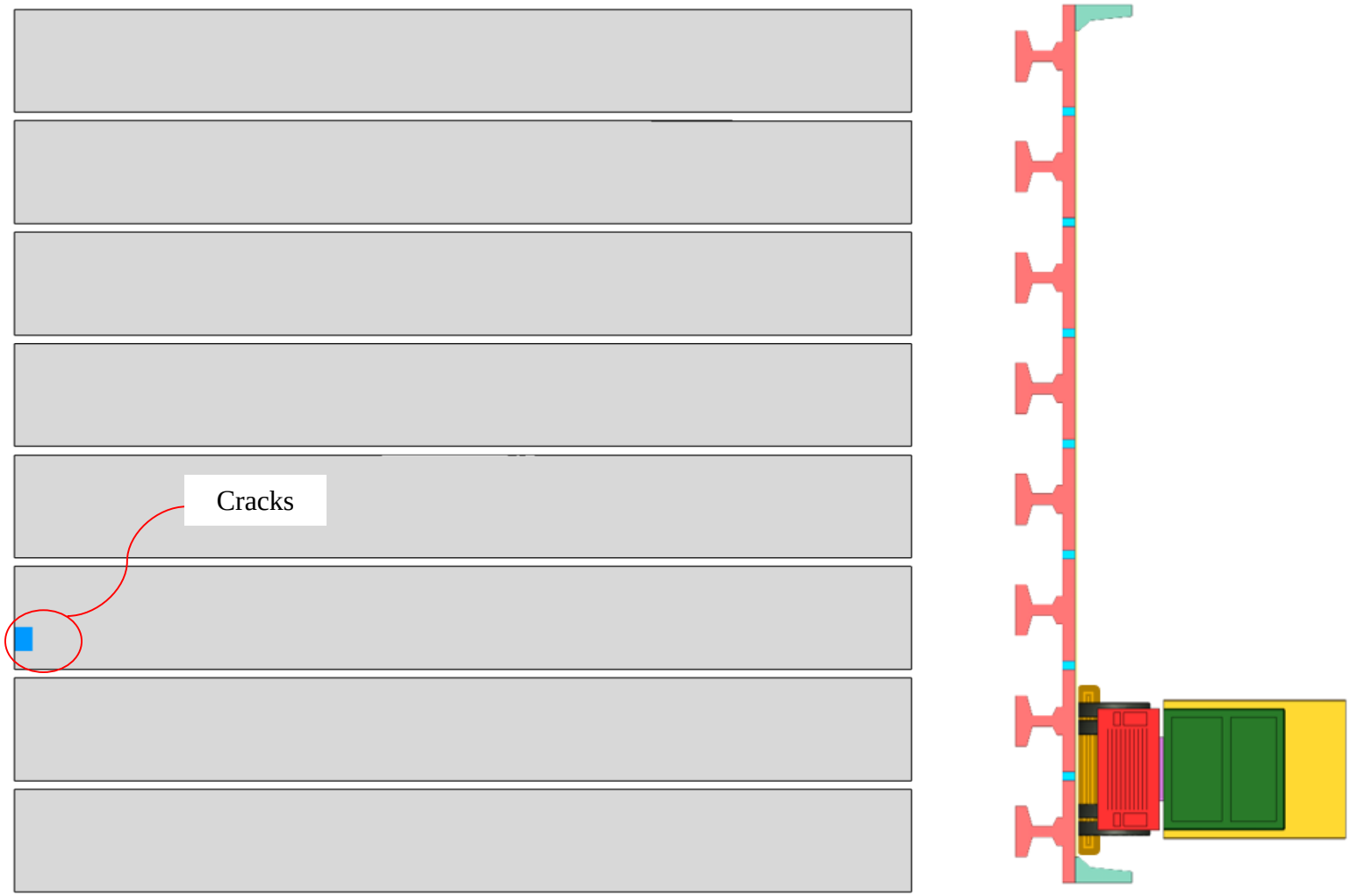

Figure 4.4-16 Typical crack pattern under traffic loads in Location I (Bridge span of 50 ft, width of 52.5 ft, no diaphragms)

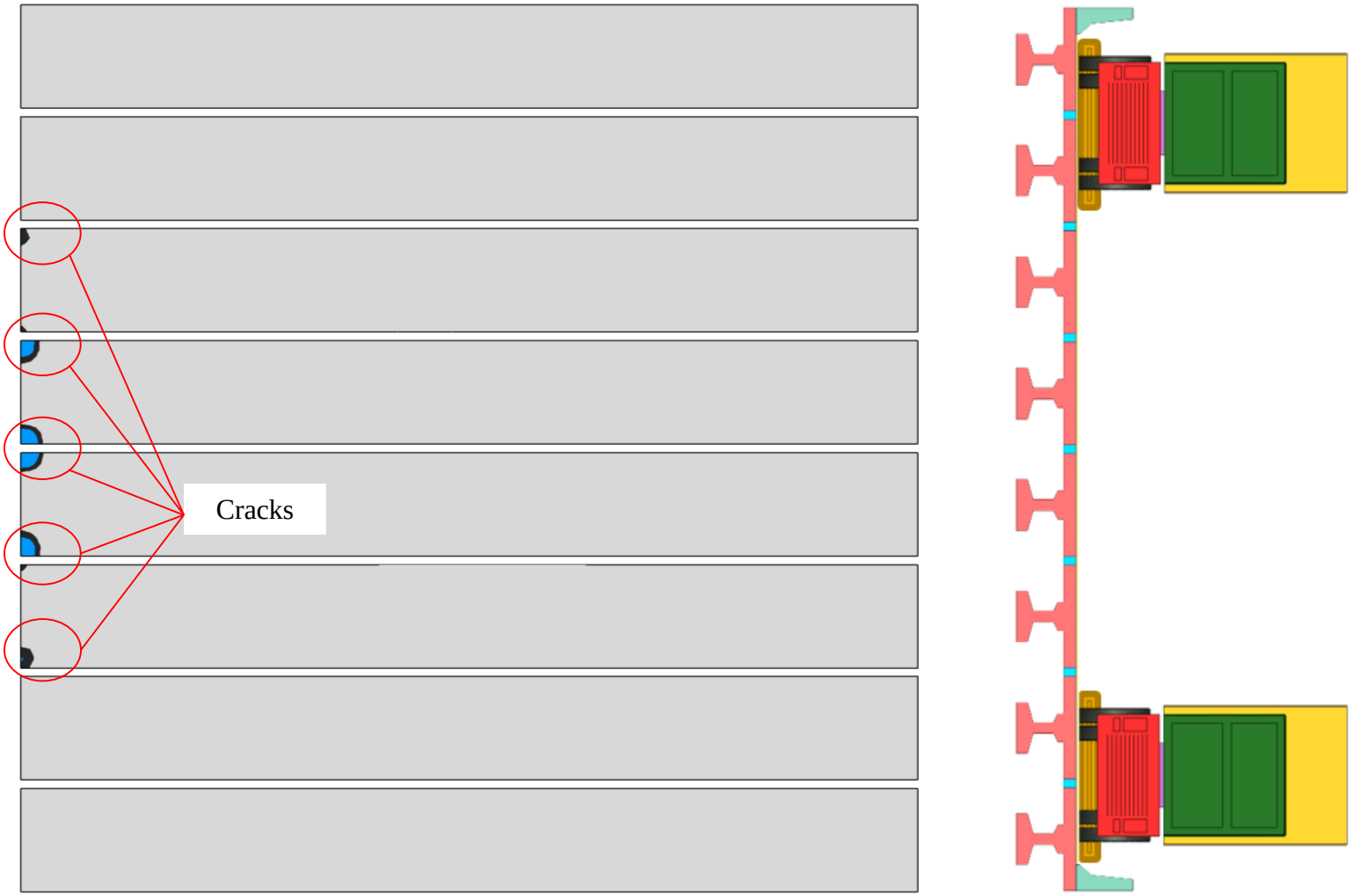

Figure 4.4-17 Typical crack pattern under traffic loads in Location II (Bridge span of 50 ft, width of 52.5 ft, no diaphragms)

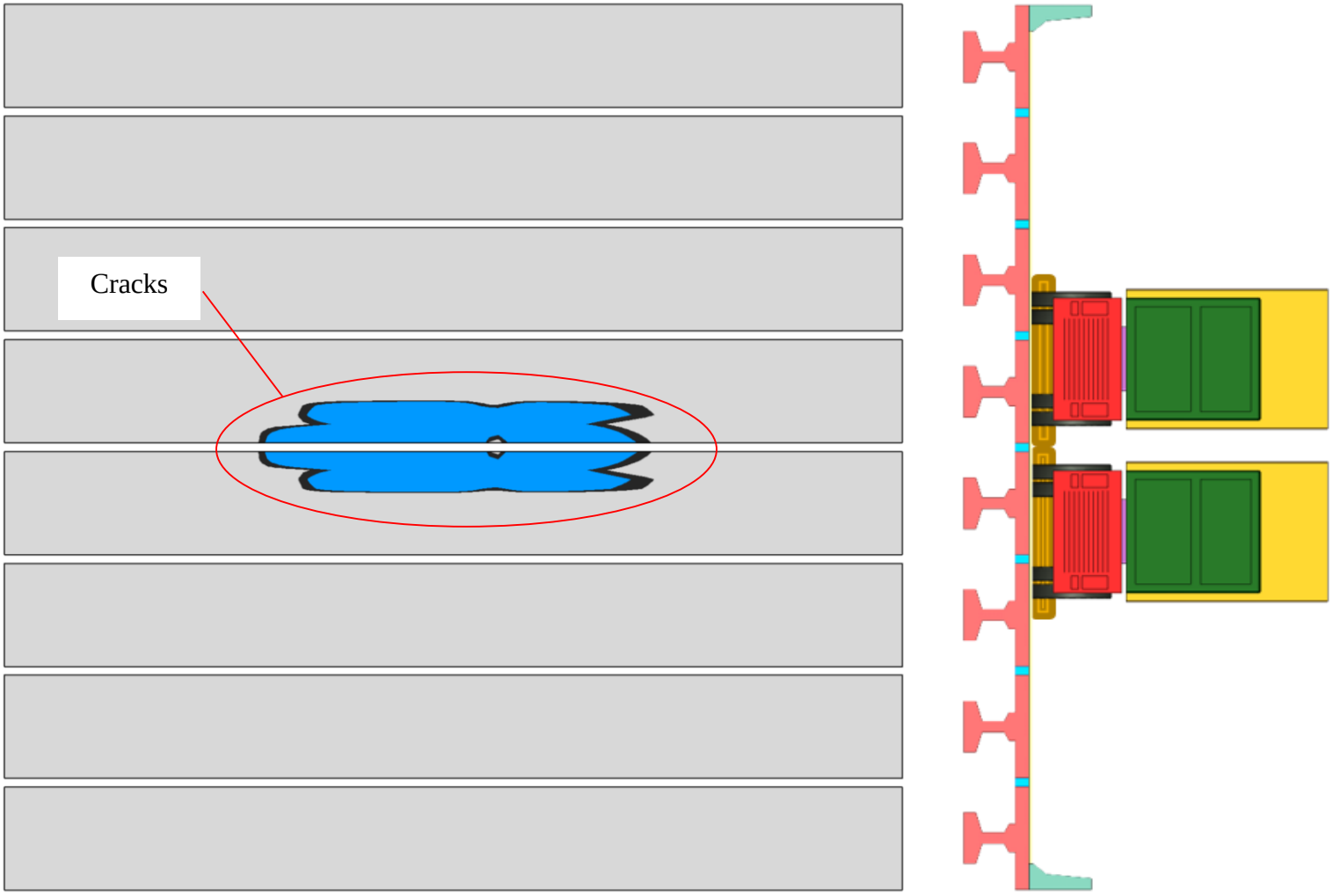

Figure 4.4-18 Typical crack pattern under traffic loads at Location III (Bridge span of 50 ft, width of 52.5 ft, no diaphragms)

4.4.4.2 Results of numerical models with a span of 75 ft

The maximum principal stresses, longitudinal stresses, and transverse stresses in the deck flanges of bridge models with a span of 70 ft are shown in Table 4.4-5, Table 4.4-6, and Table 4.4-7. The relationship between the number of diaphragms and both the span and width of the bridge models was similar to that observed in bridge models with a span of 50 ft. The case of no transverse diaphragms always yielded deck cracking regardless of the width of the bridge model. Adding two end diaphragms seemed to reduce the transverse tensile stresses under positive temperature gradient and under traffic loads in Locations I and II. However, it did not mitigate the crack development when the traffic loads were positioned in Location III. The deck cracking due to traffic loads at Location III was mitigated after adding intermediate diaphragms. In bridge models with widths of 25.5 ft and 51.5 ft, an intermediate diaphragm in addition to the two end diaphragms were sufficient to prevent deck cracking. However, in case of bridge models with a width of 77.5 ft, it was mandatory to provide five transverse diaphragms to eliminate the cracks.

It should be noted that in the case of bridge models with a span of 75 ft and a deck width of 77.5 ft, the size of the analysis file was too large to be processed. Therefore, only half of the model was analyzed and symmetry conditions were assumed along the longitudinal axis of the bridge model. Because of the symmetry, applying the traffic loads in Location I was not feasible and only the cases of traffic loads in Locations II and III were analyzed.

The concentration of the stresses took the same pattern observed in bridge models with a span of 50 ft. The superimposed dead loads did not significantly increase or decrease the stresses in the different directions. However, positive temperature gradient caused a dramatic increase in the transverse stresses and consequently the principal stresses. The increase in the stresses was relatively localized near the ends of the beams. By adding the end diaphragms, the transverse stresses were reduced and the maximum values shifted towards the mid-span.

The addition of the traffic loads in Locations I and II seemed to overstress the region with already high transverse tensile stresses due to positive temperature gradient. However, transverse stresses due to traffic loads in Location III took a different pattern and accumulated at the mid-span rather than the ends of the beams. The region of the mid-span suffered from moderate increase in tensile transverse stresses during the application of positive temperature gradient.

Table 4.4-5 Maximum principal stresses in deck flange for bridges with a span of 75 ft

Span (ft)	Width (ft)	No. Diaph.	Maximum principal stresses in deck (psi)					
			Prestress	SIDL	+ve TG	TL#I	TL#II	TL#III
75	25.5	0	357	361	592	crack	-	-
	25.5	2		360	339	381		
	25.5	3		351	329	363	-	-
	25.5	5		346	325	369	-	-
	51.5	0		383	549	crack	crack	crack
	51.5	2		383	371	433	408	crack
	51.5	3		367	365	399	361	457
	51.5	5		360	348	384	352	357
	77.5	0		360	590	-	crack	crack
	77.5	2		385	378	-	crack	crack
	77.5	3		373	369	-	crack	crack
	77.5	5		366	351	-	469	358

Table 4.4-6 Longitudinal stresses in deck flange for bridges with a span of 75 ft

Span (ft)	Width (ft)	No. Diaph.	Longitudinal stresses in deck (psi)					
			Prestress	SIDL	+ve TG	TL#I	TL#II	TL#III
75	25.5	0	357	358	258	crack	-	-
	25.5	2		356	253	290	-	-
	25.5	3		349	235	271	-	-
	25.5	5		346	229	255	-	-
	51.5	0		379	279	crack	crack	crack
	51.5	2		377	281	330	306	crack
	51.5	3		364	272	309	276	230
	51.5	5		358	269	298	266	235
	77.5	0		358	268	-	crack	crack
	77.5	2		378	277	-	crack	crack
	77.5	3		369	274	-	crack	crack
	77.5	5		364	274	-	296	237

Table 4.4-7 Transverse stresses in deck flange for bridges with a span of 75 ft

Span (ft)	Width (ft)	No. Diaph.	Transverse stresses in deck (psi)					
			Prestress	SIDL	+ve TG	TL#I	TL#II	TL#III
75	25.5	0	110	144	592	crack	-	-
	25.5	2		121	280	336	-	-
	25.5	3		117	317	359	-	-
	25.5	5		113	320	348	-	-
	51.5	0		156	547	crack	crack	crack
	51.5	2		133	367	372	337	crack
	51.5	3		124	322	345	306	457
	51.5	5		118	314	343	327	355
	77.5	0		150	590	-	crack	crack
	77.5	2		130	376	-	crack	crack
	77.5	3		126	358	-	crack	crack
	77.5	5		124	347	-	467	356

4.4.4.3 Results of numerical models with a span of 100 ft

The stresses in bridge models with a span of 100 ft followed the same trend observed in models with spans of 50 and 75 ft with the exception that the stresses were slightly higher. Deck cracking was seen as early as when positive temperature gradient was applied. This indicates that tensile stresses in the deck increases with increasing bridge span. However, five diaphragms were sufficient to mitigate the deck cracking in all bridge models with a span of 100 ft as shown in Table 4.4-8, Table 4.4-9, and Table 4.4-10. Bridge models with a span of 100 ft and a width of 51.5 ft or 77.5 ft were not analyzed with traffic loads at Location I as only half of the bridge was modeled and symmetry conditions were assumed along its longitudinal axis.

Table 4.4-8 Maximum principal stresses in deck flange for bridges with a span of 100 ft

Span (ft)	Width (ft)	No. Diaph.	Maximum principal stresses in deck (psi)					
			Prestress	SIDL	+ve TG	TL#I	TL#II	TL#III
100	25.5	0	355	319	crack	crack	-	-
	25.5	2		317	341	382	-	-
	25.5	3		310	356	370	-	-
	25.5	5		307	356	381	-	-
	51.5	0		383	549	-	crack	crack
	51.5	2		342	389	-	400	crack
	51.5	3		323	387	-	366	471
	51.5	5		318	379	-	358	357
	77.5	0		383	crack	-	crack	crack
	77.5	2		385	378	-	crack	crack
	77.5	3		373	368	-	crack	crack
	77.5	5		366	351	-	469	358

Table 4.4-9 Longitudinal stresses in deck flange for bridges with a span of 100 ft

Span (ft)	Width (ft)	No. Diaph.	Longitudinal stresses in deck (psi)					
			Prestress	SIDL	+ve TG	TL#I	TL#II	TL#III
100	25.5	0	354	317	crack	crack	-	-
	25.5	2		312	295	275	-	-
	25.5	3		308	275	264	-	-
	25.5	5		307	259	252	-	-
	51.5	0		379	279	-	crack	crack
	51.5	2		335	295	-	291	crack
	51.5	3		320	282	-	263	246
	51.5	5		318	269	-	256	235
	77.5	0		378	crack	-	crack	crack
	77.5	2		378	277	-	crack	crack
	77.5	3		368	274	-	crack	crack
	77.5	5		364	274	-	296	237

Table 4.4-10 Transverse stresses in deck flange for bridges with a span of 100 ft

Span (ft)	Width (ft)	No. Diaph.	Transverse stresses in deck (psi)					
			Prestress	SIDL	+ve TG	TL#I	TL#II	TL#III
100	25.5	0	103	134	crack	crack	-	-
	25.5	2		120	287	322	-	-
	25.5	3		105	356	363	-	-
	25.5	5		97	355	367	-	-
	51.5	0		156	547	-	crack	crack
	51.5	2		114	368	-	310	crack
	51.5	3		102	358	-	353	471
	51.5	5		98	329	-	343	355
	77.5	0		130	crack	-	crack	crack
	77.5	2		130	376	-	crack	crack
	77.5	3		126	358	-	crack	crack
	77.5	5		124	347	-	467	356

4.4.5 Effect of skew angle

The numerical investigation extended to examine the influence of the skew angle on the development of shear key cracks in a decked bulb T beam bridge system. Key bridge models with skew angles of 30, 45, and 60 degrees were generated and analyzed under the same loading and environmental conditions. The results were compared with those of bridges with no skew angle.

As shown in Table 4.4-11 through Table 4.4-18, the maximum principal stresses, longitudinal stresses, and transverse stresses in the deck flanges of the bridge models increase with increasing the skew angle. All the bridge models were analyzed with five equally spaced transverse diaphragms but without TPT force.

Compared to those with no skew angle, bridge models with a skew angle of 30° showed a remarkable increase in the overall deck flange tensile stresses. The increase in the tensile stresses due to the skew angle does not seem to be directly related to the span length. For instance, bridges with a width of 25.5 ft and span lengths of 50, 75, and 100 ft experienced an increase in the maximum principal stresses of 16, 28, and 28%, respectively from similar bridges with no skew

angles. It should be noted that the location of the maximum tensile stresses, whether near the ends of the beams or near the middle region of the span, varied from case to case depending on the loading conditions.

The bridge width also does not seem to be directly related to the increase in the deck flange tensile stresses due to the skew angle. For instance, bridges with a span of 100 ft and widths of 25.5, 51.5, and 77.5 ft experienced an increase in the maximum principal stresses of approximately 16, 29, and 30%, respectively.

Table 4.4-18 and Figure 4.4-19 through Figure 4.4-21 show the increase in the tensile stresses with increasing the skew angle. In bridges with skew angle of 60°, cracks developed at the shear key joints when the traffic loads were added at Locations I, II, and III. Similarly, the tensile stresses in bridges with a skew angle of 45° also increased from the stresses observed in bridges with no skew angle and as shown in Figure 4.4-22, the deck flange experienced shear key cracks when the traffic loads were added at Location I. Adding the traffic loads at Locations II and III in the 45°-skew bridge did not yield any shear key cracks. However, the maximum principal stresses reached approximately 511 and 463 psi, respectively.

Table 4.4-11 Deck flange stresses for bridges with a span of 50 ft and a width of 25.5 ft

	Maximum principal stresses (psi)			Longitudinal stresses (psi)			Transverse stresses (psi)		
	Skew angle		% increase	Skew angle		% increase	Skew angle		% increase
	0°	30°		0°	30°		0°	30°	
+ve TG	332	359	8%	266	275	3%	288	280	-3%
TL#I	395	457	16%	274	274	0%	339	425	25%

Table 4.4-12 Deck flange stresses for bridges with a span of 50 ft and a width of 51.5 ft

	Maximum principal stresses (psi)			Longitudinal stresses (psi)			Transverse stresses (psi)		
	Skew angle		% increase	Skew angle		% increase	Skew angle		% increase
	0°	30°		0°	30°		0°	30°	
+ve TG	347	430	24%	293	318	9%	334	341	2%
TL#I	416	507	22%	310	308	-1%	389	461	19%
TL#II	407	447	10%	296	375	27%	399	417	5%
TL#III	309	400	29%	247	260	5%	282	399	42%

Table 4.4-13 Deck flange stresses for bridges with a span of 50 ft and a width of 77.5 ft

	Maximum principal stresses (psi)			Longitudinal stresses (psi)			Transverse stresses (psi)		
	Skew angle		% increase	Skew angle		% increase	Skew angle		% increase
	0°	30°		0°	30°		0°	30°	
+ve TG	353	436	24%	302	320	6%	342	336	-2%
TL#I	431	453	5%	309	403	30%	427	447	5%
TL#II	441	475	8%	321	394	23%	435	427	2%
TL#III	322	420	30%	267	274	3%	294	417	42%

Table 4.4-14 Deck flange stresses for bridges with a span of 75 ft and a width of 25.5 ft

	Maximum principal stresses (psi)			Longitudinal stresses (psi)			Transverse stresses (psi)		
	Skew angle		% increase	Skew angle		% increase	Skew angle		% increase
	0°	30°		0°	30°		0°	30°	
+ve TG	325	322	-1%	229	286	25%	320	304	-5%
TL#I	369	473	28%	255	273	7%	348	451	30%

Table 4.4-15 Deck flange stresses for bridges with a span of 75 ft and a width of 51.5 ft

	Maximum principal stresses (psi)			Longitudinal stresses (psi)			Transverse stresses (psi)		
	Skew angle		% increase	Skew angle		% increase	Skew angle		% increase
	0°	30°		0°	30°		0°	30°	
+ve TG	348	392	13%	269	319	19%	314	364	16%
TL#I	384	470	22%	298	366	23%	343	459	34%
TL#II	352	427	21%	266	335	26%	327	420	28%
TL#III	357	415	16%	235	266	13%	355	414	17%

Table 4.4-16 Deck flange stresses for bridges with a span of 75 ft and a width of 77.5 ft

	Maximum principal stresses (psi)			Longitudinal stresses (psi)			Transverse stresses (psi)		
	Skew angle		% increase	Skew angle		% increase	Skew angle		% increase
	0°	30°		0°	30°		0°	30°	
+ve TG	351	406	16%	274	327		347	380	10%
TL#I	-	-	-	-	-	-	-	-	-
TL#II	469	475	1%	296	457	54%	467	451	-3%
TL#III	358	427	19%	237	280	18%	356	424	19%

Table 4.4-17 Deck flange stresses for bridges with a span of 100 ft and a width of 25.5 ft

	Maximum principal stresses (psi)			Longitudinal stresses (psi)			Transverse stresses (psi)		
	Skew angle		% increase	Skew angle		% increase	Skew angle		% increase
	0°	30°		0°	30°		0°	30°	
+ve TG	356	380	7%	259	297	15%	355	335	-6%
TL#I	381	486	28%	252	310	23%	367	480	31%

Table 4.4-18 Deck flange stresses for bridges with a span of 75 ft and a width of 51.5 ft

	Maximum principal stresses (psi)				Longitudinal stresses (psi)				Transverse stresses (psi)			
	Skew angle				Skew angle				Skew angle			
	0°	30°	45°	60°	0°	30°	45°	60°	0°	30°	45°	60°
+ve TG	348	392	357	427	269	319	326	375	314	364	349	403
TL#I	384	470	C	C	298	366	C	C	343	459	C	C
TL#II	352	427	511	C	266	335	355	C	327	420	500	C
TL#III	357	415	463	C	235	266	239	C	355	414	457	C

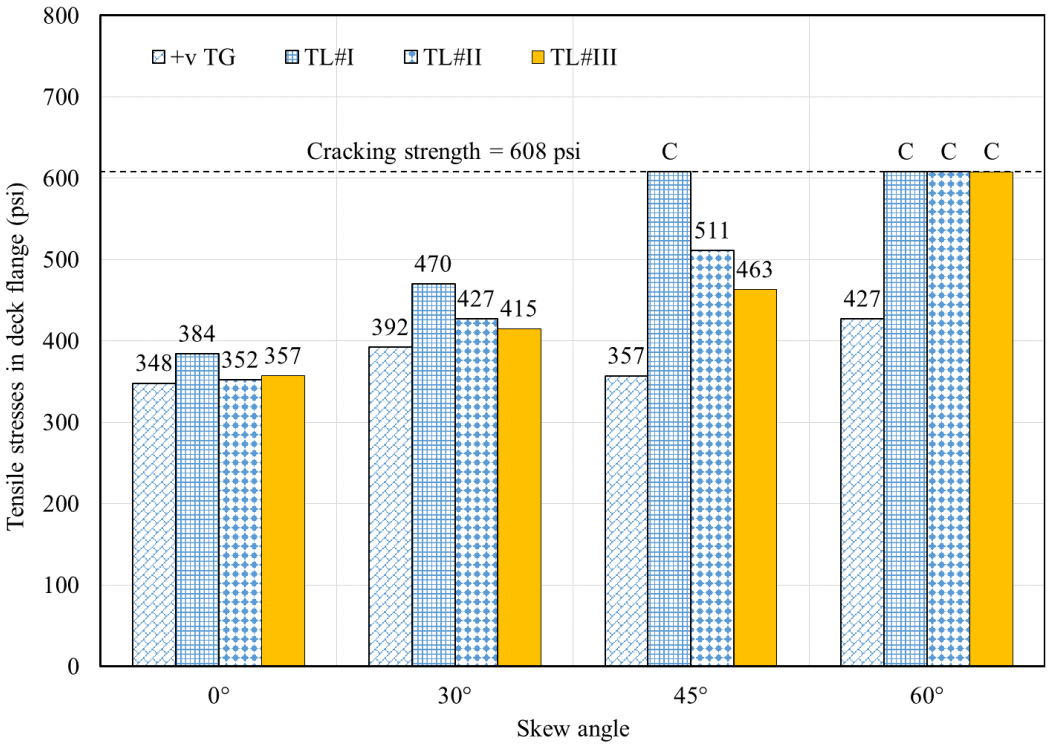

Figure 4.4-19 Effect of increasing skew angle on maximum principal stresses in deck flange

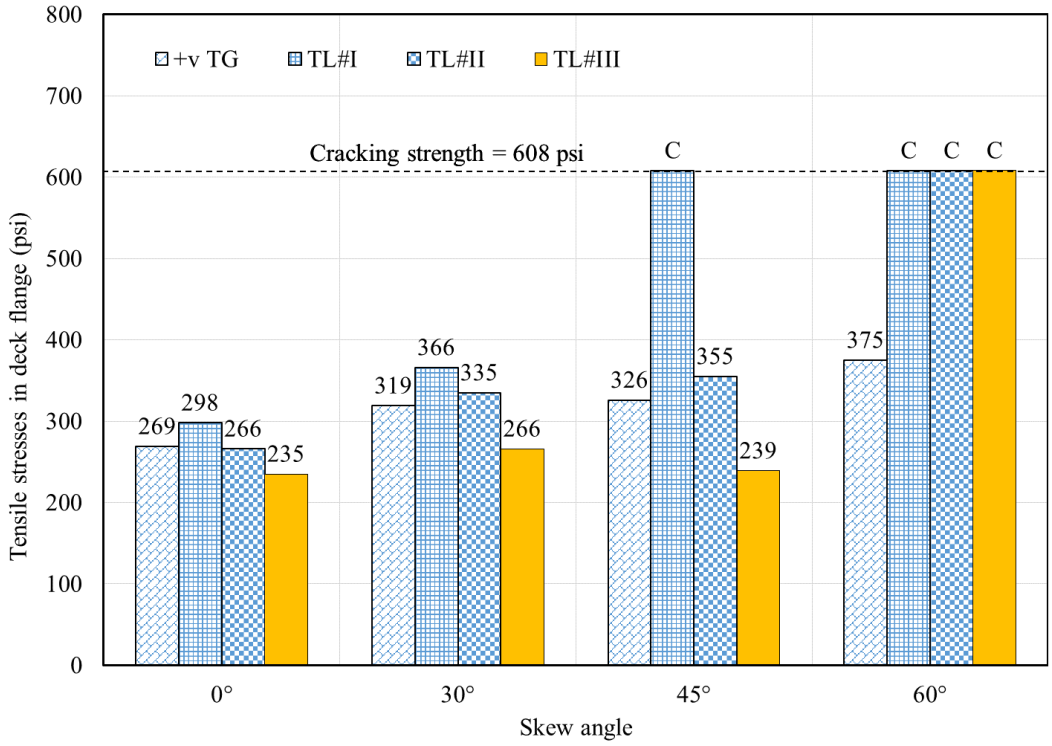

Figure 4.4-20 Effect of increasing skew angle on Longitudianl stresses in deck flange

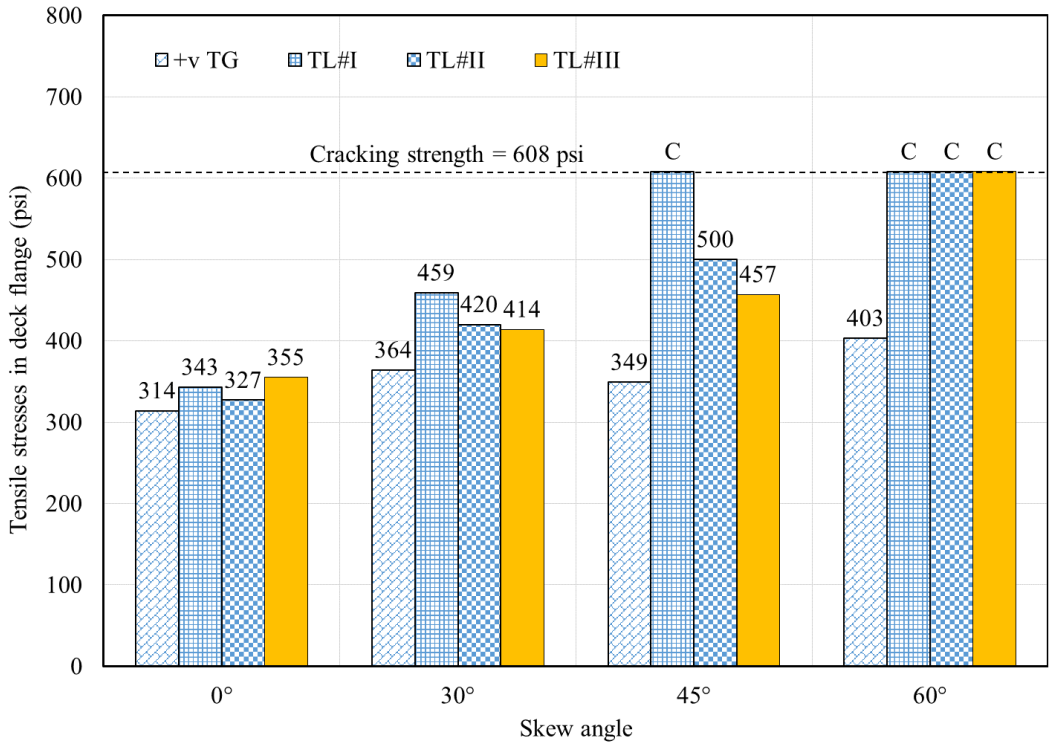

Figure 4.4-21 Effect of increasing skew angle on transverse stresses in deck flange

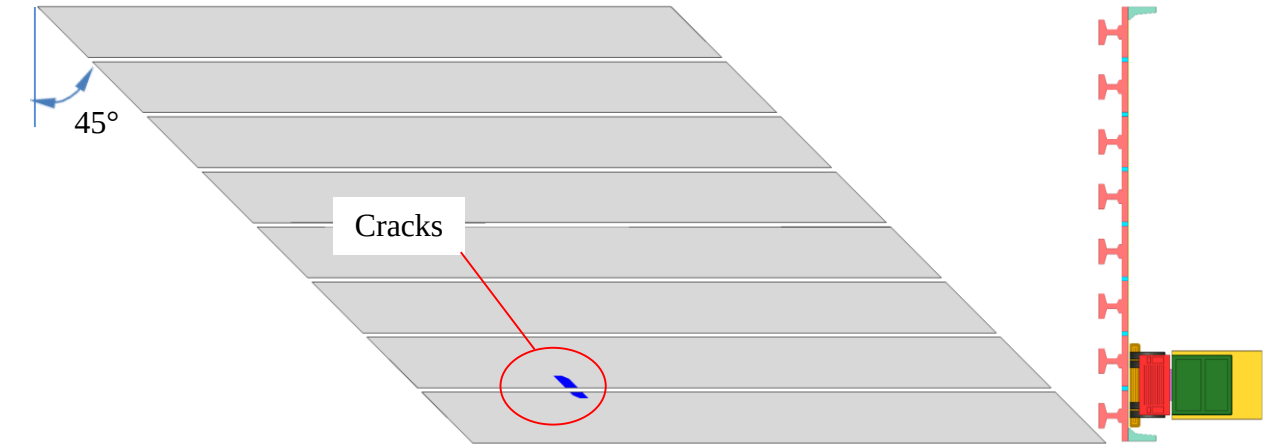

Figure 4.4-22 Development of shear key cracks in bridges with a skew angle of 45° under TL#I

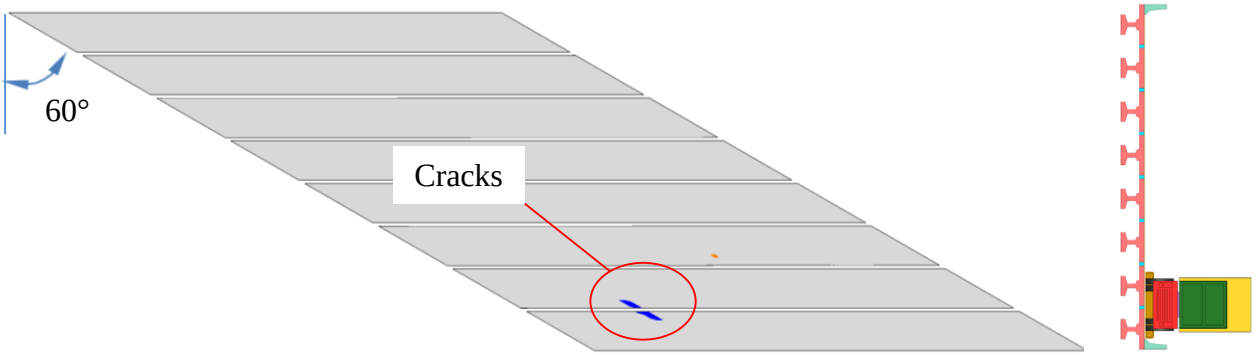

Figure 4.4-23 Development of shear key cracks in bridges with a skew angle of 60° under TL#I

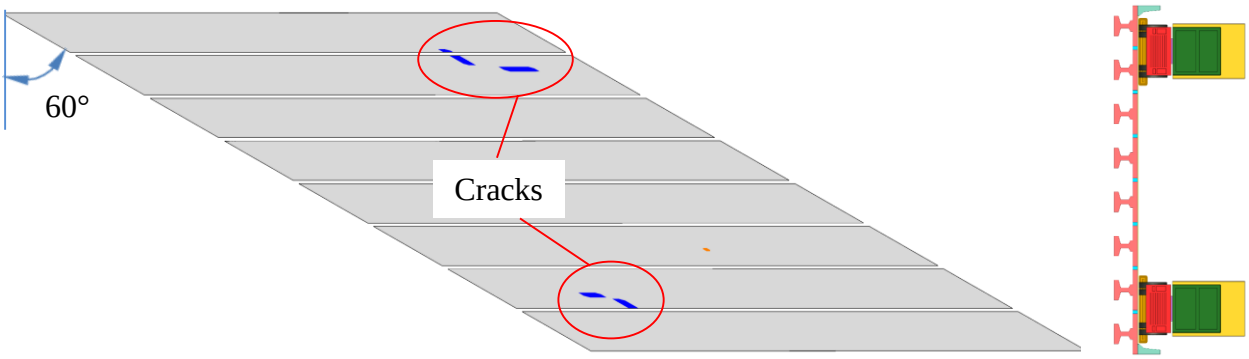

Figure 4.4-24 Development of shear key cracks in bridges with a skew angle of 60° under TL#II

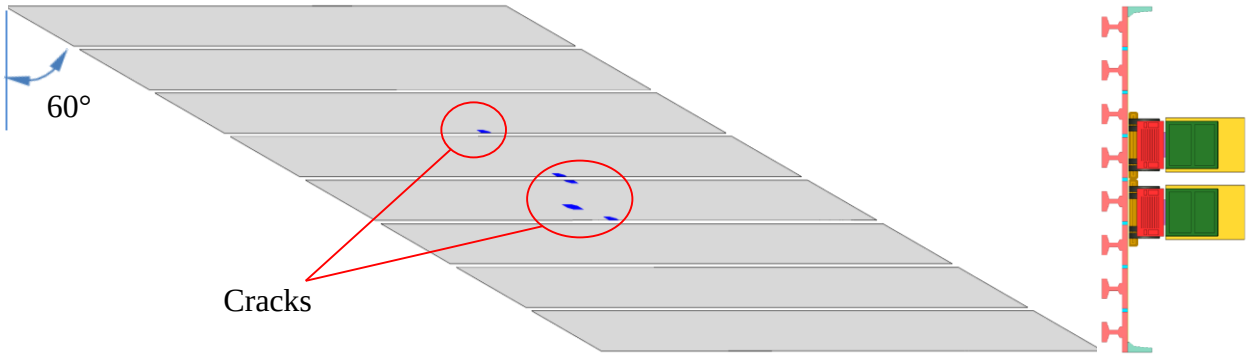

Figure 4.4-25 Development of shear key cracks in bridges with a skew angle of 60° under TL#III

4.4.6 Effect of TPT force

To evaluate the influence of providing TPT force on the lateral integrity of decked bulb T beam bridges, select bridge models were analyzed with TPT forces of 50, 100, 150, and 200 kip per diaphragm. All bridge models were provided with five equally spaced transverse diaphragms. To ensure the uniformity of the TPT through the section, the force was applied as a distributed load over the exterior face of the diaphragm.

Figure 4.4-26 through Figure 4.4-37 show the developed stresses in the deck flange of the bridge models. As shown in the figures, the effect of the TPT force was not highly significant. In general, the principal stresses in the deck flanges did not exhibit a significant change with adding the TPT force. In some models, the principal stresses tended to slightly decrease with increasing the TPT force level. In other models, the maximum principal stresses actually increased with increasing the TPT force level. The change in the maximum principal stresses whether a increase or a decrease never exceeded the limit of 100 psi.

The longitudinal tensile stresses in the deck seem to slightly increase with increasing the TPT force. This is due to the fact that TPT force usually generates a field of compressive stresses in the transverse direction, which are accompanied by tensile stresses in the longitudinal direction. Because of the longitudinal prestressing force, the top flange of the decked bulb T beam experiences longitudinal tensile stresses especially at the ends, where the moment due to the dead and live loads diminishes. Therefore, adding the TPT force, especially at the end diaphragms, seems to increase the longitudinal tensile stresses. The maximum increase in the longitudinal stresses in the deck flange did not exceed 50 psi.

On the other hand, it was noticed that the transverse tensile stresses in general decreased with increasing the TPT force. A decrease of transverse tensile stresses of approximately 150 psi was noted in some cases of loading (case of bridges with a span of 50 ft, a width of 51.5 ft, a TPT force of 200 kip per diaphragm, under TL#I). However, the decrease in the transverse tensile stresses was accompanied by an increase of the longitudinal tensile stresses, and overall, the maximum principal stresses for this particular case increased by around 71 psi.

Table 4.4-19, through Table 4.4-21 document the change in the tensile stresses in the deck flange with increasing the TPT force from zero to 200 kip per diaphragm for bridges with different spans and different widths. A direct relationship between the bridge span or width and the developed stresses with adding TPT force was not observed. The maximum principal stresses in the deck flange usually exceeded the limit of 300 psi but they were less than the limit of 500 psi under any load combination with different TPT force levels. This is considering a concrete cracking strength of 608 psi (According to AASHTO LRFD for typical 7000-psi concrete). It should be noted that the tensile stresses in the deck can be controlled by limiting the longitudinal tensile stresses in the deck due to longitudinal prestressing.

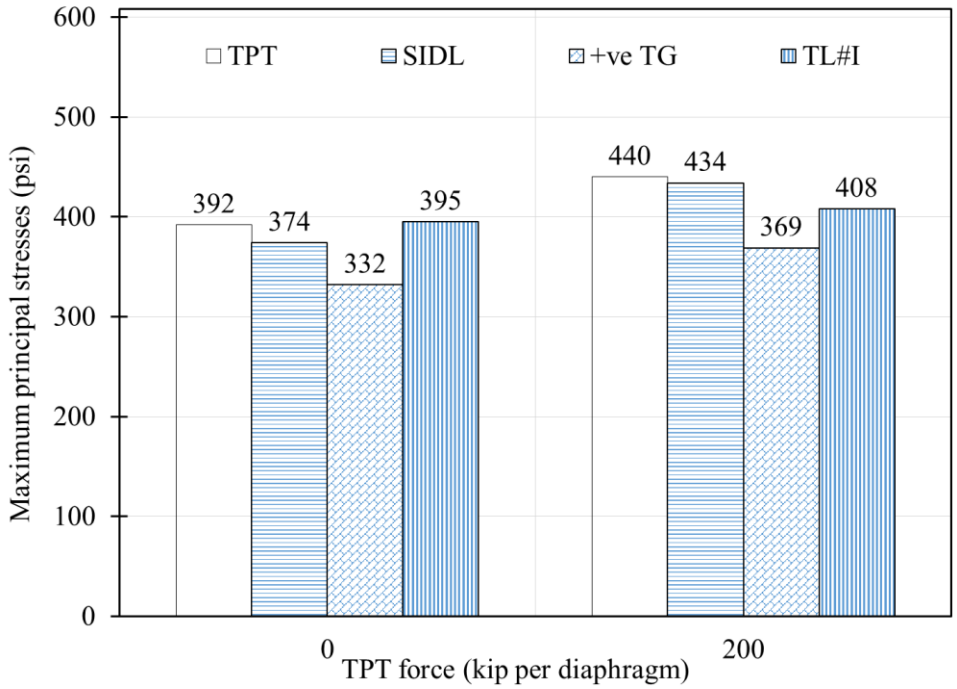

Figure 4.4-26 Maximum principal stresses in deck flange at different TPT force levels in bridge models with a span of 50 ft and a width of 25.5 ft

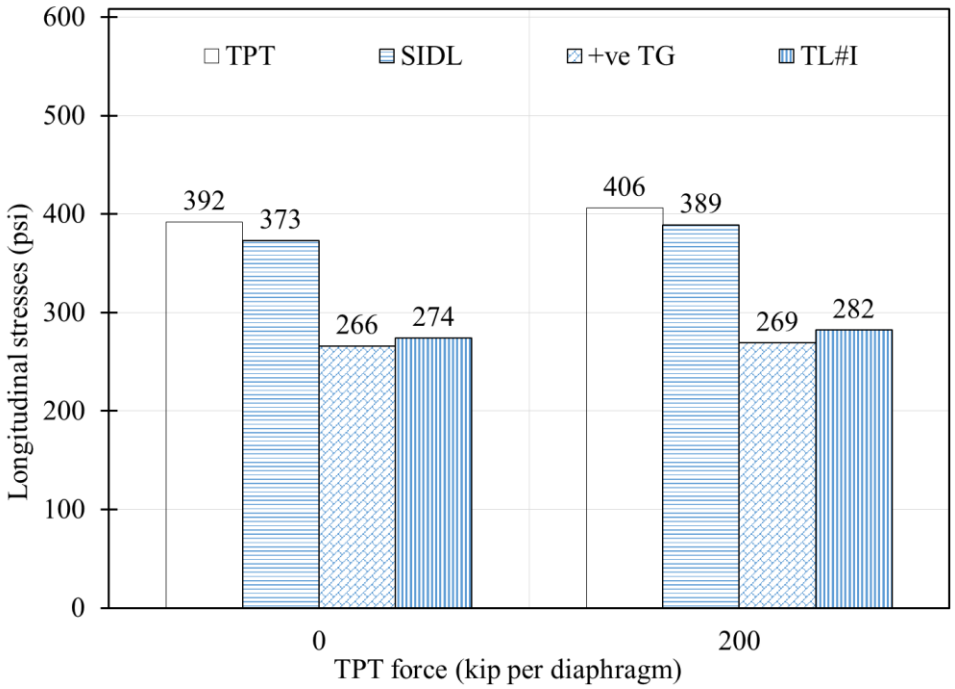

Figure 4.4-27 Longitudinal stresses in deck flange at different TPT force levels in bridge models with a span of 50 ft and a width of 25.5 ft

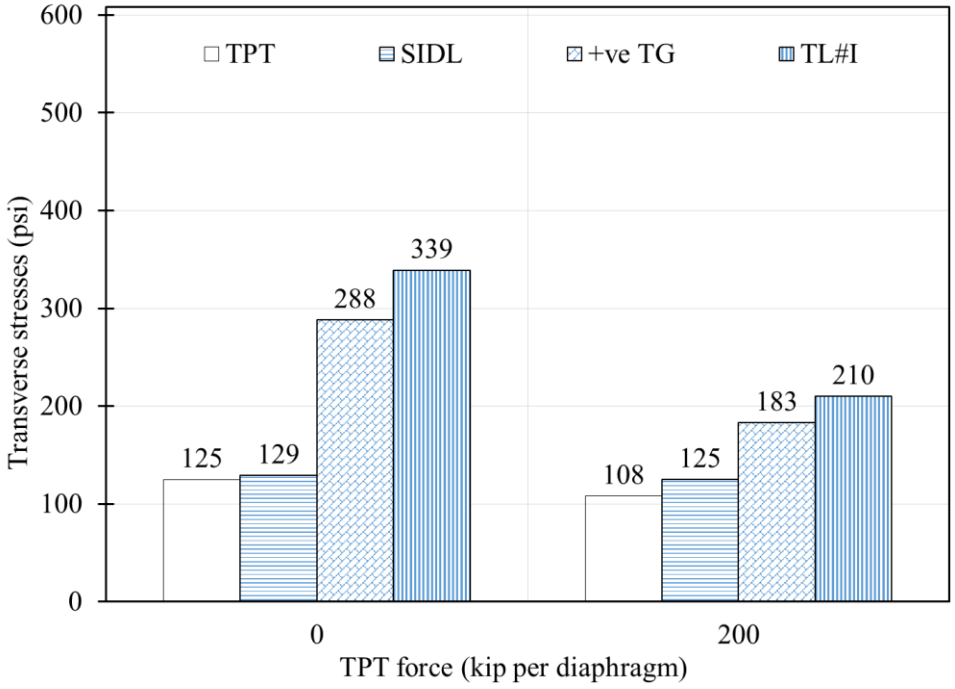

Figure 4.4-28 Transverse stresses in deck flange at different TPT force levels in bridge models with a span of 50 ft and a width of 25.5 ft

Table 4.4-19 Deck flange stresses at different TPT force levels in bridge models with a span of 50 ft and a width of 51.5 ft

	Maximum principal stresses (psi)			Longitudinal stresses (psi)			Transverse stresses (psi)		
TPT (kip/Diaph.)	0	100	200	0	100	200	0	100	200
TPT	392	431	470	392	413	434	125	110	95
SIDL	388	434.5	481	387	408	436	137	123	114
+ve TG	347	383	419	293	301	309	334	286	238
TL#I	416	452	487	310	321	331	389	314	239
TL#II	407	436	464	296	310	321	399	356	313
TL#III	309	341	373	247	257	267	282	235	181

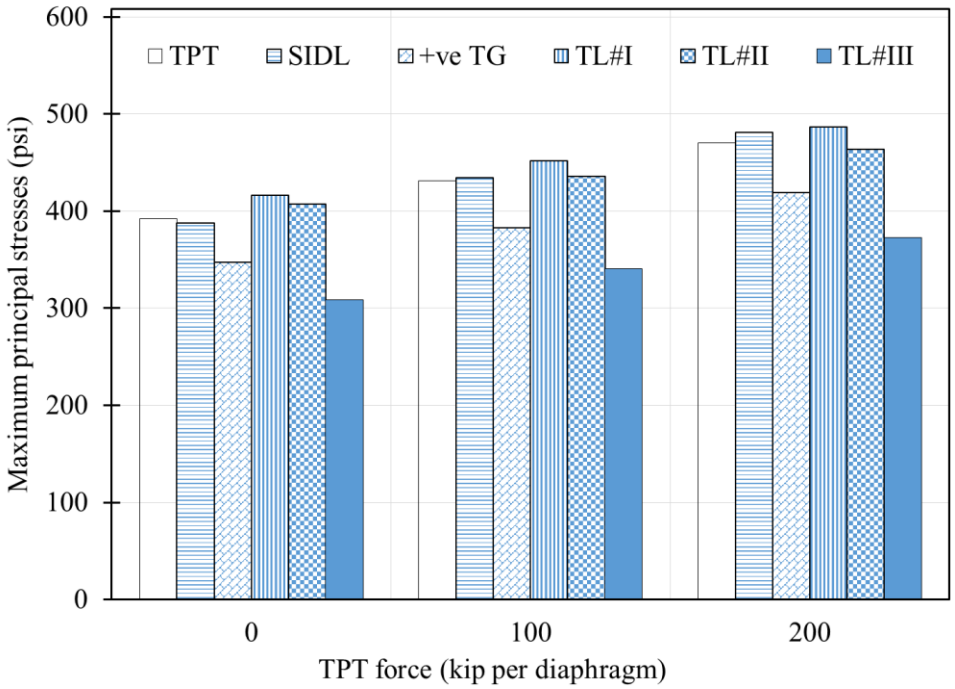

Figure 4.4-29 Maximum principal stresses in deck flange at different TPT force levels in bridge models with a span of 50 ft and a width of 51.5 ft

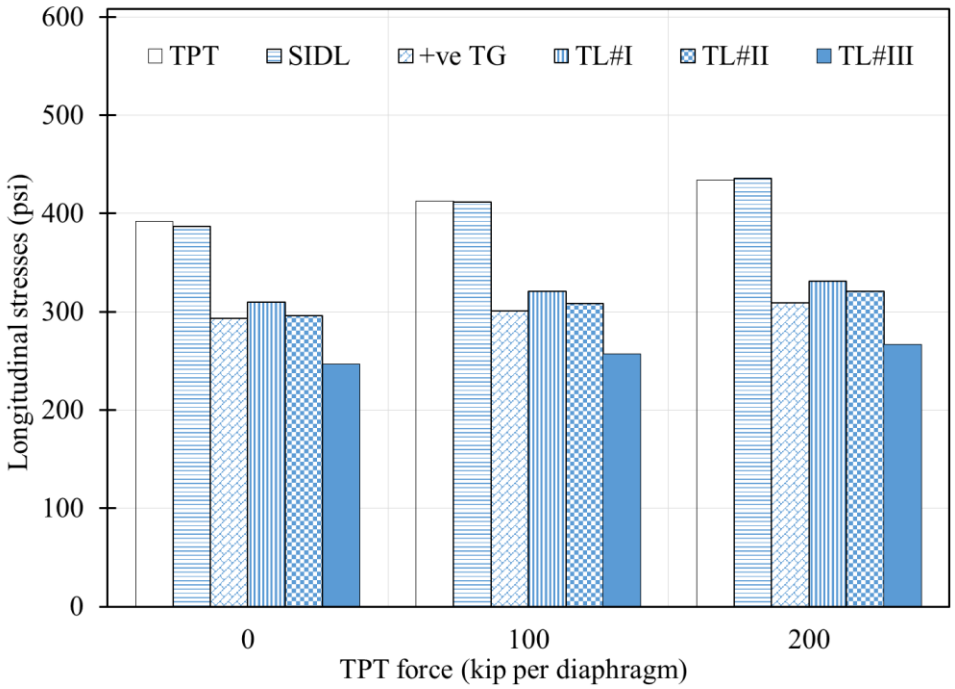

Figure 4.4-30 Longitudinal stresses in deck flange at different TPT force levels in bridge models with a span of 50 ft and a width of 51.5 ft

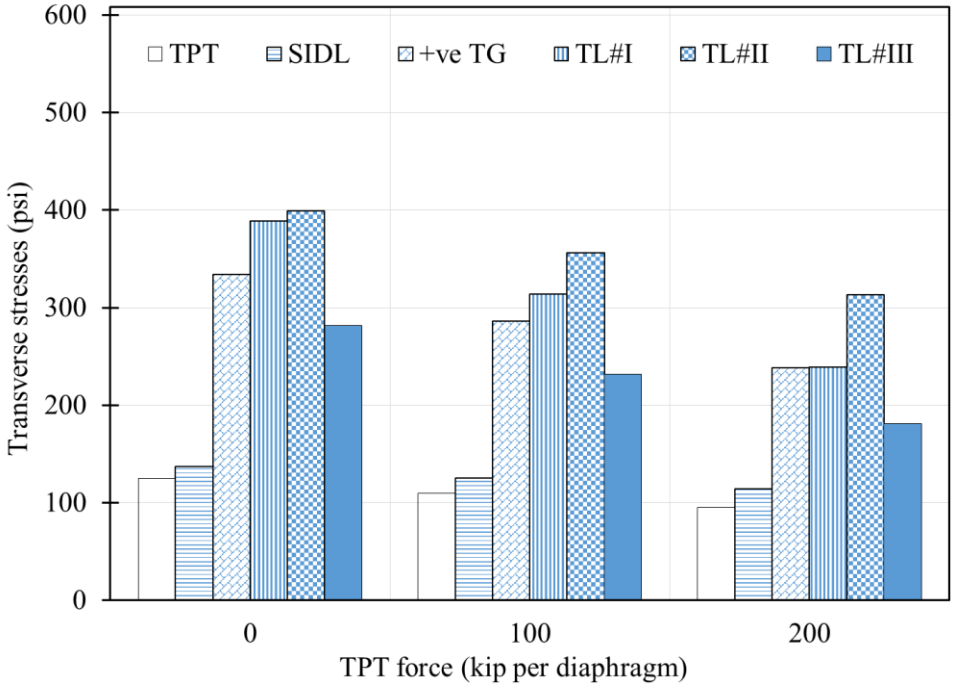

Figure 4.4-31 Transverse stresses in deck flange at different TPT force levels in bridge models with a span of 50 ft and a width of 51.5 ft

Table 4.4-20 Deck flange stresses at different TPT force levels in bridge models with a span of 75 ft and a width of 51.5 ft

	Maximum principal stresses (psi)					Longitudinal stresses (psi)					Transverse stresses (psi)				
TPT (kip/Diaph.)	0	50	100	150	200	0	50	100	150	200	0	50	100	150	200
TPT	357	363	373	385	398	357	362	369	376	384	110	85	58	46	57
SIDL	360	369	381	394	408	358	365	372	379	386	118	94	68	65	76
+ve TG	348	355	363	371	380	269	272	276	279	283	314	304	293	283	273
TL#I	384	397	409	422	434	298	302	305	308	311	343	329	317	306	295
TL#II	352	362	372	382	395	266	268	271	275	279	327	317	307	297	286
TL#III	357	359	362	364	367	235	239	243	247	252	355	335	315	295	276

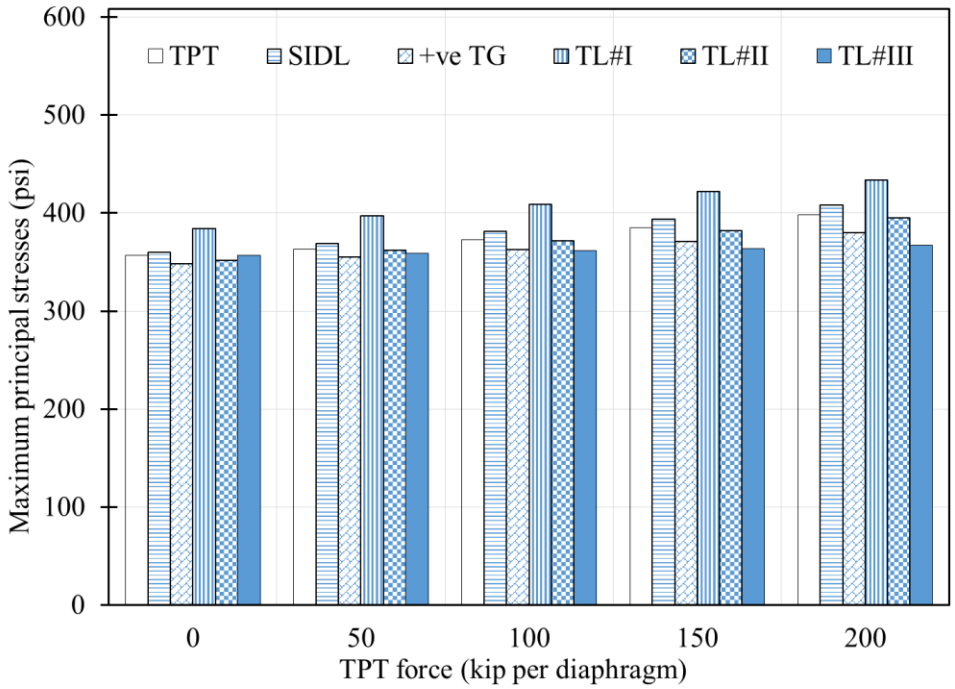

Figure 4.4-32 Maximum principal stresses in deck flange at different TPT force levels in bridge models with a span of 75 ft and a width of 51.5 ft

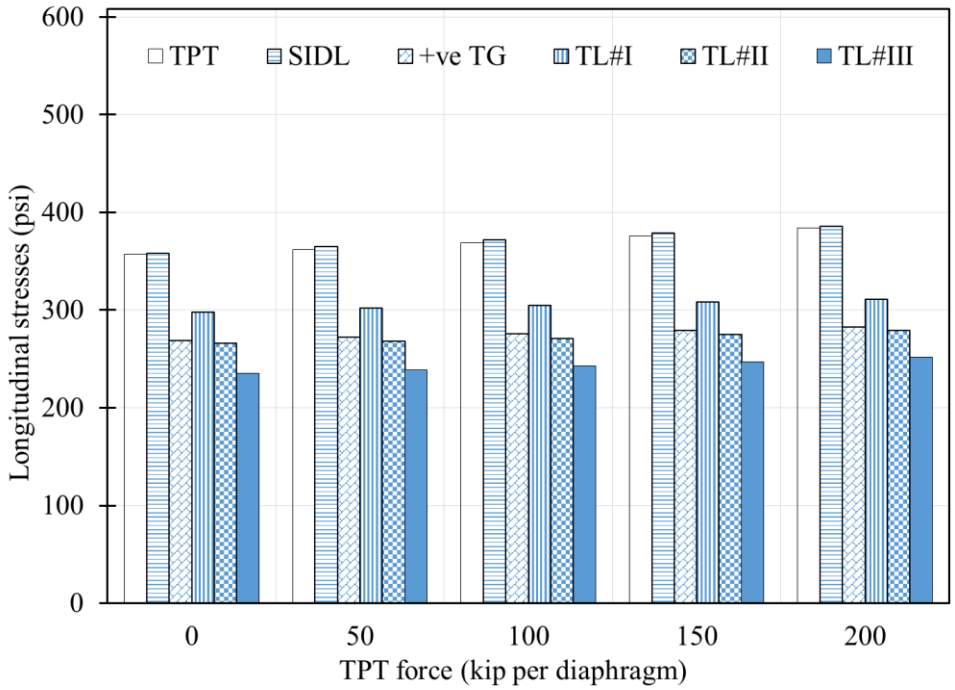

Figure 4.4-33 Longitudinal stresses in deck flange at different TPT force levels in bridge models with a span of 75 ft and a width of 51.5 ft

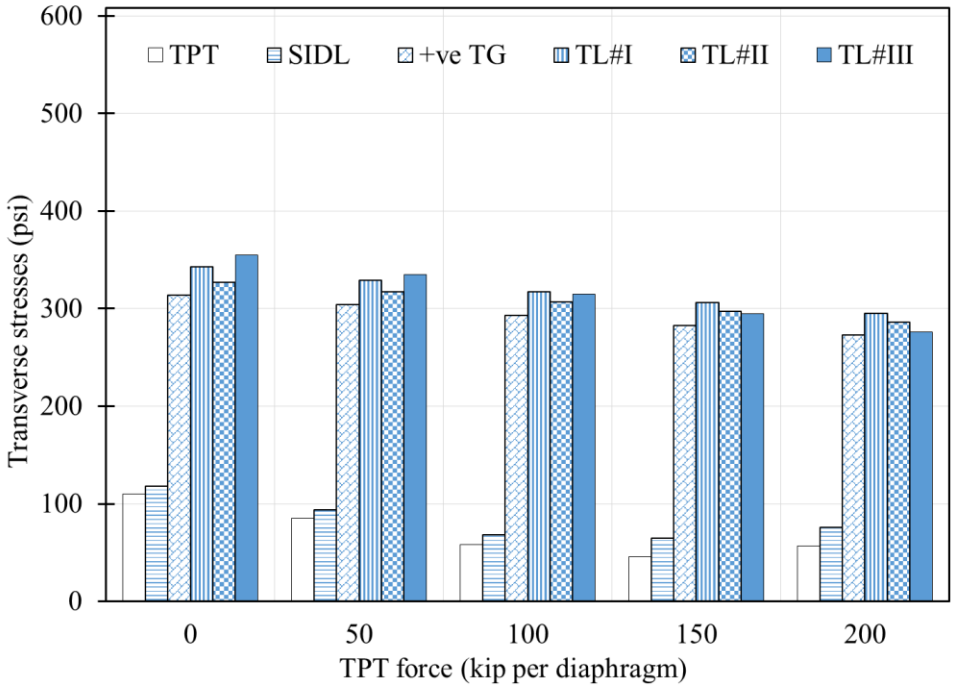

Figure 4.4-34 Transverse stresses in deck flange at different TPT force levels in bridge models with a span of 75 ft and a width of 51.5 ft

Table 4.4-21 Deck flange stresses at different TPT force levels in bridge models with a span of 100 ft and a width of 77.5 ft

	Maximum principal stresses (psi)				Longitudinal stresses (psi)				Transverse stresses (psi)			
TPT (kip/Diaph.)	0	50	100	200	0	50	100	200	0	50	100	200
TPT	355	332	341	359	354	331	339	355	103	73	63	43
SIDL	366	334	344	364	364	330	338	353	124	90	83	67
+ve TG	351	407	413	426	274	278	287	306	347	324	320	309
TL#I	-	-	-	-	-	-	-	-	-	-	-	-
TL#II	469	398	405	415	296	280	282	286	467	352	340	321
TL#III	358	373	388	403	237	249	273	287	356	344	322	309

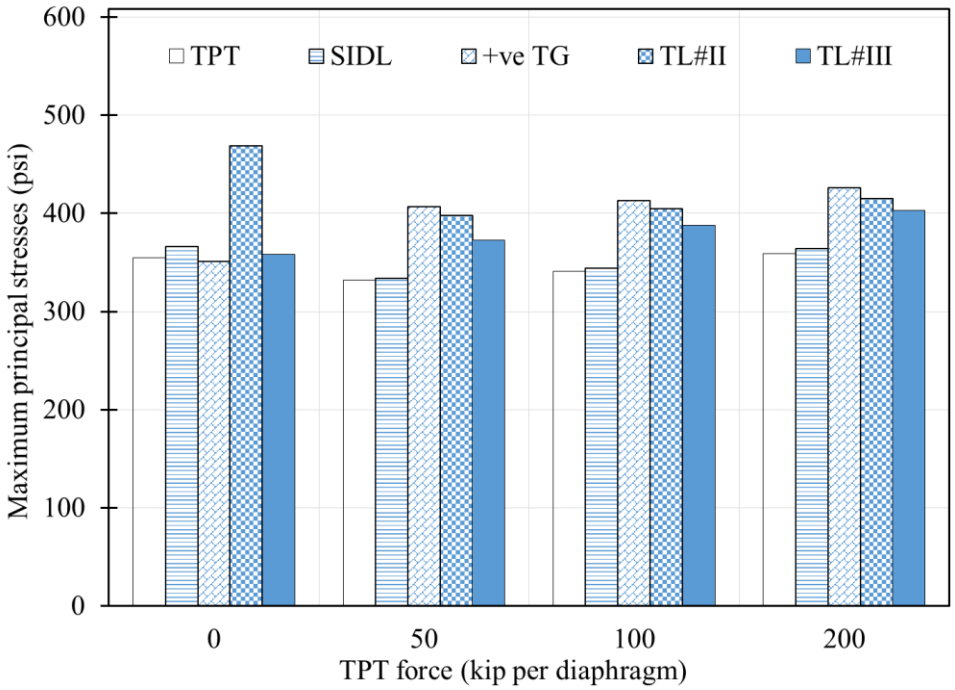

Figure 4.4-35 Maximum principal stresses in deck flange at different TPT force levels in bridge models with a span of 100 ft and a width of 77.5 ft

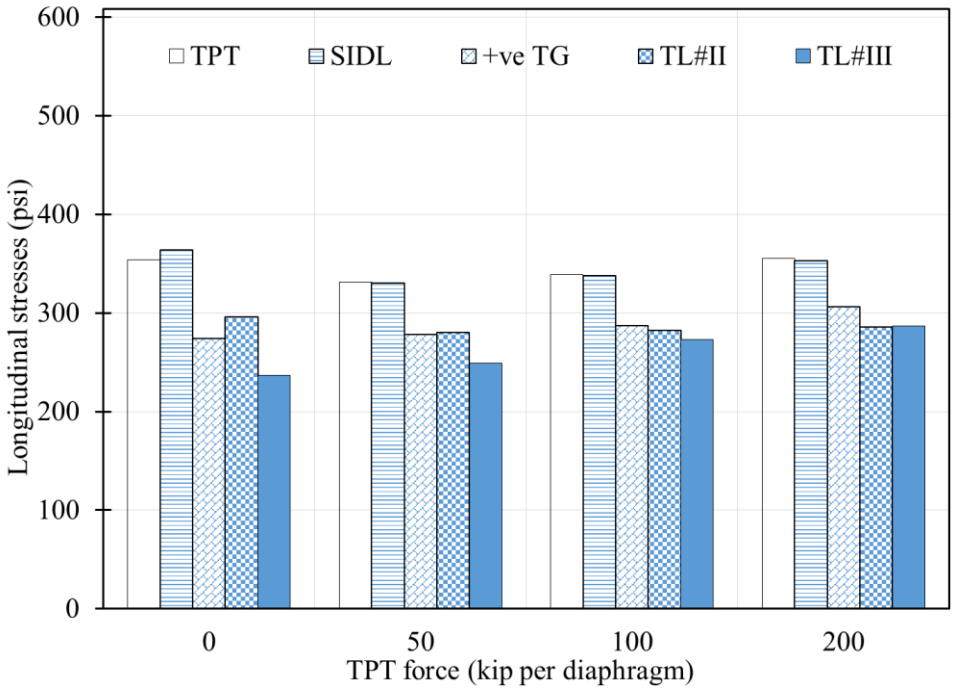

Figure 4.4-36 Longitudinal stresses in deck flange at different TPT force levels in bridge models with a span of 100 ft and a width of 77.5 ft

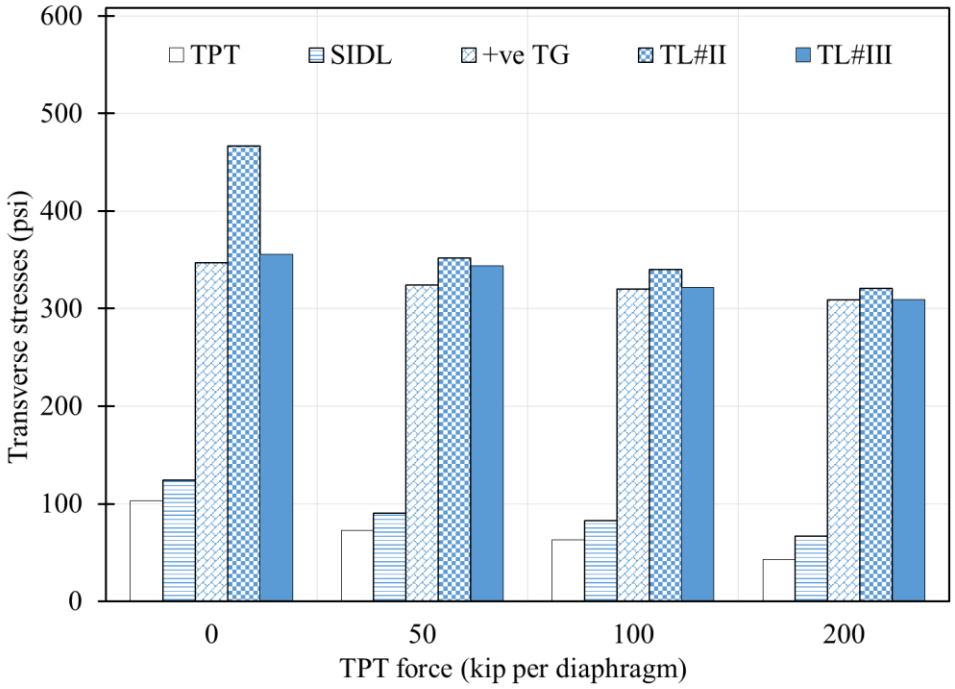

Figure 4.4-37 Transverse stresses in deck flange at different TPT force levels in bridge models with a span of 100 ft and a width of 77.5 ft

4.5 Summary

The results from the numerical analysis suggest that it is feasible to numerically and analytically predict the performance of beams and bridges with CFCC reinforcement with very good accuracy. The overall performance of such beams and bridges follows the principles of strain compatibility and force equilibrium through the section. In addition, decked bulb T beam bridges with UHPC shear key joints can be safely used in bridge construction with no deck slab. However, it is mandatory to provide transverse diaphragms along with the shear key joints. Without transverse diaphragms, the joints between the top flanges become the sole path for load transfer among the adjacent beams, resulting in additional stresses, which may crack the joints under positive temperature gradient and traffic loads. Even with the use of UHPC shear key joint, which exhibit exceptional bond strength to concrete, the cracks may develop on the concrete side of the joint. Providing shear key reinforcement is believed to be a viable line of defense against crack propagation. However, the development of cracks over time and under repeated load cycles can lead to series consequences and greatly reduce the lifespan of the joints and the entire superstructure.

Through the parametric study, it was determined that five equally spaced transverse diaphragms are sufficient to mitigate the longitudinal crack development in decked bulb T beams with spans ranging from 50 to 100 ft and widths ranging from 25 to 77 ft. The bridges were subjected to positive temperature gradient and traffic loads at different locations. For bridges with spans and widths exceeding the aforementioned ranges, it may be mandatory to increase the number of diaphragms.

In addition, the parametric study also showed that decked bulb T beam bridges with a skew angle are prone to shear key cracking. Cracks were observed in bridges with skew angles of 45° and larger. Therefore, it is highly recommended that decked bulb T beam bridge system be used with a skew angle of no more than 30°. Bridges with larger skew angles will need a special evaluation to ensure the integrity.

Furthermore, the study showed that providing transverse post-tensioning through the transverse diaphragms may not serve its purpose of mitigating the tensile stresses in the deck flange. It was observed that while the transverse post-tensioning force reduced the transverse tensile stresses in bridge models with different spans and widths under different load combinations,

it also generated a field of longitudinal tensile stresses. Since the flanges of the decked bulb T beams experience tensile stresses due to the longitudinal prestressing especially at the ends, adding transverse post-tensioning increases the overall longitudinal tensile stresses. Consequently, the maximum principal stresses in the deck flanges seem to slightly increase with adding the post-tensioning force. This increase in principal stresses may lead to the development of deck cracking (not necessarily at the shear key joints). Therefore, transverse post-tensioning needs not to be provided during construction but it may be reserved for future use, when integrity of the superstructure is jeopardized. For example, post-tensioning can be used to ensure the integrity of the superstructure after a beam replacement or when additional beams are provided. It is recommended that post-tensioning ducts through the transverse diaphragms be provided during construction for any possible future use.

CHAPTER 5: SUMMARY AND CONCLUSIONS

5.1 Summary of the work

Through this experimental/numerical investigation, a new decked bulb T beam bridge system with non-corrosive CFCC reinforcement and UHPC shear key joints was evaluated. The experimental investigation included building one-half-scale five individual control beams and one-half-scale complete bridge model. Four control beams were tested to failure under four-point flexural loading and one beam was tested to failure under shear loading. The bridge model was tested under different load levels and configurations to evaluate its performance under service, post-cracking, and strength limit states. Special attention was given to the performance of the UHPC shear key joints and to the integrity of the bridge model in the transverse direction.

The numerical study consisted of a verification phase and a parametric phase. In the verification phase, numerical models model were generated and analyzed for tested control beams and the bridge model. The results from the numerical study were compared with those of the experimental study to ensure the accuracy of the numerical models. After validation of the numerical models, the parametric study was initiated by generating a series of models for full-scale decked bulb T beam bridges with spans ranging from 50 ft to 100 ft and widths ranging from 24 ft to 78 ft. The main objective of the parametric study was to evaluate the transverse integrity of decked bulb T beam bridge system and to assess the need for transverse diaphragms and/or transverse post-tensioning. In addition, the study was extended to examine the effect of the skew angle on the stress distribution in the beams and the potential for developing longitudinal deck cracks at the shear key joints

5.2 Observations & conclusions

The following observations and conclusions are drawn based on the results of the experimental investigation:

1. Decked bulb T beams with CFCC reinforcement can be designed as under-reinforced, balanced, or over-reinforced. The difference in the ductility ratio did not vary significantly with reference to the design of the section. It was observed that the ductility ratio in all control beams with CFCC reinforcement averaged approximately 30 %, while the ductility ratio of control beam with steel strands was around 70 %. However, by examining the load

deflection curves, it was observed that beams with CFCC strands exhibited significant deflection at failure. This maximum deflection was similar to that observed in the beam with steel strands. This large deflection at failure, along with the extensive cracking, can serve as a clear visual sign before failure.

2. It was also observed that due to construction configuration of CFCC strands, the tension failure in Beam C-S-F-U did not occur suddenly. Rather, the 7-wire CFCC strands showed a gradual failure as the individual wires within the strands experienced consecutive rupture without dramatic decrease in the overall load carrying capacity.

3. The flexural failure of all control beams was accurately predicted using the method of strain compatibility. However, special attention must be made when evaluating the type of failure. In beams with multiple layers of non-prestressed and prestressed CFCC strands, the equation of balanced reinforcement ratio as recommend by ACI-440 (2006) can only be used as a rough estimate during the initial design stage. Exact failure mode can only be verified using the strain compatibility method considering the distribution of the strands and prestressing force through different reinforcement layers.

4. It is fairly accurate to assume that decked bulb T beams exhibit a bilinear load-deflection relationship. The slope of the first segment of the bilinear curve represents the flexural stiffness of the un-cracked section, while the slope of the second segment represents the flexural stiffness of the cracked section. When conducting multiple post-cracking load cycle tests, the segments of the bilinear curve meet at the decompression load, defined as the load required to decompress the beam and cause the strain in the bottom fibers of the beam to reach zero.

5. Decked bulb T beams with CFCC stirrups exhibited shear compression failure with no signs of yielding or rupture of stirrups. The failure occurred in the web struts due to excessive shear strain. The maximum recorded strain in the CFCC stirrups was approximately 0.0035, which is the maximum shear strain as given in AASHTO LRFD regardless of the type of reinforcement. This finding suggests that the strain limit of 0.002 as given in ACI 440-3R is overly conservative and needs to be changed to match that of AASHTO LRFD.

6. Under service load condition, the decked bulb T beam bridge model did not exhibit any flexural or shear key cracks. The service load was transversely distributed among the beams in a pattern similar to that of bridges with cast-in-place deck slab. The addition of transverse post-tensioning did not seem to affect the load distribution at the service limit stage. No signs of shear key distress or longitudinal shear key cracks were observed.

7. Beyond cracking, the distribution of the load followed a similar pattern to that before cracking. No signs of shear key failure were observed. The load distribution factor beyond cracking was similar to that before cracking. Similarly, transverse post-tensioning did not seem to affect the load distribution among the beams at this stage of loading.

8. To evaluate the shear key capacity, it was decided to partially crack the shear key joint by loading one of the exterior beams in the bridge model under four point-loading. The beam was loaded to approximately twice its load carrying capacity without any shear key cracking. After further increasing the load, minor cracks around the shear key joints developed. However, all the cracks were localized at the concrete side of the joint and did not seem to propagate uniformly. The most noticeable crack developed in the diaphragm joining the exterior beam to the rest of the bridge model at the mid-span. It was therefore concluded that UHPC shear key joints without transverse post-tensioning can promote the integrity of decked bulb T beam bridges given that adequate number of UHPC transverse diaphragms are provided.

9. The bridge model was loaded under four-point loading in load cycles to 160 kip, which represented 80 % of its estimated maximum load carrying capacity. The performance of the bridge model was similar to those of the control beams. The load-deflection curves demonstrated a bilinear relationship with the decompression load marking the change of slope on the bilinear curve.

10. The strength limit state testing included loading the center beam of the bridge model under four-point loading to failure. The failure took place at a load level of 220 kip. The failure started with the rupture of the prestressed CFCC strands in the loaded beam, followed by the rupture of the CFCC strands in the adjacent beams, and finally the strands in the exterior beams. The rupture of the strands was accompanied by a loud popping sound, significant cracks, and spalling of the concrete. The failure, therefore, was classified as a tension

failure. After failure, the shear key joints were inspected. It was noticed that hairline shear cracks developed at the mid-span around the shear key joints of the loaded beam. Nevertheless, the deflection of the bridge model at the maximum load showed a uniform load distribution between the beams. This suggested that these cracks developed only after the failure of the prestressing strands in the loaded beam. Overall, it is reasonable to conclude that UHPC shear key joints and UHPC transverse diaphragms were sufficient to transfer the load laterally even at the ultimate load.

The following observations and conclusions were drawn based on the results of the numerical investigation:

1. The results from the developed comprehensive numerical models for the control beams and the bridge model fairly matched the experimental results and showed a difference of less than 10%.

2. The parametric study included modeling full-scale decked bulb T beam highway bridges with various spans, widths, and skew angles, and analyzing the bridges under positive temperature gradient and under traffic loads. Both temperature gradient and traffic loads were adopted from AASTHO LRFD (2012).

3. The analysis of different highway bridges under temperature gradient alone revealed that when the bridges are exposed to positive temperature gradient, tensile stresses develop near the shear key joints. If no diaphragms are provided, the tensile stresses seem to accumulate at the ends of the simply supported bridges.

4. Adding end diaphragms has a significant influence on the development of the tensile stresses around the shear key joints. It was noticed that with adding the end diaphragms, the tensile stresses migrated from the ends to the mid-region of the bridge and they became more uniform. However, adding intermediate diaphragms did not seem to influence the distribution of the tensile stresses due to positive temperature gradient stresses any further. Therefore, it is concluded that end diaphragms are mandatory in decked bulb T beam bridges to avoid the development of shear key cracks at the ends of the bridge.

5. The traffic load (AASHTO LRFD HL-93 vehicular loading with impact allowance) was applied to the bridge model at three locations: in Location I, the vehicular loading was

applied next to the parapet at one side of the bridge. In Location II, two vehicular loadings were applied next to the parapets at both sides of the bridge model. In Location III, two vehicular loadings were applied at the mid-width of the bridge model. In the longitudinal direction, all the traffic loads were positioned as to induce the maximum bending moment of the span.

6. Positive temperature gradients with vehicular loading at Locations I and II resulted in increasing the tensile stresses near the ends of bridges with no transverse diaphragms. Adding two end diaphragms mitigated the development of tensile stresses and eliminated the potential of shear key cracking. The addition of intermediate diaphragms did not seem to influence the stress level at the ends of the bridge under this particular loading case.

7. When applying positive temperature gradient with vehicular loading at Location III, the tensile stresses developed along the span with a concentration at the middle region of the span under the truck loading. Adding end diaphragms did not seem to decrease the tensile stresses, while adding intermediate diaphragms significantly reduced the tensile stresses.

8. Bridges with skew angle exhibited an increase in tensile stresses at the shear key joints with the concentration of the tensile stresses near the corners when vehicular loading was at Locations I and II, and near the middle region of the span when vehicular loading was at Location III. As a results, it is recommended that decked bulb T beam bridge systems without TPT should not be used for a skew angle of 45 degrees or higher.

9. Overall, it was determined from the numerical investigation that for decked bulb T beam bridges with span range from 50 to 100 ft, five equally spaced transverse diaphragms would be sufficient to eliminate the shear key cracks. No TPT force is necessary. The same number of diaphragms can be used with a skew angle of 30 degrees. However, analysis of bridges with skew angles of 45 and 60 degrees showed shear key cracking under one or more load cases.

10. Applying TPT in decked bulb T beam bridges with no skew generated a field of transverse compressive stresses in the deck flange. The compressive stresses ranged between 20 to 100 psi with TPT of 50 to 200 kip/diaphragm in five diaphragms. This compressive field seemed to relieve some of the tensile stresses around the shear key joints but it was noticed

that this relief was maximized near the mid-span and minimized near the ends of the span. Overall, due to the increase in the longitudinal tensile stresses that accompanied the application of transverse post-tensioning force, the maximum principal stresses in the deck flange did not decrease and therefore, the probability of crack development remained unchanged.

5.3 Recommendations

Based on the experimental and numerical investigations, the following recommendations are drawn:

1. Based on the literature review, bulb T beams are routinely used by several states and a few states have successfully constructed decked bulb T beam bridges in their implementation for accelerated bridge construction. In addition, the comprehensive numerical models compared well to the control beams and showed a uniform distribution for traffic loads among the adjacent beams. Therefore, it is recommended that state DOT's consider Decked bulb T beam as a viable option in their bridge construction.
2. The overall procedure for the construction of CFCC decked bulb T beams is fairly simple and quick. CFCC strands are lighter than steel and they are easy to handle. However, special care shall be made to avoid shearing the strands or scratching them.
3. The coupler system of prestressed CFCC strands, while effective, is time consuming and it is strongly recommended that a simpler CFCC anchorage system be developed, tested, and verified to expedite construction process.
4. The long-term performance of CFCC strands is a crucial element in bridge performance and must be thoroughly examined and investigated. A research investigation is currently underway at Lawrence Technological University to establish a complete performance profile for CFCC material, determine the appropriate design factors, and ensure the longevity and safety of bridges with CFCC strands.

REFERENCES

1. AASHTO, 2007, "AASHTO LRFD Bridge Design Specifications," 4th ed., American Association of State Highway and Transportation Officials, Washington, DC.
2. AASHTO T 259-02, 2002, "Standard Method of Test for Resistance of Concrete to Chloride Ion Penetration," American Association of State Highway and Transportation Officials, Washington, DC.
3. Abdelrahman, A. and Rizkalla, S., 1999, "Deflection Control of Concrete Beams Pretensioned by CFRP Reinforcements," Journal of Composites for Construction, ASCE, Vol. 3, No. 2, May, pp. 55 -62.
4. American Concrete Institute (ACI), 2004, "Prestressing Concrete Structures with FRP Tendons." ACI 440.4R-04, Farmington Hills, MI.
5. American Concrete Institute (ACI), 2006, "Guide for the Design and Construction of Structural Concrete Reinforced with FRP Bars." ACI 440.1R-06, Farmington Hills, MI.
6. ASTM Standard C496, 2011, "Test Method for Splitting Tensile Strength of Cylindrical Concrete Specimens," ASTM International, West Conshohocken, PA, USA. DOI: 10.1520/C0882_C0882M-05E01, www.astm.org.
7. ASTM Standard C882, 2005, "Test Method for Bond Strength of Epoxy-Resin Systems Used With Concrete by Slant Shear," ASTM International, West Conshohocken, PA, USA. DOI: 10.1520/C0496_C0496M-11, www.astm.org.
8. ASTM Standard C666, 2008, "Test Method for Resistance of Concrete to Rapid Freezing and Thawing," ASTM International, West Conshohocken, PA, USA. DOI: 10.1520/C0666_C0666M-03R08, www.astm.org.
9. ASTM Standard C944, 2005, "Test Method for Abrasion Resistance of Concrete or Mortar Surfaces by the Rotating-Cutter Method," ASTM International, West Conshohocken, PA, USA. DOI: 10.1520/C0944_C0944M-99R05E01, www.astm.org.
10. Bache, H., 1981, "Densified Cement/Ultra-Fine Particle-Based Materials," CBL Report No. 40. Aalborg Portland, Denmark.

11. Badwan, I. and Liang R., 2007, “Performance Evaluation of Precast Posttensioned Concrete Multibeam Deck,” J. Perform. Constr. Facil. Vol. 21, Issue 5, pp. 368: 374

12. Bakht, B.; Jaeger L.G.; and Cheung M.S., 1983, “Transverse Shear in Multi Beam Bridges,” Journal of Structural Engineering, Vol. 109, No. 4, April, pp. 936–949.

13. Bhide, S., 2008, "Material Usage and Condition of Existing Bridges in the US", Portland Cement Association, PCA Report, No. SR34204, Skokie, Illinois, USA.

14. Collins, M.P.; Mitchell, D.; and Macgregor, J.G., 1993, "Structural Design Considerations for High-Strength Concrete," Concrete International, American Concrete Institute, Vol. 15, No. 5, May, pp. 27–34.

15. Dolan, C.W. and Swanson, D., 2002 “Development of Flexural Capacity of a FRP Prestressed Beam with Vertically Distributed Tendons,” Composites Part B: Engineering, Vol. 33, Issue 1, January, pp. 1-6.

16. Ebeido, T. and Kennedy J., 1996, “Girder Moments in Continuous Skew Composite Bridges,” Journal of Bridge Engineering, Vol. 1, No. 1, Feb., pp. 37-45

17. El-Remaily, A.; Tadros, M.K.; Yamane T.; and Krause, G., 1996, “Transverse Design of Adjacent Precast Prestressed Concrete Box Girder Bridges,” PCI Journal, V. 41, No. 4 , July–August, pp. 96–112.

18. El-Sayed, A.K.; El-Salawaky, E.F.; and Benmokrane, B., 2006 “Shear Capacity of High-Strength Concrete Beams Reinforced with FRP Bars,” ACI Structural Journal, Vol. 103, No. 3, May-June, pp. 383-389.

19. Fam, A.Z.; Rizkalla, S.H.; and Tadros, G., 1997 “Behavior of CFRP for Prestressing and Shear Reinforcements of Concrete Highway Bridges,” ACI Structural Journal, Vol. 94, No. 1, January-February, pp. 77-86.

20. French, C.E.; Shield, C.K.; Klaseus, D.; Smith, M.; Eriksson, W.; Ma, Z.J.; Zhu, P.; Lewis, S.; and Chapman, C; 2011, “Cast-in-Place concrete Connections for Precast Deck Systems,” Final Report, NCHRP No. 173, web-only Document 173, www.trb.org.

21. Gilberston, C.U.; Attanayake, T.; Ahlborn; and Aktan. H., 2006, "Prestressed Concrete Box-Beam Bridge Performance: Condition Assessment and Design Analysis," Transportation Research Board (TRB), Washington, D.C., U.S.A..

22. Grace, N.F.; Soliman, A.K.; Abdel-Sayed, G.; and Saleh, K.R., 1998, "Behavior and Ductility of Simple and Continuous FRP Reinforced Beams," Journal of Composites for Construction, Vol. 2, No. 4, November, pp. 186-194.

23. Grace and Abdel-Sayed, 1999, "Mathematical Solution of Skew Bridges Prestressed with CFRP Strands," ACI Structural Journal, V. 96, No. 69, Nov.-Dec.

24. Grace, 1999, "Innovative CFRP Continuous Prestressed Concrete Bridges," ACI Concrete International, V. 21, No. 10, Oct.

25. Grace; Abdel-Sayed; Soliman; and Sale, 1999, "Strengthening Reinforced Concrete Beams Using Fiber Reinforced Polymer CFRP Laminates," ACI Structural Journal, V. 96, No. 5, Sept.-Oct.

26. Grace; Enomoto, T.; and Yagi, K., 2002, "Behavior of CFCC and CFRP Leadline Prestressing Systems in Bridge Construction," PCI JOURNAL, Vol. 47, No. 3, May/June.

27. Grace; Abdel-Sayed; Navarre; Nacey; Bonus; and Collavino, 2003, "Full-Scale Test of Prestressed Double-Tee Beam," ACI-Concrete International, Vol. 25, No. 4, April.

28. Grace, N.F. and Singh, S.B. 2003 "Design Approach for Carbon Fiber-Reinforced Polymer Prestressed Concrete Bridge Beams," ACI Structural Journal, Vol. 100, No.3, May, pp. 365-376.

29. Grace, N.F.; Roller, J.J.; Navarre, F.N.; Nacey, R.B.; and Bonus, W., 2005, "Truck Load Distribution Behavior of the Bridge Street Bridge, Southfield, Michigan," PCI Journal, Vol. 50, No. 2, March/April, pp.76-89.

30. Grace, N.F.; Jensen, E.; Matsager, V.; Bebawy, M.; Hanson, J.; and Soliman, E., 2008, "Use of Un-bonded CFCC for Transverse Post-Tensioning of Side-by-Side Box-Beam Bridges," Technical Report, Michigan Department of Transportation, Lansing, MI.

31. Graybeal, B.A., 2006, "Material Property Characterization of Ultra-High Performance Concrete," Report No. FHWA-HRT-06-103, August, McLean, VA.

32. Graybeal, B.A., 2006, "Structural Behavior of Ultra-High Performance Concrete Prestressed I-Girders," Report No. FHWA-HRT-06-115, August, McLean, VA.

33. Graybeal, B.A., 2010, "Behavior of Field-Cast Ultra-High Performance Concrete Bridge Deck Connections Under Cyclic and Static Structural Loading," FHWA Publications, Report No. FHWA-HRT-11-023, Nov., McLean, VA.

34. Hansson, C.M; Poursaee A.; and Jaffer S.J., 2007, "Corrosion of Reinforcing Bars in Concrete," Portland Cement Association (PCA), R&D Serial No. 3013, Skokie, Illinois. www.cement.org

35. Hassan, T.; Rizkalla, S.; Abdelrahman, A.; and Tadros, G., 1999 "Design Recommendations for Bridge Deck Slabs Reinforced by Fiber Reinforced Polymers," Proceedings of the Fourth International Symposium on Fiber Reinforced Polymers Reinforcement for Concrete Structures, FRPRCS-4, ACI-SP-188, Baltimore, USA, pp. 313-323.

36. Hill, J.J.; McGinnis, L.G.; hughes, W.R.; and Shirole, A.M., 1988, "Design and Construction of Transversely Posttensioned Concrete Bulb Tee Beam Bridge," Transportation Research Record, Issue 1180, ISSN 0361-1981, Washington, DC, U.S.A., pp. 87-89.

37. Hlavacs, G.; Long, T.; Miller, R.; and Baseheart, T., 1996, Nondestructive Determination of Response of Shear Keys to Environmental and Structural Cyclic Loading. Transportation Research Record, V. 1574, pp. 18–24.

38. Huang, J.; French, C.E.; and Shield, C.K., 2004, "Behavior of Concrete Integral Abutment Bridges," St. Paul, Minnesota: Minnesota Department of Transportation.

39. Jo, B.W.; Tae, G.H.; and Kwon, B.Y., 2004, "Ductility Evaluation of Prestressed Concrete Beams with CFRP Tendons," Journal of Reinforced Plastics and Composites, ASCE, Vol. 23, No. 8, pp. 843-859.

40. Khaloo, A. and Mirzabozorg, H., 2003, "Load Distribution Factors in Simply Supported Skew Bridges," Journal of Bridge Engineering, Vol. 8, No. 4, July/August, pp. 241-244

41. Lall, J.; Alampalli, S.; and Di Cocco, E.F., 1998, "Performance of Full-Depth Shear Keys in Adjacent Prestressed Box Beam Bridges," PCI Journal, V. 43, No. 2, March–April, pp. 72–79.

42. Li, L.; Ma, Z.J.; and Oesterle, R.G., 2010, "Improved Longitudinal Joint Details in Decked Bulb Tees for Accelerated Bridge Construction: Fatigue Evaluation," Journal of bridge Engineering, Vol. 15, No. 5, Sept/Oct. pp. 511:522

43. Martin, L.D.; and Osborn, A.E.N., 1983, "Connections for Modular Precast Concrete Bridge Decks," Report No. FHWA/RD-82/106, US DOT, Federal Highway Administration.

44. Michigan Department of Transportation Construction and Technology Division, 2005, "Box-Beam Concerns Found Under the Bridge," C & T Research Record, No. 102, September, pp. 1-4.

45. Miller, R.A.; Hlavacs, G.M.; Long T.; and Greuel, A., 1999, "Full-Scale Testing of Shear Keys for Adjacent Box Girder Bridges," PCI Journal, V. 44, No. 6, November–December, pp. 80–90.

46. Morais, M.M. and Burgoyne, C. J., 2003 "Experimental Investigation of the Ductility of Beams Prestressed with FRP," Proceedings of the 6th International Symposium on FRP Reinforcement for Concrete Structures (FRPRCS-06), Singapore, pp.1013-1022.

47. Mutsuyoshi, H. and Machida, A., 1993, "Behavior of Prestressed Concrete Beams using FRP as Cable," Proceedings of International Symposium on FRP Reinforcement for Concrete Structures, American Concrete Institute, pp. 401–417.

48. Namaan, A.E.; Tan, K.H.; Jeong, S. M.; and Alkahiri, F.M., 1993, "Partially Prestressed Beams with Carbon Fiber Composite Cable Strands: Preliminary Tests on Strands," International Symposium on Fiber Reinforced-plastic Reinforcement for Concrete Structures, SP-138 ACI, Farmington Hills, MI, p. 441-464.

49. New York State Department of Transportation (NYSDOT), 1992, "Modifications of the Current Shear Key and Tendon System for Adjacent Beam Prestressed Concrete Structures," Engineering Instruction, pp. 1-6.

50. Oesterle, R.G. and Elremaily, A.F., 2009, “Design and Construction guidelines for Long-span Decked Precast, Prestressed concrete Girder bridge,” Final Report, NCHRP Project No. 12-69, www.trb.org

51. Owen C.R., 1987, “Continuity Strengthens South Fork Hoh River Bridge Replacement,” PCI Journal, Vol. 32, No. 1, Jan./Feb., pp. 86:103

52. Ozyildirim, C., 2011, “Case Study: Ultra High Performance Concrete with Steel Fibers for the Route 624 Bridge in Virginia,” SP-280, Advances in FRC Durability and field Applications, ACI symposium Publication 280 CD-ROM, Farmington Hill, Mich.

53. Park, H., 2003, “Model-Based Optimization of Ultra-High Performance Concrete Highway Bridge Girders,” Massachusetts Institute of Technology, Cambridge, MA.

54. Parsekian, G.A.; Shrive, N.G.; Brown, T. G.; Kroman, J.; Seibert, P. J.; Perry V. H.; and Boucher, A., 2008, “Innovative Ultra-high Performance Concrete Structures.” In Tailor Made Concrete Structures. Taylor & Francis Group, London, pp. 325-330.

55. Perry, V. and Weiss, G., 2009, “Innovative Field Cast UHPC Joints for Precast Bridge Decks Design, Prototype Testing and Projects,” UHPFRC 2009 – November 17th & 18th, Marseille, France

56. Popovics, S., 1973, "A Numerical Approach to the Complete Stress-Strain Curve of Concrete," Cement and Concrete Research, Vol. 3, No. 5, May, pp. 583–599.

57. Prestressed Concrete Institute (PCI), 2004, “PCI Design Handbook,” 6th Edition, Chicago, Illinois.

58. Soh, M., 2003, “Model-Based Design of Ultra-High Performance Concrete Prototype Highway Bridge Girder,” Massachusetts Institute of Technology, Cambridge, MA.

59. Stoll, F.; Saliba J.E.; and Casper L.E., 2000, “Experimental Study of CFRP-Prestressed High-Strength Concrete Bridge Beams,” Composite Structures (UK), Vol. 49, No. 2 pp.191-200.

60. Thorenfeldt, E.; Tomaszewicz, A.; and Jensen, J. J., 1987, "Mechanical Properties of High-Strength Concrete and Application in Design," Proceedings of the Symposium on Utilization of High-Strength Concrete, Tapir, Trondheim, pp. 149–159.

61. Tuchscherer, R.G.; Birrcher, D.B.; and Bayrak, O., 2011, “Strut-and-tie Model Design Provisions.” Precast/Prestressed Concrete Institute (PCI), winter 2011, 155-170.

62. Washington State Department of Transportation, 2008, “Bridge Standard Drawings,” http://www.wsdot.wa.gov/eesc/bridge/drawings/index.cfm?fuseaction=drawings &section_nbr=6&type_id=24

63. Youakim, S.A.; Karbhari, V.M.; Ghali, A.; and.Hida, S.E., 2007, “Prediction of Long-Term Prestress Losses,” Prestressed Concrete Institute Journal, March – April 2007, pp. 116-130.

64. Zou, P.X.W. and Shang, S., 2007, “Time-Dependent Behavior of Concrete Beams Pretensioned by Carbon Fiber-Reinforced Polymers (CFRP) Tendons.” Construction and Building Materials, Vol. 21, pp. 777-788.

65. Zsutty, T., 1971, “Shear Strength Prediction for Separate Categories of Simple Beam Tests.” ACI Structural Journal, 68 (2), 138–143.